University of Southampton

Faculty of Engineering and Physical Sciences
School of Physics and Astronomy

Applications of non-perturbative renormalisation for lattice QCD

by

Rajnandini Mukherjee

ORCiD: 0000-0003-1015-8533

A thesis for the degree of
Doctor of Philosophy

November 2024

University of Southampton

Abstract

Faculty of Engineering and Physical Sciences
School of Physics and Astronomy

Doctor of Philosophy

Applications of non-perturbative renormalisation for lattice QCD

by Rajnandini Mukherjee

The Standard Model (SM) of particle physics, despite proving to be the most robust framework for our current understanding of fundamental particles and their interactions in nature, fails to account for several observed phenomena. In order to uncover the New Physics beyond the SM and further our theoretical understanding of nature, it is important to perform precision tests on its predictions, and also explore theories beyond the Standard Model (BSM). Lattice quantum chromodynamics (QCD) is an *ab initio* framework for testing the SM in the non-perturbative regime of QCD; observables on the discrete lattice can be related to their continuum counterparts by performing a continuum extrapolation. An important corequisite for this procedure is the renormalisation of bare quantities computed on the lattice. In this thesis we present two studies that aim to make high precision predictions for SM and BSM parameters with the use of regularisation-independent momentum subtraction schemes for the non-perturbative renormalisation of lattice quantities.

We present non-perturbative results for BSM kaon mixing matrix elements in the isospin symmetric limit ($m_u = m_d$) of QCD, including a complete estimate of all dominant sources of systematic error. Our results are obtained from numerical simulations of lattice QCD with $N_f = 2+1$ flavours of dynamical domain wall fermions. We include data at three lattice spacings in the range $a = 0.11$ – $0.07\,\text{fm}$ and with pion masses ranging from the physical value up to $450\,\text{MeV}$. This improves upon earlier studies by including direct calculations at physical quark masses and a third lattice spacing, therefore making the removal of discretisation effects significantly more precise and eliminating the need for any significant mass extrapolation beyond the range of simulated data. We renormalise the lattice operators non-perturbatively using RI/SMOM off-shell schemes. These schemes eliminate the need to model and subtract non-perturbative pion poles that arise in the RI/MOM scheme. Furthermore, since the calculations are performed with domain wall fermions, the unphysical mixing between chirality sectors is suppressed. Our results for the bag parameters in the $\overline{\text{MS}}$ scheme at $3\,\text{GeV}$ are $B_K \equiv \mathcal{B}_1 = 0.5240(17)(54)$, $\mathcal{B}_2 = 0.4794(25)(35)$, $\mathcal{B}_3 = 0.746(13)(17)$, $\mathcal{B}_4 = 0.897(02)(10)$ and $\mathcal{B}_5 = 0.6882(78)(94)$,

where the first error is from lattice uncertainties and the second is the uncertainty due to the perturbative matching to $\overline{\text{MS}}$.

We also present the first numerical implementation of a massive momentum subtraction (RI/mSMOM) renormalization scheme and use it to calculate the charm quark mass. This scheme aims to curb discretisation effects in the study of heavy quark observables on the lattice. Based on ensembles with three flavours of dynamical domain wall fermions with lattice spacings in the range $0.11 - 0.08\,\text{fm}$, we demonstrate that the mass scale which defines the RI/mSMOM scheme can be chosen such that the extrapolation has significantly smaller discretisation effects than the RI/SMOM scheme which is defined in the massless limit. Converting our results to the $\overline{\text{MS}}$ scheme we obtain $\overline{m}_c(3\,\text{GeV}) = 1.008(13)\,\text{GeV}$ and $\overline{m}_c(\overline{m}_c) = 1.292(12)\,\text{GeV}$.

Contents

List of Figures

List of Tables

Declaration of Authorship

I, Rajnandini Mukherjee, declare that this thesis and the work presented in it is my own and has been generated by me as the result of my own original research.

I confirm that:

1. This work was done wholly or mainly while in candidature for a research degree at this University;
2. Where any part of this thesis has previously been submitted for a degree or any other qualification at this University or any other institution, this has been clearly stated;
3. Where I have consulted the published work of others, this is always clearly attributed;
4. Where I have quoted from the work of others, the source is always given. With the exception of such quotations, this thesis is entirely my own work;
5. I have acknowledged all main sources of help;
6. Where the thesis is based on work done by myself jointly with others, I have made clear exactly what was done by others and what I have contributed myself – this is detailed at the end of chapter 1;
7. Parts of this work have been published as: [9], [10], and [11].

Signed:..... Date:.....

Acknowledgements

First and foremost, I am grateful to my supervisor Prof Jonathan Flynn for all his support and guidance during the four years of my PhD, and for always having his door open for my questions.

I thank the University of Southampton Presidential Scholarship for funding my PhD.

I would like to thank the members of the lattice group at the University of Southampton, in particular Prof Andreas Jüttner and Prof Christopher Sachrajda, for the many useful comments, discussions, and suggestions. I am also grateful to Prof Luigi Del Debbio and Dr Nicolas Garron, as well as other members of the RBC/UKQCD collaboration for their interest, support, and inputs in the weekly discussions.

I owe a special debt of gratitude to Dr J. Tobias Tsang and Dr Felix Erben for teaching me many things and giving me so much of their time. All the work in this thesis is in collaboration with them and would not have been possible without their untiring patience, guidance, and encouragements.

I would like to thank my friends and fellow office-mates Alessandro, Dalius, Vlad, Jacan, Giorgio, Mauricio, Ahmed, and Joe for keeping me sane and in good company these past four years. I also wish to thank Bhumika Billa for being my home away from home.

Finally, I am most grateful to my family for having gone above and beyond to support me in my academic pursuits. I would like to thank my sister for being my rock and my role model. And I would like to thank Ma and Baba for a lifetime of love and support, this thesis is dedicated to them.

for Ma and Baba

Chapter 1

Introduction

Particle physics is the study of the fundamental particles and forces that govern interactions at very small length scales. The *Standard Model* (SM) is a well-established theory which describes how particles interact under three of the four known fundamental forces in nature: the electromagnetic, weak, and strong forces. It is an extremely successful theory with no confirmed inconsistency between theoretical predictions and experimental observation, and has so far allowed us to explain a wide variety of particles as well as predict some new ones. However, several observed phenomena that are not explicable within the framework of the SM lead us to believe that it must be an incomplete theory, thereby suggesting the existence of *New Physics*. These include

- The observed scale of matter-antimatter (baryon) asymmetry: although it would be a natural assumption that the universe is charge-neutral, the SM does not resolve why the universe is matter-dominant to the observed extent.
- Gravity: the SM does not include a description of the fourth fundamental force, gravity, and at present there is no known satisfactory quantum field theory (QFT) of gravity.
- Origin of SM parameters: there are 18 free parameters in the SM theory, corresponding to quark and lepton masses, gauge couplings, the mixing angles and charge-parity violation phase of the Cabbibo-Kobayashi-Maskawa (CKM) matrix, and the Higgs mass and vacuum expectation value. These parameters are measured experimentally, and at present there is no explanation for their origin, the wide range they cover, and their hierarchies.

The SM include also fails to explain, amongst other puzzles, the precise nature of neutrino masses and oscillations, dark matter and dark energy, and the size of the cosmological constant.

The aim of modern particle physics has therefore been to address these puzzles, and given the availability of high precision data from current and future experiments, there are many ways to make progress. These include making theoretically motivated extensions to the SM and testing their validity, and over-constraining the SM parameters to high precision in order to look for discrepancies with experiments.

While many SM predictions can be made to high precision using analytical calculations, this is not the case for low-energy hadronic processes due to the non-perturbative nature of strong interactions. However, interactions at this scale are often key to constraining the processes described by the SM. While there exist effective field theory treatments in this regime, lattice quantum chromodynamics (QCD) provides a systematically improvable framework for determining the observables in such non-perturbative processes from first principles by studying the theory in a discrete Euclidean spacetime inside a finite box with some boundary conditions.

In this thesis we present two studies that employ the framework of lattice QCD to constrain SM parameters as well as make predictions for beyond the Standard Model (BSM) parameters with high precision.

1. The SM allows for the violation of charge-parity (CP) symmetry in weak processes, and this is known to generate matter-antimatter asymmetry. However, the degree of CP-violation in the SM does not explain the observed extent of baryon asymmetry. It is possible to make theoretical predictions for a measure of CP-violation predicted by the SM, as well as by that predicted by BSM theories as part of the search for New Physics. A candidate process for making such theoretical prediction involves a neutral meson mixing with its anti-particle; this is mediated by weak interactions and violates CP symmetry. We study the process of neutral kaon mixing and make the following predictions for the phenomenologically relevant bag and ratio parameters in the $\overline{\text{MS}}$ scheme at an energy scale of 3 GeV:

$$\begin{aligned}
\mathcal{B}_1^{\overline{\text{MS}}} &= 0.5240(17)(54), \\
\mathcal{B}_2^{\overline{\text{MS}}} &= 0.4794(25)(35), \\
\mathcal{B}_3^{\overline{\text{MS}}} &= 0.746(13)(17), \\
\mathcal{B}_4^{\overline{\text{MS}}} &= 0.897(02)(10), \\
\mathcal{B}_5^{\overline{\text{MS}}} &= 0.6882(78)(94), \\
R_2^{\overline{\text{MS}}} &= -18.90(12)(17), \\
R_3^{\overline{\text{MS}}} &= 5.92(05)(13), \\
R_4^{\overline{\text{MS}}} &= 41.94(44)(46), \\
R_5^{\overline{\text{MS}}} &= 10.64(14)(15)\,,
\end{aligned} \tag{1.1}$$

where the parentheses report lattice and perturbative matching uncertainties. Note that $\mathcal{B}_1$ contributes to the SM measure of indirect CP-violation, ϵ_K, while the other parameters constrain BSM theories for kaon mixing.

2. Due to the discrete nature of lattice QCD, it is challenging to resolve both light and heavy quarks in the same box. With modern improvements to computing resources and simulation algorithms, we are now able to study the physics of heavy quarks (for example charm and bottom) more directly on the lattice, without needing to use discretised effective theories. We present a prediction for the mass of the charm quark at the charm scale:

$$m_c^{\overline{\text{MS}}}(m_c^{\overline{\text{MS}}}) = 1.292(5)(10)(4), \tag{1.2}$$

where the three errors arise due to statistical, systematic, and perturbative matching uncertainties, respectively.

The connecting theme in this thesis is that of *non-perturbative renormalisation* (NPR). It is often not possible to naïvely extrapolate observables measured on the lattice to the continuum (impose the limit of a vanishing lattice spacing) without running into divergences. Most bare quantities on the lattice need to go through the process of renormalisation before the continuum limit can be imposed, and the choice of renormalisation scheme used often plays a role in making continuum predictions to a high precision while controlling unwanted lattice artefacts.

In this thesis we use a non-perturbative scheme, known as RI/SMOM, to carry out the renormalisation procedure for bare lattice-generated bag and ratio parameters in the study of neutral meson mixing, in particular kaon mixing. We then do a first numerical study of an extension to this scheme, called RI/mSMOM, in order to improve its suitability to the study of heavy quarks on the lattice by reducing discretisation effects.

The remainder of this thesis is structured as follows: Chapter 2 presents a brief introduction to the SM and its properties; in particular it outlines the theoretical background for neutral meson mixing. Chapter 3 introduces the formalism of lattice QCD, presenting the essential features relevant for the projects in this thesis. Chapter 4 details non-perturbative renormalisation using the RI/SMOM scheme for bilinear and four-quark operators. Note that these three chapters do not present original work but rather a summarised literature review of the topics that make up the necessary ingredients in the subsequent chapters. Chapters 5 and 6 provide the details and results from a study of neutral kaon mixing [9], and a computation of the charm quark mass using a massive NPR scheme [10], respectively, followed by the conclusions in chapter 7.

The work presented in this thesis is my own (with guidance from my supervisor and carried out jointly with my collaborators), with the following exceptions:

- Chapters 5 & 6: the data generation procedure for the data sets used.
- Chapter 5: (on all ensembles) the combined two- and three-point functions fits for generating the bare bag and ratio parameters, fits for pion mass and decay constant, the study of binning choices for correlation functions, and the calculation of valence strange quark correction factors.
- Chapter 5: (on all ensembles) the non-perturbative renormalisation constants in the RI/SMOM$^{(\not{q},\not{q})}$ scheme.
- Chapter 6: continuum perturbation theory calculations for the matching factor $R_m^{\overline{\text{MS}}\leftarrow\text{RI/mSMOM}}$ at one-loop order in Landau gauge.

Chapter 2

The Standard Model

The Standard Model (SM) of particle physics is a quantum field theory that describes the properties and interactions of all known elementary particles under the strong, weak, and electromagnetic forces. It was developed in the second half of the twentieth century [12–20], and has been a remarkably successful theory.

The elementary particles that make up the SM can be broadly categorised into *bosons*, with integer spin (instrinsic angular momentum), and *fermions*, with half-integer spin. The *gauge* or *vector* bosons are mediators of interactions: the photon for electromagnetic interactions, gluons for strong interactions, and $W^{\pm}$ and Z-bosons for the weak interactions. The Higgs is a *scalar* boson of the Higgs field which is responsible for generating mass for all fundamental particles via the Higgs mechanism. The fermions come in three generations and can be further classed into *quarks*, particles with *colour* charge, and *leptons*, which come in pairs of a charged lepton and a neutral *neutrino*.

Many elementary particles in the SM were theoretically predicted and subsequently confirmed by experiments. These include the charm quark: proposed in 1970 [21] and detected in 1974 via the J/ψ particle [22, 23]. The Cabibbo-Kobayashi-Maskawa matrix was developed in 1973 [24, 25] predicting a third generation of quarks and introducing CP-violation in the SM; the bottom and top quarks were subsequently confirmed in experiments in 1977 [26] and in 1995 [27], respectively. The $W^{\pm}$ and Z bosons were predicted to be mediators of weak interactions in the SM [17] and were experimentally observed in 1983 [28, 29]. Most recently, the tau neutrino was detected in 2001 [30], and the Higgs boson in 2012 [31, 32]; completing the experimental confirmation of all elementary particles predicted in the SM.

Despite its tremendous success, the model is unable to explain many other phenonema: gravity, neutrino masses and oscillations, the degree of baryogenesis in the primordial universe, among others. Accounting for these phenomena may require the introduction of New Physics via Beyond the Standard Model (BSM) theories. Of particular relevance

to this thesis is the study of neutral meson-mixing interactions within and beyond the SM which violate charge-parity (CP) symmetry since the degree of CP-violation in the SM is not enough to explain the matter-antimatter asymmetry in the observed universe [33–35].

In this chapter, we begin by briefly introducing the formalism of a quantum field theory (QFT) as well as symmetry groups. The description of the underlying physics of the Standard Model – a QFT with $SU(3)_C \times SU(2)_L \times U(1)_Y$ gauge symmetry – is then split into the $SU(3)_C$ sector, known as Quantum Chromodynamics, and the $SU(2)_L \times U(1)_Y$ electroweak sector. We then derive the theory of neutral meson mixing, in particular kaon mixing in and beyond the SM.

2.1 Quantum field theory

The modern description of quantum physics is in the language of mathematical fields. A field theory is a framework derived from fields that take some value over all spacetime points. The fields in a quantum field theory (QFT) are derived by *quantising* classical fields: this can achieved via Dirac's *canonical quantisation* [36], wherein fields are interpreted as operators acting on a Fock space and satisfying commutation relations; or via Feynman's *path integral quantisation* [37], where the basis of the QFT is formed by considering the path travelled by a particle to be the superposition of all possible paths each weighted by its action. In this description particles are viewed as excitations of the fields, as part of a many-body theory which allows for particle creation and annihilation.

In this thesis we work within the path integral formalism of QFT, wherein the vacuum expectation value of an observable $\mathcal{O}$ in a theory with n fields $\psi_1, \ldots, \psi_n$ is given by

$$\langle \mathcal{O} \rangle \equiv \langle \Omega | \hat{\mathcal{O}} | \Omega \rangle = \frac{1}{Z} \int \mathcal{D}\left[\psi_1, \ldots, \psi_n\right] \, \mathcal{O} e^{iS[\psi_1, \ldots, \psi_n]}, \tag{2.1}$$

where $\hat{\mathcal{O}}$ is the operator for the observable, acting on the Fock space of all possible states. Z is the partition function

$$Z = \int \mathcal{D}\left[\psi_1, \ldots, \psi_n\right] \, e^{iS[\psi_1, \ldots, \psi_n]}, \tag{2.2}$$

and $\mathcal{D}$ is the measure for the integral over all possible field configurations. Each path is weighted by the action, S, which is defined as a functional of the fields as

$$S\left[\psi_1, \ldots, \psi_n\right] = \int d^4x \mathcal{L}\left[\psi_1(x), \ldots, \psi_n(x)\right], \tag{2.3}$$

where $\mathcal{L}$ is the *Lagrangian* density that encodes the dynamics of the theory. A field theory is therefore defined by specifying its Lagrangian density.

The SM is specified by a Lagrangian density that can be decomposed as

$$\mathcal{L}_{\mathrm{SM}} = \mathcal{L}_{\mathrm{QCD}} + \mathcal{L}_{\mathrm{EW}}, \tag{2.4}$$

into Quantum Chromodynamics (QCD) and the electroweak (EW) theories. In the subsequent sections, we look into these two sectors in greater detail. However, it is useful to first start with the description of the underlying symmetries of the SM Lagrangian.

2.2 Symmetries of the Standard Model

Symmetries form the basic guiding principle to building a physical theory. These represent field transformation under which the physics of the model remains invariant. In the SM, these transformations derive from the symmetries of spacetime, such as Lorentz invariance, as well as from internal *gauge* symmetries that transform the field representation $\Phi(x)$ as

$$g:\ \Phi(x) \to \Phi'(x) = R_g(x)\Phi(x), \quad g \in G, \tag{2.5}$$

where R_g, a function of the four-position x, is some representation of the element g of a symmetry group G. The Standard Model is a gauge theory based on the symmetry group

$$G_{\mathrm{SM}}:\ SU(3)_C \times SU(2)_L \times U(1)_Y, \tag{2.6}$$

where C stands for *colour*, L for *(left-handed) weak isospin*, and Y for *hypercharge*.

In addition to these continuous symmetries, there are also three discrete symmetries of importance called *parity* (P), *charge conjugation* (C), and *time reversal* (T). P and T are spacetime symmetries that reverse the spatial and temporal coordinates of each point in spacetime respectively

$$\begin{aligned} P:\ x_\mu = (x_0, \mathbf{x}) &\to x'_\mu = (x_0, -\mathbf{x}), \\ T:\ x_\mu = (x_0, \mathbf{x}) &\to x'_\mu = (-x_0, \mathbf{x}), \end{aligned} \tag{2.7}$$

Charge conjugation is a global internal symmetry that reverses the sign of all charges, thereby turning a particle into its antiparticle

$$C:\ \psi \to \overline{\psi}^T; \quad \phi \to \left(\phi^\dagger\right)^T; \quad A_\mu \to -A_\mu, \tag{2.8}$$

where ψ represents a fermion field, ϕ a charged scalar field, and A_μ a gauge field. While strong and electromagnetic interactions are invariant under parity transformations, it was experimentally found that weak interactions are not [38, 39]. This is reflected in the Lagrangian density of the weak interactions as we will see in section 2.4. It was

postulated that weak interactions may still conserve the combined CP symmetry, but evidence of CP-violation in the weak sector was found in Cronin and Fitch's kaon regeneration experiment [40]. It has been shown that all three forces, strong, weak and electromagnetic, obey the combined CPT symmetry.

Symmetries may or may not be exact, and they can be broken explicitly or spontaneously based on how they modify the action and the vacuum of the theory. In the sections that follow, we will derive how the underlying symmetries of the SM generate force carriers and give rise to the known interactions.

2.3 Quantum chromodynamics

Quantum Chromodynamics (QCD) is the quantum theory of the *strong force* which binds quarks into composite particles. It is a gauge theory deriving from the $SU(3)_C$ colour symmetry of the SM gauge group [12,41] and describes quark-gluon interactions. The QCD Lagrangian density is given by

$$\mathcal{L}_{\text{QCD}} = -\frac{1}{4}F^C_{\mu\nu}(x)F^{C,\mu\nu}(x) + \sum_f^{N_f}\overline{\psi}_{f,a}(x)\left(i\not{D}_{ab} - m_f\delta_{ab}\right)\psi_{f,b}(x), \tag{2.9}$$

where the index $f = 1, \ldots, N_f$ sums over the $N_f = 6$ quark flavours present in the theory[1]. The lowercase Greek indices $\mu, \nu = 0, 1, 2, 3$ run over the spacetime components t, x, y, z, and the lowercase Roman indices $a, b = 1, \ldots, N_C$ run over the "colour" indices where $N_C = 3$. The quark fields ψ_f with masses m_f are in the fundamental (triplet) respresentation of $SU(3)_C$ and $\not{D} = \gamma_\mu D^\mu$, where γ_μ are the generators of Clifford algebra (explicit forms provided in appendix A.2), and D_μ is the QCD covariant derivative given by

$$D_\mu = \partial_\mu + ig_sA_\mu = \partial_\mu + ig_sA^C_\mu t^C. \tag{2.10}$$

Here g_s is the QCD coupling constant, and A^C_μ are the components of the gluon field in the adjoint (octet) representation

$$A_{\mu,ab}(x) = A^C_\mu(x)t^C_{ab}. \tag{2.11}$$

The capital Roman index $C = 1, \ldots, 8$ iterates over the 8 generators of $SU(3)_C$ algebra given by $t^C_{ab} = \frac{i}{2}\lambda^C_{ab}$, where λ^C are the Gell-Mann matrices. These generators are represented by traceless anti-hermitian 3×3 matrices, their explicit forms are listed in appendix A.1. A generic $SU(3)_C$ gauge group element represented by $h(x)$ transforms

[1]Note that in addition to the terms in eqn (2.9) one also needs gauge fixing term if working in perturbation theory. These are omitted in the discussion in this chapter.

the quark and gluon fields as

$$\psi_{f,a}(x) \to \psi'_{f,a}(x) = h_{ab}(x)\psi_{f,b}(x), \tag{2.12}$$

$$A_\mu(x) \to A'_\mu(x) = h(x)A_\mu(x)h^{-1}(x) - \frac{1}{g_s}\left(\partial_\mu h(x)\right)h^{-1}(x). \tag{2.13}$$

The gluonic field strength tensor $F_{\mu\nu}$ in eqn (2.9) is defined in terms of the covariant derivative as

$$F_{\mu\nu}(x) = [D_\mu(x), D_\nu(x)] := F^C_{\mu\nu}(x)t^C, \tag{2.14}$$

$$\text{with} \quad F^C_{\mu\nu} = \partial_\mu A^C_\nu - \partial_\nu A^C_\mu + g_s \left[A_\mu, A_\nu\right]^C, \tag{2.15}$$

where the gluon fields have a non-trivial commutation relation owing to QCD being a non-Abelian gauge theory:

$$[A_\mu, A_\nu]^C = if^{ABC}A^A_\mu A^B_\nu. \tag{2.16}$$

Here f^{ABC} are the $SU(3)$ structure constants. This non-Abelian structure allows for gluon-gluon interactions in QCD, in specific, three and four-gluon interactions are present in the theory.

We can count the number of fundamental parameters needed to fully define QCD by inspecting eqn (2.9): these are the $N_f = 6$ quark masses and the strong coupling g_s. This coupling is uniquely weak at high energies and strong at low energies – a phenomenon known as *asymptotic freedom* [42, 43]. The consequence of this is the *confinement* of quarks into bound states, called hadrons, at low energies; hadrons are further categorised into two-quark bound states, or *mesons*, or three-quark bound states, *baryons*. More exotic states such as tetraquarks [44–46] and pentaquarks [47,48] have also been observed in recent experiments. The onset of the confinement or the hadronisation regime of the strong coupling is often characterised by a scale known as $\Lambda_{\text{QCD}} \approx 250 - 700\,\text{MeV}$. The primary degrees of freedom in this regime are quark bilinears, and the symmetries of QCD allow for bilinears of the form $\overline{\psi}\Gamma\psi$ with 16 possible Dirac structures Γ. These can be spanned using a basis of five types of transformations as listed in table 2.1.

In this thesis, we are interested in probing interactions in the SM and beyond at low energy scales, comparable to Λ_{QCD}, where we cannot neglect the non-perturbative nature of the strong coupling. The asymptotic freedom of the QCD coupling implies that the perturbative approach of ordering processes via powers of the coupling constant cannot be applied in this regime. This necessitates the use of the non-perturbative method of lattice QCD for the study of hadronic interactions, as will be discussed in chapter 3.

Γ structure	# of components	$SO(3,1)$ transformation
$\mathbb{1}$	1	scalar
γ_5	1	pseudoscalar
γ_μ	4	vector
$\gamma_\mu\gamma_5$	4	axial vector
$\sigma_{\mu\nu} := \frac{1}{2}[\gamma_\mu, \gamma_\nu]$	6	tensor

Table 2.1: The 16 quark bilinears of QCD grouped into 5 structure-types based on their transformations under Lorentz symmetry.

2.3.1 Chiral symmetry

Consider a massless version of the QCD Lagrangian

$$\mathcal{L}_{\text{QCD}} = -\frac{1}{4}F^C_{\mu\nu}(x)F^{C,\mu\nu}(x) + i\overline{\psi}_{f,a}(x)\not{D}_{ab}\psi_{f,b}(x). \tag{2.17}$$

In addition to $SU(3)_C$ gauge and Lorentz invariance, this Lagrangian has a $U(N_f)_L \times U(N_f)_R$ global symmetry associated with the N_f quark flavours [49, 50]. To illustrate this, let us decompose the quark fields ψ into the *left* and *right*-handed components using left and right projectors:

$$\psi(x) = \psi_L(x) + \psi_R(x), \quad \text{where} \quad \psi_{L,R}(x) = P_{L,R}\psi(x), \tag{2.18}$$

$$\text{with} \quad P_L = \frac{\mathbb{1} - \gamma_5}{2},\ P_R = \frac{\mathbb{1} + \gamma_5}{2}. \tag{2.19}$$

In this *chiral* description, the massless Lagrangian is invariant under $U(N_f)_L \times U(N_f)_R$ transformations

$$\begin{aligned} U(N_f)_L &: \psi_L \to U_L\psi_L, \\ U(N_f)_R &: \psi_R \to U_R\psi_R, \end{aligned} \tag{2.20}$$

where $U_{L,R}$ are represented by unitary matrices in the N_f-dimensional flavour space.

The symmetry group $U(N_f)_L \times U(N_f)_R$ can be decomposed as $SU(N_f)_V \times SU(N_f)_A \times U(1)_A \times U(1)_V$, that is, a combination of non-singlet and singlet vector (V) and axial-vector (A) gauge transformations. As these are symmetries of the massless QCD Lagrangian, Noether's theorem posits the existence of conserved charges or currents j_μ associated with each of them such that $\partial_\mu j_\mu = 0$. We note that

1. The $U(1)_V$ symmetry gives rise to *baryon number* conservation, which is an extremely good symmetry of QCD.

2. The $U(1)_A$ is anomalous, that is, when quantising the theory, one finds that the $U(1)_A$ symmetry changes the measure in the path integral [51, 52] and therefore

it is not an actual symmetry of QCD even in the massless limit. This is known as the *axial anomaly*.

3. The conserved currents associated with the $SU(N_f)_V \times SU(N_f)_A$ part are given by

$$\begin{aligned} j_V^{F,\mu} &= \overline{\psi}\frac{\sigma^F}{2}\gamma^\mu\psi, \\ j_A^{F,\mu} &= \overline{\psi}\frac{\sigma^F}{2}\gamma^\mu\gamma_5\psi. \end{aligned} \tag{2.21}$$

where σ^F are associated with the generators of the $SU(N_f)$ group algebra[2] with $F = 1, \ldots, N_f^2 - 1$. In the massless case, these currents are conserved.

2.3.2 Breaking of chiral symmetry

The ground state of QCD is experimentally known to have a non-zero expectation value for the quark condensate, $\langle 0|\overline{\psi}\psi|0\rangle \neq 0$, therefore indicating that chiral symmetry is broken spontaneously [53–55]. The formation of this chiral condensate arises due to strong coupling dynamics of non-Abelian gauge theories and currently lacks a complete theoretical explanation. Nonetheless, from Goldstone's theorem, the broken generators of the QCD chiral symmetry give rise to massless Goldstone bosons; however this picture is altered with the introduction of non-zero quark masses.

Consider re-introducing a mass matrix $\mathcal{M} = \text{diag}\left(m_1, \ldots, m_{N_f}\right)$ into the QCD Lagrangian. In this case, the mass terms break chiral symmetry *exactly* and the Noether currents of the flavour non-singlet vector and axial vector transformations in eqn (2.21) diverge as

$$\partial_\mu J_V^{F,\mu} = i\overline{\psi}\left[\mathcal{M}, \sigma^F\right]\psi, \tag{2.22}$$

$$\partial_\mu J_A^{F,\mu} = i\overline{\psi}\left\{\mathcal{M}, \sigma^F\right\}\gamma_5\psi, \tag{2.23}$$

where the second equation is known as the non-singlet *axial Ward identity* (AWI) and its right hand side vanishes only for zero quark masses.

Let us consider theories with only a few quark flavours to see how this affects the QCD chiral symmetry:

- $N_f = 2$, with $m_u = m_d \ll \Lambda_{\text{QCD}}$

  Adding a mass term to the QCD Lagrangian explicitly breaks chiral symmetry, however the two quarks are much lighter than the typical interaction scale given by Λ_{QCD}, so this theory posseses *approximate* chiral symmetry. For mass degenerate

[2] For example, for $N_f = 2$ these are the Pauli matrices, and for $N_f = 3$ these are the Gell-Mann matrices; their explicit forms are provided in appendix A.1.

quarks, the commutator in eqn (2.22) vanishes and $SU(2)_V$ becomes an exact symmetry known as *isospin*. From Goldstone's theorem, we expect pseudo-Goldstone bosons corresponding to the generators of the slightly broken $SU(2)_A$ symmetry - these are the three pions π^0, π^+ and π^-.

- $N_f = 3$, with $m_u = m_d \approx m_s \ll \Lambda_{\text{QCD}}$

  Once again in this case there is an explicit breaking of chiral symmetry such that $SU(3)_V$ is conserved, and there are eight pseudo-Goldstone bosons corresponding to the eight broken generators of $SU(3)_A$. These are the three pions, $\pi^{0,+,-}$, four kaons, $K^{0,+}$ and $\overline{K}^{0,-}$, and the η^0 meson.

2.3.3 Chiral perturbation theory (with kaons)

We are interested in the kaon sector for the purposes of this thesis and wish to use the non-perturbative framework of lattice QCD (introduced in chapter 3) to study the phenomenon of kaon mixing (introduced in section 2.5) at low energies. However, it is also possible to describe the low-energy dynamics of QCD in terms of its Goldstone bosons as effective degrees of freedom rather than in terms of quarks and gluon. The resulting low-energy approximation is called *chiral perturbation theory* (χPT) [56]. The agreement or disagreement of this perturbative method to non-perturbative results from the lattice provides insight into the non-perturbative properties of QCD in a given regime of the strong coupling.

For our study, we consider the $N_f = 2$ χPT combined with kaons, that is, $m_u = m_d \equiv m_l \ll m_s, \Lambda_{\text{QCD}}$. In this effective field theory (EFT) the quark masses and momenta are used for power counting. The degrees of freedom in the $N_f = 2$ EFT are the pions, and the lowest order Lagrangian, following the conventions in [57], is given by

$$\mathcal{L}_{N_f=2} = \frac{f^2}{8}\text{Tr}\left(\partial_\mu U^\dagger \partial^\mu U + U^\dagger \chi + \chi^\dagger U\right), \tag{2.24}$$

where U is defined in terms of the pion fields as

$$\begin{aligned} &U(x) = \exp(i\Theta(x)/f), \\ \text{with} \quad &\Theta(x) = \begin{pmatrix} \pi^0(x)/\sqrt{2} & \pi^+(x) \\ \pi^-(x) & -\pi^0(x)/\sqrt{2} \end{pmatrix}, \end{aligned} \tag{2.25}$$

and $\chi = 2B\,\text{diag}\,(m_l, m_l)$. B and f are the *low-energy constants* (LECs) of the EFT. At leading order they are related to the pion mass, $2B^{\text{LO}} m_l = m_\pi^2 \approx (139\,\text{MeV})^2$ and decay constant, $f^{\text{LO}} = f_\pi \approx 130\,\text{MeV}$.

We may now introduce the auxilliary kaon fields

$$K = \begin{pmatrix} K^+ \\ K^0 \end{pmatrix}, \; K^\dagger = \begin{pmatrix} \overline{K}^0 & K^- \end{pmatrix}. \tag{2.26}$$

The interaction of the kaons with pions in this theory – known as kaon chiral perturbation theory or KχPT – is described by the Lagrangian (at leading order)

$$\mathcal{L}^{\mathrm{LO}}_{N_f=2,K} = D_\mu K^\dagger D^\mu K - m_K^2 K^\dagger K, \tag{2.27}$$

where m_K is the kaon mass and the covariant derivative D_μ is given by

$$D_\mu = \partial_\mu + V_\mu. \tag{2.28}$$

The V_μ term induces pion-kaon interactions via the field $u \equiv \sqrt{U}$ as

$$V_\mu = \frac{1}{2}\left(u\partial_\mu u^\dagger + u^\dagger \partial_\mu u\right). \tag{2.29}$$

We can write down the chiral behaviour of the kaon mass and decay constant in this theory using the expansion

$$\begin{aligned} m_K^2 &= Bm_s\left(1 + \frac{a}{f^2}\chi_l\right), \\ f_K &= f\left(1 + \frac{b}{f^2}\chi_l - \frac{3}{4}\frac{\chi_l}{(4\pi f)^2}\log\frac{\chi_l}{\Lambda^2_{\mathrm{QCD}}}\right), \end{aligned} \tag{2.30}$$

where m_s is the strange quark mass, $\chi_l = 2Bm_l$, and a and b are LECs of KχPT.

We will employ KχPT to determine the chiral behaviour of parameters describing neutral kaon mixing in section 2.5.4. In the SM, neutral meson mixing arises from CP-violation in the electroweak sector, as we shall discuss in the following section.

2.4 Electroweak theory

The electroweak (EW) theory, as the name suggest, combines the theory of weak interactions with quantum electrodynamics (QED) [14, 17, 58], deriving from the $SU(2)_L \times U(1)_Y$ sector of the SM gauge group. The $SU(2)_L$ and $U(1)_Y$ groups are referred to as the weak isospin and hypercharge groups, respectively. The electroweak Lagrangian density is given by

$$\mathcal{L}_{\mathrm{EW}} = \mathcal{L}_{\mathrm{gauge}} + \mathcal{L}_{\mathrm{fermions}} + \mathcal{L}_{\mathrm{Higgs}} + \mathcal{L}_{\mathrm{Yukawa}}, \tag{2.31}$$

where each of the four terms represents a different component of the theory. We shall now have a closer look at each of these terms before discussing the Higgs mechanism and its effect on the EW theory.

2.4.1 Gauge and fermionic terms

The gauge component of the EW Lagrangian describes the propagators and interactions of the gauge bosons of the theory as seen before in the case of the QCD Lagrangian

$$\mathcal{L}_{\text{gauge}} = -\frac{1}{4} F^a_{\mu\nu} F^{a,\mu\nu}. \tag{2.32}$$

The field strength tensor is defined in terms of gauge fields as

$$\begin{aligned} F_{\mu\nu} &= [D_\mu, D_\nu]\,, \\ \text{where} \quad D_\mu &= \partial_\mu + i g_W W^I_\mu(x) t^I + \frac{1}{2} i g_B B_\mu(x) Y. \end{aligned} \tag{2.33}$$

The gauge bosons $W_\mu(x)^I$ with $I = 1, 2, 3$ are $SU(2)_L$ group elements in the adjoint representation, and $t^I = \frac{1}{2}\sigma^I$ are the generators of the Lie algebra, with σ^I being the Pauli matrices. Similarly, the gauge field $B_\mu(x)$ is an element of the $U(1)_Y$ group and Y the generator of the group algebra. g_W and g_B are the couplings of these gauge fields.

The fermionic part of the EW Lagrangian describes interactions between the fermions (quarks, leptons) and gauge bosons of the theory. Recall from section 2.3.1 that the fermion fields can be decomposed into the left and right-handed components using chiral projectors as $\psi(x) = \psi_L(x) + \psi_R(x)$. These left and right-handed components of the six quark fields (u, d, c, s, t, b) and the six leptons (ν_e, e, ν_μ, μ, ν_τ, τ) transform differently under the EW gauge group and this is described in the Lagrangian as

$$\mathcal{L}_{\text{fermionic}} = \underbrace{i\overline{Q}^j_L \not{D} Q^j_L + i\overline{u}^j_R \not{D} u^j_R + i\overline{d}^j_R \not{D} d^j_R}_{\text{quarks}} + \underbrace{i\overline{l}^j_L \not{D} l^j_L + i\overline{e}^j_R \not{D} e^j_R}_{\text{leptons}}, \tag{2.34}$$

where $\not{D} = \gamma_\mu D_\mu$, with D_μ being the covariant derivative for the $SU(2)_L \times U(1)_Y$ group as defined in eqn (2.33). The left-handed quark fields form $SU(2)_L$-doublets such that the two fields in a doublet carry weak isospins $+1/2$ and $-1/2$, while the right-handed fields form $SU(2)_L$-singlets with weak isopsin 0:

$$\begin{aligned} Q^i_L &= \left(\begin{pmatrix} u_L \\ d_L \end{pmatrix}, \begin{pmatrix} c_L \\ s_L \end{pmatrix}, \begin{pmatrix} t_L \\ b_L \end{pmatrix} \right) =: \begin{pmatrix} u^i_L \\ d^i_L \end{pmatrix}, \\ u^i_R &= (u_R, c_R, t_R)\,,\ d^i_R = (d_R, s_R, b_R)\,. \end{aligned} \tag{2.35}$$

The leptons obey the same properties with the exception of there existing no right-handed neutrinos in the SM.[3] This means we have

$$\begin{aligned} l_L^i &= \left(\begin{pmatrix} \nu_e \\ e_L \end{pmatrix}, \begin{pmatrix} \nu_\mu \\ \mu_L \end{pmatrix}, \begin{pmatrix} \nu_\tau \\ \tau_L \end{pmatrix} \right) =: \begin{pmatrix} \nu_L^i \\ e_L^i \end{pmatrix}, \\ e_R^i &= (e_R, \mu_R, \tau_R)\,. \end{aligned} \tag{2.36}$$

In this context, the index $i = 1, 2, 3$ labels the three generations of quarks and leptons. We see here explicitly that the weak interactions are not invariant under parity transformations (which exchange left and right-handed particles).

2.4.2 Higgs and Yukawa terms

The Higgs part of the EW Lagrangian describes the propagators and interactions of the Higgs field ϕ with the EW gauge bosons, and is given by

$$\mathcal{L}_{\text{Higgs}} = |D_\mu \phi|^2 - \mu^2 |\phi|^2 - \frac{\lambda}{2} \left(|\phi|^2 \right)^2, \tag{2.37}$$

where μ^2 relates to the mass of the Higgs field and λ is the coefficient of the quartic potential term. The complex scalar field ϕ transforms as a $SU(2)_L$-doublet, parameterised as

$$\phi = \begin{pmatrix} \phi^+ \\ \phi^0 \end{pmatrix}. \tag{2.38}$$

As the Higgs field is in the fundamental representation of $SU(2)_L$, the component fields ϕ^+ and ϕ^0 carry weak isospins of $+1/2$ and $-1/2$ respectively. The covariant derivative is once again defined via the EW gauge group, as given in eqn (2.33).

The Yukawa term of the EW Lagrangian couples the Higgs field to the fermions, and is given by

$$\mathcal{L}_{\text{Yukawa}} = \underbrace{Y_d^{ij} \overline{Q}_L^i \phi d_R^j + Y_u^{ij} \overline{Q}_L^i \phi^\dagger u_R^j}_{\text{quarks}} + \underbrace{Y_l^{ij} \overline{l}_L \phi e_R^j}_{\text{leptons}} + h.c.\,, \tag{2.39}$$

where Y^{ij} are Yukawa couplings between the generations i and j represented by complex matrices.

[3] Although they do not interact via any of the fundamental interactions in the SM, right-handed *sterile* neutrinos are hypothesised to be a possible source of neutrino masses.

2.4.3 Electroweak symmetry breaking

So far we have discussed a theory of four massless gauge bosons that mediate long-range interactions between massless fermions. However, in nature we observe a weak force with short-range interactions mediated by massive bosons, and an electromagnetic force with long-range interactions mediated by a masses boson. This suggests that the $SU(2)_L \times U(1)_Y$ gauge symmetry in the electroweak sector breaks to $U(1)_{\text{EM}}$. This occurs due to spontaneous symmetry breaking in the Higgs sector, introducing gauge-invariant mass terms to the theory via the Yukawa sector [18, 20, 59].

Consider the Higgs potential

$$V_{\text{Higgs}}(\phi) = \mu^2 |\phi|^2 + \frac{\lambda}{2} |\phi|^4 . \tag{2.40}$$

By differentiating with respect to $|\phi|^2$, we see that the potential has an extremum at

$$|\phi| = \left(\frac{-\mu^2}{\lambda} \right)^{1/2} =: v. \tag{2.41}$$

From this, we can make the following deductions:

- In order for the potential to be physical it must have a global minimum, thus the coefficient of the quartic potential must obey $\lambda > 0$.
- In the case of $\mu^2 \geq 0$, we have a parabolic potential with a unique minimum at $|\phi|^2 = 0$. In this regime the vacuum expectation value (VEV) of the Higgs field disappears.
- In the case of $\mu^2 < 0$, we have competing quadratic and quartic terms, schematically similar to a "Mexican hat" potential. In this regime the minima are degenerate under $SU(2)_L$ gauge symmetry, and the Higgs field picks up a non-zero VEV. Although all ground states or vacua are equivalent, the Higgs field must still choose to exist in one of them – this choice is made under some particular infinitessimal perturbation. Although the Lagrangian retains the full $SU(2)_L \times U(1)_Y$ symmetry, the Higgs field making this choice leads to spontaneous breaking of the $SU(2)_L$ symmetry of the vacuum.

Let us looks at the effects of the Higgs field acquiring a non-zero VEV on the electroweak theory. To start, it can be shown that, without loss of generality, we can choose a *unitary* gauge $\theta^I = 0$ for a $SU(2)_L$ rotation of the Higgs field

$$\phi(x) = e^{i\frac{\sigma^I}{2}\theta^I(x)} \frac{1}{\sqrt{2}} \begin{pmatrix} 0 \\ v + h(x) \end{pmatrix}, \tag{2.42}$$

$$\text{where, } \exp\left(i\frac{\sigma^I}{2}\theta^I(x) \right) = \mathbb{1} - \frac{h(x)}{v}, \text{ with } \langle h \rangle = 0, \tag{2.43}$$

such that the VEV of the Higgs field is aligned with the vector

$$\langle\phi\rangle = \frac{1}{\sqrt{2}}\begin{pmatrix}0\\v\end{pmatrix}. \tag{2.44}$$

Inserting this ground state into the kinetic term in the Higgs part of the EW Lagrangian in eqn (2.37) and looking only at the terms quadratic in the gauge fields gives us

$$|D_\mu\phi|^2 = \left|\left(\partial_\mu + ig_W W_\mu^I(x)t^I + \frac{1}{2}ig_B B_\mu(x)Y\right)\frac{1}{\sqrt{2}}\begin{pmatrix}0\\v\end{pmatrix}\right|^2 \tag{2.45}$$

$$= -\frac{v^2}{8}\left[g_W^2\left(\left|W_\mu^1\right|^2 + \left|W_\mu^2\right|^2\right) + \left|g_W W_\mu^3 - g_B B_\mu\right|^2\right]. \tag{2.46}$$

We can simplify this expression by combining the gauge fields as

$$\begin{aligned} W_\mu^\pm &= W_\mu^1 \mp iW_\mu^2, \\ Z_\mu &= \frac{1}{\sqrt{g_W^2 + g_B^2}}\left(g_W W_\mu^3 - g_B B_\mu\right) \end{aligned} \tag{2.47}$$

which gives us

$$|D_\mu\phi|^2 = -\frac{v^2}{8}\left(g_W^2 W^{+,\mu}W_\mu^- + (g_W^2 + g_B^2)Z^\mu Z_\mu\right). \tag{2.48}$$

These look like mass terms for the newly-defined W^+, W^- and Z fields with

$$m_W = \frac{vg_W}{2},\ m_Z = \frac{v\sqrt{g_W^2 + g_B^2}}{2}. \tag{2.49}$$

The unitary gauge therefore turns three of the four Goldstone modes of the spontaneously broken $SU(2)$ symmetry of the Higgs field into longitudinal modes of $W^\pm$ and Z bosons, thereby rendering them massive. This is known as the *Higgs mechanism*, and the massive gauge bosons are said to have *eaten* the massless Goldstone bosons. The final Goldstone boson is called the Higgs boson.

There is a remaining degree of freedom in eqn (2.46) which did not pick up a mass term and therefore vanished. We can identify this field by comparing the normalisation of the new fields with the original gauge boson fields. This give us the fourth (massless) field

$$A_\mu = \frac{1}{\sqrt{g_W^2 + g_B^2}}\left(g_W W_\mu^3 + g_B B_\mu\right). \tag{2.50}$$

type	particle(s)	strong	weak	EM	I_3	Y	Q
neutral leptons	ν_e, ν_μ, ν_τ	✗	✓	✗	$+1/2$	-1	0
LH charged leptons	e_L, μ_L, τ_L	✗	✓	✓	$-1/2$	-1	-1
RH charged leptons	e_R, μ_R, τ_R	✗	✓	✓	0	-2	-1
LH up-type quarks	u_L, c_L, t_L	✓	✓	✓	$+1/2$	$+1/3$	$+2/3$
RH up-type quarks	u_R, c_R, t_R	✓	✓	✓	0	$+4/3$	$+2/3$
LH down-type quarks	d_L, s_L, b_L	✓	✓	✓	$-1/2$	$+1/3$	$-1/3$
RH down-type quarks	d_R, s_R, b_R	✓	✓	✓	0	$-2/3$	$-1/3$
massless gauge bosons	γ (photon)	✗	✗	✓	0	0	0
	g (gluon)	✓	✗	✗	0	0	0
massive gauge bosons	Z	✗	✓	✗	0	0	0
	$W^\pm$	✗	✓	✓	±1	0	±1
	H	✗	✓	✗	$-1/2$	$+1$	0

Table 2.2: SM particles and their properties: weak isospin eigenvalue (I_3), weak hypercharge (Y) and electromagnetic quantum number (Q); and the SM interactions they participate in: strong, weak and electromagnetic (EM).

We can identify this as the photon field. Re-writing the covariant derivative of the EW gauge group in terms of our new fields gives us

$$D_\mu = \partial_\mu - i\frac{g_W}{\sqrt{2}}\left(t^+W_\mu^+ + t^-W_\mu^-\right) - i\frac{1}{\sqrt{g_W^2+g_B^2}}Z_\mu\left(g_W^2 I_3 - g_B^2 Y\right) - ieA_\mu Q, \quad (2.51)$$

where $t^\pm = \frac{1}{2}(\sigma^1 \pm \sigma^2)$, and I_3 is the eigenvalue of the third component of the weak isospin. The massless photon field A_μ encodes the surviving symmetry of the vacuum state, denoted by $U(1)_{\mathrm{EM}}$, and the electric charge e and electric charge quantum number Q are defined as

$$e = \frac{g_W g_B}{\sqrt{g_W^2+g_B^2}}, \quad Q = I_3 + \frac{Y}{2}. \quad (2.52)$$

In this definition, we can see that the electric charge quantum number is related to the weak isospin eigenvalue and hypercharge. The values of I_3, Y and Q for all SM particles are listed in table 2.2.

2.4.4 Fermion masses and the CKM matrix

Let us now turn to what the Higgs mechanism does to the fermions in this theory. After EWSB, the Yukawa term of the EW Lagrangian density in the chosen ground state of the Higgs field becomes [51]

$$\mathcal{L}_{\mathrm{Yukawa}} = -vY_l^{ij}e_L^i\left(1+\frac{h}{v}\right)e_R^j - vY_d^{ij}d_L^i\left(1+\frac{h}{v}\right)d_R^j - vY_u^{ij}u_L^i\left(1+\frac{h}{v}\right)u_R^j + h.c.\,. \quad (2.53)$$

This gives us some interaction terms with the Higgs and others that look like mass terms for the fermions, if not for the Yukawa couplings. The Yukawa couplings are not expected to be diagonal *a priori*, but we can diagonalise them to come up with a basis of quark fields which correspond to fixed masses. This tells us that quark fields can be packaged into weak eigenstates or into mass eigenstates, and to maintain the normalisation of the theory, there should be unitary transformation between these bases. To find the mass eigenstates, we must diagonalise the Yukawa coupling matrices; it is a property of Hermitian matrices that they are diagonalisable with unitary matrices, so we should diagonalise the products $Y_q Y_q^\dagger$ and $Y_q^\dagger Y_q$ (with $q \in \{l, d, u\}$) which are Hermitian by construction. For this purpose, we define the diagonalising unitary matrices U_q and W_q such that

$$Y_q Y_q^\dagger = U_q M_q^2 U_q^\dagger, \quad Y_q^\dagger Y_q = W_q M_q^2 W_q^\dagger, \tag{2.54}$$

where M is the diagonal mass matrix. Using this parameterisation, the Yukawa couplings can be re-written as

$$Y_q = U_q M_q W_q^\dagger, \tag{2.55}$$

and we can obtain the quark fields as mass eigenstates $\tilde{q}$ from the weak eigenstates q as well as the quark masses via

$$\begin{gathered} \tilde{q}_R^i = W_q^{ij,\dagger} q_R^j, \quad \tilde{q}_L^i = U_q^{ij,\dagger} q_L^j, \\ m_q^i = \frac{1}{\sqrt{2}} M_q^{ii} v. \end{gathered} \tag{2.56}$$

However, here we note an interesting feature: the mass matrices for the up and down-type quarks are not simultaneously diagonalisable, that is, $U_u \neq U_d$. This means that interaction terms involving both up and down-type quarks (mediated by a $W^\pm$ boson) take the following forms in the mass eigenbasis

$$\frac{1}{2} \overline{\tilde{u}}_L^i \left(U_u^\dagger U_d \right)^{ij} \gamma^\mu \tilde{d}_L^i. \tag{2.57}$$

The elements of the matrix $(U_u^\dagger U_d)$ are transition amplitudes for flavour changing interactions between the quark flavours in $\tilde{u}$ and $\tilde{d}$. We call this the Cabibbo-Kobayashi-Maskawa (CKM) matrix [24, 25]

$$V_{\text{CKM}} = U_u^\dagger U_d = \begin{pmatrix} V_{ud} & V_{us} & V_{ub} \\ V_{cd} & V_{cs} & V_{cb} \\ V_{td} & V_{ts} & V_{tb} \end{pmatrix}. \tag{2.58}$$

The matrix elements V_{ij} are free parameters of the SM that feature in all flavour-changing interactions, and must be determined from experiments. Only the weak sector

quark	mass (MeV) [6]	$\overline{\text{MS}}$-scale	I	I_z	$\mathcal{S}$	$\mathcal{C}$	$\mathcal{B}$	$\mathcal{T}$
up (u)	$2.16^{+0.49}_{-0.26}$	2 GeV	1/2	+1/2	0	0	0	0
down (d)	$4.67^{+0.48}_{-0.17}$	2 GeV	1/2	−1/2	0	0	0	0
strange (s)	$93.4^{+8.6}_{-3.4}$	2 GeV	0	-	−1	0	0	0
charm (c)	$1.27(2) \times 10^3$	m_c	0	-	0	1	0	0
bottom (b)	$4.18^{+0.03}_{-0.02} \times 10^3$	m_b	0	-	0	0	−1	0
top (t)	$1.727(3) \times 10^5$	m_t	0	-	0	0	0	1

Table 2.3: Masses and flavour quantum numbers of quarks in the mass eigenbasis. Quark masses are dependent on renormalisation scheme ($\overline{\text{MS}}$ in this case) and scale. Light quarks u and d have isospin quantum numbers while heavy quarks have quantum numbers called *strangeness* ($\mathcal{S}$), *charm* ($\mathcal{C}$), *bottom* ($\mathcal{B}$), and *top* ($\mathcal{T}$).

of the SM allows for these flavour-changing interactions, and these are characterised using quantum numbers described in table 2.3.

Note however that the kinetic terms of the fermionic Lagrangian (eqn (2.34)) only link the left-handed up-type quarks to ups, and the left-handed down-type quarks to downs. This means that at tree-level in the SM, there are no flavour-changing neutral currents (FCNCs) that mix the left-handed up-type quarks with down-type quarks. We will see later the effect of FCNCs in the context of neutral meson mixing via weak interactions which take place at the loop-level and are therefore highly sensitive to new physics.

Although the CKM matrix elements are free parameters, we can place several constraints on their values. Since each of the matrices U_q is unitary, we expect the CKM matrix to be unitary by construction; testing this unitarity is a principal direction of research in order to validate the SM theory. The unitarity constraint leads to conditions of the form

$$\sum_j V_{ij}V_{ij}^* = 1 = \sum_j V_{ji}V_{ji}^*, \ \forall\, i, \tag{2.59}$$

$$\sum_j V_{ij}V_{kj}^* = 0 = \sum_j V_{ji}V_{jk}^*, \ \forall\, i \neq k. \tag{2.60}$$

Any departure from these predicted values for sums of CKM matrix elements would indicate the existence of New Physics (NP); for example, if in eqn (2.59) the summation adds up to be lower than 1, it could hint at a possible fourth generation of quarks.

The condition in eqn (2.60) is often interpreted in literature as a so-called *unitarity triangle*. To see this, consider for example $i = d$ and $k = b$, and suppose each term in the summation to be a vector in the complex plane:

$$\begin{aligned} &V_{ud}V_{ub}^* + V_{cd}V_{cb}^* + V_{td}V_{tb}^* = 0, \\ \implies &\frac{V_{ud}V_{ub}^*}{V_{cd}V_{cb}^*} + \frac{V_{td}V_{tb}^*}{V_{cd}V_{cb}^*} = -1. \end{aligned} \tag{2.61}$$

This traces out a closed triangle in the complex plane with sides of length 1, $|V_{ud}V_{ub}^*/V_{cd}V_{cb}^*|$, and $|V_{td}V_{tb}^*/V_{cd}V_{cb}^*|$. The condition of unitarity corresponds to this creating a closed triangle. Experimental data needs to be combined with theoretical predictions to determine the lengths of the sides and angles (α, β, γ) of this triangle.

Being a complex matrix, V_{CKM} has 9 complex, or 18 real parameters. Unitarity conditions provide 9 constraints, and redefinitions of quark fields can be used to absorb 5 more parameters. This leaves us with 4 remaining degrees of freedom: 3 rotations and 1 phase. These are often expressed via the *Wolfenstein parameterisation* of the CKM matrix which introduces 3 real parameters (λ, ρ, A) and one complex phase η [60]. The relative sizes of the CKM matrix elements are strongly hierarchical, with the largest values along the principal diagonal, smaller entries on the sub-diagonal, and the smallest entries in the remaining corners. The Wolfenstein parameterisation highlights this hierarchy, and the CKM matrix is represented as

$$V_{\text{CKM}} = \mathbb{1} + \begin{pmatrix} -\lambda^2/2 & \lambda & A\lambda^3(\rho - i\eta) \\ -\lambda & -\lambda^2/2 & A\lambda^2 \\ A\lambda^3(1 - \rho - i\eta) & -A\lambda^2 & 0 \end{pmatrix} + O(\lambda^4). \tag{2.62}$$

The unitarity triangle is commonly plotted in the $(\overline{\rho}, \overline{\eta})$ plane, using the definitions

$$\overline{\rho} = \rho\left(1 - \lambda^2/2 + O(\lambda^4)\right), \; \overline{\eta} = \eta\left(1 - \lambda^2/2 + O(\lambda^4)\right). \tag{2.63}$$

This ensures that $\overline{\rho} + i\overline{\eta} = -V_{ud}V_{ub}^*/V_{cd}V_{cb}^*$. A global fit combining theoretical and experimental data and imposing unitarity constraints currently predicts [1][4]

$$\begin{aligned} A &= 0.810^{(18)}_{(24)}, \quad \lambda = 0.22548^{(68)}_{(34)}, \\ \overline{\rho} &= 0.145^{(13)}_{(7)}, \quad \overline{\eta} = 0.343^{(11)}_{(12)}, \end{aligned} \tag{2.64}$$

and the fit results for the magnitudes of all nine CKM matrix elements are [6]

$$|V_{\text{CKM}}| = \begin{pmatrix} 0.97435(16) & 0.22500(67) & 0.00369(11) \\ 0.22486(67) & 0.97349(16) & 0.04182^{(85)}_{(74)} \\ 0.00857^{(20)}_{(18)} & 0.04110^{(83)}_{(72)} & 0.999118^{(31)}_{(36)} \end{pmatrix}. \tag{2.65}$$

Unitarity of the first row and column of the CKM matrix have been tested extensively and at current precision the results are compatible with unitarity [61]. The most persisten tension in the CKM matrix lies in the determination of the world average of the elements V_{ub} and V_{cb} using inclusive (unspecified final state) and exclusive (specific final state) processes.

[4] The notation $x.xxxx^{(yy)}_{(z)}$ denotes asymmetric errors: the 68% confidence interval in the value of x lies between $x.xxxx - 0.000z$ and $x.xxxx + 0.00yy$.

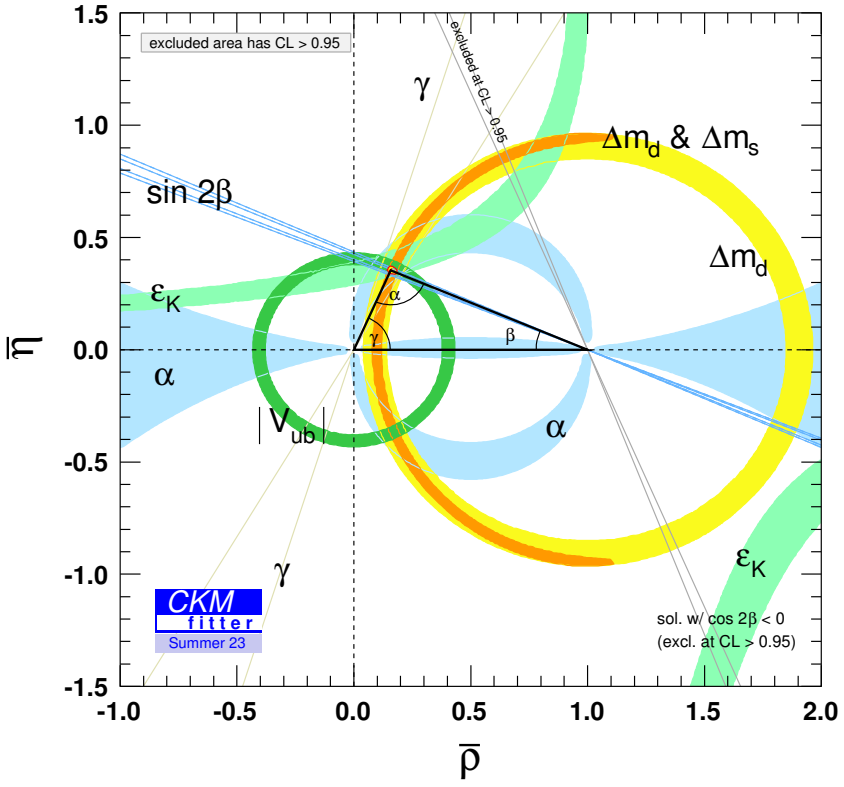

Figure 2.1: The unitarity triangle in the $(\overline{\rho}, \overline{\eta})$ plane (source:[1]). Lengths of the sides and the angles are constrained from various measurements: predictions for the indirect CP violation parameter ε_K come from kaon mixing, while the mass splittings Δm_d and Δm_s are computed from B^0 and B_s^0-meson mixing respectively.

At minimal order in α_{EM}, that is, ignoring electromagnetic interactions between quarks and the W-boson, quarks and leptons, and W-boson and leptons, one can schematically factorise an experimental observable in a flavour changing process as

$$\Gamma_{\text{exp}} = |\text{CKM}| \times (\text{weak}) \times (\text{EM}) \times (\text{strong}), \tag{2.66}$$

where contributions from weak and electromagnetic interactions can be computed perturbatively, while those from strong interactions must be computed non-perturbatively. Combining these theoretical calculations with experimental inputs allows for precise measurements of the CKM matrix elements.

It is worth noting that the complex phase η is the only source of CP violation in the SM[5]. This manifests in processes involving flavour changing interactions such as neutral meson mixing, as will be discussed in greater detail in the following section.

[5] CP symmetry is also violated by introducing a term of the form $\theta \frac{\alpha_s}{\pi} \text{Tr}\{\mathbf{E} \cdot \mathbf{B}\}$ to the SM Lagrangian, where $\mathbf{E}$ and $\mathbf{B}$ are the chromo-electric and chromo-magnetic fields. However, the angle θ is experimentally found to be particularly small – $O(10^{-10})$ [62], this is known as the strong CP problem [63]; the discussion of this term is beyond the scope of this thesis.

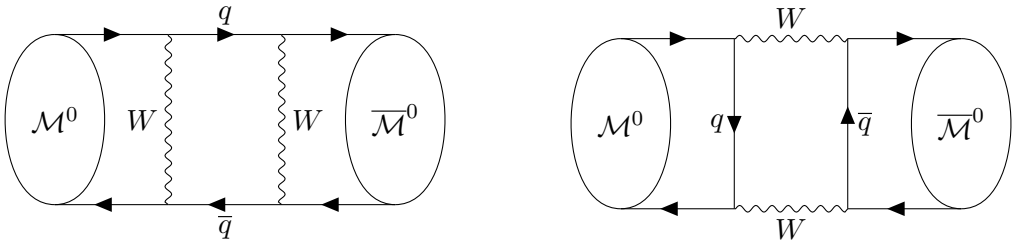

Figure 2.2: Mixing of a neutral meson $\mathcal{M}^0$ with its antiparticle $\overline{\mathcal{M}}^0$ via second-order weak interactions ("box" diagrams) with two W bosons and two quarks. For K^0 and B^0 mixing, $q = u, c, t$ (*up*-type quark); for D^0 mixing, $q = d, s, b$ (*down*-type quark).

2.5 Neutral meson mixing

Neutral mesons in the Standard Model can *mix* or oscillate between meson and anti-meson states, that is, an initial meson $\mathcal{M}^0 \in \{K^0, D^0, B^0\}$ (with quantum number $F = \pm 1$ where $F \in \{\mathcal{S}, \mathcal{C}, \mathcal{B}\}$), can transform into a final anti-meson $\overline{\mathcal{M}}^0$ (with quantum number $F = \mp 1$). Strong and electromagnetic interactions conserve these quantum numbers and therefore no such flavour-changing interaction is allowed. Weak interactions, however, need not conserve these quantum numbers, and therefore neutral meson mixing occurs via weak interactions with the exchange of two W-bosons, as shown in figure 2.2. As this process occurs at second-order in the Fermi constant G_F, parameters of neutral meson mixing provide stringent tests of the SM and windows into possible New Physics.

In the following sections we discuss mixing in the neutral kaon system. However the general framework applies to $D^0 - \overline{D}^0$ and $B^0 - \overline{B}^0$ mixing as well and we shall return to them specifically in later sections.

2.5.1 Kaon mixing in the SM

Neutral kaons are produced copiously via strong interactions, for example

$$\begin{aligned} \pi^- + p &\to \Lambda + K^0, \\ \pi^+ + p &\to K^+ + \overline{K}^0 + p. \end{aligned} \tag{2.67}$$

Weak interactions allow the flavour eigenstates K^0 and $\overline{K}^0$ to mix as well as decay, thereby allowing transitions between them. A neutral kaon at time t is thus described by the superposition

$$|\psi(t)\rangle = K^0(t)|K^0\rangle + \overline{K}^0(t)|\overline{K}^0\rangle, \tag{2.68}$$

which evolves in time as

$$i\frac{\partial}{\partial t}\begin{pmatrix}K^0(t)\\ \overline{K}^0(t)\end{pmatrix} = \mathbf{\Lambda}\begin{pmatrix}K^0(t)\\ \overline{K}^0(t)\end{pmatrix} = \left(\mathbf{M} - \frac{i}{2}\mathbf{\Gamma}\right)\begin{pmatrix}K^0(t)\\ \overline{K}^0(t)\end{pmatrix}, \tag{2.69}$$

where $\mathbf{M}$ is the dispersive part defining the masses of the neutral kaon states, and $\mathbf{\Gamma}$ is the absorptive part defining the decay width in the presence of weak interaction. We parameterise $\mathbf{\Lambda}$ with eight real and positive parameters

$$\mathbf{\Lambda} = \begin{pmatrix}m_{K^0} & M_{12}e^{i\phi_M}\\ M_{12}e^{-i\phi_M} & m_{\overline{K}^0}\end{pmatrix} - \frac{i}{2}\begin{pmatrix}\Gamma_{K^0} & \Gamma_{12}e^{i\phi_\Gamma}\\ \Gamma_{12}e^{-i\phi_\Gamma} & \Gamma_{\overline{K}^0}\end{pmatrix}, \tag{2.70}$$

where m_{K^0} and $m_{\overline{K}^0}$ are the masses, and $1/\Gamma_{K^0}$ and $1/\Gamma_{\overline{K}^0}$ the lifetimes of the K^0 and $\overline{K}^0$ states respectively.

The eigenstates of $\mathbf{\Lambda}$ are the physical neutral kaons, corresponding to eigenvalues

$$\lambda_{L,S} = \frac{\Lambda_{11}+\Lambda_{22}}{2} \pm \sqrt{\frac{(\Lambda_{22}-\Lambda_{11})^2}{4} + \Lambda_{12}\Lambda_{21}} := m_{L,S} - \frac{i}{2}\Gamma_{L,S}, \tag{2.71}$$

where the subscripts L and S preemptively refer to the two neutral kaons observed in nature which are called K-"*long*" and K-"*short*". These are kaons with very similar masses but very different lifetimes described as long (L) or short (S). The corresponding eigenvectors are given by

$$|K_{L,S}\rangle = \frac{e^{i\varphi_{L,S}}}{\sqrt{1+|r_{L,S}|^2}}\left(r_{L,S}|K^0\rangle + |\overline{K}^0\rangle\right), \tag{2.72}$$

with arbitrary phases φ_L and φ_S and

$$r_{L,S} = \frac{2M_{12}}{\Lambda_{22}-\Lambda_{11} \pm (\lambda_L - \lambda_S)}. \tag{2.73}$$

It is also useful to define

$$\Delta m_K = m_L - m_S, \quad \Delta\Gamma_K = \Gamma_L - \Gamma_S, \tag{2.74}$$

which are known as the mass and width splitting parameters respectively.

2.5.2 CP violation

Neutral kaons often decay to pions (the lightest hadrons); to either two or three-pion states. These are eigenstates of CP symmetry with

$$CP|\pi\pi\rangle = +|\pi\pi\rangle, \quad CP|\pi\pi\pi\rangle = -|\pi\pi\pi\rangle. \tag{2.75}$$

If CP symmetry were conserved in weak decays of neutral kaons, one would expect decays to pions to occur from states of definite CP. The flavour eigenstates are not CP eigenstates and transform as

$$CP|K^0\rangle = -|\overline{K}^0\rangle, \quad CP|\overline{K}^0\rangle = -|K^0\rangle, \tag{2.76}$$

but we can build CP eigenstates from their linear combinations which relate to the decays to two or three-pion states

$$\begin{aligned} |K_1\rangle &= \frac{1}{\sqrt{2}}\left(|K^0\rangle - |\overline{K}^0\rangle\right), \quad CP|K_1\rangle = +|K_1\rangle, \quad K_1 \to \pi\pi \\ |K_2\rangle &= \frac{1}{\sqrt{2}}\left(|K^0\rangle + |\overline{K}^0\rangle\right), \quad CP|K_2\rangle = -|K_2\rangle, \quad K_2 \to \pi\pi\pi. \end{aligned} \tag{2.77}$$

The expected lifetimes of these CP eigenstates depend on the phase space available for the corresponding decays. For decay to two pions, the energy available ($m_K - 2m_\pi \approx 220\,\text{MeV}$) is much higher than that for decays to three pions ($m_K - 3m_\pi \approx 80\,\text{MeV}$), thus we expect decays to two pions to be more rapid due to a larger phase space. This predicts a short-lived K_1 state and a long-lived K_2 state. These can be identified with the observed neutral kaon states

$$K_1 \equiv K_S, \quad K_2 \equiv K_L. \tag{2.78}$$

However, Fitch and Cronin in 1964 observed $K_L \to \pi\pi$ decay, which violates CP-symmetry if the above equations were true. This CP violation was observed at a two per mille level and has two possible explanations[6]:

1. that K_L and K_S do not correspond exactly to the CP eigenstates K_1 and K_2 but instead to some admixture parameterised by a small ε_K

$$\begin{aligned} |K_S\rangle &= \frac{1}{\sqrt{1+|\varepsilon_K|^2}}\left(|K_1\rangle + \varepsilon_K|K_2\rangle\right), \\ |K_L\rangle &= \frac{1}{\sqrt{1+|\varepsilon_K|^2}}\left(|K_2\rangle + \varepsilon_K|K_1\rangle\right), \end{aligned} \tag{2.79}$$

   leading to indirect CP violation when the small CP-even component of K_L decays as $K_1 \to \pi\pi$,

2. and/or CP symmetry is violated directly in the decay $K_2 \to \pi\pi$, parameterised by ε'_K.

[6] this not a complete description – additional violations of discrete symmetries may occur in the decay of particles. The kaon system, due to the low mass of the kaon, has a limited number of different final states compared to other neutral meson systems (D^0, B_d^0, and B_s^0), with one dominant decay channel ($K^0 \to (\pi\pi)_{I=0}$), which leads to a suppresion of the additional CP-violation effects. This is addressed in part in eqn (2.84) and in section 2.5.6.

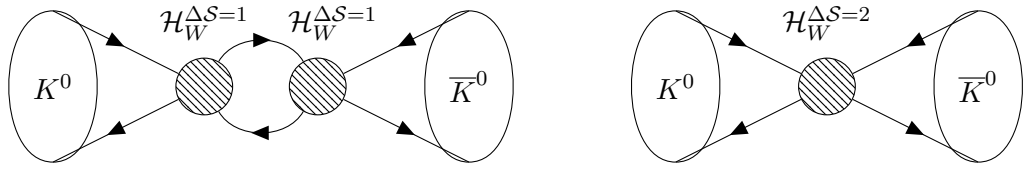

Figure 2.3: Long (left) and short (right) - distance contributions to kaon mixing parameters.

Both of these parameters, ε_K (indirect) and ε'_K (direct) contribute to the mechanism for CP violation in the kaon system, however the indirect contribution has been experimentally shown to dominate. The dominant source of CP violation is therefore a result of the mixing between K^0 and $\overline{K}^0$ causing admixture of the CP eigenstates. We can combine eqns. (2.79) and (2.77) to express the neutral kaon states in terms of the flavour eigenstates and the indirect CP violation parameter ε_K

$$|K_{L,S}\rangle = \frac{1}{\sqrt{2}} \frac{1}{\sqrt{1+|\varepsilon_K|^2}} \left[(1+\varepsilon_K)|K^0\rangle \pm (1-\varepsilon_K)|\overline{K}^0\rangle \right], \tag{2.80}$$

which can be rearranged as

$$|K_{L,S}\rangle = \frac{1}{\sqrt{1+\left|\frac{1+\varepsilon_K}{1-\varepsilon_K}\right|^2}} \left[\pm \left(\frac{1+\varepsilon_K}{1-\varepsilon_K} \right) |K^0\rangle + |\overline{K}^0\rangle \right]. \tag{2.81}$$

In this form, we can use eqns. (2.72) and (2.73) to identify

$$\pm \left(\frac{1+\varepsilon_K}{1-\varepsilon_K} \right) \equiv r_{L,S} e^{i\varphi_{L,S}} = \frac{2M_{12} e^{i\varphi_{L,S}}}{\Lambda_{22} - \Lambda_{11} \pm (\lambda_L - \lambda_S)}. \tag{2.82}$$

The indirect CP violation parameter ϵ_K

The indirect CP violation parameter has been introduced in eqn (2.79) as a measure of admixture of CP-definite states in K_L and K_S. However, in literature it is formally defined in terms of $K \to \pi\pi$ decay amplitudes

$$\epsilon_K = \frac{2\eta_{+-} + \eta_{00}}{3}, \quad \eta_{ij} = \frac{\mathcal{A}\left[K_L \to \pi^i \pi^j\right]}{\mathcal{A}\left[K_S \to \pi^i \pi^j\right]}. \tag{2.83}$$

This is related to ε_K in eqn (2.79) via

$$\epsilon_K \approx \varepsilon_K + i \frac{\mathrm{Im}\,(A_0)}{\mathrm{Re}\,(A_0)}, \quad A_0 \equiv \mathcal{A}\left[K^0 \to (\pi\pi)_{I=0}\right], \tag{2.84}$$

where A_0 corresponds to the decay amplitude in the isospin $I = 0$ channel. Determinations of $\mathrm{Im}(A_0)$ and $\mathrm{Re}(A_0)$ have also been subjects of lattice computations in [64, 65].

The off-diagonal element of the mass matrix M_{12} is therefore a key parameter, and is related to the $\Delta\mathcal{S} = 2$ flavour-changing neutral current (FCNC) responsible for the mixing of K^0 and $\overline{K}^0$. The corresponding leading-order SM processes are the box diagrams (figure 2.2) with two pairs of vertices joined by a W exchange each. We can represent these vertices with effective weak hamiltonians, using $\mathcal{H}_W^{\Delta\mathcal{S}=1}$ for *long-distance* spatial separation between the two vertices (of order $1/\Lambda_{\text{QCD}}$) or $\mathcal{H}_W^{\Delta\mathcal{S}=2}$ for the *short-distance* case (separations much smaller than $1/\Lambda_{\text{QCD}}$), as shown in figure 2.3. We can thus split the parameter M_{12} as

$$M_{12} = M_{12}^{\text{SD}} + M_{12}^{\text{LD}}. \tag{2.85}$$

The long-distance contribution to ε_K is typically subdominant ($\sim 5\%$ [66–68]) and is not investigated in this thesis, however it has been a subject of lattice calculations in [68–70]. In this thesis, the focus is on the dominant short-distance contribution to the kaon mixing parameter, M_{12}^{SD}, with the goal of making high-precision predictions that constrain the indirect CP violation parameter ε_K.

2.5.3 M_{12}^{SD} and the effective weak Hamiltonian

The short-distance contribution to the kaon mixing parameter is given by the matrix element of an effective four-quark interaction vertex as shown in figure 2.3:

$$M_{12}^{\text{SD}} = \frac{\langle K^0|\mathcal{H}_W^{\Delta\mathcal{S}=2}|\overline{K}^0\rangle}{2m_K}, \tag{2.86}$$

with $m_K = m_{K^0} = m_{\overline{K}^0}$, where the effective weak Hamiltonian can be generically expressed using the operator product expansion

$$\mathcal{H}_W^{\Delta\mathcal{S}=2} = \sum_{i=1}^{5} C_i(\mu) O_i(\mu). \tag{2.87}$$

Here, O_i are six-dimensional, four-quark local operators, and C_i are the corresponding Wilson coefficients. The Wilson coefficients capture the high-energy physics and are calculated in perturbation theory, while the four-quark operators encode the low-energy dynamics and therefore need to be computed non-perturbatively. The scale μ is in principle arbitrary, but must be the same for the Wilson coefficients and the local operators in order for the final amplitudes to be scale-independent. It must also be chosen to allow for reliability of computing the Wilson coefficients perturbatively – this is typically in the range of $1 - 3$ GeV.

The four-quark operators, in the so-called "SUSY" basis introduced in [71], are

$$\begin{aligned} O_1 &= (\overline{s}_a\gamma_\mu(1-\gamma_5)d_a)(\overline{s}_b\gamma_\mu(1-\gamma_5)d_b), \\ O_2 &= (\overline{s}_a(1-\gamma_5)d_a)(\overline{s}_b(1-\gamma_5)d_b), \\ O_3 &= (\overline{s}_a(1-\gamma_5)d_b)(\overline{s}_b(1-\gamma_5)d_a), \\ O_4 &= (\overline{s}_a(1-\gamma_5)d_a)(\overline{s}_b(1+\gamma_5)d_b), \\ O_5 &= (\overline{s}_a(1-\gamma_5)d_b)(\overline{s}_b(1+\gamma_5)d_a), \end{aligned} \tag{2.88}$$

where a and b denote colour indices. O_1 describes kaon-mixing in the SM, while O_{2-5} are BSM operators. The operator O_1 belongs to the $(27,1)$ representation of the chiral symmetry group $SU(3)_L \times SU(3)_R$, while operators $O_{2,3}$ belong to the $(6,\overline{6})$ and $O_{4,5}$ to the $(8,8)$ representations. This allows for mixing amongst operators in the same representations during the procedures of renormalisation or matching; this is described in greater detail in chapter 4.

The generic weak Hamiltonian may also have contributions from the parity partners of operators O_{1-3} (by swapping $1-\gamma_5$ with $1+\gamma_5$), but the two variations differ only in parity-odd cross terms which do not contribute to the matrix element $\langle\overline{K}^0|O_i|K^0\rangle$ owing to the parity invariance of QCD. This means we are only interested in the parity-even part of the operators, denoted by O_i^+:

$$\begin{aligned} O_1^+ &= \overline{s}_a\gamma_\mu d_a\ \overline{s}_b\gamma_\mu d_b + \overline{s}_a\gamma_\mu\gamma_5 d_a\ \overline{s}_b\gamma_\mu\gamma_5 d_b, \\ O_2^+ &= \overline{s}_a d_a\ \overline{s}_b d_b + \overline{s}_a\gamma_5 d_a\ \overline{s}_b\gamma_5 d_b, \\ O_3^+ &= \overline{s}_a d_b\ \overline{s}_b d_a + \overline{s}_a\gamma_5 d_b\ \overline{s}_b\gamma_5 d_a, \\ O_4^+ &= \overline{s}_a d_a\ \overline{s}_b d_b - \overline{s}_a\gamma_5 d_a\ \overline{s}_b\gamma_5 d_b, \\ O_5^+ &= \overline{s}_a d_b\ \overline{s}_b d_a - \overline{s}_a\gamma_5 d_b\ \overline{s}_b\gamma_5 d_a. \end{aligned} \tag{2.89}$$

The matrix elements of these four-quark operators are obtained non-perturbatively and this computation is performed using the framework of lattice QCD as part of this thesis and the results are presented in chapter 5. For this purpose, it is useful to work in the so-called "lattice" or "NPR" basis as introduced in [72], with $Q_1 \equiv O_1$ and

$$\begin{aligned} Q_2 &= \overline{s}_a\gamma_\mu(1-\gamma_5)d_a\ \overline{s}_b\gamma_\mu(1+\gamma_5)d_b, \\ Q_3 &= \overline{s}_a(1-\gamma_5)d_a\ \overline{s}_b(1+\gamma_5)d_b, \\ Q_4 &= \overline{s}_a(1-\gamma_5)d_a\ \overline{s}_b(1-\gamma_5)d_b, \\ Q_5 &= \frac{1}{4}\overline{s}_a\sigma_{\mu\nu}(1-\gamma_5)d_a\ \overline{s}_b\sigma_{\mu\nu}(1+\gamma_5)d_b. \end{aligned} \tag{2.90}$$

Note that all operators are color-unmixed in this basis. Once again, we are interested only in the parity-even part of these operators, given by

$$\begin{aligned}
Q_1^+ &= \overline{s}_a\gamma_\mu d_a\ \overline{s}_b\gamma_\mu d_b + \overline{s}_a\gamma_\mu\gamma_5 d_a\ \overline{s}_b\gamma_\mu\gamma_5 d_b, && \text{(VV + AA)}\\
Q_2^+ &= \overline{s}_a\gamma_\mu d_a\ \overline{s}_b\gamma_\mu d_b - \overline{s}_a\gamma_\mu\gamma_5 d_a\ \overline{s}_b\gamma_\mu\gamma_5 d_b, && \text{(VV − AA)}\\
Q_3^+ &= \overline{s}_a d_a\ \overline{s}_b d_b - \overline{s}_a\gamma_5 d_a\ \overline{s}_b\gamma_5 d_b, && \text{(SS − PP)}\\
Q_4^+ &= \overline{s}_a d_a\ \overline{s}_b d_b + \overline{s}_a\gamma_5 d_a\ \overline{s}_b\gamma_5 d_b, && \text{(SS + PP)}\\
Q_5^+ &= \sum_{\nu>\mu} \overline{s}_a\gamma_\mu\gamma_\nu d_a\ \overline{s}_b\gamma_\mu\gamma_\nu d_b, && \text{(TT)}
\end{aligned} \tag{2.91}$$

where the labels on the right indicate the Dirac structures of the operators. The same operators – with identical Dirac structures but different quark content – make up the weak effective Hamiltonian for the short-distance contribution relevant to the mixing of other neutral mesons.

The operators in the NPR basis (used for lattice computations) map to those in the SUSY basis (used in phenomenological applications) via the linear transformation

$$\begin{pmatrix} O_1^+ \\ O_2^+ \\ O_3^+ \\ O_4^+ \\ O_5^+ \end{pmatrix} = \begin{pmatrix} 1 & 0 & 0 & 0 & 0 \\ 0 & 0 & 0 & 1 & 0 \\ 0 & 0 & 0 & -\frac{1}{2} & \frac{1}{2} \\ 0 & 0 & 1 & 0 & 0 \\ 0 & -\frac{1}{2} & 0 & 0 & 0 \end{pmatrix} \begin{pmatrix} Q_1^+ \\ Q_2^+ \\ Q_3^+ \\ Q_4^+ \\ Q_5^+ \end{pmatrix} = \begin{pmatrix} Q_1^+ \\ Q_4^+ \\ \frac{1}{2}\left(Q_5^+ - Q_4^+\right) \\ Q_3^+ \\ -\frac{1}{2}Q_2^+ \end{pmatrix}. \tag{2.92}$$

2.5.4 Bag and ratio parameters

In order to compute the short-distance contribution M_{12}^{SD}, we are interested in the matrix element $\langle\overline{K}^0|\mathcal{H}_W^{\Delta\mathcal{S}=2}|K^0\rangle$, as shown in eqn (2.86), and therefore in the non-perturbative computation of the matrix elements of the four-quark operators $\langle\overline{K}^0|Q_i|K^0\rangle$.

The conventional way to parameterise these hadronic matrix elements is through the so-called *bag parameters*, defined as the ratio

$$\mathcal{B}_i(\mu) = \frac{\left\langle\overline{K}^0|Q_i(\mu)|K^0\right\rangle}{\left\langle\overline{K}^0|Q_i(\mu)|K^0\right\rangle_{\mathrm{VSA}}}, \tag{2.93}$$

using the vacuum saturation approximation (VSA), whereby the vacuum is inserted between all possible quark-antiquark pairs in the four-quark operators. In practice,

lattice calculations construct the following ratios [2, 73, 74][7]

$$\mathcal{B}_1(\mu) = \frac{\left\langle \overline{K}^0 | Q_1(\mu) | K^0 \right\rangle}{N_1 \langle \overline{K}^0 | \bar{s}\gamma_\mu\gamma_5 d|0\rangle\langle 0|\bar{s}\gamma_\mu\gamma_5 d|K^0\rangle} = \frac{1}{N_1 m_K^2 f_K^2}\left\langle \overline{K}^0 | Q_1(\mu) | K^0 \right\rangle, \tag{2.94}$$

$$\mathcal{B}_{i>1}(\mu) = \frac{\left\langle \overline{K}^0 | Q_i(\mu) | K^0 \right\rangle}{N_i \langle \overline{K}^0 | \bar{s}\gamma_5 d|0\rangle\langle 0|\bar{s}\gamma_5 d|K^0\rangle} = \frac{(m_s(\mu)+m_d(\mu))^2}{N_i m_K^4 f_K^2}\left\langle \overline{K}^0 | Q_i | K^0 \right\rangle. \tag{2.95}$$

The normalisation factors depend on the operator basis used

$$N_i^{\text{SUSY}} = \left[\frac{8}{3}, -\frac{5}{3}, \frac{1}{3}, 2, \frac{2}{3}\right], \tag{2.96}$$

$$N_i^{\text{NPR}} = \left[\frac{8}{3}, -\frac{4}{3}, 2, -\frac{5}{3}, -1\right]. \tag{2.97}$$

and f_K is kaon decay constant defined by the coupling of the kaon to the renormalised axial-vector current $j^\mu_{\mathcal{A},\text{R}}$

$$\langle 0|j^\mu_{\mathcal{A},\text{R}}(x)|K(p)\rangle = i f_K\, p^\mu\, e^{-ip\cdot x}, \tag{2.98}$$

where p_μ is the 4-momentum of the kaon. Note that the bag parameter corresponding to the SM operator $\mathcal{B}_1$ can be identified with the quantity commonly referred to in literature as B_K[8].

Another parameterisation of the hadronic matrix elements of the BSM four-quark operators is via the *ratio parameters* [74–76]

$$R_{i>1}(\mu) = \frac{\left\langle \overline{K}^0 | Q_i(\mu) | K^0 \right\rangle}{\left\langle \overline{K}^0 | Q_1(\mu) | K^0 \right\rangle}. \tag{2.99}$$

There is clear advantage to the ratio parameters over the bag parameters: the lack of explicit quark-mass dependence allows us to recover the BSM matrix elements using $R_i(\mu)$, $\mathcal{B}_1(\mu)$, and the experimentally measured values of m_K and f_K (using eqn (2.94)). Furthermore, the similarity of the quantities in the numerator and denominator allow for partial cancellations of systematic and statistical errors in the computation of these ratio parameters on the lattice.

The chiral behaviour of the bag and ratio parameters can be predicted using kaon chiral perturbation theory (as described in section 2.3.3). The bag parameters are given by [2]

$$\mathcal{B}_i = \mathcal{B}_i^\chi\left[1 + \frac{c_i}{f^2}\chi_l + s_i\frac{\chi_l}{2(4\pi f)^2}\log\frac{\chi_l}{\Lambda^2_{\text{QCD}}}\right], \tag{2.100}$$

[7] An alternative definition of the bag parameters has been proposed in [75].

[8] Another frequently quoted quantity is the renormalisation group invariant version of the SM bag parameter, $\hat{B}_K$, this is defined in section 4.5.

where c_i are s_i are low energy constants of KχPT. At next-to-leading order, this can be written as

$$\mathcal{B}_i = \mathcal{B}_i^{\chi}\left[1 + \frac{m_\pi^2}{f_\pi^2}\left(\beta_i^{\mathcal{B}} + \frac{C_i^{\mathcal{B}}}{16\pi^2}\log\frac{m_\pi^2}{\Lambda_{\text{QCD}}^2}\right)\right], \tag{2.101}$$

where the coefficients of the chiral logarithm terms $C_i^{\mathcal{B}}$ are known constants from KχPT to be $C_{i=1,2,3}^{\mathcal{B}} = -0.5$ and $C_{i=4,5}^{\mathcal{B}} = 0.5$ in the SUSY basis. Similarly, the chiral behaviour of the ratio parameters is parameterised as

$$R_i = R_i^{\chi}\left[1 + \frac{m_\pi^2}{f_\pi^2}\left(\beta_i^{R} + \frac{C_i^{R}}{16\pi^2}\log\frac{m_\pi^2}{\Lambda_{\text{QCD}}^2}\right)\right], \tag{2.102}$$

where the chiral logarithm coefficients are given by $C_{i=2,3}^{R} = 0$ and $C_{i=4,5}^{R} = 1$, once again in the SUSY basis.

The bag and ratio parameters form convenient mathematical parameterisations for the hadronic matrix elements of the four-quark operators, which are the actual quanitites of interest. These parameterisations allow for improved precision in the prediction of kaon mixing parameters when using the framework of lattice QCD.

2.5.5 Status of kaon mixing in and beyond the SM

Within the Standard Model, the dominant short-distance contribution to the indirect CP-violation parameter ε_K is calculated using the matrix element of the SM operator Q_1 in eqn (2.88). Theoretical predictions of this matrix elements have been computed on the lattice using isospin-symmetric pure QCD in [2,3,5,76–86] and the latest values have errors comparable to sizes of isospin-breaking and electromagnetic effects. The inclusion of these effects would need to be accompanied by a reduction in the uncertainty in the CKM matrix element $|V_{cb}|$ [7,87]. Long-distance contributions to the mixing parameters also need to be taken into account in order to make further progress in this avenue.

The BSM operators Q_{2-5} help quantify the possibility of New Physics contributions to ε_K. These operators have color-Dirac structures that are not present in SM contributions, thus making it easier to detect any New Physics arising from them. Additionally, the matrix elements of the BSM operators are enhanced in the chiral limit in comparison to the SM operator, so upon combination with experimental measurements they constrain the parameter space for BSM theories [88]. Previous computations of BSM kaon mixing has been performed using various frameworks of lattice QCD in [2, 3, 5, 74–76, 88–90].

2.5.6 $B_d^0 - \overline{B}_d^0$, $B_s^0 - \overline{B}_s^0$, and $D^0 - \overline{D}^0$ mixing

Neutral B, B_s and D meson mixing follow closely the theoretical framework of kaon mixing, with differences in relative contributions of the various mixing parameters to CP violation and other processes. For instance, the dominant sources CP violation in the B system are via interference of the decay and oscillation amplitudes and the interference of two decay amplitudes with different weak phases [91]. These effects are suppressed in the kaon system. The B meson is also much heavier than the kaon, and therefore has a larger phase space available for decay. This means that the difference in lifetimes between B_L and B_S is small in comparison to the kaon system.

The B_q^0 meson (with $q \in \{d, s\}$) oscillations provide many insights into quark flavour dynamics. These systems feature physical observables of great interest for probing our understanding of the SM as well as looking for New Physics: these include the mass and width splitting parameters Δm_d, Δm_s and $\Delta\Gamma_d$, $\Delta\Gamma_s$. A statistically significant discrepancy between the theoretical prediction and experimental measurement for the mass splittings would be suggestive of contributions from New Physics via unknown heavy particles at the loop-order.

The B meson mixing parameter M_{12}, like kaons, is dominated by the short-distance contribution. The SM prediction for the mass splitting of the B_q^0 meson is therfore given by

$$\Delta m_q = \frac{G_F^2 m_W^2 m_{B_q}}{6\pi^2} \left|V_{tq}^* V_{tb}\right|^2 S_0\left(\tfrac{m_t^2}{M_W^2}\right) \eta_{2B} f_{B_q}^2 \hat{B}_{B_q}, \tag{2.103}$$

where G_F is the Fermi constant, m_W and m_t are the masses of the W-boson and top quark respectively, m_{B_q} is the mass of the flavour eigenstate B_q^0, V_{tq} and V_{tb} are elements of the CKM matrix, S_0 is an Inami-Lim function which describes the basic electroweak loop contributions without QCD [92], and η_{2B} is the short-distance QCD correction factor [87]. Finally, $\hat{B}_{B_q}$ is the renormalisation group invariant (RGI) bag parameter derived from the SM $\Delta\mathcal{B} = 2$ operator $Q_{1,q} = [\bar{b}\gamma_\mu(1-\gamma_5)q][\bar{b}\gamma_\mu(1-\gamma_5)q]$. The procedure to derive RGI bag parameters $\hat{B}$ from $\mathcal{B}(\mu)$ is described in section 4.5.

In lattice QCD calculations, the flavour $SU(3)$-breaking ratio [93]

$$\xi^2 = \frac{f_{B_s}^2 \hat{B}_{B_s}}{f_{B_d}^2 \hat{B}_{B_d}}, \tag{2.104}$$

can be computed at greater precision than the individual RGI bag parameters in part due to cancellation of statistical and systematic errors. The quantity ξ^2 gives access to a precise determination of ratio of CKM matrix elements $|V_{td}/V_{ts}|$, which is used to constrain the apex of the unitarity triangle [94, 95].

While the SM operator Q_1 is used for predicting the mass splittings Δm_q, the matrix elements or bag parameters of the BSM operators are also useful for estimating the width splitting between the CP eigenstates of the B meson, where combinations of the matrix elements of $Q_{1-3,q}$ contribute to $\Delta\Gamma_q$ at $O(1/m_b)$ [7, 96, 97].

At present, the short-distance contribution to B-mixing via $\Delta\mathcal{B} = 2$ operators has been investigated by many groups using varying lattice QCD frameworks [98–106] and there are tensions between them. These tensions must be understood and resolved in order to infer the presence of New Physics in the neutral B-system [107–109].

Neutral D meson mixing offers complementary constraints on the CKM matrix. The hadronic contributions to the mixing parameters can once again be decomposed into the short-distance (with $\Delta\mathcal{C} = 2$ interactions) and long-distance contributions (with $\Delta\mathcal{C} = 1$ interactions). In this case, the short-distance contribution is subdominant and has been a subject of lattice predictions at $5 - 10\%$ precision [5, 110, 111] which are comparable to experimental measurements. However, experimental precision is expected to improve [112] therefore improvements in theoretical predictions are required for continued impact. In the $D^0 - \overline{D}^0$ system, the long-distance contributions of the $\Delta\mathcal{C} = 1$ operators pose a more difficult theoretical hurdle, and there is ongoing theoretical and algorithmic work for the computation of the relevant matrix elements. Despite this challenge, it is possible to validate or exclude New Physics models by studying the BSM extension to the $\Delta\mathcal{C} = 2$ sector only [113], and therefore warrants a systematic and high-precision study of the short-distance contribution.

2.5.7 Implications beyond the SM

Neutral K, D, B and B_s meson decay and mixing due to physics at higher scales – via interactions involving W, Z, t and H in the SM and unknown heavier particles in BSM theories – can be parameterised using operators composed of SM fields obeying the SM gauge symmetry. These flavour-changing neutral current (FCNC) interactions are suppressed in the SM and therefore sensitive to BSM contributions and thus to New Physics.

These BSM contributions are suppressed by powers of the scale at which they are generated, that is, at one-loop level at the lowest order in the case of neutral meson mixing. Even at lowest order, there are many dimension-6 operators as described in eqn (2.87), and BSM effects are encoded in their Wilson coefficients. These BSM contributions may or may not obey SM relations, for example, the Minimal Supersymmetric Standard Model (MSSM) introduces 40 *new* CP violating phases in its flavour sector [114, 115].

One can illustrate the level of suppression required for New Physics effects by considering a class of BSM models where unitarity of the CKM matrix is maintained. Assume that the dominant BSM effects modify the neutral meson mixing amplitudes as

$(z_{ij}/\Lambda_{\rm NP}^2)(\overline{q}_i\gamma_\mu(1-\gamma_5)q_j)^2$ where z_{ij} is some unknown constant and the scale $\Lambda_{\rm NP}$ suppresses the BSM contribution [116–119]. The existing data predicts that $\Lambda_{\rm NP}/|z_{ij}|^{1/2}$ would have to exceed 10^4 TeV for $K^0-\overline{K}^0$ mixing, 10^3 TeV for $D^0-\overline{D}^0$ mixing, 500 TeV for $B^0-\overline{B}^0$ mixing, and 100 TeV for $B_s^0-\overline{B}_s^0$ mixing [119, 120]. Thus, for New Physics to enter at the TeV scale we need $|z_{ij}| \ll 1$, which can have percent-level effects on processes at one-loop order, and may be observable in upcoming flavour physics experiments.

This tells us that constraining the measurements of the magnitudes and phases of FCNC interaction amplitudes to high precision allows for good sensitivity to New Physics beyond the SM.

Chapter 3

Lattice quantum chromodynamics

Quantum field theories (QFTs), as briefly introduced in section 2.1, are extensions of Lagrangian mechanics to the quantum domain, where the typical fluctuations of the action are of the order of the Planck constant $\hbar$[1]. In this regime the quantum effects are relevant, and the aim of quantum field theory in the path integral formulation is to describe these effects quantitatively.

However most QFTs, if *unregularised*, are ill-defined due to ultraviolet divergences. In terms of the path integral formulation, this means that the vacuum expectation value of an operator $\mathcal{O}$ given by the integral over all possible configurations of the field(s) ψ

$$\langle \mathcal{O} \rangle \equiv \langle \Omega | \mathcal{O} | \Omega \rangle = \frac{\int \mathcal{D}[\psi] \mathcal{O}[\psi] e^{iS[\psi]}}{\int \mathcal{D}[\psi] e^{iS[\psi]}}, \tag{3.1}$$

has an ill-defined measure $\mathcal{D}[\psi]$. To define a robust formalism for the path integral expectation values this measure must be addressed, and this process is known is *regularisation*. Typical schemes for this purpose are, amongst others, dimensional regularisation [121–123] and Pauli-Villars regularisation [124]; these are specific to perturbation theory where processes are expanded as asympototic series in powers of a small expansion parameter, for example a coupling constant. This works well for most QFTs, however in the case of Quantum Chromodynamics (QCD) the asympotic freedom of the QCD coupling constant implies that pertubation theory has poor convergence in the low energy regime where interesting hadronic interactions take place. In this case, the path integral formalism can be regularised non-perturbatively by restricting field configurations to live on a discrete hypercubic spacetime *lattice*, L[125]. The spacing a between adjacent sites on the lattice cuts off fluctuations of the field with energies higher than $\sim \pi/a$, thus reducing the ill-defined continuum measure to a well-defined measure over a discrete set

[1] Note that in this thesis we work in units wherein $\hbar = 1$

of integrals

$$\int_L \mathcal{D}[\psi] = \int \prod_{x \in L} d\psi(x). \tag{3.2}$$

While the lattice spacing, the 'minimum' length scale, renders all ultraviolet divergences finite, the calculation of the path integral can only be tractable if this discrete set of integrals is finite. This is done by further restricting the lattice to be of finite spacetime volume, thereby introducing a 'maximum' length scale that prevents infrared divergence. Typically lattices are square in the spatial dimensions (X) and elongated in the temporal dimension (T) such that there are $X^3 \times T$ lattice sites. The finite maximum length scale leads to quantised momentum modes, and the minimum length scale restricts these momenta to the Brillouin zone. In order to study the dynamics of the QFT at some energy/momentum scale of interest Λ, the two length scales must be well separated with

$$\frac{1}{aX} \ll \Lambda \ll \frac{1}{a}\,, \tag{3.3}$$

since the lattice cannot resolve states with energies greater than $1/a$ or fit those with energies lower than $1/aX$. Note that placing the theory in a finite box calls for a choice of appropriate boundary conditions (BCs); common choices include *periodic*, *anti-periodic*, *open* and *twisted* BCs [126, 127].

The phase in eqn (3.1) gives rise to poorly converging integrals, and we circumvent this issue by working in an Euclidean framework instead. We start by transforming from Minkowski space to Euclidean space via a Wick rotation of the time coordinate ($t \to i\tau$). The regularised Euclidean path integral is then defined by

$$\langle \mathcal{O} \rangle_{\text{Eucl.}L} = \frac{\int_L \mathcal{D}[\psi] \mathcal{O}[\psi] e^{-S[\psi]}}{\int_L \mathcal{D}[\psi] e^{-S[\psi]}}, \tag{3.4}$$

with respect to the weights $e^{-S[\psi]}$ where the Euclidean action S is real and positive. The continuum limit in the Euclidean theory corresponds to tuning the lattice parameters towards a second order critical point at which all correlation functions[2] in lattice units diverge and the lattice spacing a is therefore sent to zero relative to fixed physical correlation lengths.

While Wick rotating to a Euclidean spacetime gives us converging integrals, it is important to note that the analytic continuation of Euclidean quantities back to Minkowski spacetime is not always guaranteed. Quantities such as propagators and matrix elements – with at most one hadron in the initial and final states – are analytic functions that can be easily continued and studied in Minkowski space, however this is not true for

[2]Typical observables of a QFT are correlation functions (also known as n-point functions) of operators, defined via vacuum expectation values of time-ordered products of n fields.

multi-hadron state observables. In this thesis, we will only deal with quantities of the former kind.

The Euclidean path integral in eqn (3.4) is defined in terms of S and ψ, the discretised Euclidean action and field(s) repsectively. The specific choice of discretisation affects the approach to the continuum [128] and we shall now discuss this in greater detail in the context of QCD.

3.1 Discretising QCD

Let us recall the QCD action in Minkowski spacetime as introduced in eqn (2.9) for the case of $N_f = 1$

$$\begin{aligned} S_{\text{QCD}} &= \int d^4x \mathcal{L}_{\text{QCD}} \\ &= \int d^4x \left[-\frac{1}{4} F^C_{\mu\nu} F^{C,\mu\nu} + \overline{\psi}_a \left(i \not{D}_{ab} - m\delta_{ab} \right) \psi_b \right] \\ &:= S_G[A] + S_F[\overline{\psi}, \psi, A], \end{aligned} \tag{3.5}$$

where we have split the action into the pure gauge part S_G and the fermionic part S_F. The Euclidean versions of these are given by

$$S_G = \frac{1}{4g_s^2} \int d^4x F^C_{\mu\nu}(x) F^{C,\mu\nu}(x), \tag{3.6}$$

$$S_F = \int d^4x \overline{\psi} \left(\gamma^E_\mu D_\mu + m \right) \psi, \tag{3.7}$$

where γ^E_μ are the Euclidean gamma matrices (detailed in appendix A.2). Here we have introduced the rescaling of the gluon fields $g_s A^C_\mu \to A^C_\mu$ for later convenience.

We now wish to discretise this Euclidean action and there is significant freedom on how we achieve this as long as the discretised version is gauge invariant under the QCD gauge group and reduces to the continuum expression above in the limit $a \to 0$. To start, the integral over continuous spacetime in the action is replaced by a Riemann sum over the lattice sites given by

$$\int d^4x \to a^4 \sum_n, \text{ with } n = (\mathbf{n}, n_4), \tag{3.8}$$

such that $n_i = 1, \ldots, X$ and $n_4 = 1, \ldots, T$. Furthermore, the continuous spacetime

derivative ∂_μ is replaced by finite differences; we can define the forward (∂_μ) and backward (∂^*_μ) derivatives

$$\begin{aligned} \partial_\mu f(n) &= \frac{1}{a}\left(f(n+a\hat{\mu}) - f(n)\right), \\ \partial^*_\mu f(n) &= \frac{1}{a}\left(f(n) - f(n-a\hat{\mu})\right), \end{aligned} \tag{3.9}$$

where $\hat{\mu}$ is the lattice unit vector in the μ direction. We can choose to define the discrete derivative to be either of these or the symmetric combination $\Delta_\mu := (\partial_\mu + \partial^*_\mu)/2$.

3.1.1 Pure gauge action

Having made a choice for the discretisation of the spacetime derivative, we must investigate how this affects our covariant derivative and gauge fields in order to ensure that the fermion fields on the lattice transform correctly under the QCD gauge symmetry $SU(3)_C$.

Let us start by associating an $SU(3)_C$ element, represented by $\Omega(n)$, with each lattice site n. To ensure gauge invariance of the action, the fermion fields must transform as

$$\begin{aligned} \Omega : \psi(n) \to \psi'(n) &= \Omega(n)\psi(n), \\ \Omega : \overline{\psi}(n) \to \overline{\psi}'(n) &= \overline{\psi}(n)\Omega^\dagger(n). \end{aligned} \tag{3.10}$$

Now consider choosing the discretisation wherein the continuous spacetime derivative ∂_μ is replaced by the symmetric finite difference

$$\Delta_\mu \psi(x) = \frac{\psi(x+a\hat{\mu}) - \psi(x-a\hat{\mu})}{2a}. \tag{3.11}$$

We see that this leads to mixing of fields at neighbouring sites in the discretised QCD lagrangian, introducing terms like $\overline{\psi}(n)\psi(n+\hat{\mu})$, which are no longer gauge invariant since

$$\Omega : \overline{\psi}(n)\psi(n+\hat{\mu}) \to \overline{\psi}(n)\Omega^\dagger(n)\Omega(n+\hat{\mu})\psi(n+\hat{\mu}). \tag{3.12}$$

$SU(3)_C$ invariance can be restored by introducing a new field $U_\mu(n)$ in the finite derivative

$$\Delta_\mu \psi(x) = \frac{U_\mu(n)\psi(x+a\hat{\mu}) - U_{-\mu}(n)\psi(x-a\hat{\mu})}{2a}, \tag{3.13}$$

which transforms as

$$\Omega : U_\mu(n) \to U'_\mu(n) = \Omega(n)U_\mu(n)\Omega^\dagger(n+\hat{\mu}). \tag{3.14}$$

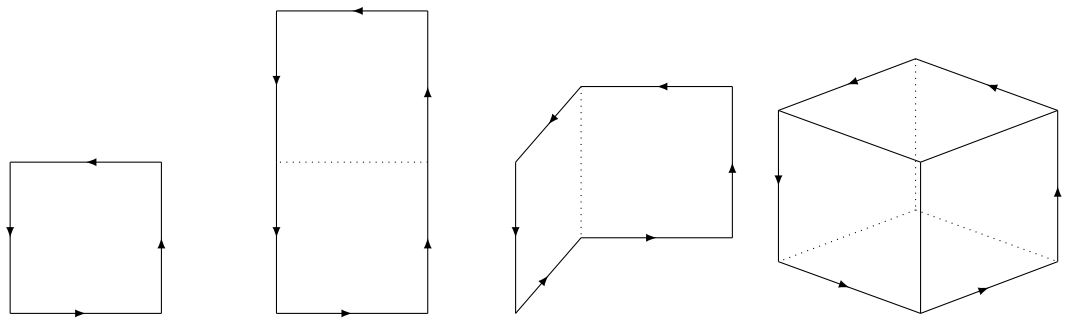

(a) plaquette (b) rectangle (c) chair-type (d) 3-dimensional

Figure 3.1: Types of Wilson loops that enter the Iwasaki gauge action: plaquette is a square loop, rectangle and chair-type loops are planar and non-planar 2×1 loops, 3-dimensional loop is a six-link path connecting opposite vertices of a cube.

In this definition, the term $\overline{\psi}(n)U_\mu(n)\psi(n+\hat{\mu})$ is gauge invariant under $SU(3)_C$ tranformations. We use the notation $U_{-\mu}(x) \equiv U_\mu^\dagger(n - a\hat{\mu})$. This field is related to the gauge field as

$$U_\mu(n) = e^{iag_s A_\mu(n)}, \tag{3.15}$$

and can be interpreted as linking the lattice site n to the site $n + \hat{\mu}$; hence it is called a *gauge link*.

Consecutive gauge links in a series inherit similar properties under gauge transformations:

$$\begin{aligned} U_\mu(n)U_\nu(n + a\hat{\mu}) \rightarrow &\Omega(n)U_\mu(n)\Omega^\dagger(n + a\hat{\mu})\Omega(n + a\hat{\mu})U_\nu(n + a\hat{\mu})\Omega^\dagger(n + a\hat{\mu} + a\hat{\nu}) \\ &= \Omega(n)U_\mu(n)U_\nu(x + a\hat{\mu})\Omega^\dagger(x + a\hat{\mu} + a\hat{\nu}). \end{aligned} \tag{3.16}$$

This implies that by chaining a number of consecutive gauge links in a closed loop, we end up with $\Omega(n)$ and $\Omega^\dagger(n)$ on the left and right side of the expression above, making the trace of a closed path over gauge links gauge invariant. Such an object is known as a *Wilson loop* [125]; the smallest Wilson loop, called a *plaquette*, is formed of four lattice sites in a square (see figure 3.1a),

$$U_{\mu\nu}(n) = U_\mu(n)U_\nu(n + a\hat{\mu})U_\mu^\dagger(n + a\hat{\nu})U_\nu^\dagger(n). \tag{3.17}$$

We are interested in constructing a discrete pure gauge action which is gauge invariant and reproduces the continuum QCD pure gauge action in the limit $a \to 0$, and gauge invariant Wilson loops make good candidates for this purpose. For example, the Wilson gauge action [125] is built from the plaquette:

$$S_G[U] = \frac{2}{g_s^2} \sum_{n \in L} \sum_{\mu<\nu} \mathfrak{Re}\left[\mathrm{Tr}\left(\mathbb{1} - U_{\mu\nu}(n)\right)\right]. \tag{3.18}$$

To demonstrate the equivalence to eqn (3.5) in the continuum limit, we can substitute in eqn (3.17) and Taylor expand eqn (3.15) upto $O(a)$; this gives us

$$S_G[U] = \frac{a^4}{4g_s^2} \sum_{n \in L} \mathrm{Tr}\left(F^C_{\mu\nu}(n) F^C_{\mu\nu}(n)\right) + O(a^2), \tag{3.19}$$

with leading order discretisation errors of $O(a^2)$. It is possible to obtain a better scaling of errors or more desirable simulation properties by making a different discretisation of the pure gauge action. There are two methods for systematically reducing discretisation errors: the Symanzik improvement program [128–131] and renormalisation group transformations [132–134].

The lattice simulations used for generating data for the projects in this thesis utilise the renormalisation-improved Iwasaki gauge action [135–137] which is schematically given by

$$\begin{aligned} S_G = \frac{2}{g_s^2} \sum_{n \in L} (&c_0 \mathrm{Tr}[\text{plaquette}] + c_1 \mathrm{Tr}[\text{rectangle loop}] \\ &+ c_2 \mathrm{Tr}[\text{chair-type loop}] + c_3 \mathrm{Tr}[\text{3-dim loop}] + \text{constant}) \end{aligned} \tag{3.20}$$

where the four types of loops are depicted in figure 3.1. The renormalisation constraint on the coefficients is given by $c_0 + 8c_1 + 16c_2 + 8c_3 = 1$ [135]. The Iwasaki gauge action has $O(a^2)$-improved discretisation errors and allows for a small residual mass parameter am_{res} in the Domain-Wall fermion action [138] (discussed in greater detail in section 3.1.4). The simulations for this project use the Iwasaki gauge ensembles calculated by the RBC-UKQCD collaboration [57, 77, 139] as input.

3.1.2 Naïve and Wilson fermions

Recall the symmetric discretisation of the spacetime derivative in eqn (3.13). We can use this to make a first attempt in writing down the discretised version of the fermionic part of the QCD action S_F by defining quark fields at the lattice sites and replacing derivatives with their discrete counterparts. This *naïve* fermion action takes the form

$$S_F[\overline{\psi}, \psi, U] = a^4 \sum_{n,m \in L} \overline{\psi}_{a,\alpha}(n) D(n|m)^{\,ab}_{\,\alpha\beta} \psi_{b,\beta}(m), \tag{3.21}$$

where $D(n|m)$ is the *Dirac operator* connecting the lattice sites n and m, given by

$$D(n|m)^{\,ab}_{\,\alpha\beta} = (\gamma_\mu)_{\alpha\beta} \left(\frac{U_\mu(n)_{ab} \delta_{n+\hat{\mu},m} - U_{-\mu}(n)_{ab} \delta_{n-\hat{\mu},m}}{2a} \right) + m \delta_{ab} \delta_{\alpha\beta} \delta_{n,m}. \tag{3.22}$$

The lowercase Latin letters denote colour indices as introduced in section 2.3, and the lowercase Greek letters denote Dirac or *spin* indices.

We can compute the Dirac operator of the free theory by setting $g_s = 0$, which makes all $U_\mu(n) = \mathbb{1}$. The Dirac operator is inversely related to the *propagator* for a free fermion with some momentum p_μ in the momentum space, so we Fourier transform as

$$\begin{aligned}\tilde{D}(p|q) &= \frac{1}{X^3 \times T} \sum_{n,m \in L} e^{-ip\cdot na} D(n|m) e^{iq\cdot ma} \\ &= \frac{1}{X^3 \times T} \sum_{n,m \in L} e^{-i(p-q)\cdot na} \left(\gamma_\mu \frac{e^{iq_\mu a} - e^{-iq_\mu a}}{2a} + m\mathbb{1} \right) \\ &:= \delta_{p,q} \tilde{D}(p),\end{aligned} \tag{3.23}$$

where we define

$$\tilde{D}(p) = m\mathbb{1} + \frac{i}{a}\gamma_\mu \sin(p_\mu a)\,. \tag{3.24}$$

The inverse of this is the momentum-space propagator given by

$$\tilde{D}(p)^{-1} = \frac{m\mathbb{1} - ia^{-1}\gamma_\mu \sin(p_\mu a)}{m^2 + a^{-2}\sum_\mu \sin^2(p_\mu a)}. \tag{3.25}$$

In a QFT, the masses of physical particles are inferred from the poles of the propagator. If we consider the case of massless quarks (set $m = 0$), the physical pole of the quark propagator corresponds to $p = (0,0,0,0)$ where $p^2 = m^2$. In the naïve discretisation of fermions on the lattice, the poles of the quark propagator in eqn (3.25) correspond to the corners of the Brillouin zone where $\sin^2(p_\mu a)$ vanishes, that is, where any component of p_μ is 0 or π/a. This generates $2^4 = 16$ poles (two poles in each dimension), of which only one is physical and 15 are unphysical poles describing additional massive particles. These spurious poles are called *doublers* and need to be removed to recover the physical continuum behaviour.

The first suggestion for removing the unphysical doublers came from Wilson using the observation that we may add any irrelevant higher dimesional operators to the discrete theory as long as they disappear in the continuum limit $a \to 0$. He proposed adding a dimension-5 term, such that the momentum-space Dirac operator becomes

$$\tilde{D}^{\text{Wilson}}(p) = \tilde{D}^{\text{naïve}}(p) + \mathbb{1}\frac{1}{a}\sum_\mu (1 - \cos(p_\mu a))\,. \tag{3.26}$$

For the case $p_\mu = (0,0,0,0)$, this term disappears, leaving the physical pole unchanged. For any momentum with at least one component being π/a, this term adds a contribution to the mass as $m + 2l/a$ where l is the number of components equal to π/a. In the continuum limit this mass term becomes divergent and the unphysical poles decouple from the theory, leaving behind only the physical one.

3.1.3 Chiral symmetry on the lattice

While adding the Wilson term solves the doubling problem, it comes at a cost: it explicitly breaks the chiral symmetry of the discrete QCD action – one can see this by writing the Wilson action in position space:

$$D(n|m)^{\text{Wilson}} = D(n|m)^{\text{naïve}} - a\sum_{\mu}\frac{U_{\mu}(n)\delta_{n+\hat{\mu},m} - 2\delta_{n,m} + U_{-\mu}(n)\delta_{n-\hat{\mu},m}}{2a^2}, \quad (3.27)$$

where $D(n|m)^{\text{naïve}}$ is given in eqn (3.22). In fact, the Nielsen-Ninomiya theorem states more generally that it is impossible to construct a local action[3] that is both free of doublers and preserves chiral symmetry [140].

In terms of the Dirac operator, a fermion action invariant under chiral symmetry satisfies the condition

$$\{D, \gamma_5\} = D\gamma_5 + \gamma_5 D = 0, \quad (3.28)$$

and maintaining this chiral symmetry is a desirable feature in a choice of fermion discretisation for the following reasons:

- The leading order, discretisation errors of a theory that possesses chiral symmetry are of $O(a^2)$, that is, simulations are automatically $O(a)$-improved.
- In the study of weak matrix elements (relevant to this thesis) the lack of chiral symmetry introduces mixing between operators that otherwise don't mix in the continuum theory due to being in different representations of the chiral symmetry group. This problem, however, can be resolved during the process of *renormalisation* – the matching of lattice fields to the continuum fields. It is argued in [141] that it is possible to place conditions on the renormalisation such that QCD-like behaviour is recovered in the continuum by adding terms that reconstruct the chiral basis of QCD. However, this means that chirally symmetric fermion actions enjoy a simpler, multiplicative renormalisation procedure, while chirally asymmetric actions require additive renormalisation.

A trick to get around the Nielsen-Ninomiya theorem was formulated in [142] by replacing the condition in eqn (3.28) with

$$\{D, \gamma_5\} = aD\gamma_5 D. \quad (3.29)$$

This is known as the Ginsparg-Wilson relation, and it matches the continuum condition for chiral symmetry in the limit $a \to 0$.

[3] for an even number of dimensions in a Euclidean theory

Lattice fields that obey the Ginsparg-Wilson relation therefore enjoy the benefits of chiral symmetry as discribed above, and the only known exact solution at present is given by *overlap* fermions [143–148]. The overlap formulation is related to another version of chiral lattice QCD using *domain wall* fermions which obey the Ginsparg-Wilson relation in a strict limit; this is the framework used for the projects in this thesis and we shall now discuss this in greater detail.

3.1.4 Domain wall fermions

The domain wall fermion (DWF) formulation, introduced in [149, 150] and developed further in [151–156], introduces an extra, unphysical fifth dimension in an attempt to circumvent the Nielsen-Ninomiya theorem [140]. The DWF Dirac operator satisfies the Ginsparg-Wilson relation and reproduces the overlap operator [147] in the limit of the fifth dimension extending out to infinity.

Continuum theory of DWFs

Before discussing the domain wall setup on the lattice, let us review its properties in the continuum. Consider a fermion field Ψ living in a 5-dimensional Euclidean spacetime with coordinates $X = (x, s)$ where $x = (\mathbf{x}, t)$ are the usual four infinite spacetime coordinates, and s is the coordinate of the fifth dimension. Furthermore, we assume that the fermion has a mass term that depends on s as

$$m(s) = m\theta(s) = \begin{cases} +m & s > 0 \\ -m & s < 0 \end{cases}. \tag{3.30}$$

The Lagrangian equation of motion for this DWF is then given by

$$\left[\not{D} + \gamma_5 \partial_s + m(s)\right] \Psi(x, s) = 0, \tag{3.31}$$

where D is the Dirac operator of the 4-dimensional theory. This equation is an eigenvalue problem which can be satisfied using separation of variables in a solution of the form [150]

$$\Psi(x, s) = \sum_n \left[a_n(s) P_R + b_n(s) P_L\right] \psi_n(x), \tag{3.32}$$

where $\psi_n(x)$ is the nth eigenvector of the 4-dimensional Dirac operator, $P_{R,L}$ are the chiral projectors introduced in eqn (2.19), and $a_n(s)$ and $b_n(s)$ are the right and left-handed solutions in the 5th dimension. By substituting eqn (3.32) into eqn (3.31) we

find that

$$\begin{aligned} [\partial_s + m(s)]\, a_n(s) &= \lambda_s b_n(s) \\ [-\partial_s + m(s)]\, b_n(s) &= \lambda_s a_n(s) \\ \left(\not{D} + \lambda_n\right) \psi_n(x) &= 0 \end{aligned} \tag{3.33}$$

where λ_n is the eigenvalue corresponding to $\psi_n(x)$. In the case $\lambda_n = 0$, the last line above is the equation of motion for a massless fermion (in four dimensions), and the equations for $a_n(s)$ and $b_n(s)$ decouple and can be satisfied by the ansatze

$$\begin{aligned} a_n(s) &= Ae^{-\int_0^s ds' m(s')} = Ae^{-m|s|} \\ b_n(s) &= Be^{+\int_0^s ds' m(s')} = Be^{+m|s|}\,. \end{aligned} \tag{3.34}$$

Note that the solution for $b_n(s)$ is not normalisable and therefore unphysical.

In the continuum theory, the DWF setup leads to an infinite tower of fermion states $\psi_n(x)$ each with mass $|\lambda_n| > 0$; these are called the *bulk modes*. The solution for $a_n(s)$ corresponds to a single massless right-handed fermion that is exponentially localised near the domain wall at $|s| = 0$. Due to the mass gap between the massless and bulk modes, at low energies only the massless chiral fermion is encountered.

DWFs on the lattice

The picture above holds for a theory with an infinite 5th dimension. However, on the lattice, we are restricted to a finite 5th dimension – forcing us to have a second domain wall. Consider for example a compact 5th dimension of extent L_s with periodic boundary conditions $\Psi(s) = \Psi(s + 2L_s)$ with two domain walls at $s = 0$ and $L_s - 1$. In this case, both the solutions in eqn (3.34) are normalisable (thus physical) and correspond to two exponentially localised massless modes: a right-handed mode at $|s| = 0$ and a left-handed mode at $|s| = \pm L_s - 1$. In the end, the resulting theory has two opposite-chirality 4-dimensional massless fermions localised on two domain walls, decaying exponentially in the 5th dimension.

Let us now write down the $N_f = 1$ DWF action on the lattice with the fermion $\Psi(n, s)$ of mass m_f (suppressing spin and colour indices):

$$S_F^{\mathrm{DW}}\left[\overline{\Psi}, \Psi, U\right](m_f, M_5) = \sum_{\substack{n,m\in L \\ s,t\in L_s}} \overline{\Psi}(n,s) D_5^{\mathrm{DW}}(n,s|m,t;m_f,M_5)\Psi(m,t)\,. \tag{3.35}$$

Here, D_5^{DW} is the 5-dimensional DWF Dirac operator which can be decomposed into components parallel and perpendicular to the 4-dimensional spacetime slices as

$$D_5^{\mathrm{DW}}(n,s|m,t;m_f,M_5) = \delta_{s,t} D^{\parallel}(n|m;M_5) + \delta_{n,m} D^{\perp}(s|t;m_f). \tag{3.36}$$

The parallel component is a discrete 4-dimensional Dirac operator connecting sites n and m given by

$$D^{\parallel}(n|m;M_5) = (4 - M_5)\,\delta_{n,m} - \frac{1}{2a}\sum_{\mu=\pm1}^{\pm4}(1-\gamma_\mu)\,U_\mu(n)\delta_{n+a\hat{\mu},m}, \tag{3.37}$$

where the parameter M_5 separates the two domain wall sites $s = 0$ and $s = L_s - 1$ and is known as the *domain wall height*. The perpendicular component connects the sites in the 5th dimension and is given by

$$\begin{aligned} D^{\perp}(s|t;m_f) =& \delta_{s,t} - (1-\delta_{s,L_s-1})\,P_L\delta_{s+1,t} - (1-\delta_{s,0})\,P_R\delta_{s-1,t} \\ &+ m_f\left(P_L\delta_{s,L_s-1}\delta_{0,t} + P_R\delta_{s,0}\delta_{L_s-1,t}\right). \end{aligned} \tag{3.38}$$

Note that the only term connecting the two domain wall sites resembles a mass term and is proportional to m_f. Also note that the gauge links $U_\mu(n)$ live in the usual 4-dimensional spacetime and therefore don't appear in $D^{\perp}$.

Chiral symmetry with DWFs

It has been shown in [157, 158] that domain wall fermions, in the limit $L_s \to \infty$, are equivalent to overlap fermions [146] which are exact solutions to the Ginsparg-Wilson relation (eqn (3.29)). However, as we are restricted to finite L_s on the lattice, the chiral symmetry in our theory is not exact and we will now discuss the effects of this in greater detail.

Let us start by looking at the physical 4-dimensional fields that live on the 4-dimensional boundary of $L \times L_s$; these are constructed as superpositions of the left and right-handed chiral modes at $s = 0$ and $s = L_s - 1$ respectively:

$$\begin{aligned} \psi(n) &\equiv \psi_L(n) + \psi_R(n) = P_L\Psi(n,0) + P_R\Psi(n,L_s-1), \\ \overline{\psi}(n) &\equiv \overline{\psi}_L(n) + \overline{\psi}_R(n) = \overline{\Psi}(n,0)P_R + \overline{\Psi}(n,L_s-1)P_L. \end{aligned} \tag{3.39}$$

By this definition, chiral symmetry is preserved when the left and right-handed fields decouple as $L_s \to \infty$; this is because terms breaking chiral symmetry mix left and right-handed components. This mixing can be minimised by restricting the overlap between the two chiral modes in the theory by separating them via a sufficiently large extent of the 5th dimension, L_s.

We are thus interested in defining a measure for the residual chiral symmetry breaking as a function of L_s. With this in mind, let us look at the chiral symmetries of the domain wall action: there is a symmetry under $\psi \to e^{i\frac{1}{2}\alpha^F t^F}\psi$ vector transformations (where the $SU(N_f)$ generators t^F were introduced in section 2.3.1), with associated 5-dimensional

conserved currents

$$\begin{aligned} j_\mu^F(n,s) &= \frac{1}{2}\Big[\overline{\psi}(n+\hat{\mu},s)(1+\gamma_\mu)U_\mu^\dagger(n)t^F\psi(n,s) \\ &\quad - \overline{\psi}(n,s)(1-\gamma_\mu)U_\mu(n)t^F\psi(n+\hat{\mu},s)\Big], \\ j_5^F(n,s) &= \frac{1}{2}\Big[\overline{\psi}(n,s+1)(1+\gamma_\mu)U_\mu^\dagger(n)t^F\psi(n,s) \\ &\quad - \overline{\psi}(n,s)(1-\gamma_\mu)U_\mu(n)t^F\psi(n,s+1)\Big]. \end{aligned} \tag{3.40}$$

The associated conserved 4-dimensional vector current is defined by summing over the 5th dimension

$$j_{\mathcal{V},\mu}^F(n) = \sum_{s=0}^{L_s-1} j_\mu^F(n,s). \tag{3.41}$$

The action is also symmetric under axial vector transformations $\psi \to e^{i\frac{1}{2}\alpha^F t^F q(s)}\psi$ following the conventions in [154], with $q(s) = \operatorname{sgn}\left(\frac{L_s-1}{2} - s\right)$. In this notation the associated conserved 4-dimensional axial current can be written using eqn (3.40) as

$$j_{\mathcal{A},\mu}^F(n) = \sum_{s=0}^{L_s-1} q(s) j_\mu^F(n,s). \tag{3.42}$$

We can also construct *local* vector and axial currents (with non-curly V and A) using the 4-dimensional quark fields

$$\begin{aligned} j_{V,\mu}^F(n) &= \overline{\psi}(n)t^F\gamma_\mu\psi(n), \\ j_{A,\mu}^F(n) &= \overline{\psi}(n)t^F\gamma_\mu\gamma_5\psi(n), \end{aligned} \tag{3.43}$$

which are related to their conserved counterparts via

$$\begin{aligned} Z_V j_{V,\mu}^F(n) &= j_{\mathcal{V},\mu}^F(n), \\ Z_A j_{A,\mu}^F(n) &= j_{\mathcal{A},\mu}^F(n), \end{aligned} \tag{3.44}$$

where $Z_{V,A}$ are multiplicative renormalisation constants. The exact conservation of chiral symmetry demands $Z_A = Z_V$ [159], and that the conserved currents have zero divergence $\Delta_\mu j_{\mathcal{V},\mu}^F(n) = 0$ and $\Delta_\mu j_{\mathcal{A},\mu}^F(n) = 0$, by Noether's theorem[4].

As we are working in the $N_f = 1$ theory, we will now remove the index F for the remainder of this discussion.

[4] We define $\Delta_\mu f(n) = f(n) - f(n-\hat{\mu})$

With a finite L_s and non-zero quark mass, chiral symmetry is broken and the conserved axial current picks up a non-zero divergence

$$a\Delta_\mu j_{\mathcal{A},\mu}(n) = 2am_f J_5(n) + 2J_{5q}(n), \tag{3.45}$$

where the first term accounts for the non-zero quark mass with $J_5(n) := j_5(n, L_s)$, and the second term – defined at the mid-point of the 5th dimension with $J_{5q}(n) := j_5(n, \frac{L_s}{2} - 1)$ – accounts for finite L_s. This condition is known as the *partially conserved* axial Ward identity (PCAWI).

However, we know that the axial Ward identity (AWI) in eqn (2.23), arising from non-zero masses, must be recovered in the continuum limit. This implies that in the limit $a \to 0$, $Z_A = Z_V = 1$. Furthermore, in the case of $N_f = 1$, the AWI can be written as

$$\sum_n \langle (\Delta_\mu j_{\mathcal{A},\mu})(n)\mathcal{O}(n)\rangle = 2m_f \sum_n \langle J_5(n)\mathcal{O}(n)\rangle\,, \tag{3.46}$$

where $\mathcal{O}(n)$ is some correlation function[5]. To recover this, the two terms in the PCAWI relation in eqn (3.45) must be combined, leaving us with

$$\begin{aligned}\sum_n \langle (\Delta_\mu j_{\mathcal{A},\mu})\mathcal{O}\rangle &= 2\sum_n \left\langle \left(2m_f J_5(n) + \frac{2}{a}J_{5q}(n)\right)\mathcal{O}(n)\right\rangle \\ &= 2\left(m_f + \frac{1}{a}\frac{\sum_n \langle J_{5q}(n)\mathcal{O}(n)\rangle}{\sum_n \langle J_5(n)\mathcal{O}(n)\rangle}\right)\sum_n \langle J_5(n)\mathcal{O}(n)\rangle\,.\end{aligned} \tag{3.47}$$

Comparing with eqn (3.46), we see that the second term in eqn (3.47) is a mass-like term arising due to the finiteness of the fifth dimension. We define this to be our measure of the residual chiral symmetry breaking attributed to finite L_s, and call it the *residual* mass. This is extracted from the asymptotic time behaviour of the ratio of correlation functions with current insertions:

$$am_{\text{res}} = \left.\frac{\sum_{\mathbf{n}}\langle J_{5q}(\mathbf{n},t)\mathcal{O}(\mathbf{n},t)\rangle}{\sum_{\mathbf{n}}\langle J_5(\mathbf{n},t)\mathcal{O}(\mathbf{n},t)\rangle}\right|_{t\gg 0}. \tag{3.48}$$

The effective mass of the DWF is therefore given by

$$m_{\text{eff}} = m_f + m_{\text{res}}. \tag{3.49}$$

As long as the value of the residual mass m_{res} is sufficiently small relative to m_f, the four-dimensional fermions of the theory are chiral up to $O(a^2)$ corrections. Note that in this framework, the chiral limit corresponds to $m_f \to -m_{\text{res}}$, instead of $m_f \to 0$.

[5]This relation arises because J_5 is equivalent to the conserved pseudoscalar density.

Other DWF kernels

In the projects in this thesis, we use both the Shamir [153] and Möbius [160–162] formulations of DWFs, corresponding to the choice made for the parallel component of the DWF Dirac operator. They are explicitly defined by the kernels

$$D^{\text{Shamir}} = \frac{a_5 D^{\parallel}}{2 + a_5 D^{\parallel}}, \tag{3.50}$$

$$D^{\text{Möbius}} = \frac{(b_5 + c_5) D^{\parallel}}{2 + (b_5 - c_5) D^{\parallel}}, \tag{3.51}$$

where $D^{\parallel}$ was defined in eqn (3.37). The Möbius kernel is a rescaling of the Shamir kernel $D^{\text{Möbius}} \equiv \alpha D^{\text{Shamir}}$ where $a_5 = b_5 - c_5$ and $\alpha a_5 = b_5 + c_5$. It can be shown that the two actions are identical in the limit $L_s \to \infty$ [77], however the Möbius action leads to a smaller m_{res} compared to the Shamir action at the same value of L_s.

3.1.5 γ_5-hermiticity

Let us finally remark on an important symmetry of lattice Dirac operators; almost all of them are γ_5-hermitian, that is, they obey

$$\begin{aligned} H : D &\to \gamma_5 D^{\dagger} \gamma_5 = D, \\ \implies (\gamma_5 D)^{\dagger} &= \gamma_5 D. \end{aligned} \tag{3.52}$$

Apart for being a useful mathematical tool for simplifying expressions, this also implies that the Dirac operator has eigenvalues that are either real or come in complex conjugate pairs. This means the determinant of the Dirac operator is real – this is a useful property for the numerical evaluation of the path integral as we will briefly touch upon in section 3.2.2.

Furthermore, the γ_5-hermiticity is inherited by the inverse Dirac operator making it a useful tool for manipulating Wick-contracted fermion fields in correlation functions.

3.2 Simulating the path integral

So far we have developed a framework for discretising the gauge and fermionic fields in QCD, and are ultimately intersted in studying hadronic observables calculated using Euclidean path integrals as defined in eqn (3.4). To get there, we must first dicuss the practical aspects of lattice computations. The problem of numerically evaluating the path integral can be split into two broad parts:

1. generating a set of gauge configurations known as a *gauge ensemble*, and

2. computing a path integral of a fermionic observable of interest over the gauge configurations.

In this section, we will discuss the steps involved in generating gauge ensembles using dynamical fermions, and in the next section we will detail the process of measuring fermionic observables using these ensembles.

3.2.1 Markov chain Monte Carlo sampling

Since we are interested in computing high-dimensional integrals, we turn to the Monte Carlo stochastic method for numerical integration.

The Monte Carlo approach to evaluating an integral requires drawing a set of samples by summing evaluations of integrand at random points in its domain. Mathematically, this is equivalent to computing the average value

$$\int dx\, f(x) = \lim_{N\to\infty} \frac{V}{N} \sum_{n=0}^{N-1} f(x_n), \tag{3.53}$$

where f is some function with domain x, and N is the number of Monte Carlo samples. The volume factor is given by the sum over the domain $V = \int dx$. Note that in this definition the Monte Carlo method samples uniformly from the domain of f. Also note that the error in the Monte Carlo estimation of integrals scales as $\sim 1/\sqrt{N}$ as we vary the sample size N. This scaling behaviour is favourable over to other methods for numerical integration as it has no dependence on the dimensionality of the problem.

In our path integral, the integration over the points x in the domain of our function is weighted by the Boltzmann factor $e^{-S(x)}$, where S is the action. In order to efficiently sample points with higher weights, we must bias our Monte Carlo method to draw from a non-uniform probability distribution; this is known as *importance sampling*. In this way, the *expectation* value of f biased to some probability distribution is given by

$$\langle f \rangle = \int dP(x) f(x) = \lim_{N\to\infty} \frac{1}{N} \sum_{n=0}^{N-1} f(x_n), \tag{3.54}$$

where x_n are generated by the probability density $dP(x)$ known as the *Gibbs measure*, given by

$$dP(x) = \frac{dx\, e^{-S(x)}}{\int dx'\, e^{-S(x')}}. \tag{3.55}$$

The sequential drawing of $x_1, x_2, \ldots, x_i, x_{i+1}, \ldots$ from the domain, in order to guide our starting guess x_0 towards the region of the domain that carries the highest weight, is

given by a Markov chain process. We can associate the probability of accepting (not rejecting) a proposed update step with the transition function

$$P(x_k = X'|x_{k-1} = X) := T(X'|X). \tag{3.56}$$

In order to ensure no preference in the direction of update, we demand the probability of reversing an update step be equal to that of traversing it. In practice this is enforced by the *detailed balance* condition

$$T(X'|X)P(X) = T(X|X')P(X'), \tag{3.57}$$

and the distribution of the Markov chain whose transition function satisfies this condition is called an equilibrium distribution. A typical Markov chain process needs a certain number of *thermalisation* steps to allow the algorithm to converge to equilibrium. Once it has, we can draw a Monte carlo samples using equilibrium distributions.

Note that a method for generating the transition function T associated with accepting/rejecting a proposed update step in the Markov chain is also needed; the Metropolis algorithm [163] is one such prescription. The transition probability between the current step with $x_i = X$ and a proposed next step with $x_{i+1} = X'$ is expressed as

$$T_{i+1}(X'|X) = \min\left(1, \frac{T_i(X|X')e^{-S(X')}}{T_i(X'|X)e^{-S(X)}}\right), \tag{3.58}$$

where the argument 'min' sets an upper bound of 1 on the transition probability.

3.2.2 The QCD Gibbs measure

Before we compute the expectation value of an observable using Monte Carlo sampling, we need to determine the Gibbs measure for generating samples from the domain, as described in eqn (3.54).

The path integrals for QCD involve drawing samples from a domain of high dimensionality, since the integration variables include paths of gauge links, fermion fields, as well as spatial coordinates. We call a single sampling from this domain a *configuration*. The Gibbs measure for generating configurations from the domain of QCD is therefore given by (using eqn (3.55))

$$dP[\Psi, \overline{\Psi}, U] = \frac{\mathcal{D}[\Psi, \overline{\Psi}, U] \exp\left(-S_G[U] - \sum_f^{N_f} S_F\left[\Psi_f, \overline{\Psi}_f, U\right]\right)}{\int \mathcal{D}[\Psi', \overline{\Psi}', U'] \exp\left(-S_G[U'] - \sum_f^{N_f} S_F\left[\Psi'_f, \overline{\Psi}'_f, U'\right]\right)}. \tag{3.59}$$

Note that the denominator is just the QCD partition function.

The fermionic part

In practice, the fermionic part of the path integral is typically integrated out analytically [164,165]. This is because fermions fields anti-commute and are therefore represented by Grassman variables, which are difficult to treat computationally. The partition function thus reduces to an integration over gauge fields

$$Z = \int \mathcal{D}\left[U\right] \left(\Pi_f^{N_f} \det\left[D_f[U]\right]\right) \exp\left(-S_G[U]\right), \tag{3.60}$$

where D_f is the Dirac operator[6] corresponding to the quark of mass m_f.

The Gibbs measure therefore also reduces to

$$dP[U] = \frac{1}{Z}\mathcal{D}\left[U\right] \left(\Pi_f^{N_f} \det\left[D_f[U]\right]\right) \exp\left(-S_G[U]\right), \tag{3.61}$$

where the dynamical effects of the quarks in the "gluonic sea" are captured via the N_f factors of the determinant of the Dirac operator. The "quenched" approximation, where we set $D_f = \mathbb{1}$, is ignorant of these sea-quark excitations. In un-quenched lattice QCD, the determinant of the Dirac operator is calculated in practice by simulating *pseudo*-fermion fields[7], Φ, by noting that [166]

$$\det D = \int \mathcal{D}\Phi \exp\left(-\Phi^\dagger(n) D^{-1}(n|m)\Phi(m)\right). \tag{3.62}$$

This is useful because the Dirac operator for a single fermion flavour is a very large matrix of size $N_{\text{colour}} \times N_{\text{spin}} \times X^3 \times T$, and direct evaluation of the determinant is extremely expensive in computation time. This is made more manageable by folding the determinant into the probability distribution using pseudo-fermion fields which act as noisy estimators of the fermion determinant. Note that the rewriting of the fermion determinant as an integral over pseudo-fermion fields is possible only when the determinant of the Dirac operator is real, a property derived from its γ_5-hermiticity, as mentioned in section 3.1.5. The final version of the Gibbs measure is therefore given by

$$dP[U,\Phi] = \frac{\mathcal{D}\left[U,\Phi\right] \exp\left(-S_G[U] - \sum_f^{N_f} \Phi_f^\dagger D_f^{-1} \Phi_f\right)}{\int \mathcal{D}\left[U',\Phi'\right] \exp\left(-S_G[U'] - \sum_f \Phi_f'^\dagger D_f^{-1} \Phi_f'\right)}, \tag{3.63}$$

which generates configurations of gauge fields as well as pseudo-fermion fields.

[6] As the QCD action is quadratic in the fermion fields, we can use the Berezin rules to analytically integrate $\int d\overline{\psi} d\psi \exp(\overline{\psi}_a D_{ab} \psi_b) = \det[D]$.

[7] called 'pseudo' since they commute

The gauge part

In practice, we can generate paths U_n starting from an arbitrary configuration of gauge links and follow the Markov chain process with the Metropolis accept/reject step to probabilistically perturb the links to a new path configuration. If we consider the Gibbs measure in the quenched approximation, we notice that it is highly local; however adding the fermion determinant part to it causes it to become non-local. This can lead to very large changes between one Markov chain step and the next one proposed, possibly leading to a low acceptance rate and thereby diminishing the efficiency of the algorithm greatly.

There are many techniques designed for addressing this problem, and the one used to generate the gauge configuration used in this thesis is known as the hybrid Monte Carlo (HMC) algorithm [167]; other algorithms include heat-bath [168,169] and over-relaxation [170, 171].

3.2.3 Gauge fixing

The gauge configurations in the Markov chain process are generated using the gauge-invariant QCD Lagrangian. The gauge symmetry (presented below in its discrete version), demands that physical observables remain unchanged under a local transformation of the gauge links of the form

$$g(n)U_\mu(n)g(n+\hat{\mu})^\dagger, \tag{3.64}$$

where $g(n)$ represents an arbitrary $SU(3)_C$ gauge group element. When computing the path integral over all possible configurations of the gauge links, there exists an inherent gross over-counting of the gauge links U_μ that are equivalent under $SU(3)_C$ gauge group transformations – each such set is called a gauge *orbit*. Where needed, this over-counting can be removed via gauge fixing, that is, restricting the path integral to sample only once from each gauge orbit.

Recall that the gauge links are defined as $U_\mu(n) = e^{iag_sA_\mu(n)}$ (see eqn (3.15)) where $A_\mu(n)$ are the $SU(3)_C$ Lie algebra-valued gauge fields. A typical gauge fixing condition in the continuum that is enforced at all spacetime points is the (minimal) Landau gauge

$$\partial_\mu A_\mu(x) = 0. \tag{3.65}$$

On the lattice, this is equivalent to demanding that the lattice gauge functional

$$F^{(g)}_{\text{Landau}}[U] = \frac{1}{12X^3T}\mathfrak{Re}\sum_{\mu,n\in L}\text{Tr}\left[g(n)U_\mu(n)g(n+\hat{\mu})^\dagger\right] \tag{3.66}$$

resides in a stationary point with respect to gauge transformations $g(n) \in \text{Rep}(SU(3)_C)$ [172–175].

The need for gauge fixing on the lattice

Unlike continuum QCD, the lattice formulation of gauge theories does not strictly require gauge fixing as we integrate over a compact gauge group, and the over-counting of gauge links in the same orbit simply emerges in the form of an overall normalisation constant. While physical observables are gauge-invariant, gauge fixing is needed for studying gauge-dependent intermediate quantities of interest such as correlation functions as well as in some non-perturbative renormalisation schemes which use gauge-dependent matrix elements to renormalise composite operators [176], as we will see in chapter 4. Where required, lattice measurements used in the projects in this thesis are gauge fixed using the Landau gauge.

3.2.4 Ensemble generation and scale setting

Given a starting configuration of fields $\mathcal{T}_i$, we evolve it via a Markov chain process which updates according to the Metropolis accept/reject condition to create *trajectories* of field configurations $\{\mathcal{T}_i\}$, generated using the Gibbs measure in eqn (3.63). The Monte Carlo method samples intermittently from the trajectories in the ensemble in order to reduce autocorrelations between consecutive field configurations. Such a set of configurations is called a gauge ensemble; these are computed for a particular lattice and are then used as integration variables for fermionic observables.

Before we move on to discussing how fermionic observables are computed using these gauge ensembles, let us take stock of the all the input parameters needed for computing these ensembles on a given lattice. As discussed in section 2.3, QCD is fully defined with seven input parameters: the $N_f = 6$ quark masses and the strong coupling constant g_s. The hierarchy of masses between the lightest and heaviest quarks makes it very difficult to simulate all six quarks on the same lattice. Simulations are instead restricted to a smaller number of quarks for the purpose of ensemble generation, for example $N_f = 2$, $N_f = 2 + 1$, or $N_f = 2 + 1 + 1$, where 2 refers to mass degenerate light quarks (l) - up and down (this further reduces the number of parameters). The quarks included in the ensemble generation process are called *sea* quarks. The projects in this thesis use lattices with $N_f = 2 + 1$ quarks in the sea.

In order to fix the remaining parameters, experimentally determined values of m_π, m_K and m_Ω are used as physical inputs to set the values of m_l, m_s and the lattice spacing a respectively. In this thesis we will also study physics at the charm scale, which we will fix using a physical input such as the η_c meson mass, however the charm quark is simulated only in the *valence* sector and its sea effects are neglected.

3.3 Correlation functions

Correlation functions, also known as n-point functions or Green's functions, are the building blocks for observables in a QFT. These are given by expectation values of products of fermionic fields with some Dirac structure. Recall from eqn (3.54) that expectation values on the lattice are estimated stochastically by averaging over *measurements* made on a set of configurations generated by the Gibbs measure for our theory.

Having generated an ensemble of gauge configurations, we are now ready to measure the expectation values of fermionic observables.

3.3.1 Propagators

Let us start with the simplest flavour-diagonal correlation function of two fermion fields known as a propagator

$$S_f(x,y)^{\alpha\beta}_{ab} = \left\langle \psi^{\alpha}_{f,a}(x)\overline{\psi}^{\beta}_{f,b}(y) \right\rangle_g , \tag{3.67}$$

where the Greek and Latin letters denote Dirac (also known as spin) and colour indices respectively, and the subscript g denotes the expectation value over gauge configurations. This describes a quark of flavour f created at point y propagating to and annihilated at point x. As discussed in section 3.1.2, the quark propagator is given by the expectation value of the inverse Dirac operator

$$S_f(x,y)^{\alpha\beta}_{ab} = \left\langle \left[D_f^{-1}(x,y) \right]^{\alpha\beta}_{ab} \right\rangle_g . \tag{3.68}$$

It also inherits the γ_5-hermiticity property of the Dirac operator (as mentioned in section 3.1.5) and is therefore trivially related to the quark propagator in the opposite direction (from x to y) by

$$S_f(y,x)^{\alpha\beta} = \gamma_5^{\alpha\rho} S_f^{\dagger}(x,y)^{\rho\sigma} \gamma_5^{\sigma\beta}, \tag{3.69}$$

where the Hermitian conjugation acts on the spin and colour indices.

Point sources

Propagators are ubiquitous to all lattice computations and make up the dominant expense as they require multiple *solves* of linear equations using the Dirac operator on each gauge configuration, as they are gauge-dependent quantities. The Dirac operator is a large matrix connecting every possible "source point" (source site, spin, colour) to

every possible "sink point" (sink site, spin, colour) [177]. In practice, propagators are computed by inverting the Dirac operators using a *source operator* $s(x, y)$ as

$$S_f(x,y)^{\alpha\beta}_{ab} = \left\langle D_f^{-1}(x,z)^{\alpha\rho}_{ac} s(z,y)^{\rho\beta}_{cb} \right\rangle_g . \tag{3.70}$$

The *all-to-all* propagator is computed by inverting the Dirac operator at every source and sink point using the source operator

$$s(x,y)^{\alpha\beta}_{ab} = \delta_{x,y}\delta_{\alpha\beta}\delta_{ab}. \tag{3.71}$$

This is very expensive to compute, and the task can be somewhat simplified by noting that the matrix elements of the full propagator will be highly correlated owing to translation invariance on the hypercubic lattice[8]. We can instead be much more memory efficient by storing entries from only one source point to every possible sink point, thereby removing largely redundant information. This is equivalent to retaining a single column of the inverse Dirac operator by using a source *vector*

$$s_{\mathrm{pt}}(x; y_0) = \delta_{x,y_0}\delta_{\alpha\beta}\delta_{ab}, \tag{3.72}$$

$$S_f(x,y_0)^{\alpha\beta}_{ab} = \left\langle D_f^{-1}(x,z)^{\alpha\rho}_{ac} s_{\mathrm{pt}}(z;y_0)^{\rho\beta}_{cb} \right\rangle_g , \tag{3.73}$$

at a single source site y_0. This restricts us to only 12 inversions (4 Dirac $\times$ 3 colour combinations) contributing to each choice of a sink point.

As point sources are placed at specific lattice sites, they are sensitive to local fluctuations; it is therefore common practice to average over many sources across the lattice sites in order to maximise the information extracted and reduce the statistical noise.

Stochastic sources

An overall reduction of noise in the inversion of the Dirac operator can be achieved with the use of stochastic sources [178], a method that has long been used in physics [179–181]. The stochastic approach to estimating the inverse of an $M \times M$ matrix D employs the introduction of an ensemble of N_{hits} column vectors $\eta^{(n)}$ with $n = 1, \ldots, N_{\mathrm{hits}}$ each with dimension $M \times 1$ with the properties of white noise

$$\langle \eta_i \rangle_n = \frac{1}{N_{\mathrm{hits}}} \sum_{n=1}^{N_{\mathrm{hits}}} \eta_i^{(n)} = 0, \quad \left\langle \eta_i \eta_j^\dagger \right\rangle_n = \frac{1}{N_{\mathrm{hits}}} \sum_{n=1}^{N_{\mathrm{hits}}} \eta_i^{(n)} \eta_j^{\dagger,(n)} \overset{N_{\mathrm{hits}}\to\infty}{=} \delta_{ij}, \tag{3.74}$$

where the second property allows for a noisy estimation of the inverse $\langle D^{-1}_{ij} \eta_i \eta_j^\dagger \rangle_n = D^{-1}_{ij}$ in the limit of a large number of hits.

[8] Note that translation invariance for lattice observables on a given ensemble is only approximate and is restored fully only after gauge averaging.

For the projects in this thesis we use N_{hits} stochastic $\mathbb{Z}_2$-*wall* sources $\eta_a^\alpha(\mathbf{x}, t_0)$ [182, 183] (called "wall" since the time component is fixed at some t_0) such that their hit-expectation value satisfies

$$\left\langle \eta_a^\alpha(\mathbf{x}, t_0)\eta_b^{\dagger,\beta}(\mathbf{y}, t_0)\right\rangle_n \equiv \frac{1}{N_{\text{hits}}}\sum_{n=1}^{N_{\text{hits}}} \eta_a^{(n),\alpha}(\mathbf{x}, t_0)\eta_b^{\dagger,(n),\beta}(\mathbf{y}, t_0) \overset{N_{\text{hits}}\to\infty}{=} \delta_{\mathbf{x},\mathbf{y}}\delta_{\alpha\beta}\delta_{ab}. \quad (3.75)$$

These are used for computing the propagator as

$$S_f(x, y)_{ab}^{\alpha\beta} = \left\langle D_f^{-1}(x, z)_{ac}^{\alpha\rho}\, s_{\mathbb{Z}_2}(z, y; t_0)_{cb}^{\rho\beta}\right\rangle_{g,n}, \quad (3.76)$$

$$\begin{aligned} \text{where} \quad s_{\mathbb{Z}_2}^{(n)}(x, y; t_0)_{ab}^{\alpha\beta} &= \eta_a^{(n),\alpha}(\mathbf{x}, t_0)\eta_b^{\dagger,(n),\beta}(\mathbf{y}, t_0)\delta_{t_x,t_y} \\ &= \eta^{(n)}(\mathbf{x})\eta^{\dagger,(n)}(\mathbf{y})\delta_{\mathbf{x},\mathbf{y}}\delta_{t_x,t_y}\delta_{\alpha\beta}\delta_{ab}, \end{aligned} \quad (3.77)$$

where each entry of the noise vector at the lattice site $\mathbf{x}$ corresponds to a $\mathbb{Z}_2 \times \mathbb{Z}_2$ complex number

$$\eta^{(n)}(\mathbf{x}) \in \left\{\frac{1}{\sqrt{2}}(\pm 1 \pm i)\right\}. \quad (3.78)$$

It is worth noticing that the gauge and hit averages commute, so the large hit limit (and therefore a good estimation of S) can be achieved by placing only a few noise sources per gauge configuration.

Note also that in lattice calculations we often extract only the time-dependence of correlation functions, and average over the spatial volume; this means the propagator is computed as

$$S_f(t_x, t_y)_{ab}^{\alpha\beta} = \left\langle \sum_{\mathbf{x},\mathbf{y}} D_f^{-1}(x, z)_{ac}^{\alpha\rho}\, s_{\mathbb{Z}_2}(z, y; t_0)_{cb}^{\rho\beta}\right\rangle_{g,n}. \quad (3.79)$$

If we assume the stochastic source vector $s_{\mathbb{Z}_2}$ to be diagonal in the spin indices, then for a given source time t_y, we only need to invert the Dirac matrix once per flavour. This means that by introducing noise we are able to sample the entire spatial volume of the source time-plane with only one inversion; this is known as the *one-end-trick* [183, 184].

Some other noise reduction techniques that are beyond the scope of this thesis include deflation [185], distillation [186], low-mode-averaging [187, 188], and all-mode-averaging [189–191].

Gaussian smeared sources

The point-like sources we have discussed so far place the quark field $\psi(x)$ on a specific lattice site x, which has only a small overlap with the physical wavefunction since particles are not point-like. We can consider modelling the physical wavefunction by

using more point sources, however this increases the number of inversions required (of the Dirac operator); so we instead use *smeared* fields to optimise our signal of interest. For this we use a "smearing function" – a standard choice for this is the Jacobi smearing which follows the Gaussian shape like those of simple wavefunctions [192], making it easy to create gauge-invariant smeared interpolating operators. This corresponds to smearing at the source and/or sink point as

$$s_{\omega}^{AB}(x,y) = \sum_{\mathbf{w},\mathbf{z}} \omega^{A}(\mathbf{x},\mathbf{z})\delta_{t_x,t_z}\, s(z,w)\, \omega^{B}(\mathbf{w},\mathbf{y})\delta_{t_w,t_y}; \quad A,B \in \{S,L\}, \tag{3.80}$$

$$\text{with} \quad \omega^{S}(\mathbf{x},\mathbf{y}) = \left(1+\frac{\sigma^2}{4N}\right) H(\mathbf{x},\mathbf{y};N); \quad \omega^{L}(\mathbf{x},\mathbf{y}) = \delta_{\mathbf{x},\mathbf{y}} \tag{3.81}$$

where S and L stand for smeared and local respectively; σ is the smearing width, N is the number of smearing steps, and $H(\mathbf{x},\mathbf{y})$ is the smearing function

$$H(\mathbf{x},\mathbf{y};N) = \sum_{i=1}^{3} \left(U_i(\mathbf{x})\delta_{x+\hat{i},y} + U_i(\mathbf{x}-\hat{i})\delta_{x-\hat{i},y} \right)^{N}. \tag{3.82}$$

The projects in this thesis use correlation functions with both local and smeared quark fields, and further details about the smearing parameters σ and N used are provided in [105].

3.3.2 Meson interpolators

As discussed in section 2.3, the confining nature of QCD dictates that there are no colour-singlet states at low energies, and quarks are confined into colour-neutral hadrons. In the low energy regime, we are interested in hadrons and therefore must discuss the properties of relevant operators and relate their correlation functions to hadronic observables.

Hadrons are characterised by their spin (J), parity (P) and charge conjugation (C) quantum numbers. To study these hadrons on the lattice, we must identify *interpolating* operators that create states with the appropriate quantum numbers from the vacuum. Some general forms of mesonic interpolators are quark bilinears which act as local creation and annihilation operators given respectively by

$$\mathcal{O}(x) = \overline{\psi}_{f}(x)\Gamma\psi_{f'}(x), \quad \mathcal{O}^{\dagger} = \overline{\psi}_{f'}(x)\Gamma^{\dagger}\psi_{f}(x). \tag{3.83}$$

Here, f and f' correspond to the flavours of the two quark fields, and Γ is a generic Dirac structure used for inducing the appropriate quantum numbers – table 3.1 lists various choices of Γ and the quantum numbers induced by each. In this thesis, we are interested in the properties of pseudoscalar mesons such as π, K, D, D_s, η_c, B, and B_s, which are created by interpolators of the form $\overline{\psi}_{f}\gamma_5\psi_{f'}$.

Γ	Lorentz	J^{PC}	mesons
$\mathbb{1}$	scalar	0^{++}	a_0, f_0, ...
γ_5	pseudoscalar	0^{-+}	π, K, D, D_s, η_c, B, B_s, ...
γ_μ	vector	1^{--}	ρ, ω, ϕ, J/ψ, K^*, D^*, ...
$\gamma_\mu\gamma_5$	axial vector	1^{++}	a_1, f_1, ...
$\sigma_{\mu\nu}$	tensor	1^{+-}	b_1, h_1, ...

Table 3.1: Quantum numbers induced by various Dirac structures in meson interpolators: J is psin, P is parity and C is charge conjugation. Some of the lightest mesons are listed as examples [6, 7].

Two-point functions

Let us begin by studying the two-point correlation function of a meson interpolator $\mathcal{O}(x)$ between the source and sink sites x_{src} and x_{snk} given by the time-ordered vacuum expectation value

$$C_{\text{2pt}}(x_{\text{snk}}, x_{\text{src}}) = \left\langle T\{\mathcal{O}(x_{\text{snk}})\, \mathcal{O}(x_{\text{src}})^\dagger\} \right\rangle . \tag{3.84}$$

We are often interested only in the temporal separation and therefore average over the spatial volume to get

$$C_{\text{2pt}}(t) = \left\langle \sum_{\mathbf{x}} T\{\mathcal{O}(\mathbf{x}, t)\, \mathcal{O}(\mathbf{0}, 0)^\dagger\} \right\rangle . \tag{3.85}$$

By making the expectation values explicit, inserting a complete set of states, and pulling out the time-dependence of the operators, one can show that this equation is analytically equivalent to

$$C_{\text{2pt}}(t) = \frac{1}{Z} \sum_{\mathbf{x},n} \frac{1}{4E_n E_0} \langle 0|e^{-E_0(T-t)} \mathcal{O}(\mathbf{x}, 0) e^{-E_n t}|n\rangle\langle n|\mathcal{O}(\mathbf{0}, 0)|0\rangle, \tag{3.86}$$

where E_n is the energy of the nth state, and T is the lattice time extent. The partition function is given by

$$Z = \sum_n \frac{1}{2E_n} \langle n|e^{-\hat{H}T}|n\rangle = \sum_n \frac{1}{2E_n} e^{-E_n T}. \tag{3.87}$$

One can show that by neglecting the finite-size effects, the two-point function can be simplied to the form

$$C_{\text{2pt}}(t) = \sum_n \frac{|A_n|^2}{2E_n} \left(e^{-E_n t} + e^{-E_n(T-t)} \right), \tag{3.88}$$

where A_n is the transition amplitude between the vacuum and the nth energy state $A_n = |\langle 0|\mathcal{O}|n\rangle| = |\langle 0|\mathcal{O}^\dagger|n\rangle|$. The two-point function therefore behaves as a cosh-like

function, where the second term captures the "around-the-world" effect of the toroidal lattice.

We commonly refer to the $n = 0$ state as the *ground state* and to all others ($n > 0$) as *excited states*. Since $E_{n>0} > E_0$, at large time separations we can assume ground state dominance and isolate the ground state energy from the asymptotic time behaviour of the *effective mass*, given by the ratio[9]

$$m_{\text{eff}}(t) = \cosh^{-1}\left(\frac{C_{\text{2pt}}(t+1) + C_{\text{2pt}}(t-1)}{C_{\text{2pt}}(t)}\right); \quad 0 \ll t \ll T/2. \tag{3.89}$$

Note that source smearing is often used to increase overlap with the ground state and reduce excited state contamination in correlation functions.

Three-point functions

The three-point functions we study in this thesis are those of flavour-changing neutral currents corresponding to pseudoscalar meson mixing. In this section, we term the quark which does not change flavour as the *spectator* quark, ψ_s, and the one that does change flavour from and initial state flavour f_1 to a final state flavour f_2 as the *valence* quark. The initial state creation and final state annihilation operators are therefore given by

$$\begin{aligned} \mathcal{O}_1^\dagger(x) &= \overline{\psi}_s(x)\gamma_5\psi_{f_1}(x), \\ \mathcal{O}_2(x) &= \overline{\psi}_{f_2}(x)\gamma_5\psi_s(x). \end{aligned} \tag{3.90}$$

The interaction is mediated by some flavour-changing operator $Q(x)$ with the appropriate Dirac structure and quark content, for example the operators in eqn (2.91) in the case of neutral kaon mixing. The three-point function of the interaction is thus given by

$$C_{\text{3pt}}(t, \Delta T) = \left\langle \sum_{\mathbf{x},\mathbf{y}} \mathcal{O}_2(\mathbf{x}, \Delta T) Q(\mathbf{y}, t) \mathcal{O}_1^\dagger(\mathbf{0}, 0) \right\rangle, \tag{3.91}$$

with the operator inserted at t and the initial and final states separated by ΔT. Smearing can be applied in various combinations for the different quark fields – spectator or valence – in the inital and final state operators in order to improve the overlap with the ground state. Additionally the source and sink separation ΔT can be optimised for extracting a stable signal with the least amount of statistical fluctuations.

[9] Note that this is only one choice for defining the effective mass and there exist other definitions that are often used.

3.4 Statistical analysis

3.4.1 Resampling and error propagation

Correlation functions are defined as expectation values over an ensemble of gauge configurations, where we compute an average over data from our simulations. This alone only provides a single average value for the correlation function and it is important to estimate statistical errors. While it is possible to assign a statistical error by studying the variance in measurements over configuration for *primary* quantities (measured directly on gauge configurations), it becomes difficult to define the errors for *secondary* quantities that are derived from primary ones (especially if there is a non-linear dependence). This problem is typically addressed by employing *resampling* methods.

In this thesis we adopt the *bootstrap* resampling method [193] which is a generalisation of the *jackknife* method. Given a random variable x with N measurements, the bootstrap resampling method generates a resampled dataset made up of K "bootstrap samples" that define the mean and variance for the unbiased estimator $\tilde{x}$ via

$$\langle \tilde{x} \rangle = \frac{1}{K} \sum_k b_k; \quad \sigma_{\tilde{x}}^2 = \frac{1}{K-1} \sum_k (b_k - \langle x \rangle)^2, \tag{3.92}$$

where b_k is the kth bootstrap sample given by the average of N randomly selected values from the measurement sample with replacement, and $\langle x \rangle$ is the measurement sample average. Statistical errors are therefore propagated via bootstrap samples, and secondary data is constructed from primary data using operations performed bootstrap-sample-by-bootstrap-sample.

In practice, the N measurements each represent the configuration value of x, and the bootstrap resample method assumes that these are uncorrelated. This is a valid assumption as long as the Monte Carlo sampling takes place over configurations sufficiently separated in the Markov chain process.

The number of bootstrap samples K is a free parameter, and the estimator $\tilde{x}$ is expected to converge to x in the limit $K \to \infty$. For all quantities in the projects in this thesis, we use 1000 bootstrap samples. It is important to note that the resampling method provides an estimate and therefore carries an associated resampling error [194].

In this thesis, we use datasets of varying sizes depending on how many configurations are used in the measurement for a given quantity, and we typically wish to combine the data for example to produce results for an observable in the combined continuum limit derived from lattices of varying lattice spacings. The resampling method provides a simple and statistically robust way for computing estimators for such observables.

3.4.2 Data fitting

Lattice data is typically conceived in the form of volume-averaged correlation functions. We are often interested in extracting information – for example amplitudes and energies – by fitting the lattice data to some analytic form. In this section we outline our procedure for the fitting of data.

As a simple example, consider a correlation function dependent on time-separation t, $C(t)$, which we wish to describe with an ansatz $f(\alpha, t)$ where α is the vector of input parameters we wish to extract using a tuning procedure that converges on the value $\alpha^\star$ such that $f(\alpha^\star, t)$ best describes $C(t)$. The procedure followed for all such fits in this thesis is the generalised least-squares method which optimises α by minimising the quantity

$$\chi^2 = (C(t_i) - f(\alpha, t_i))\mathtt{COV}^{-1}(t_i, t_j)(C(t_j) - f(\alpha, t_j)), \tag{3.93}$$

where $C(t) - f(\alpha, t)$ is known as the residual or difference vector, and $\mathrm{cov}(t_i, t_j)$ is the covariance between the time slices t_i and t_j. The covariance is estimated from the samples of the correlation function, and is given by

$$\mathrm{cov}(t_i, t_j) = \langle (C(t_i) - \langle C(t_i)\rangle)(C(t_j) - \langle C(t_j)\rangle)\rangle\,, \tag{3.94}$$

where "samples" can mean the configuration samples or the bootstrap (re)samples. The diagonal elements are the variances $\sigma^2(t_i)$ at each time slice, and are useful for relating the covariance matrix to the *correlation* matrix

$$\mathrm{cor}(t_i, t_j) = \frac{1}{\sigma(t_i)}\mathrm{cov}(t_i, t_j)\frac{1}{\sigma(t_j)}, \tag{3.95}$$

which captures the statistical correlations between different times.

Having determined the optimal values of the fit parameters $\alpha^\star$ that minimise the χ^2, we can quantify the suitability of the ansatz $f(\alpha^\star, t)$ for describing the data $C(t)$. This goodness-of-fit is calculated by reporting the two-tailed p-value of the fit corresponding to the reduced χ^2 distribution given by $\chi^2_{\mathrm{red}} \equiv \chi^2/\mathrm{d.o.f.}$, where d.o.f. stands for the degrees of freedom in the fit. The p-value measures the probability of obtaining the observed data assuming the null hypothesis is true. In this thesis, we almost always characterise fits that reject the null hypothesis to have $5\% \leq p \leq 95\%$, where the upper bound typically punishes over-fitting.

In the case where we neglect the inherent correlations in the data (by imposing $\mathrm{cor}(t_i, t_j) = \delta_{ij}$) and perform an uncorrelated fit, the χ^2_{red} distribution provides no probabilistic interpretation for the goodness-of-fit.

3.5 Lattice systematic errors

In addition to statistical errors associated to the Monte Carlo stochastic estimation of quantities on the lattice, the lattice methodology inherently introduces systematic errors that must be estimated, controlled, and reduced when making a prediction for a physical observable. Note that systematic errors need to be estimated individually for different observables, and the methodologies used in the projects in this thesis will separately account for them in chapter 5 and chapter 6. In this section, we give a brief overview of some of the common sources of systematic errors in lattice computations.

Finite volume effects

As we briefly saw in the case of two-point functions in section 3.3.2, the finite volume as well as the periodic boundary conditions of the lattice introduce "around-the-world" effects, that is, self interactions between particles on the lattice and their counterparts across the boundary. For the quantities in this thesis, these effects are exponentially suppressed by the mass of the particle as e^{-mL} [195]. This means that the minimum volume required to keep finite volume effects at a sub-percent level is determined by the mass of the lightest hadron on the lattice, which is usually the pion; this threshold is typically imposed by ensuring $m_\pi L \gtrsim 4$ [196].

Discretisation errors

In order to calculate a continuum observable using lattice data, it is necessary to compute the same physical observable on lattices with different spacings so as to parameterise the lattice spacing dependence and extrapolate to the continuum limit $a \to 0$. The various choices involved in discretising the theory on a lattice leads to various discretisation errors in the value of observables in the continuum limit.

As we discussed in section 3.1.4, retaining chiral symmetry automatically limits discretisation errors to $O(a^2)$, but the finite size of the fifth dimension of the domain wall fermion discretisation still introduces residual chiral symmetry breaking effects measured by the quantity am_{res}.

In addition to this, discretisation errors are also expected to grow in powers of am_q, where m_q are input quark masses, and the largest errors are induced by the heaviest quark in the valence sector. For all hadrons to be well resolved on the lattice, the pion mass m_π and the mass of the heaviest quark need to satisfy

$$L^{-1} \ll m_\pi < m_q < a^{-1}, \tag{3.96}$$

however this hierarchy is often violated when working with charm or bottom quarks. There are many proposed methods of controlling discretisation errors caused by heavy quark masses, and in chapter 6 of this thesis, we will discuss a specific methodology that addresses this problem via the procedure of non-perturbative renormalisation (NPR).

Chiral extrapolation

As discussed in section 3.2.4, lattice computations use ensembles of gauge configurations, for example with $N_f = 2+1$ quark flavours in the sea, where the quark masses and lattice spacing are tuned using physical values of the pion, kaon, and omega-meson masses as input. However, it is often computationally expensive to generate ensembles at the *physical point*, that is, where the quark masses are tuned using the physical values of the meson masses. For this reason lattice calculations often use gauge ensembles generated using meson masses heavier than their physical values. In order to control the systematic error arising from the use of unphysical meson masses for tuning the lattice parameters, it is necessary to compute physical observables on lattices differing on the values of the input meson masses, and extrapolate to the physical values of the meson masses. Note that chiral perturbative theory provides a symmetry-based, model-independent approach to parameterising the quark mass dependence of observables, as discussed briefly in section 2.3.3.

In the meson mixing project in this thesis (reported in chapter 5), we make use of lattices tuned using both physical and unphysical meson masses. In the massive NPR project in this thesis (reported in chapter 6), we only use lattices tuned at unphysical pion masses, and therefore study the pion mass-dependence of our results as part of the analysis of systematic errors.

Chapter 4

Non-perturbative renormalisation

The spacetime lattice can be viewed as a regularisation where the lattice spacing and finite box size play the roles of ultraviolet and infrared regulators respectively. In order to obtain physical results from numerical simulations, lattice regularised quantities need to be identified with observables in the continuum theory via the process of *renormalisation*.

Masses of hadronic bound states are scale-independent and therefore physical (that is, experimentally measurable), and can be measured directly from the exponential decay of two-point correlation functions without a need for renormalisation. However, scale-dependent observables such as hadronic matrix elements and quark masses require renormalisation parameters that must be assigned via a chosen scheme.

Lattice perturbation theory – using series exapansions in powers of the small lattice spacing a – has been used historically for comparing lattice and continuum results [197]. However this method has poor convergence in certain cases and reducing uncertainties below 5% is difficult. As a result, non-perturbative renormalisation (NPR) methods have been proposed for removing the regularisation-dependence of observables, yielding quantities in the so-called *regularisation-independent* (RI) schemes [198] which may then be matched to some favoured continuum scheme — commonly the $\overline{\text{MS}}$ scheme — using continuum perturbation theory.

The procedure is therefore the following: we start with lattice regularised data which are outputs from our numerical simulations, we use an intermediate NPR scheme and extrapolate to the continuum limit to produce regularisation-independent quantities which are then matched to $\overline{\text{MS}}$ scheme using continuum perturbation theory.

4.1 The Rome-Southampton method

A renormalisation scheme demands that in the continuum limit ($a \to 0$), renormalised lattice operators must correspond to finite operators which have the same symmetries

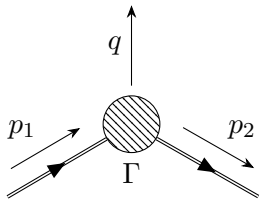

Figure 4.1: Choice of kinematics for bilinear Green's functions. The dashed bubble represents the operator insertion (with Dirac structure Γ) and higher order corrections, p_1 and p_2 are the momenta of the external off-shell quark lines.

and renormalisation conditions as those in the continuum theory. In what follows, we describe the NPR prescription in the Rome-Southampton symmetric momentum-subtraction scheme - RI/SMOM [199]. Note that all discussions use Euclidean quantities.

Consider a bare lattice operator $\mathcal{O}(a)$. The regularisation-independent operator at some renormalisation scale μ is defined by introducing a renormalisation constant $Z_{\mathcal{O}}$ as

$$\mathcal{O}^{\mathrm{RI}}(\mu) = \lim_{a\to 0} Z_{\mathcal{O}}(a\mu)\mathcal{O}(a). \tag{4.1}$$

In the RI/SMOM scheme, $Z_{\mathcal{O}}$ is found by demanding that in a fixed gauge, for a chosen set of external momenta, the renormalised amputated Green's function of $\mathcal{O}$ coincide with its tree level value. This is described in further detail in the following subsections in the cases of bilinear and fourquark operators.

Renormalisation of bilinear operators

Consider the Green's function of a quark bilinear operator $\mathcal{O}^F_\Gamma = \overline{\psi}_f \Gamma \tau^F \psi_{f'}$ between two external off-shell quark lines in a fixed (Landau) gauge

$$G^F_\Gamma(p_2, p_1) = \langle \psi_f(p_2) \mathcal{O}^F_\Gamma(q) \overline{\psi}_{f'}(p_1) \rangle, \tag{4.2}$$

where ψ_f and $\psi_{f'}$ are quark fields of flavours f and f', and $q = p_1 - p_2$ (see figure 4.1 for conventions used). τ^F represents a generator of the $SU(N_f)$ symmetry; note that for the remainder of the discussion we suppress the sum over the adjoint flavour index F. Γ indicates the Dirac structure of the operator; we are interested in scalar, 'S' ($\Gamma = \mathbb{1}$), pseudoscalar, 'P' ($\Gamma = i\gamma_5$), vector, 'V' ($\Gamma = \gamma^\mu$), axial vector, 'A' ($\Gamma = \gamma^\mu\gamma_5$), and tensor, 'T' ($\Gamma = \frac{1}{2}[\gamma_\mu, \gamma_\nu] := \sigma_{\mu\nu}$) bilinears. The quark propagator is defined as

$$S_f(p) = \langle \psi_f(p) \overline{\psi}_f(p) \rangle, \tag{4.3}$$

and the amputated Green's function is obtained by amputating each leg with the inverse quark propagator of the corresponding flavour

$$\Lambda_\Gamma(p_1, p_2) = S_f^{-1}(p_2) G_\Gamma(p_2, p_1) S_{f'}^{-1}(p_1). \tag{4.4}$$

Renormalised (subscript 'R') and bare quantities (no subscript) are related via renormalisation constants Z as

$$\begin{aligned} \psi_R = Z_q^{1/2}\psi, \quad m_R = Z_m m, \quad \mathcal{O}_{\Gamma,R} = Z_\Gamma \mathcal{O}_\Gamma, \\ \implies S_R(p) = Z_q S(p), \quad \Lambda_{\Gamma,R}(p_1,p_2) = \frac{Z_\Gamma}{Z_q}\Lambda_\Gamma(p_1,p_2). \end{aligned} \tag{4.5}$$

The Z-factors in the RI/SMOM scheme are defined by imposing the condition

$$\begin{aligned} \lim_{m_R\to 0} \hat{P}_\Gamma \left[\Lambda_{\Gamma,R}(a,p_1,p_2)\right]_{\text{sym}} = F_\Gamma \equiv \hat{P}_\Gamma \left[\Lambda_\Gamma^{(0)}(p_1,p_2)\right]_{\text{sym}}, \\ \implies \lim_{m_R\to 0} \frac{Z_\Gamma}{Z_q}(a,\mu)\hat{P}_\Gamma \left[\Lambda_\Gamma(a,p_1,p_2)\right]_{\text{sym}} = F_\Gamma, \end{aligned} \tag{4.6}$$

where $\Lambda_\Gamma^{(0)}$ is the tree level amputated Green's function, $\hat{P}_\Gamma$ is a projector, and F_Γ is the corresponding tree level value. 'sym' denotes the symmetric momentum configuration characteristic to the SMOM scheme which sets the renormalisation scale

$$p_1^2 = p_2^2 = q^2 \equiv \mu^2. \tag{4.7}$$

RI/MOM vs RI/SMOM scheme

Originally, the Rome-Southampton method used the choice of kinematics

$$p_1 = p_2 = \mu\,;\, (p_1-p_2)^2 = q^2 = 0, \quad \text{(RI/MOM)} \tag{4.8}$$

where the momentum inserted at the operator is $q = 0$, called an *exceptional* channel – where the square of the momentum, q^2, is much smaller than the typical scale μ^2. For this choice of kinematics, the effects of chiral symmetry breaking vanish slowly as $1/p^2$ for large external momenta p^2, which can be seen via the differences $(\Lambda_V - \Lambda_A)$ and $(\Lambda_S - \Lambda_P)$ [200], and other unwanted infrared effects, need to be subsequently treated with a pion-pole subtraction procedure. An alternate choice of kinematics was proposed to address this issue, by employing *non-exceptional* kinematics

$$p_1 \neq p_2\,;\, p_1^2 = p_2^2 = (p_1-p_2)^2 = q^2 = \mu^2. \quad \text{(RI/SMOM)} \tag{4.9}$$

The choice of such a symmetric subtraction point is convenient, as all renormalised quantities depend on a single scale μ^2, chiral symmetry breaking effects and other unwanted infrared effects vanish faster as $1/p^6$, and are therefore better behaved. As an added bonus, the RI/SMOM to $\overline{\text{MS}}$ conversion factor for Z_m [201, 202] is much closer to unity (upto $O(\alpha^2)$) than its RI/MOM counterpart [203,204], meaning that $Z_m^{\overline{\text{MS}}(\leftarrow\text{RI/SMOM})}$ can be computed with smaller systematic uncertainty [199].

There are two variations of the scheme depending on the choice of projectors denoted by (γ_μ) and $(\not{q})$; listed below explicitly are all the renormalisation conditions [199]:

$$Z_m : \gamma_\mu, \not{q} \quad \lim_{m_R\to 0} \frac{1}{m_R}\left\{ \mathrm{Tr}\left[S_R(p)^{-1}\right]_{p^2=\mu^2} + \frac{1}{2}\,\mathrm{Tr}\left[\left(iq\cdot\Lambda_{\mathrm{A},R}\right)\gamma_5\right]_{\mathrm{sym}}\right\} = 12, \tag{4.10}$$

$$Z_P : \gamma_\mu, \not{q} \quad \lim_{m_R\to 0} \mathrm{Tr}\left[\Lambda_{\mathrm{P},R}\gamma_5\right]_{\mathrm{sym}} = 12i, \tag{4.11}$$

$$Z_S : \gamma_\mu, \not{q} \quad \lim_{m_R\to 0} \mathrm{Tr}\left[\Lambda_{\mathrm{S},R}\right]_{\mathrm{sym}} = 12, \tag{4.12}$$

$$Z_T : \gamma_\mu, \not{q} \quad \lim_{m_R\to 0} \sum_{\mu>\nu} \mathrm{Tr}\left[\Lambda^{\mu\nu}_{\mathrm{T},R}\sigma_{\mu\nu}\right]_{\mathrm{sym}} = 12. \tag{4.13}$$

$$Z_V : \gamma_\mu \quad \lim_{m_R\to 0} \mathrm{Tr}\left[\Lambda^{\mu}_{\mathrm{V},R}\gamma_\mu\right]_{\mathrm{sym}} = 48, \tag{4.14}$$

$$\not{q} \quad \lim_{m_R\to 0} \frac{1}{q^2}\,\mathrm{Tr}\left[\left(q\cdot\Lambda_{\mathrm{V},R}\right)\not{q}\right]_{\mathrm{sym}} = 12, \tag{4.15}$$

$$Z_A : \gamma_\mu \quad \lim_{m_R\to 0} \mathrm{Tr}\left[\Lambda^{\mu}_{\mathrm{A},R}\gamma_\mu\gamma_5\right]_{\mathrm{sym}} = 48, \tag{4.16}$$

$$\not{q} \quad \lim_{m_R\to 0} \frac{1}{q^2}\,\mathrm{Tr}\left[\left(q\cdot\Lambda_{\mathrm{A},R}\right)\gamma_5\not{q}\right]_{\mathrm{sym}} = 12, \tag{4.17}$$

$$Z_q : \gamma_\mu \quad \lim_{m_R\to 0} \mathrm{Tr}\left[\frac{\partial S_R^{-1}(p)}{\partial p_\mu}\gamma_\mu\right]_{p^2=\mu^2} - \frac{i}{2}\,\mathrm{Tr}\left[q_\mu\gamma_\nu\frac{\partial}{\partial q_\nu}\Lambda^{\mu}_{V,R}(p_1,p_2)\right]_{\mathrm{sym}} = 48, \tag{4.18}$$

$$\not{q} \quad \lim_{m_R\to 0} \frac{1}{p^2}\,\mathrm{Tr}\left[-iS_R(p)^{-1}\not{p}\right]_{p^2=\mu^2} = 12. \tag{4.19}$$

Note that the projectors for the scalar, pseudoscalar and tensor operators, and the renormalisation condition for the fermion mass are identical in the (γ_μ) and $(\not{q})$ schemes.

By design, the Z-factors in this scheme have the same properties to those in the continuum $\overline{\mathrm{MS}}$ scheme

$$Z_A = Z_V = 1, \quad Z_S = Z_P = 1/Z_m, \tag{4.20}$$

and the renormalised quantities satisfy the vector and axial-vector Ward-Takahashi identities

$$q_\mu\Lambda^{\mu}_{V,R}(p_2,p_2) = iS_R^{-1}(p_2) - iS_R^{-1}(p_1), \tag{4.21}$$

$$q_\mu\Lambda^{\mu}_{A,R}(p_2,p_2) = -2m_R\Lambda_{P,R}(p_2,p_2) + i\gamma_5 S_R^{-1}(p_1) + S_R^{-1}(p_2)i\gamma_5. \tag{4.22}$$

Renormalisation of $\Delta F = 2$ four-quark operators

Consider a color-unmixed four-quark operator

$$\mathcal{O} = \left(\overline{\psi}^{\alpha}_{f,a}\Gamma^{A}_{\alpha\beta}\psi^{\beta}_{f',b}\right)\left(\overline{\psi}^{\gamma}_{f,c}\Gamma^{B}_{\gamma\delta}\psi^{\delta}_{f',d}\right)\delta^{ab}\delta^{cd}, \tag{4.23}$$

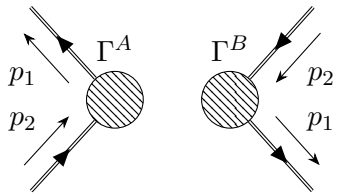

Figure 4.2: Choice of kinematics for a four-quark operator with $\Gamma^A \otimes \Gamma^B$ Dirac structure. The dashed bubbles represent the operator insertions and higher order corrections, p_1 and p_2 are the momenta of the external off-shell quark lines.

where Greek and Latin letters denote spin and colour indices respectively, and Γ^A and Γ^B are generic Dirac structures. Operators of this kind can be related to ones that make up an effective weak $\Delta F = 2$ Hamiltonian which encodes the short-distance contribution to meson-mixing interactions as described in section 2.5.3. We are interested in the five parity-even operators (spin indices are suppressed),

$$\begin{aligned}
Q_1^+ &= \overline{\psi}_{f,a}\gamma_\mu\psi_{f',a}\,\overline{\psi}_{f,b}\gamma_\mu\psi_{f',b} + \overline{\psi}_{f,a}\gamma_\mu\gamma_5\psi_{f',a}\,\overline{\psi}_{f,b}\gamma_\mu\gamma_5\psi_{f',b}\,, && \text{(VV + AA)}\\
Q_2^+ &= \overline{\psi}_{f,a}\gamma_\mu\psi_{f',a}\,\overline{\psi}_{f,b}\gamma_\mu\psi_{f',b} - \overline{\psi}_{f,a}\gamma_\mu\gamma_5\psi_{f',a}\,\overline{\psi}_{f,b}\gamma_\mu\gamma_5\psi_{f',b}\,, && \text{(VV − AA)}\\
Q_3^+ &= \overline{\psi}_{f,a}\psi_{f',a}\,\overline{\psi}_{f,b}\psi_{f',b} - \overline{\psi}_{f,a}\gamma_5\psi_{f',a}\,\overline{\psi}_{f,b}\gamma_5\psi_{f',b}\,, && \text{(SS − PP)}\\
Q_4^+ &= \overline{\psi}_{f,a}\psi_{f',a}\,\overline{\psi}_{f,b}\psi_{f',b} + \overline{\psi}_{f,a}\gamma_5\psi_{f',a}\,\overline{\psi}_{f,b}\gamma_5\psi_{f',b}\,, && \text{(SS + PP)}\\
Q_5^+ &= \sum_{\nu>\mu} \overline{\psi}_{f,a}\gamma_\mu\gamma_\nu\psi_{f',a}\,\overline{\psi}_{f,b}\gamma_\mu\gamma_\nu\psi_{f',b}\,, && \text{(TT)}
\end{aligned} \tag{4.24}$$

where the labels on the right correspond to their Dirac structures. Q_1^+ is the parity-even part of the Standard Model $\Delta F = 2$ four-quark mixing operator, and the rest are related to Beyond the Standard Model (BSM) operators. Under $SU(3)_L \times SU(3)_R$ quark flavour symmetry, Q_1^+ transforms as $(27,1)$, $Q_{2,3}^+$ as $(8,8)$, and $Q_{4,5}^+$ as $(6,\overline{6})$. This implies that operators 2 and 3, and 4 and 5 mix under renormalisation:

$$Q_{i,R}^+(a,\mu) = Z_{ij}(a,\mu)Q_j^+(a)\,, \tag{4.25}$$

$$\begin{bmatrix} Q_{1,R}^+ \\ Q_{2,R}^+ \\ Q_{3,R}^+ \\ Q_{4,R}^+ \\ Q_{5,R}^+ \end{bmatrix} = \begin{bmatrix} Z_{11} & 0 & 0 & 0 & 0 \\ 0 & Z_{22} & Z_{23} & 0 & 0 \\ 0 & Z_{32} & Z_{33} & 0 & 0 \\ 0 & 0 & 0 & Z_{44} & Z_{45} \\ 0 & 0 & 0 & Z_{54} & Z_{55} \end{bmatrix} \begin{bmatrix} Q_1^+ \\ Q_2^+ \\ Q_3^+ \\ Q_4^+ \\ Q_5^+ \end{bmatrix}. \tag{4.26}$$

These Z-factors are defined via renormalisation conditions similar to those in the case of bilinear operators

$$\lim_{m_R\to 0} \hat{P}_k \left[\Lambda_{i,R}(a,p_1,p_2)\right]_{\text{sym}} = F_{ik} \equiv \hat{P}_k \left[\Lambda_i^{(0)}(p_1,p_2)\right]_{\text{sym}}, \tag{4.27}$$

$$\implies \lim_{m_R\to 0} \hat{P}_k \left[\frac{Z_{ij}}{Z_q^2}(a,\mu)\Lambda_i(a,p_1,p_2)\right]_{\text{sym}} = F_{ik}, \tag{4.28}$$

where the vertex function is derived by amputating the four quark legs of the corresponding Green's function,

$$G^{\delta\gamma;\beta\alpha} = \langle \psi_f^{\delta}(p_2)\overline{\psi}_{f'}^{\gamma}(p_1)\mathcal{O}\psi_f^{\beta}(p_2)\overline{\psi}_{f'}^{\alpha}(p_1)\rangle, \tag{4.29}$$

$$\Lambda^{\delta\gamma;\beta\alpha} = \left[S_f^{-1}(p_2)\right]^{\delta\overline{\delta}} \left[S_f^{-1}(p_2)\right]^{\beta\overline{\beta}} G^{\overline{\delta}\overline{\gamma};\overline{\beta}\overline{\alpha}} \left[S_{f'}^{-1}(p_1)\right]^{\overline{\gamma}\gamma} \left[S_{f'}^{-1}(p_1)\right]^{\overline{\alpha}\alpha}. \tag{4.30}$$

Once again, there are variations of the scheme corresponding to two sets of projectors denoted by (γ_μ) and $(\not{q})$ and these are listed below explicitly [72].

For the $(27,1)$ operator,

$$\left[\hat{P}_1^{(\gamma_\mu)}\right]^{ba;dc}_{\beta\alpha;\delta\gamma} = \left[(\gamma_\mu)_{\beta\alpha}(\gamma_\mu)_{\delta\gamma} + (\gamma_\mu\gamma_5)_{\beta\alpha}(\gamma_\mu\gamma_5)_{\delta\gamma}\right]\delta^{ba}\delta^{dc}, \tag{4.31}$$

$$\left[\hat{P}_1^{(\not{q})}\right]^{ba;dc}_{\beta\alpha;\delta\gamma} = \frac{1}{q^2}\left[(\not{q})_{\beta\alpha}(\not{q})_{\delta\gamma} + (\not{q}\gamma_5)_{\beta\alpha}(\not{q}\gamma_5)_{\delta\gamma}\right]\delta^{ba}\delta^{dc}. \tag{4.32}$$

For the $(8,8)$ doublet,

$$\left[\hat{P}_2^{(\gamma_\mu)}\right]^{ba;dc}_{\beta\alpha;\delta\gamma} = \left[(\gamma_\mu)_{\beta\alpha}(\gamma_\mu)_{\delta\gamma} - (\gamma_\mu\gamma_5)_{\beta\alpha}(\gamma_\mu\gamma_5)_{\delta\gamma}\right]\delta^{ba}\delta^{dc}, \tag{4.33}$$

$$\left[\hat{P}_3^{(\gamma_\mu)}\right]^{ba;dc}_{\beta\alpha;\delta\gamma} = \left[\delta_{\beta\alpha}\delta_{\delta\gamma} - (\gamma_5)_{\beta\alpha}(\gamma_5)_{\delta\gamma}\right]\delta^{ba}\delta^{dc}, \tag{4.34}$$

$$\left[\hat{P}_2^{(\not{q})}\right]^{ba;dc}_{\beta\alpha;\delta\gamma} = \frac{1}{q^2}\left[(\not{q})_{\beta\alpha}(\not{q})_{\delta\gamma} - (\not{q}\gamma^5)_{\beta\delta}(\not{q}\gamma^5)_{\delta\gamma}\right]\delta^{ba}\delta^{dc}, \tag{4.35}$$

$$\left[\hat{P}_3^{(\not{q})}\right]^{ba;dc}_{\beta\alpha;\delta\gamma} = \frac{1}{q^2}\left[(\not{q})_{\beta\alpha}(\not{q})_{\delta\gamma} - (\not{q}\gamma^5)_{\beta\delta}(\not{q}\gamma^5)_{\delta\gamma}\right]\delta^{bc}\delta^{da}. \tag{4.36}$$

Finally, for the $(6,\overline{6})$ doublet,

$$\left[\hat{P}_4^{(\gamma_\mu)}\right]^{ba;dc}_{\beta\alpha;\delta\gamma} = \left[\delta_{\beta\alpha}\delta_{\delta\gamma} + (\gamma^5)_{\beta\alpha}(\gamma^5)_{\delta\gamma}\right]\delta^{ba}\delta^{dc}, \tag{4.37}$$

$$\left[\hat{P}_5^{(\gamma_\mu)}\right]^{ba;dc}_{\beta\alpha;\delta\gamma} = \left[\sum_{\nu>\mu}(\gamma^\mu\gamma^\nu)_{\beta\alpha}(\gamma^\mu\gamma^\nu)_{\delta\gamma}\right]\delta^{ba}\delta^{dc}, \tag{4.38}$$

$$\left[\hat{P}_4^{(\not{q})}\right]^{ba;dc}_{\beta\alpha;\delta\gamma} = \frac{1}{p_1^2p_2^2-(p_1.p_2)^2}\left[(p_1^\mu(\sigma^{\mu\nu}P_L)p_2^\nu)_{\beta\alpha}\,(p_1^\rho(\sigma^{\rho\sigma}P_L)p_2^\sigma)_{\delta\gamma}\right]\delta^{bc}\delta^{da}, \tag{4.39}$$

$$\left[\hat{P}_5^{(\not{q})}\right]^{ba;dc}_{\beta\alpha;\delta\gamma} = \frac{1}{p_1^2p_2^2-(p_1.p_2)^2}\left[(p_1^\mu(\sigma^{\mu\nu}P_L)p_2^\nu)_{\beta\alpha}\,(p_1^\rho(\sigma^{\rho\sigma}P_L)p_2^\sigma)_{\delta\gamma}\right]\delta^{ba}\delta^{dc}, \tag{4.40}$$

with $P_L = \frac{1}{2}(\mathbb{1}-\gamma_5)$. The matrices corresponding to the projecting the tree-level four-quark vertex functions are given by

$$P_j\left[\Lambda_i^{(0)}\right] = [P_j]^{ba;dc}_{\beta\alpha;\delta\gamma}\left[\Lambda_i^{(0)}\right]^{ab;cd}_{\alpha\beta;\gamma\delta} = F_{ij}. \tag{4.41}$$

For the choice of projectors $P^{(\gamma_\mu)}$ and $P^{(\not{q})}$, these are (for $N_{\text{colors}} = 3$) [72]

$$F^{(\gamma_\mu)} = \begin{pmatrix} 3072 & 0 & 0 & 0 & 0 \\ 0 & 2304 & -384 & 0 & 0 \\ 0 & -384 & 576 & 0 & 0 \\ 0 & 0 & 0 & 480 & 288 \\ 0 & 0 & 0 & 288 & 2016 \end{pmatrix}, \tag{4.42}$$

$$F^{(\not{q})} = \begin{pmatrix} 768 & 0 & 0 & 0 & 0 \\ 0 & 576 & 192 & 0 & 0 \\ 0 & -92 & -288 & 0 & 0 \\ 0 & 0 & 0 & 72 & 24 \\ 0 & 0 & 0 & 120 & 168 \end{pmatrix}. \tag{4.43}$$

It is common practice to remove the Z_q-dependence of the renormalisation constants by making use of a bilinear renormalisation constant such that

$$\lim_{m_R \to 0} \left(\frac{Z_{ij}}{Z_\Gamma^2}(a\mu) \right)^{(\mathcal{A},\mathcal{B})} \left. \frac{\hat{P}_k^{(\mathcal{A})} \left[\Lambda_i^{4q}(a, p_1, p_2) \right]}{\left(\hat{P}_\Gamma^{(\mathcal{B})} \left[\Lambda_\Gamma^{2q}(a, p_1, p_2) \right] \right)^2} \right|_{\text{sym}} = \frac{F_{ik}}{F_\Gamma^2}, \tag{4.44}$$

where we combine the renormalisation condition of the four-quark ($4q$) operator in scheme ($\mathcal{A}$) and the renormalisation condition of the bilinear ($2q$) operator in scheme ($\mathcal{B}$) (where $\mathcal{A}, \mathcal{B} \in \{\gamma_\mu, \not{q}\}$) to arrive at renormalisation constant (Z_{ij}/Z_Γ^2) in the $(\mathcal{A}, \mathcal{B})$ scheme.

4.2 Implementation in numerical simulation

On the lattice, we numerically compute Landau gauge-fixed Green's functions of the operators of interest between incoming and outgoing quarks in a given kinematic configuration. The momenta are chosen from the Fourier modes of the simulated lattice

$$ap_\mu = \frac{2\pi}{L} n_\mu, \quad n_\mu \in \{0, 1, \ldots, L\}, \tag{4.45}$$

where L is the extent of the lattice in the spatial directions. Twisted boundary conditions are used in the valence sectors, so the momenta are not restricted only to the Fourier modes. In practice we can interpolate between the integer Fourier modes by using

$$ap_\mu = \frac{2\pi}{L} n_\mu + \frac{\pi}{L} \theta_\mu, \quad \theta_\mu \in \left\{ 0, \frac{1}{N}, \ldots, \frac{N-1}{N} \right\}, \tag{4.46}$$

where θ is the twist angle of the boundary condition, and $1/N$ is some choice of interval.

Furthermore, for a precise lattice calculation, the momentum scale is restricted to lie within the Rome-Southampton *window*

$$\Lambda^2_{\rm QCD} \ll p^2 \ll \left(\frac{\pi}{a}\right)^2, \tag{4.47}$$

where the upper limit controls discretisation effects and the lower limit guards against potentially large non-perturbative effects in the infrared (which are prevalent in the RI/MOM scheme when using exceptional kinematics).

We associate a momentum with each quark flavour (see figures 4.1 and 4.2), so we need two momentum source propagators. The following convention is used (with respect to the vertex position x):

1. An incoming quark ψ_f with momenta p_1 is denoted by

$$S_{f,x}(p_1) = \sum_y S_f(x,y) e^{ip_1\cdot(y-x)}. \tag{4.48}$$

2. An outgoing quark $\psi_{f'}$ with momenta p_2 is denoted by

$$\overline{S}_{f',x}(p_2) = \gamma_5 S_{f',x}(p_2)\gamma_5^\dagger = \sum_y e^{-ip_2\cdot(y-x)} S_{f'}(y,x), \tag{4.49}$$

A bilinear Green's function in momentum space with external quark legs $\psi_f(p_2)$ (outgoing) and $\overline{\psi}_{f'}(p_1)$ (incoming) – see eqn (4.2) – is computed as

$$G^{\beta\alpha}_\Gamma(p_1,p_2) = \sum_{x,x_1,x_2} \langle 0|\psi^\beta_f(x_2)\left[\mathcal{O}_\Gamma(x)\right]\overline{\psi}^\alpha_{f'}(x_1)|0\rangle e^{-ip_1\cdot\tilde{x}_1 + ip_2\cdot\tilde{x}_2} \tag{4.50}$$

$$= \sum_x \langle \left[\overline{S}_{f,x}(p_2)\Gamma S_{f',x}(p_1)\right]^{\beta\alpha}\rangle. \tag{4.51}$$

where $\tilde{x}_i = x_i - x$. The vertex function is obtained by amputating each leg as

$$\Lambda^{\beta\alpha}_\Gamma(p_1,p_2) = \left[\overline{S}^{\beta\overline{\beta}}_f(p_2)\right]^{-1} G^{\overline{\beta}\overline{\alpha}}_\Gamma(p_1,p_2)\left[S^{\overline{\alpha}\alpha}_{f'}(p_1)\right]^{-1}, \tag{4.52}$$

where we amputate using the inverse of the *full momentum* propagator

$$S_f(p) = \sum_x S_{f,x}(p). \tag{4.53}$$

In a similar way, the momentum space Green's function for a four-quark vertex with two incoming quarks legs, $\psi_f(p_2)$, and two outgoing legs, $\overline{\psi}_{f'}(p_1)$, – see eqn (4.29) – is

computed as

$$G^{\delta\gamma;\beta\alpha}_{\Gamma^A\otimes\Gamma^B}(p_1,p_2) = \sum_{x,x_1,\ldots,x_4} \langle 0|\psi^\delta_f(x_4)\overline{\psi}^\gamma_{f'}(x_3)\left[\mathcal{O}_{\Gamma^A\otimes\Gamma^B}(x)\right]\psi^\beta_f(x_2)\overline{\psi}^\alpha_{f'}(x_1)|0\rangle \times e^{-ip_1\cdot\tilde{x}_1+ip_2\cdot\tilde{x}_2-ip_1\cdot\tilde{x}_3+ip_2\cdot\tilde{x}_4} \tag{4.54}$$

$$= 2\sum_x \Big(\langle \left[\overline{S}_{f,x}(p_2)\Gamma^A S_{f',x}(p_1)\right]^{\delta\gamma} \left[\overline{S}_{f,x}(p_2)\Gamma^B S_{f',x}(p_1)\right]^{\beta\alpha}\rangle - \langle \left[\overline{S}_{f,x}(p_2)\Gamma^A S_{f',x}(p_1)\right]^{\delta\alpha} \left[\overline{S}_{f,x}(p_2)\Gamma^B S_{f',x}(p_1)\right]^{\beta\gamma}\rangle \Big). \tag{4.55}$$

The vertex function is once again computed by amputating each quark leg using the inverse of the appropriate full momentum propagator

$$\Lambda^{\delta\gamma;\beta\alpha}(p_1,p_2) = \left[\overline{S}_f^{-1}(p_2)\right]^{\delta\overline{\delta}} \left[\overline{S}_f^{-1}(p_2)\right]^{\beta\overline{\beta}} G^{\overline{\delta}\overline{\gamma};\overline{\beta}\overline{\alpha}}(p_1,p_2) \left[S_{f'}^{-1}(p_1)\right]^{\overline{\gamma}\gamma} \left[S_{f'}^{-1}(p_1)\right]^{\overline{\alpha}\alpha}. \tag{4.56}$$

4.3 Matching in continuum perturbation theory

Quantities in the RI/SMOM scheme are typically converted to a continuum scheme such as $\overline{\text{MS}}$ so that they can be used for producing phenomenological predictions. We are interested in the conversion factor

$$\langle\mathcal{O}\rangle^{\overline{\text{MS}}}(\mu) = R^{\overline{\text{MS}}\leftarrow\text{RI/SMOM}}(\mu)\langle\mathcal{O}\rangle^{\text{RI/SMOM}}(\mu) \tag{4.57}$$

$$R^{\overline{\text{MS}}\leftarrow\text{RI/SMOM}}(\mu) = \frac{Z^{\overline{\text{MS}}}(\mu)}{Z^{\text{RI/SMOM}}(\mu)}, \tag{4.58}$$

which we compute using perturbation theory up to some fixed loop order. The conversion factor can be parameterised as (where α_s is the strong coupling)

$$R^{\overline{\text{MS}}\leftarrow\text{RI/SMOM}}(\mu) = 1 - \frac{\alpha_s(\mu)}{4\pi}\Delta r^{\overline{\text{MS}}\leftarrow\text{RI/SMOM}} + O(\alpha_s^2), \tag{4.59}$$

and the coefficients $\Delta r^{\overline{\text{MS}}\leftarrow\text{RI/SMOM}}$ are presented the following sections.

Matching coefficients for bilinear operators

The matching coefficients for the bilinear operators have been calculated perturbatively using dimensional regularisation to one-loop level for the RI/SMOM scheme in [199], and are presented here in the Landau gauge

$$\Delta r_q^{\overline{\text{MS}}\leftarrow(\gamma_\mu)} = -\frac{4}{3}, \qquad \Delta r_q^{\overline{\text{MS}}\leftarrow(\not{q})} = 0, \tag{4.60}$$

$$\Delta r_m^{\overline{\text{MS}}\leftarrow(\gamma_\mu)} = \frac{20}{3} - 2C_0, \qquad \Delta r_m^{\overline{\text{MS}}\leftarrow(\not{q})} = \frac{16}{3} - 2C_0, \tag{4.61}$$

where (γ_μ) and $(\not{q})$ are the two distinct RI/SMOM schemes, and

$$C_0 = \frac{2\psi^{(1)}(\frac{1}{3})}{3} - \left(\frac{2\pi}{3}\right)^2, \tag{4.62}$$

wherein ψ is the polygamma function. For the scalar and pseudoscalar currents, $Z_S = Z_P = 1/Z_m$ in both $\overline{\text{MS}}$ and RI/SMOM, which gives us $\Delta r_{S,P}^{\overline{\text{MS}}\leftarrow(\gamma_\mu),(\not{q})} = -\Delta r_m^{\overline{\text{MS}}\leftarrow(\gamma_\mu),(\not{q})}$. For the tensor operator, we have

$$\Delta r_T^{\overline{\text{MS}}\leftarrow(\gamma_\mu)} = \frac{4}{9} - \frac{2}{3}C_0, \quad \Delta r_T^{\overline{\text{MS}}\leftarrow(\not{q})} = \frac{16}{9} - \frac{2}{3}C_0. \tag{4.63}$$

As $Z_A = Z_V = 1$ in both $\overline{\text{MS}}$ and RI/SMOM, the conversion factor $R_{V,A}^{\overline{\text{MS}}\leftarrow(\gamma_\mu),(\not{q})}(\mu) = 1$.

Matching coefficients for $\Delta F = 2$ four-quark operators

The matching coefficients for the $\Delta F = 2$ four-quark operators have been calculated at the one-loop level in literature and we present them here in the Landau gauge for the $(\mathcal{A},\mathcal{A})$-type schemes using $N_{\text{colors}} = 3$. The coefficients of the one-loop conversion factor for the (27,1) operator is given by [84]

$$\Delta r_{11}^{\overline{\text{MS}}\leftarrow(\gamma_\mu,\gamma_\mu)} = \frac{16}{3} - 8\log(2), \quad \Delta r_{11}^{\overline{\text{MS}}\leftarrow(\not{q},\not{q})} = 6 - 8\log(2). \tag{4.64}$$

For the $(8,8)$ doublet, we have [205]

$$\begin{aligned}
\Delta r_{22}^{\overline{\text{MS}}\leftarrow(\gamma_\mu,\gamma_\mu)} &= \Delta r_{22}^{\overline{\text{MS}}\leftarrow(\not{q},\not{q})} = -\frac{C_0}{2} + \frac{2}{3} + \frac{2\log(2)}{3}, \\
\Delta r_{23}^{\overline{\text{MS}}\leftarrow(\gamma_\mu,\gamma_\mu)} &= \Delta r_{23}^{\overline{\text{MS}}\leftarrow(\not{q},\not{q})} = -3C_0 + 4 + 4\log(2), \\
\Delta r_{32}^{\overline{\text{MS}}\leftarrow(\gamma_\mu,\gamma_\mu)} &= \log(2) - \frac{3}{2}, \quad \Delta r_{32}^{\overline{\text{MS}}\leftarrow(\not{q},\not{q})} = \log(2) - 1, \\
\Delta r_{33}^{\overline{\text{MS}}\leftarrow(\gamma_\mu,\gamma_\mu)} &= 4C_0 - \frac{43}{3} + \frac{2\log(2)}{3}, \quad \Delta r_{33}^{\overline{\text{MS}}\leftarrow(\not{q},\not{q})} = 4C_0 - \frac{34}{3} + \frac{2\log(2)}{3}.
\end{aligned} \tag{4.65}$$

Finally, for the $(6,\overline{6})$ doublet we have [72]

$$\begin{aligned}
\Delta r_{44}^{\overline{\text{MS}}\leftarrow(\gamma_\mu,\gamma_\mu)} &= \frac{13C_0}{4} - \frac{40}{3} + \frac{2\log(2)}{3}, \quad \Delta r_{44}^{\overline{\text{MS}}\leftarrow(\not{q},\not{q})} = \frac{47C_0}{12} - 5 - \frac{10\log(2)}{3}, \\
\Delta r_{45}^{\overline{\text{MS}}\leftarrow(\gamma_\mu,\gamma_\mu)} &= -\frac{C_0}{12} + \frac{7}{12} - \frac{7\log(2)}{3}, \quad \Delta r_{45}^{\overline{\text{MS}}\leftarrow(\not{q},\not{q})} = -\frac{11C_0}{36} + \frac{11}{9} - \frac{14\log(2)}{9}, \\
\Delta r_{54}^{\overline{\text{MS}}\leftarrow(\gamma_\mu,\gamma_\mu)} &= \frac{11C_0}{4} - \frac{1}{3} - \frac{14\log(2)}{3}, \quad \Delta r_{54}^{\overline{\text{MS}}\leftarrow(\not{q},\not{q})} = \frac{73C_0}{12} - 7 - \frac{14\log(2)}{3}, \\
\Delta r_{55}^{\overline{\text{MS}}\leftarrow(\gamma_\mu,\gamma_\mu)} &= -\frac{23C_0}{12} + \frac{29}{9} - \frac{58\log(2)}{9}, \Delta r_{55}^{\overline{\text{MS}}\leftarrow(\not{q},\not{q})} = -\frac{109C_0}{36} - \frac{73}{9} - \frac{58\log(2)}{9}.
\end{aligned} \tag{4.66}$$

The one-loop coefficients for converting from $(\mathcal{A},\mathcal{B})$-type schemes are presented in [72].

4.4 Step scaling

The scale evolution function to a scale μ_1 from another scale μ_2

$$\sigma(\mu_1, \mu_2) = Z(\mu_1)Z^{-1}(\mu_2) \tag{4.67}$$

can be computed perturbatively as well as non-perturbatively. This comparison helps us estimate the systematic errors affecting the renormalisation procedure and gauge the quality of the perturbative series for the various schemes – we present this comparison in section 5.3.2. We present here the details of perturbative scale evolution.

The renormalisation constant Z (a real number in the case of bilinears, a matrix in case of four-quark operators) scales as

$$\mu\frac{dZ}{d\mu} = -\gamma(\mu)Z(\mu), \tag{4.68}$$

where $\gamma(\mu)$ is the anomalous scaling dimension of Z. We can relate the renormalisation constants from two different scales using

$$\begin{aligned}\int_{Z_1}^{Z_2} dZ &= -\int_{\mu_1}^{\mu_2} d\mu \frac{\gamma(\mu)Z(\mu)}{\mu} \\ \implies Z(\mu_2) &= Z(\mu_1) - \int_{\mu_1}^{\mu_2} d\mu \frac{\gamma(\mu)Z(\mu)}{\mu}.\end{aligned} \tag{4.69}$$

We can recursively substitute for $Z(\mu)$ in the integral to get

$$\begin{aligned}Z(\mu_2) &= Z(\mu_1) - \int_{\mu_1}^{\mu_2} d\mu \frac{\gamma(\mu)}{\mu}\left[Z(\mu_1) - \int_{\mu_1}^{\mu} d\mu' \frac{\gamma(\mu')Z(\mu')}{\mu'}\right] \\ &= T_\mu \exp\left[-\int_{\mu_1}^{\mu_2} d\mu \frac{\gamma(\mu)}{\mu}\right] Z(\mu_1),\end{aligned} \tag{4.70}$$

where T_μ is denotes μ-ordering.

We can use the running of the strong coupling $\alpha_s(\mu) = g_s(\mu)^2/4\pi$, ie, the β-function, to swap out the integral in μ for an integral in g_s,

$$\beta(g_s) = \mu\frac{dg_s}{d\mu} \implies \frac{d\mu}{\mu} = \frac{dg_s}{\beta(g)}, \tag{4.71}$$

which we use in eqn (4.70) to get

$$\begin{aligned}Z(\mu_2) &= T_g \exp\left[-\int_{g_1}^{g_2} dg_s \frac{\gamma(g_s)}{\beta(g_s)}\right] Z(\mu_1) \\ \implies \sigma_{pt}(\mu_1, \mu_2) = Z(\mu_1)Z^{-1}(\mu_2) &= T_g \exp\left[-\int_{g_2}^{g_1} dg_s \frac{\gamma(g_s)}{\beta(g_s)}\right].\end{aligned} \tag{4.72}$$

The β-function and the anomalous dimension can be expanded in powers of the strong coupling

$$\beta(\mu) = -g_s(\mu)\sum_{i=0}^{\infty}\left(\frac{g_s^2(\mu)}{16\pi^2}\right)^{i+1}\beta^{(i)} = -\frac{g_s^3(\mu)}{16\pi^2}\beta^{(0)} - \frac{g_s^5(\mu)}{(16\pi^2)^2}\beta^{(1)} + \mathcal{O}(g_s^7), \tag{4.73}$$

$$\gamma(\mu) = \sum_{i=0}^{\infty}\left(\frac{g_s^2(\mu)}{16\pi^2}\right)^{i+1}\gamma^{(i)} = \frac{g_s^2(\mu)}{16\pi^2}\gamma^{(0)} + \left(\frac{g_s^2(\mu)}{16\pi^2}\right)^2\gamma^{(1)} + \mathcal{O}(g_s^6). \tag{4.74}$$

The coefficients of the anomalous magnetic moment are operator-dependent while the coefficients of the β-function are universal and known upto many orders. The values upto first order are (for N_f quark flavours)

$$\beta^{(0)} = 11 - \frac{2}{3}N_f, \quad \beta^{(1)} = 102 - \frac{38}{3}N_f. \tag{4.75}$$

At leading order (LO) in α_s, the perturbative scaling is given by

$$\begin{aligned}\sigma_{pt}^{(0)}(\mu_1,\mu_2) &= T_g \exp\left[-\int_{g_2}^{g_1}\frac{dg_s}{g_s}\frac{\gamma^{(0)}}{-\beta^{(0)}}\right] = \exp\left[\frac{\gamma^{(0)}}{\beta^{(0)}}\log\left(\frac{g_s(\mu_1)}{g_s(\mu_2)}\right)\right] \\ &= \left(\frac{g_s(\mu_1)}{g_s(\mu_2)}\right)^{\gamma^{(0)}/\beta^{(0)}} = \left(\frac{\alpha_s(\mu_1)}{\alpha_s(\mu_2)}\right)^{\gamma^{(0)}/2\beta^{(0)}}.\end{aligned} \tag{4.76}$$

At next-to-leading order (NLO), we have

$$\sigma_{pt}^{(1)}(\mu_1,\mu_2) = T_g \exp\left[\int_{g_2}^{g_1}\frac{dg_s}{g_s}\frac{\left(\gamma^{(0)} + \gamma^{(1)}(\frac{g_s^2}{16\pi^2})\right)}{\left(\beta^{(0)} + \beta^{(1)}(\frac{g_s^2}{16\pi^2})\right)}\right], \tag{4.77}$$

where $\gamma^{(0)}$ is scheme-independent and $\gamma^{(1)}$ is typically scheme-dependent. If $\gamma^{(1)}$ is known in a scheme A, we can convert it to another scheme B via

$$\gamma^{(1),B} = \gamma^{(1),A} + \left[\Delta r^{B\leftarrow A}, \gamma^{(0)}\right] + 2\beta^{(0)}\Delta r^{B\leftarrow A}, \tag{4.78}$$

where $\Delta r^{B\leftarrow A}$ is the coefficient of the scheme conversion factor at leading order (as defined in eqn (4.59)). This means, given $\gamma^{(0)}$, $\gamma^{(1),\overline{\text{MS}}}$, and $\Delta r^{\overline{\text{MS}}\leftarrow\text{RI/SMOM}}$ (provided in preceeding sections), we can compute $\gamma^{(1),\text{RI/SMOM}}$ and NLO perturbative scale evolution in RI/SMOM. We present the values of $\gamma^{(0)}$ and $\gamma^{(1),\overline{\text{MS}}}$ for bilinear and four-quark renormalisation factors in the following sections.

Note that for numerical computations, our inputs were [6]

$$\begin{aligned}\alpha_s(M_Z) &= 0.1180, \quad M_Z &&= 91.1876\,\text{GeV}, \\ \bar{m}_b(\bar{m}_b) &= 4.18\,\text{GeV}, \quad \bar{m}_c(\bar{m}_c) &&= 1.28\,\text{GeV},\end{aligned} \tag{4.79}$$

and we determine

$$\alpha_s(2\,\mathrm{GeV}) = 0.293347, \quad \alpha_s(3\,\mathrm{GeV}) = 0.243580. \tag{4.80}$$

Perturbative scaling of bilinear operators

In the case of bilinear operators, $\gamma^{(i)}$ are just c-numbers, and often known to many-loop orders [199, 206, 207]. The coefficients of the anomalous dimension of some bilinear quantities up to order $\mathcal{O}(\alpha_s^2)$ are presented below in $\overline{\mathrm{MS}}$

$$\begin{aligned} \gamma_q^{(0)} &= 0, \quad \gamma_q^{(1),\overline{\mathrm{MS}}} = \frac{1}{16}\left(\frac{67}{3} - \frac{4}{3}N_f\right), \\ \gamma_m^{(0)} &= 1, \quad \gamma_m^{(1),\overline{\mathrm{MS}}} = \frac{1}{16}\left(\frac{202}{9} - \frac{20}{9}N_f\right), \\ \gamma_T^{(0)} &= \frac{1}{3}, \quad \gamma_T^{(1),\overline{\mathrm{MS}}} = \frac{1}{16}\left(\frac{362}{9} - \frac{52}{27}N_f\right). \end{aligned} \tag{4.81}$$

Once again by exploiting the chiral symmetry relation $Z_S = Z_P = 1/Z_m$, we get

$$\gamma_S(\mu) = \gamma_P(\mu) = -\gamma_m(\mu). \tag{4.82}$$

Perturbative scaling of $\Delta F = 2$ four-quark operators

The leading order anomalous dimension matrix of the $\Delta F = 2$ four-quark operators is scheme-independent and is calculated in [208–210]. For $N_{\mathrm{colors}} = 3$, it's given by

$$\gamma^{(0)} = \begin{pmatrix} 4 & 0 & 0 & 0 & 0 \\ 0 & 2 & 12 & 0 & 0 \\ 0 & 0 & -16 & 0 & 0 \\ 0 & 0 & 0 & -10 & \frac{2}{3} \\ 0 & 0 & 0 & -10 & \frac{34}{3} \end{pmatrix}. \tag{4.83}$$

Following the procedure in [209], we can diagonalise $\gamma^{(0)}$ as

$$V^{-1}\gamma^{(0)}V = \gamma_D^{(0)}, \tag{4.84}$$

$$\sigma_{\mathrm{pt}}^{(0)}(\mu_1,\mu_2) = V\left(\frac{\alpha_s(\mu_1)}{\alpha_s(\mu_2)}\right)^{\gamma_D^{(0)}/2\beta^{(0)}} V^{-1}, \tag{4.85}$$

where $\gamma_D^{(0)}$ is the diagonal matrix of eigenvalues

$$\gamma_D^{(0)} = \mathrm{diag}\left(4, 2, -16, \frac{2}{3}\left(1+\sqrt{241}\right), \frac{2}{3}\left(1-\sqrt{241}\right)\right). \tag{4.86}$$

The scale evolution beyond the leading order can be written as

$$\sigma_{\rm pt}(\mu_1,\mu_2) \equiv K(\mu_1)\sigma^{(0)}_{\rm pt}(\mu_2,\mu_1)K^{-1}(\mu_2), \tag{4.87}$$

where the matrix $K(\mu)$ satisfies

$$\frac{\partial K}{\partial g_s} + \frac{1}{g_s}\left[K, \frac{\gamma^{(0)}}{\beta^{(0)}}\right] = \left(\frac{\gamma(g_s)}{\beta(g_s)} + \frac{1}{g_s}\frac{\gamma^{(0)}}{\beta^{(0)}}\right) K. \tag{4.88}$$

To compute the scale evolution at next-to-leading order (NLO) in α_s we use K at leading order, which can be parameterised as[1] [9]

$$K = 1 + J\frac{g_s^2}{16\pi^2} + L\frac{g_s^2}{16\pi^2}\ln(g_s). \tag{4.89}$$

Substituting this into eqn (4.88), we find that the matrices J and L must satisfy

$$\begin{aligned} L &= \frac{1}{2}\left[\frac{\gamma^{(0)}}{\beta^{(0)}}, L\right], \\ 2J + L + \left[J, \frac{\gamma^{(0)}}{\beta^{(0)}}\right] &= \frac{1}{\beta^{(0)}}\gamma^{(1)} - \frac{\beta^{(1)}}{\left(\beta^{(0)}\right)^2}\gamma^{(0)}. \end{aligned} \tag{4.90}$$

Using the LO diagonalising matrix V from eqn (4.85), we can rewrite this system of equations as

$$\begin{aligned} T_{ij} &= (a_i - a_j)\, T_{ij}, \\ S_{ij} + \frac{1}{2}T_{ij} - (a_i - a_j)S_{ij} &= \frac{1}{2\beta^{(0)}}G_{ij} - \frac{\beta^{(1)}}{\beta^{(0)}}a_i\delta_{ij}, \end{aligned} \tag{4.91}$$

where

$$a = \frac{1}{2\beta^{(0)}}\gamma_D^{(0)}, \quad G = V^{-1}\gamma^{(1)}V, \quad S = V^{-1}JV, \quad T = V^{-1}LV. \tag{4.92}$$

Eqn (4.91) determines the matrix elements of T_{ij} when $(a_i - a_j) = 1$, and those of S_{ij} when $(a_i - a_j) \neq 1$. With S and T, we can detemine J and L, and therefore compute the matrix K and the NLO expression for the perturbative scale evolution. The two-loop coefficients of the anomalous dimension matrix in $\overline{\rm MS}$ for $N_{\rm colors} = 3$ and N_f quark

[1] We thank Dr Nikolai Husung for proposing the inclusion of the logarithmic term in this parameterisation.

flavours is given by [209, 210]

$$\gamma^{(1),\overline{\text{MS}}} = \begin{pmatrix} \frac{4N_f}{9} - 7 & 0 & 0 & 0 & 0 \\ 0 & \frac{71}{3} - \frac{22N_f}{9} & 198 - \frac{44N_f}{3} & 0 & 0 \\ 0 & \frac{225}{4} - 2N_f & \frac{17}{18}(8N_f - 237) & 0 & 0 \\ 0 & 0 & 0 & \frac{1}{9}(74N_f - 1459) & -\frac{2N_f}{27} - \frac{35}{9} \\ 0 & 0 & 0 & \frac{1}{9}(146N_f - 1583) & \frac{1}{27}(6195 - 394N_f) \end{pmatrix} \overset{(N_f=3)}{=} \begin{pmatrix} -\frac{17}{3} & 0 & 0 & 0 & 0 \\ 0 & \frac{49}{3} & 154 & 0 & 0 \\ 0 & \frac{201}{4} & -\frac{1207}{6} & 0 & 0 \\ 0 & 0 & 0 & -\frac{1237}{9} & -\frac{37}{9} \\ 0 & 0 & 0 & -\frac{1145}{9} & \frac{557}{3} \end{pmatrix}. \tag{4.93}$$

4.5 Renormalisation group invariant quantities

An operator $Q(\mu)$, renormalised in some scheme S such that the anomalous dimension $\gamma(\mu)$ is known, can be related to its scheme-independent renormalisation group invariant (RGI) version $\hat{Q}$ via the exact relation [210]

$$\hat{Q} = [\alpha_s(\mu)]^{-\gamma^{(0)}/2\beta^{(0)}} \exp\left(- \int_{g_s(\mu)}^{0} dg_s \left[\frac{\gamma(g_s)}{\beta(g_s)} + \frac{\gamma^{(0)}}{\beta^{(0)} g_s} \right] \right) Q(\mu), \tag{4.94}$$

which, at NLO in perturbation theory, reduces to

$$\hat{Q} = [\alpha_s(\mu)]^{-\gamma^{(0)}/2\beta^{(0)}} \left(1 + \frac{\alpha_s}{4\pi} \left[\frac{\beta^{(1)}\gamma^{(0)} - \beta^{(0)}\gamma^{(1)}}{2(\beta^{(0)})^2} \right] \right) Q(\mu) \tag{4.95}$$

$$= [\alpha_s(\mu)]^{-\gamma^{(0)}/2\beta^{(0)}} K^{-1}(\mu) Q(\mu), \tag{4.96}$$

where $K(\mu)$ is defined via eqn (4.88).

Phenomenologically interesting RGI quantities of interest in the context of this thesis are those derived from the SM bag parameter as introduced in section 2.5.4 in eqn (2.94). The 11 element of the anomalous dimension and K matrix help convert the bag paramter $\mathcal{B}_1(\mu)$ to $\hat{B}$ via

$$\hat{B}_1 = \alpha_s(\mu)^{-\gamma_{11}^{(0)}/2\beta^{(0)}} K_{11}^{-1}(\mu) \mathcal{B}_1^{\text{MS}}(\mu). \tag{4.97}$$

To construct the $\hat{B}_i$ for the BSM four-quark mixing operators, one would additionally need to take into account the running of the quark masses in the definition in eqn (2.95).

Chapter 5

Kaon mixing from lattice QCD

Neutral kaon mixing, as introduced in section 2.5, has long been an important area of study in standard model (SM) and beyond the standard model (BSM) particle physics. The process is mediated by a flavour changing neutral current interaction (absent at tree level) whereby the neutral kaon K^0 oscillates with its antiparticle $\overline{K}^0$. The parameters of neutral kaon mixing relating to CP-violation have been the subject of many lattice calculations. In specific, the short-distance contributions to the indirect CP-violation parameter ε_K using both SM and BSM operators – parameterised by the kaon bag parameters – have been reviewed by the Flavour Lattice Averaging Group (FLAG) [7] with consistent results from multiple collaborations [2, 3, 5, 76, 76–86, 88, 90, 211].

The short-distance contribution to the neutral kaon mixing process depends on matrix elements of $\Delta\mathcal{S} = 2$ four-quark mixing operators, listed in eqn (2.88). While lattice QCD is as a natural candidate for computing these matrix elements, the calculation is made more challenging by the mixing pattern between these operators under renormalisation, as described in eqn (4.25). In this project, we take advantage of the good chiral properties of the domain wall fermion (DWF) formulation to constrain the mixing pattern on the lattice to be the same as that in the continuum theory[1] (see eqn (4.26)) upto $O(am_{\text{res}})$ corrections. In practice, these corrections are suppressed by controlling the extent of the fifth dimension of the domain wall.

In this chapter, we report the details of a high-precision lattice computation of bag and ratio parameters for SM and BSM neutral kaon mixing in the DWF framework, using the RI/SMOM non-perturbative scheme for the renormalisation of $\Delta\mathcal{S} = 2$ four-quark operators. At the end of this chapter we provide a comprehensive comparison, including the discussion of tensions, with previous lattice computations of these quantities, and demonstrate that this study improves upon previous results from the RBC-UKQCD collaboration. The current status of neutral kaon mixing in and beyond the SM is

[1] Chiral symmetry on the lattice becomes exact in the limit $L_s \to \infty$.

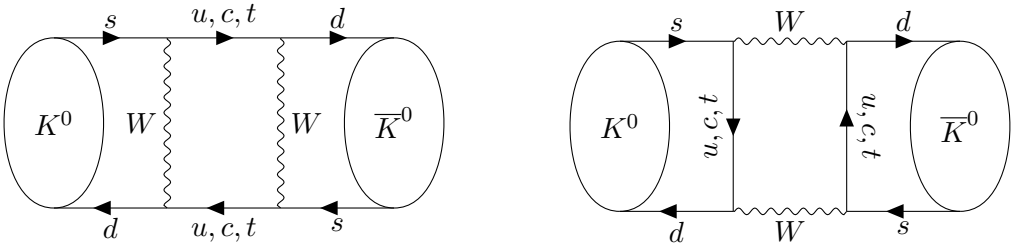

Figure 5.1: W exchange box diagrams mediating neutral kaon mixing in the SM.

summarised briefly in section 2.5.5, and for broader reviews of its status and prospects we refer the reader to references [212–214].

5.1 Background

The theoretical background for neutral kaon mixing has been introduced in detail in section 2.5, and the non-perturbative renormalisation of four-quark operators in section 4.1. In this section we briefly repeat the main ingredients needed for the calculations that follow in the remainder of this chapter, in order for the discussion to be self-contained.

The hadronic contributions to the short-distance part of neutral kaon mixing is given via the matrix elements of the parity-conserving part of $\Delta\mathcal{S} = 2$ four-quark operators given by (in the "SUSY" basis):

$$\begin{aligned}
O_1^+ &= \overline{s}_a\gamma_\mu d_a\ \overline{s}_b\gamma_\mu d_b + \overline{s}_a\gamma_\mu\gamma_5 d_a\ \overline{s}_b\gamma_\mu\gamma_5 d_b,\\
O_2^+ &= \overline{s}_a d_a\ \overline{s}_b d_b + \overline{s}_a\gamma_5 d_a\ \overline{s}_b\gamma_5 d_b,\\
O_3^+ &= \overline{s}_a d_b\ \overline{s}_b d_a + \overline{s}_a\gamma_5 d_b\ \overline{s}_b\gamma_5 d_a,\\
O_4^+ &= \overline{s}_a d_a\ \overline{s}_b d_b - \overline{s}_a\gamma_5 d_a\ \overline{s}_b\gamma_5 d_b,\\
O_5^+ &= \overline{s}_a d_b\ \overline{s}_b d_a - \overline{s}_a\gamma_5 d_b\ \overline{s}_b\gamma_5 d_a.
\end{aligned} \tag{5.1}$$

It is often more convenient to work in the "NPR" basis where they are all the operators are colour-unmixed, given by

$$\begin{aligned}
Q_1^+ &= \overline{s}_a\gamma_\mu d_a\ \overline{s}_b\gamma_\mu d_b + \overline{s}_a\gamma_\mu\gamma_5 d_a\ \overline{s}_b\gamma_\mu\gamma_5 d_b, && \text{(VV + AA)}\\
Q_2^+ &= \overline{s}_a\gamma_\mu d_a\ \overline{s}_b\gamma_\mu d_b - \overline{s}_a\gamma_\mu\gamma_5 d_a\ \overline{s}_b\gamma_\mu\gamma_5 d_b, && \text{(VV − AA)}\\
Q_3^+ &= \overline{s}_a d_a\ \overline{s}_b d_b - \overline{s}_a\gamma_5 d_a\ \overline{s}_b\gamma_5 d_b, && \text{(SS − PP)}\\
Q_4^+ &= \overline{s}_a d_a\ \overline{s}_b d_b + \overline{s}_a\gamma_5 d_a\ \overline{s}_b\gamma_5 d_b, && \text{(SS + PP)}\\
Q_5^+ &= \sum_{\nu>\mu} \overline{s}_a\gamma_\mu\gamma_\nu d_a\ \overline{s}_b\gamma_\mu\gamma_\nu d_b, && \text{(TT)},
\end{aligned} \tag{5.2}$$

where the labels on the right indicate the Dirac structures of each operator. We perform the lattice calculations and renormalisation in the NPR basis and transform to the SUSY basis prior to performing the necessary chiral and continuum limit extrapolations; note

that all results in this chapter (unless otherwise stated) are therefore quoted in the SUSY basis. The conversion between the two bases is given by the linear transformation

$$\begin{pmatrix} O_1^+ \\ O_2^+ \\ O_3^+ \\ O_4^+ \\ O_5^+ \end{pmatrix} = \begin{pmatrix} 1 & 0 & 0 & 0 & 0 \\ 0 & 0 & 0 & 1 & 0 \\ 0 & 0 & 0 & -\frac{1}{2} & \frac{1}{2} \\ 0 & 0 & 1 & 0 & 0 \\ 0 & -\frac{1}{2} & 0 & 0 & 0 \end{pmatrix} \begin{pmatrix} Q_1^+ \\ Q_2^+ \\ Q_3^+ \\ Q_4^+ \\ Q_5^+ \end{pmatrix} = \begin{pmatrix} Q_1^+ \\ Q_4^+ \\ \frac{1}{2}\left(Q_5^+ - Q_4^+\right) \\ Q_3^+ \\ -\frac{1}{2}Q_2^+ \end{pmatrix}. \tag{5.3}$$

We observe that under $SU(3)_L \times SU(3)_R$ quark flavour symmetry, Q_1^+ transforms as $(27,1)$, $Q_{2,3}^+$ as $(8,8)$ and $Q_{4,5}^+$ as $(6,\overline{6})$, and therefore the matrix elements of these operators mix under renormalisation as

$$Q_{i,R}^+(a,\mu) = Z_{ij}(a,\mu) Q_j^+(a)\,, \tag{5.4}$$

$$\begin{bmatrix} Q_{1,R}^+ \\ Q_{2,R}^+ \\ Q_{3,R}^+ \\ Q_{4,R}^+ \\ Q_{5,R}^+ \end{bmatrix} = \begin{bmatrix} Z_{11} & 0 & 0 & 0 & 0 \\ 0 & Z_{22} & Z_{23} & 0 & 0 \\ 0 & Z_{32} & Z_{33} & 0 & 0 \\ 0 & 0 & 0 & Z_{44} & Z_{45} \\ 0 & 0 & 0 & Z_{54} & Z_{55} \end{bmatrix} \begin{bmatrix} Q_1^+ \\ Q_2^+ \\ Q_3^+ \\ Q_4^+ \\ Q_5^+ \end{bmatrix}, \tag{5.5}$$

where the Z-factors and their corresponding projectors as well as tree-level values are listed in section 4.1.

The bag parameters are a conventional choice of parameterisation for the hadronic matrix elements of these operators, and are given by

$$\mathcal{B}_i(\mu) = \frac{\left\langle \overline{K}^0 | Q_i(\mu) | K^0 \right\rangle}{\left\langle \overline{K}^0 | Q_i(\mu) | K^0 \right\rangle_{\text{VSA}}} = \langle \overline{K}^0 \left| Q_i(\mu) \right| K^0 \rangle \cdot \begin{cases} \frac{1}{N_1 m_K^2 f_K^2} & i = 1, \\ \frac{(m_s(\mu)+m_d(\mu))^2}{N_i m_K^4 f_K^2} & i > 1 \end{cases}, \tag{5.6}$$

where the vacuum saturation approximation (VSA) replaces the four-quark matrix elements with products of two-quark matrix elements, and the basis-dependent normalisation factors N_i are given by

$$N_i^{\text{SUSY}} = \left[\frac{8}{3}, -\frac{5}{3}, \frac{1}{3}, 2, \frac{2}{3}\right], \tag{5.7}$$

$$N_i^{\text{NPR}} = \left[\frac{8}{3}, -\frac{4}{3}, 2, -\frac{5}{3}, -1\right]. \tag{5.8}$$

We also define the ratio parameters for the matrix elements of the BSM operators as

$$R_{i>1}(\mu) = \frac{\left\langle \overline{K}^0 | Q_i(\mu) | K^0 \right\rangle}{\left\langle \overline{K}^0 | Q_1(\mu) | K^0 \right\rangle}. \tag{5.9}$$

The chiral behaviour of the bag and ratio parameters, derived using chiral perturbation theory, is discussed in section 2.5.4.

5.2 Ingredients and simulation details

For the numerical simulation, we use RBC/UKQCD ensembles [8, 9, 57, 77, 84, 105, 139] with Iwasaki gauge action (section 3.1.1) and domain wall fermion action (section 3.1.4). These are $N_f = 2 + 1$ gauge ensembles with dynamical up, down and strange quarks. There are three lattice spacings in the range $a = 0.11 - 0.07\,\text{fm}$, labelled by 'coarse' (C), 'medium' (M) and 'fine' (F), each with either Shamir or Möbius domain wall kernels (see eqns (3.50) & (3.51)) denoted by the last letter 'S' or 'M'. The parameters of these kernels are chosen such that they lie on the same scaling trajectory and therefore a combined continuum limit is possible [77].

There are two ensembles simulated at the physical pion mass (denoted with middle number '0' in their names) at the coarse and medium lattice spacings, and the remaining ensembles have heavier pion masses ranging up to $m_\pi \approx 450\,\text{MeV}$, which are used for guiding the (small) chiral extrapolation on the fine ensemble. On each ensemble, the light valence quark mass was chosen to be identical to the light quark mass in the sea $am_l^{\text{val}} = am_l^{\text{sea}} \equiv am_l^{\text{uni}}$ (hence we use the superscript "uni" for unitary). The strange valence quark mass was simulated near its physical value which typically differs from the sea quark mass $am_s^{\text{val}} \sim am_s^{\text{phys}} \neq am_s^{\text{sea}}$. The main ensemble properties and the simulated masses are listed in table 5.1. We also use for the first time the ensembles C1M and M1M, which are Möbius equivalents of the C1S and M1S, used only for constraining the chiral extrapolation of the Z-factors at each lattice spacing for each choice of DWF kernel. Large parts of the data used in this project were generated using the Grid and Hadrons frameworks [215–217].

In order to compute the bare bag and ratio parameters on each ensemble we combine the necessary ingredients as detailed in the following sections.

5.2.1 Correlation functions

The quark propagators $S(y, x)$, where we denote $x = (\mathbf{x}, t_x)$, are obtained by inverting the domain wall Dirac operator on $\mathbb{Z}_2$-wall noise sources which are further Gaussian-smeared using a Jacobi procedure, as described in section 3.3.1. At the sink, we consider both the local (L) and smeared (S) case such that

$$S^{L,S}(x, y) = \sum_{\mathbf{z}} \omega_{\text{snk}}^{L,S}(\mathbf{x}, \mathbf{z}) S(z, y) \delta_{t_x, t_z}, \tag{5.10}$$

name	X/a	T/a	a^{-1}[GeV]	m_π[MeV]	$N_{\text{conf}} \times N_{\text{src}}$	am_l^{uni}	am_s^{sea}	am_s^{val}	am_s^{phys}
C0M	48	96	1.7295(38)	139	90×48	0.00078	0.0362	0.0358	0.03580(16)
C1S	24	64	1.7848(50)	340	100×32	0.005	0.04	0.03224	0.03224(18)
C2S	24	64	1.7848(50)	431	99×32	0.01	0.04	0.03224	0.03224(18)
M0M	64	128	2.3586(70)	139	82×64	0.000678	0.02661	0.0254	0.02539(17)
M1S	32	64	2.3833(86)	304	83×32	0.004	0.03	0.02477	0.02477(18)
M2S	32	64	2.3833(86)	361	76×32	0.006	0.03	0.02477	0.02477(18)
M3S	32	64	2.3833(86)	411	80×32	0.008	0.03	0.02477	0.02477(18)
F1M	48	96	2.708(10)	232	72×48	0.002144	0.02144	0.02144	0.02217(16)
C1M†	24	64	1.7295(38)	276	-	0.005	0.0362	-	0.03580(16)
M1M†	32	64	2.3586(70)	286	-	0.004	0.02661	-	0.02539(17)

Table 5.1: Summary of the main parameters of the ensembles used in this work. In the ensemble name the first letter (C, M or F) stand for coarse, medium and fine, respectively. The last letter (M or S) stands for Möbius and Shamir kernels, respectively. The column N_{conf} denotes the number of de-correlated gauge field configurations, N_{src} the number of equivalent measurements per configuration. Ensembles labelled with '†' only enter the analysis in order to constrain the chiral extrapolation of the renormalisation constants described in section 5.3.1.

where ω_{snk} is a (spatial) smearing function. Two-point functions are constructed as

$$\begin{aligned} C^{s_1,s_2}_{\Gamma_1,\Gamma_2}(t) &= \sum_{\mathbf{x}} \left\langle \left(O^{s_2}_{\Gamma_2}(\mathbf{x},t)\right) \left(O^{s_1}_{\Gamma_1}(\mathbf{0},0)\right)^\dagger \right\rangle \\ &= \sum_n \frac{\left(M^{s_2}_{\Gamma_2}\right)_n \left(M^{s_1}_{\Gamma_1}\right)^*_n}{2E_n} \left(e^{-E_n t} \pm e^{-E_n(T-t)}\right), \end{aligned} \tag{5.11}$$

where O^s_Γ is a bilinear with the flavour content of a kaon (with s denoting the choice of smearing and Γ denoting the Dirac structure), defined as

$$O^s_\Gamma(\mathbf{x},t) = \left(\overline{q}_2(\mathbf{x},t) \sum_{\mathbf{y}} \omega_s(\mathbf{x},\mathbf{y}) \Gamma q_1(\mathbf{y},t)\right). \tag{5.12}$$

The hadronic matrix elements are denoted by $(M^s_\Gamma)_n = \langle X_n | (O^s_\Gamma)^\dagger | 0 \rangle$ (with $(\overline{M}^s_\Gamma)_n = (M^s_\Gamma)^*_n = \langle 0 | O^s_\Gamma | X_n \rangle$) where the n^{th} excited meson states $|X_n\rangle$ has the corresponding energy E_n. For the bilinear operator, we only consider pseudoscalar ($\Gamma = \gamma_5 \equiv P$) and the temporal component of the axial current ($\Gamma = \gamma_0\gamma_5 \equiv A$) as kernels. The superscripts s_1, s_2 label the smearing combination; in our setup, we use local (L) and smeared (S) propagators at source and sink. At the source, all our quark fields are smeared, $s_1 = SS$. We also require the smearing at the sink to be the same for both the strange and the down quark, $s_2 \in \{SS, LL\}$. An exception to this is the ensemble F1M, where we keep both the source and sink local, $s_1 = s_2 = LL$.

For three-point correlation functions, in contrast to the two-point functions, we consider only pseudoscalar operators $O^{s,\dagger}_P$ (O^s_P) inducing the quantum numbers of a $\overline{K}$ (K) at the source (sink). These operators are smeared ($s = SS$) on all ensembles apart from the F1M, where they are local ($s = LL$). For notational convenience we drop the smearing indices for the operators for the remainder of the discussion where unnecessary. The three-point function for the four-quark operator Q^+_i is then given by

$$\begin{aligned} C^i_{\text{3pt}}(t,\Delta T) &\equiv \left\langle O_P(\Delta T) Q^+_i(t) O^\dagger_P(0) \right\rangle \\ &= \sum_{n,n'} \frac{(M^s_P)_n}{4E_n E_{n'}} \langle X_n | Q^+_i(t) | X_{n'} \rangle (M^s_P)^*_{n'} e^{-(\Delta T - t)E_n} e^{-tE_{n'}}, \end{aligned} \tag{5.13}$$

where we obtain the second equation by neglecting the around-the-world effects. $C^i_{\text{3pt}}(t,\Delta T)$ describes a three-point correlation function with a source at $t = 0$, sink at $t = \Delta T$ and a four-quark operator insertion Q^+_i at t, and the summation is over all energy states (labelled by n and n') of the initial and final state mesons.

By placing sources on every second time plane, we compute the above correlation functions for $T/2a$ time translations, where T/a is the integer number of time slices for a given ensemble. We time-translate and average equivalent measurements on a given configuration into a single effective measurement prior to further analysis; this helps reduce

the variance in the measurements of the correlation functions. The only exception is that we use all available measurements to estimate the correlation matrix.

Covariance and correlation matrices

In this project our fits are correlated frequentist minimisations of the χ^2-function as described in section 3.4.2. Since we jointly fit multiple two-point and three-point functions, it is important to be able to accurately invert the covariance matrix that appears in the χ^2-function. On a given ensemble, we have $N_{\text{meas}} = N_{\text{conf}} \times N_{\text{src}}$ estimators for the data y_i (compare table 5.1). When estimating the correlation matrix and the standard deviations, we therefore need to choose whether we treat measurements on different time translations on the same configuration as independent or whether we bin them into an effective measurement. From these two choices we obtain $(\sigma_i, \text{cor}(y_i, y_j))^{\text{unbinned}}$ and $(\sigma_i, \text{cor}(y_i, y_j))^{\text{binned}}$ based on $N_{\text{conf}} \times N_{\text{src}}$ measurements and N_{conf} effective measurements, respectively. Our reasoning is based on stochastic locality [218], that is, the fact that observables measured in sufficiently distant regions of a gauge field configuration can be treated as independent[2]. Since we only have access to measurements with sources shifted in the time direction, we do not pursue a master field analysis [219] but instead use binning studies to gain insight into the level of independence of different measurements on the same configuration.

When defining the covariance matrix that enters the χ^2 function, we consider two factors: the overall normalisation, stemming from the estimate of the variances, and the normalised *correlation* matrix that measures the degree of correlations between different time slices. The separation of these components is motivated by the following observation: if each measurement of a dataset with N_{conf} independent measurements is duplicated and (falsely) assumed to constitute a dataset with $2N_{\text{conf}}$ independent measurements then the mean values and the correlation matrix will remain unchanged while the variance of the mean will be underestimated by a factor 2. The variance is hence far more sensitive to the assumption of statistical independence; this leads us to assess the properties of the covariance of the mean and the correlation matrix separately.

The left-hand plot of figure 5.2 shows a binning study on the M0M ensemble. In the top panel the relative uncertainty of the pseudoscalar-pseudoscalar kaon two-point function is shown as a function of the inverse bin-size. The right-most data points correspond to considering every measurement as independent, whereas the left-most data point corresponds to the "fully binned" case, i.e. where all measurements on a given configuration are averaged into a single effective measurement. We find that the uncertainty only mildly depends on the bin size, however we take the conservative approach of taking the

[2]The separation that is required for this statement to hold strongly depends on the observable under consideration.

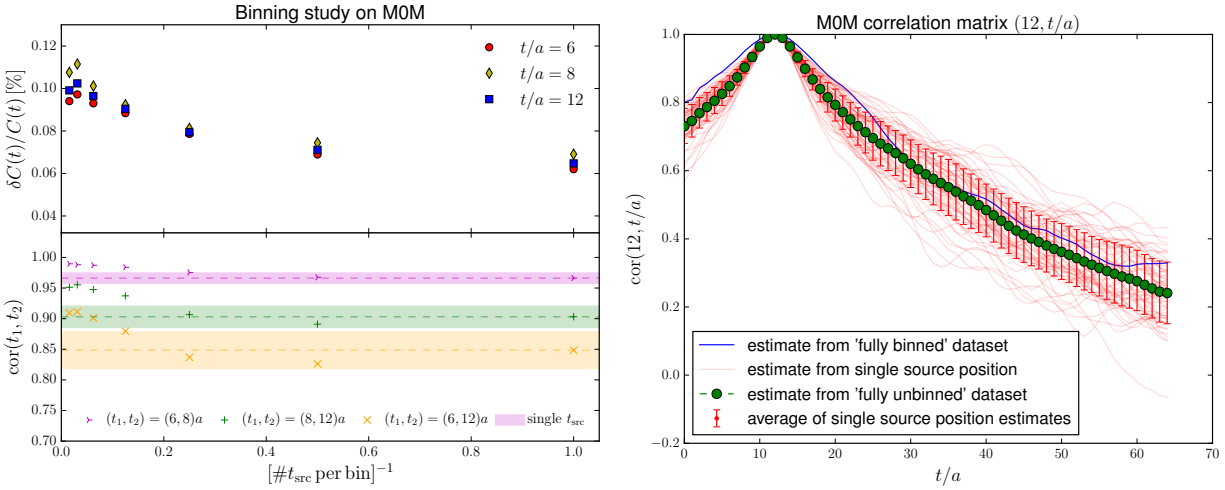

Figure 5.2: Investigation of binning choices for a typical kaon two-point function on the M0M ensemble. Further details are provided in the text.

variance from the maximally binned version of the dataset, in order to ensure that the uncertainties are not underestimated.

We now turn our attention to the correlation matrix. The right hand plot of figure 5.2 shows a slice of the correlation matrix where one time index is fixed to be $t/a = 12$. The blue solid line shows the estimate of the correlation matrix based on the "fully binned" case. The green dashed line with the circles on it, shows the "fully unbinned" estimate of the correlation matrix. The faint red lines correspond to estimates based on a single source plane, i.e. only include one measurement per configuration and are therefore based on a sub-statistic of $1/N_{\mathrm{src}}$ measurements. Comparing these N_{src} estimators of the correlation matrix provides an indication of the uncertainty in the correlation matrix elements (depicted by the red error-bars). We note that the "fully unbinned" estimate agrees very well with this average.

In the bottom panel of the left-hand plot we perform the binning study for three representative elements of the correlation matrix and superimpose the uncertainty obtained from the N_{src} estimates as horizontal bands. In each case, we find that for sufficiently small number of sources per bin the values stabilise. We therefore conclude to use "fully unbinned" estimates for the correlation matrix, whilst using the "fully binned" estimate of the variance. We now construct the covariance matrix we use in the fit to the correlation functions as

$$\mathrm{cov}(y_i, y_j) = \mathrm{diag}(\sigma_i^{\mathrm{binned}})\mathrm{cor}(y_i, y_j)^{\mathrm{unbinned}}\mathrm{diag}(\sigma_j^{\mathrm{binned}})\,. \tag{5.14}$$

This has the benefit that it resolves the correlations but estimates the statistical uncertainties without any assumption of independence for measurements from different source positions on the same configurations.

$N_i\mathcal{B}_i^{\text{bare}}$	$i=1$	$i=2$	$i=3$	$i=4$	$i=5$
C0M	1.5565(17)	-1.22385(96)	1.8631(15)	-0.96015(86)	-0.49446(43)
C1S	1.5692(28)	-1.2294(18)	1.8574(27)	-0.9907(17)	-0.51051(86)
C2S	1.5949(24)	-1.2366(16)	1.8586(23)	-1.0118(15)	-0.52241(74)
M0M	1.4890(21)	-1.2052(11)	1.8461(17)	-0.87841(86)	-0.44361(42)
M1S	1.5038(35)	-1.2066(26)	1.8374(41)	-0.9051(23)	-0.4577(11)
M2S	1.5101(24)	-1.2119(20)	1.8409(31)	-0.9133(17)	-0.46219(80)
M3S	1.5223(45)	-1.2129(30)	1.8380(47)	-0.9252(26)	-0.4684(13)
F1M	1.4776(34)	-1.1901(20)	1.8218(30)	-0.8691(14)	-0.43601(70)

Table 5.2: Bare bag parameters on all ensembles quoted in the NPR basis.

R_i^{bare}	$i=2$	$i=3$	$i=4$	$i=5$
C0M	-23.511(30)	35.788(48)	-18.439(28)	-9.494(15)
C1S	-20.587(55)	31.098(85)	-16.592(59)	-8.549(31)
C2S	-18.368(35)	27.604(56)	-15.001(43)	-7.747(23)
M0M	-28.144(39)	43.113(60)	-20.516(29)	-10.361(15)
M1S	-25.125(72)	38.25(11)	-18.848(72)	-9.531(36)
M2S	-23.505(51)	35.704(81)	-17.742(67)	-8.979(33)
M3S	-22.107(56)	33.501(88)	-16.866(65)	-8.538(33)
F1M	-28.621(80)	43.82(13)	-20.929(70)	-10.500(36)

Table 5.3: Bare ratio parameters on all ensembles quoted in the NPR basis.

5.2.2 Combined fits to two-point and three-point functions

For each of the four-quark operators Q_i^+, we extract the desired masses and matrix elements from a combined fit to several two-point and three-point functions. In particular, we jointly fit C_{PP}^{SL}, C_{PP}^{SS} and C_{PA}^{SL} (C_{PP}^{LL} and C_{PA}^{LL} on F1M) and $C_{3\text{pt}}^{i}(t;\Delta T)$ for multiple choices of ΔT, using a typical parameterisation of the ground state and the first excited state.

From these fits we extract the main quantities of interest: the bare bag parameters $\mathcal{B}_i^{\text{bare}}$; and the ratios of operators R_i^{bare}. They are determined and quoted in the NPR basis (see tables 5.2 and 5.3) but can subsequently be translated into the SUSY basis. For completeness we also quote the meson masses and bare decay constants at our simulation points for the pion and the kaon in table 5.4.

We pursue two independent fit strategies (described below as 'primary' and 'alternative') and systematically vary the fit ranges of the two-point and three-point functions (including the choice of which source-sink separations enter the fit) until we see stability in all fit parameters.

ens	am_π	af_π^{bare}	am_K	af_K^{bare}
C0M	0.08048(10)	0.10654(12)	0.28696(13)	0.126852(89)
C1S	0.19052(40)	0.11902(27)	0.30630(39)	0.13201(22)
C2S	0.24159(38)	0.12743(20)	0.32518(35)	0.13737(18)
M0M	0.059078(74)	0.074620(86)	0.21065(10)	0.089081(60)
M1S	0.12750(35)	0.08292(28)	0.22491(36)	0.09379(20)
M2S	0.15123(36)	0.08680(22)	0.23208(35)	0.09578(17)
M3S	0.17238(42)	0.09023(25)	0.23994(40)	0.09775(20)
F1M	0.08581(16)	0.06768(15)	0.18810(19)	0.07821(15)
C1M†	0.15987(50)	0.11659(60)	0.30560(51)	0.13261(52)
M1M†	0.12116(52)	0.07943(39)	0.22778(62)	0.09193(32)

Table 5.4: Masses and bare decay constants of the pion and kaons for all of the ensembles used in this work. The ensembles labelled with '†' only enter the analysis in order to constrain the chiral extrapolation of the renormalisation constants.

Primary strategy

We jointly fit several two-point and three-point functions directly to their functional forms given by eqn (5.11) and eqn (5.13). As a first step, we start by only fitting the two-point functions. We determine fit ranges $t_{\text{min}}^{\text{2pt}}$ and $t_{\text{max}}^{\text{2pt}}$ for the two-point functions which produce stable ground and first excited state results for masses and overlap factors. For each four-quark operator Q_i^+ we then perform a joint fit to the same two-point functions but also the corresponding three-point functions $C_3^i(t, \Delta T)$ for several values of ΔT. To begin with we keep $t_{\text{min}}^{\text{2pt}}$, $t_{\text{max}}^{\text{2pt}}$ from above for the two-point functions. For the three-point functions we use the same $t_{\text{min}}^{\text{3pt}}$ irrespective of ΔT. This is determined by choosing an integer δ to set $t_{\text{min}}^{\text{3pt}} = t_{\text{min}}^{\text{2pt}} + \delta$ and $t_{\text{max}}^{\text{3pt}} = \Delta T - t_{\text{min}}^{\text{3pt}}$. Typically we have $\delta \in \{0, 1\}$. We then vary δ by ± 1, vary the choice of which values of ΔT enter the fit and vary $t_{\text{min}}^{\text{2pt}}$ by ± 1. We adjust these choices until we see stability in all fit parameters.

Figure 5.3 demonstrates this stability for the example of Q_2^+ on the C0M ensemble for the first strategy. The superimposed dashed lines and magenta bands in the first two panels correspond to the chosen fit if only the two-point functions are fitted. The green bands illustrate our preferred choice of fit. Each set of three data points corresponds to variations in the fit range (by $-1, 0, +1$) for the three-point functions compared to the chosen fit. Finally, the different blocks correspond to following fit variations; the same fit but only to the middle (first, last) half of the source-sink separations; including an additional excited-to-excited matrix element in the fit ansatz; the same fit but for a varied choice of t_{min} for the two point functions which enter the fit. We find that the ground state fit results are insensitive to any of these choices.

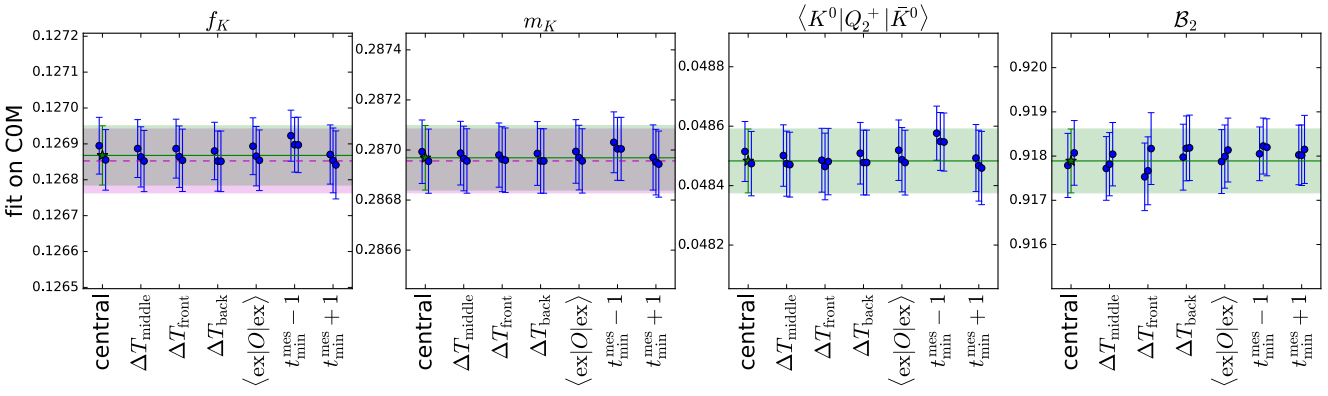

Figure 5.3: Stability of correlation function fits, illustrated on the example of the C0M ensemble for Q_2^+. All numbers quoted in lattice units and NPR basis. Details of fit variations and coloured bands explained in main text.

Alternative strategy

In this method we perform a combined fit to the two-point functions C_{PP}^{SL}, C_{PP}^{SS}, C_{PA}^{SL} and *ratios* of three and two-point functions (as opposed to three-point functions only). We start by defining the ratios of two-point functions in eqn (5.11) and three-point functions in eqn (5.13)

$$\begin{aligned} r^1(t,\Delta T) &= \frac{C_3^1(t,\Delta T)}{C_{PA}(t)C_{AP}(\Delta T - t)}\,, \\ r^i(t,\Delta T) &= \frac{C_3^i(t,\Delta T)}{C_{PP}(t)C_{PP}(\Delta T - t)}\,,\ i>1 \end{aligned} \tag{5.15}$$

which are purposefully constructed to asymptotically approach the bag parameters

$$r^i(t,\Delta T) \xrightarrow[0\ll t\ll \Delta T\ll T]{} N_i\mathcal{B}_i\,. \tag{5.16}$$

Expanding numerator and denominator of the first line of eqn (5.15) using eqn (5.11) and eqn (5.13) taking into account the ground state ($|0\rangle$) and first excited state ($|1\rangle$) contributions ($n, n' = 0, 1$) (but neglecting the excited-to-excited matrix elements) yields

$$r^1(t,\Delta T) = \frac{\langle 0|\mathcal{O}_1|0\rangle}{M_{A,0}^2}\left[1 + X_1(t,\Delta T)e^{-\Delta E\Delta T/2} + Y_1(t,\Delta T)e^{-\Delta E\Delta T}\right]. \tag{5.17}$$

where we defined

$$\begin{aligned} X_1(t,\Delta T) &= 2\frac{M_{P,1}E_0}{M_{P,0}E_1}\cosh\left[\Delta E(t-\Delta T/2)\right]\left(\frac{\langle 0|\mathcal{O}_1|1\rangle}{\langle 0|\mathcal{O}_1|0\rangle} - \frac{M_{A,1}}{M_{A,0}}\right), \\ Y_1(t,\Delta T) &= -4\frac{M_{P,1}^2E_0^2}{M_{P,0}^2E_1^2}\cosh^2\left[\Delta E(t-\Delta T/2)\right]\frac{\langle 0|\mathcal{O}_1|1\rangle}{\langle 0|\mathcal{O}_1|0\rangle}\frac{M_{A,1}}{M_{A,0}}\,, \end{aligned} \tag{5.18}$$

and $\Delta E = E_1 - E_0$. The expression for r^i ($i > 1$) is very similar.

We now define a version of the ratio summed over the interval $[t_c, \Delta T - t_c]$

$$r^i(t_c, \Delta T) \equiv \sum_{t=t_c}^{\Delta T - t_c} r^i(t, \Delta T). \tag{5.19}$$

Using the identity

$$\sum_{t=t_c}^{\Delta T - t_c} \cosh[\Delta E(t - \Delta T/2)] = \frac{\sinh[\Delta E/2(\Delta T - 2t_c + 1)]}{\sinh[\Delta E/2]}, \tag{5.20}$$

the summed ratio can be expressed as

$$r^1(t_c, \Delta T) = \frac{\langle 0|\mathcal{O}_1|0\rangle}{M_{A,0}^2}\left[\hat{t} + 2\frac{M_{P,1}E_0}{M_{P,0}E_1}e^{-\Delta E \Delta T/2}\frac{\sinh[\Delta E/2\hat{t}]}{\sinh[\Delta E/2]}\left(\frac{\langle 0|\mathcal{O}_1|1\rangle}{\langle 0|\mathcal{O}_1|0\rangle} - \frac{M_{A,1}}{M_{A,0}}\right)\right], \tag{5.21}$$

where $\hat{t} \equiv \Delta T - 2t_c + 1$. For a given operator $\mathcal{O}_i$ and choice of t_c we then jointly fit the correlation functions and $C_{PP}^{SL}(t)$, $C_{PA}^{SL}(t)$, $C_{PP}^{SS}(t)$ and ratios $r^i(t_c, \Delta T)$ (and the LL equivalent for F1M). The fit ranges of $t \in [t_{\text{min}}^{\text{2pt}}, t_{\text{max}}^{\text{2pt}}]$ and $\Delta T \in [\Delta T_{\text{min}}^{\text{3pt}}, \Delta T_{\text{max}}^{\text{3pt}}]$ are chosen such that all fit parameters remain stable when these ranges are varied by small amounts.

5.2.3 Valence strange quark correction

As is evident from table 5.1, the valence strange quark mass on the F1M ensemble is slightly mistuned from the physical strange quark mass value. We account for this effect by repeating the simulation at the physical strange quark mass on one eighth of the full statistics. We then compute the appropriate correction factors as

$$\begin{aligned}
\alpha_{R_i} &\equiv \frac{R_i^{\text{phys}}}{R_i^{\text{uni}}} = \lim_{0 \ll t \ll \Delta T} \frac{R_i^{\text{eff}}(t, \Delta T)\big|_{m_s^{\text{phys}}}}{R_i^{\text{eff}}(t, \Delta T)\big|_{m_s^{\text{uni}}}}, \\
\alpha_{\mathcal{B}_i} &\equiv \frac{\mathcal{B}_i^{\text{phys}}}{\mathcal{B}_i^{\text{uni}}} = \lim_{0 \ll t \ll \Delta T} \frac{\mathcal{B}_i^{\text{eff}}(t, \Delta T)\big|_{m_s^{\text{phys}}}}{\mathcal{B}_i^{\text{eff}}(t, \Delta T)\big|_{m_s^{\text{uni}}}},
\end{aligned} \tag{5.22}$$

α_X	$i=1$	$i=2$	$i=3$	$i=4$	$i=5$
$X = \mathcal{B}_i$	1.004983(99)	1.004231(66)	1.003036(65)	1.003193(71)	1.003583(61)
$X = R_i$		0.97005(18)	0.96890(18)	0.96904(17)	0.96942(17)

Table 5.5: Correction factors to be applied to the bare values of R_i and $\mathcal{B}_i$ on the F1M ensemble in the NPR basis in order to correct the observables to the physical strange quark mass.

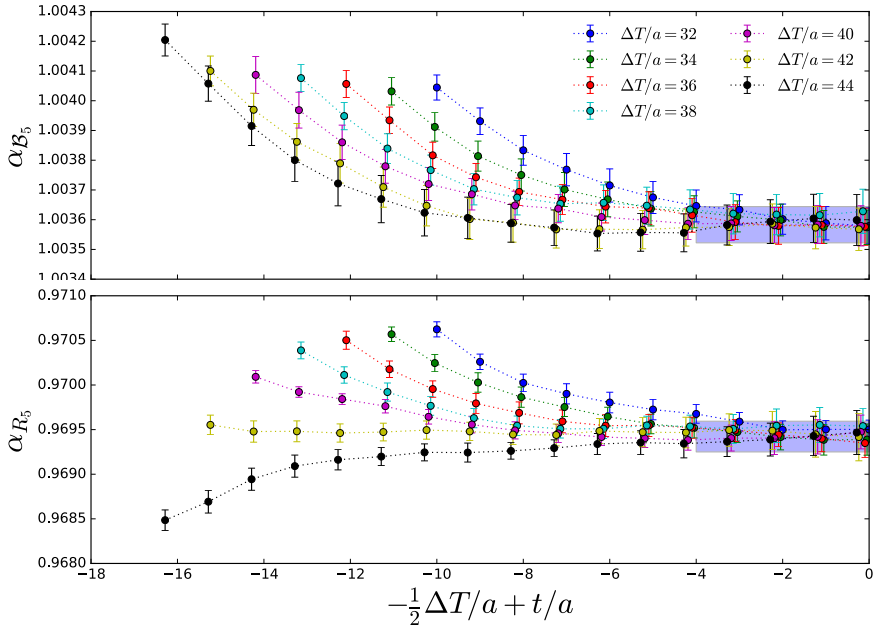

Figure 5.4: Strange valence mistuning quark correction on the F1M ensemble for the example of $\mathcal{B}_5$ (*top*) and R_5 (*bottom*). The shaded band indicates the fit value of the correction factor.

where

$$R_i^{\text{eff}}(t, \Delta T) = \frac{C_3^i(t, \Delta T)}{C_3^1(t, \Delta T)}\,,$$
$$\mathcal{B}_i^{\text{eff}}(t, \Delta T) = \frac{C_3^i(t, \Delta T)}{N_i C_2(t) C_2(\Delta T - t)}\,. \tag{5.23}$$

We find that the effect of the approximately 3% mistuning of the strange quark valence mass leads to around $0.3 - 0.5\%$ correction for the bag parameters and around 3% correction for the ratio of operators — see table 5.5. Given that the relative uncertainty of the correction factor is more than an order of magnitude smaller than that of the values it is applied to, we treat this correction factor as uncorrelated. Figure 5.4 illustrates this correction factor for the case of $\mathcal{B}_5$ and R_5.

Figure 5.5 shows the bare effective ratios $R_i^{\text{eff}}(t, \Delta T)$ (defined in eqn (5.23)) in the NPR basis for the C0M (left) and M0M (right) ensembles for various typical source-sink separations ΔT. For sufficiently large ΔT values these ratios plateau to the same value, indicating ground-state saturation.

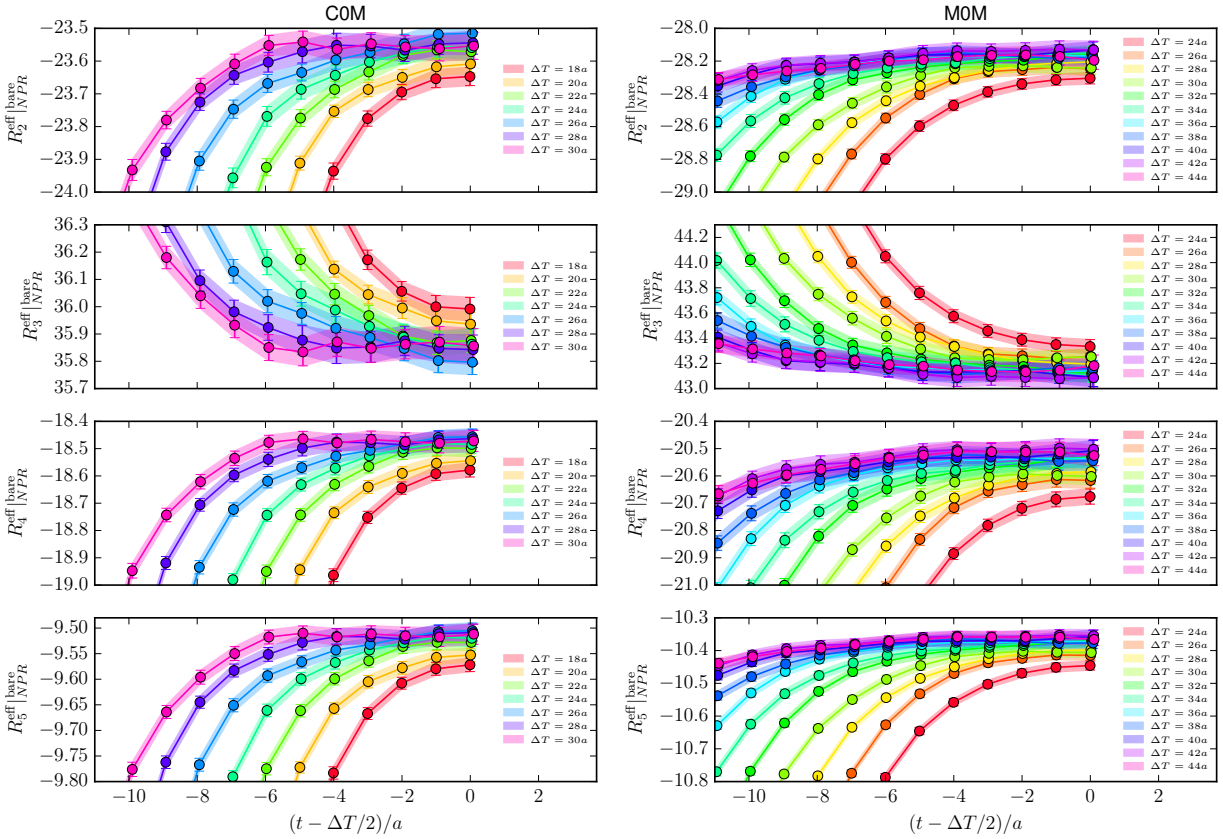

Figure 5.5: Illustration of the quality of our data for the C0M (*left*) and M0M (*right*) ensembles. We show the bare effective ratios $R_i^{\text{eff}}(t, \Delta T)$ in the NPR basis as defined in eqn (5.23).

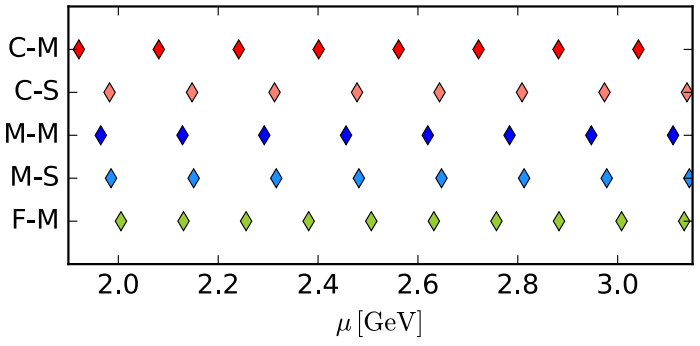

Figure 5.6: Simulation values of the scale μ on the various ensembles.

5.3 Non-perturbative renormalisation

Having computed the bare bag and ratio parameters, we now move to the step of renormalisation using the non-perturbative RI/SMOM scheme. The numerical setup for the computation of renormalisation constants for $\Delta\mathcal{S} = 2$ four-quark operators has been outlined in section 4.2.

We compute the relevant Green's functions for the four-quark operators (given by eqn (4.55)) as well as quark propagators. We then amputate the four quark legs of each Green's function using the appropriate inverse propagators to get the vertex functions needed for implementing the RI/SMOM renormalisation conditions. We then use the projectors and tree-level matrices in the two separate schemes γ_μ and $\not{q}$ (see section 4.1) to compute the set of renormalisation constants for bag and ratio parameters over a range of simulated momenta that cover the region $2\,\text{GeV} \lesssim \mu \lesssim 3\,\text{GeV}$, as shown in figure 5.6. In specific, using $\mathcal{A}$ to indicate γ_μ or $\not{q}$ we define the renormalisation factors $Z_{ij}^{(\mathcal{A},\mathcal{A})}/Z_A^2$ as[3]

$$\frac{Z_{ij}^{(\mathcal{A},\mathcal{A})}(\mu,a)}{Z_A^2(a)} \times \lim_{m_q\to 0} \frac{P_k^{(\mathcal{A})}[\Pi_j^{\text{bare}}(a,p_1,p_2)]}{(P_A^{(\mathcal{A})}[\Pi_A^{\text{bare}}(a,p_1,p_2)])^2}\bigg|_{\text{sym}} = \frac{F_{ik}^{(\mathcal{A})}}{(F_A^{(\mathcal{A})})^2}\,. \tag{5.24}$$

Our conventions are such that from eqn (5.24) we can define $Z_{\mathcal{B}_1} \equiv Z_{B_K} = Z_{11}/Z_A^2$. Finally, to obtain the renormalised BSM bag parameters we also need to renormalise the quark mass. Making use of $Z_m = 1/Z_S$ we impose

$$\frac{Z_A^{(\mathcal{A})}(\mu,a)}{Z_S(\mu,a)} \times \lim_{m_q\to 0} \frac{P_A^{(\mathcal{A})}[\Pi_A^{\text{bare}}(a,p_1,p_2)]}{P_S[\Pi_S^{\text{bare}}(a,p_1,p_2)]}\bigg|_{\text{sym}} = \frac{F_A^{(\mathcal{A})}}{F_S}\,. \tag{5.25}$$

The use of two schemes provides a way of estimating systematic errors in the renormalisation by examining the spread of the results. In order to ensure reproducibility, we provide numerical values of the renormalisation constants at some choice of lattice momenta on the lightest pion mass ensemble for each distinct lattice spacing in tables B.1-B.8 in appendix B.

Finally, we use these values to renormalise the quantities of interest. In particular we find

$$\begin{aligned} R_i^{\text{ren}}(\mu) &= \frac{Z_{ij}}{Z_{11}} R_j^{\text{bare}}(\mu,a)\,, \\ \mathcal{B}_1^{\text{ren}}(\mu) &= \frac{Z_{11}}{Z_A^2}\mathcal{B}_1^{\text{bare}}(\mu,a)\,, \\ N_i\mathcal{B}_i^{\text{ren}}(\mu) &= \frac{Z_{ij}}{Z_P^2} N_j\mathcal{B}_j^{\text{bare}}(\mu,a) \qquad i,j = 2,\cdots,5. \end{aligned} \tag{5.26}$$

Note that in practice we make use of the relation $Z_S \approx Z_P$, following from chiral symmetry (which is well-preserved by the DWF action).

[3] We can also define $Z_{ij}^{(\mathcal{A},\mathcal{B})}$ with $\mathcal{A} \neq \mathcal{B}$, but in this work we consider only (γ_μ,γ_μ) and $(\not{q},\not{q})$.

5.3.1 Chiral extrapolation of Z factors

Formally the RI/SMOM renormalisation constants are defined in the massless (zero quark mass) limit. In order to perform this limit lattice-spacing-by-lattice-spacing we proceed as follows:

1. We first extrapolate the valence quark mass to zero ensemble-by-ensemble. As the C0M and M0M ensemble are computationally most expensive, we simulate only at $am_q^{\text{val}} = am_s^{\text{sea}}/2$ in the valence sector. On all other ensembles we have additional simulation points at $am_q^{\text{val}} = am_l^{\text{sea}}$ and $am_q^{\text{val}} = 2am_l^{\text{sea}}$. On each of these ensembles we extrapolate the renormalisation constants to the massless limit $am_q^{\text{val}} \to 0$ (see figure 5.7). The extrapolation of the data on the physical pion mass ensembles is performed by applying the slope of the C1M (M1M) ensemble to the C0M (M0M) data.

2. We then interpolate the renormalisation constants on all ensembles to a fixed scale μ. We perform a linear fit to the two closest simulated values of μ and a quadratic fit to the three closest points and assign the spread as a systematic error.

3. We then perform a chiral extrapolation in $(am_\pi)^2$ to all ensembles that share an identical lattice spacing (C1S and C2S; C0M and C1M; M1S, M2S and M3S; M0M and M1M) as illustrated in figure 5.8 for the M-S ensembles at a momentum point close to 2 GeV. Since we only have a single sea quark mass data point on the F1M ensemble, in practice we first interpolate the results on all ensembles to a common renormalisation scale and then perform the sea-light quark mass to zero limit for each choice of distinct lattice spacing. For the F-M ensemble this is done by applying each of the four slopes (obtained from C-S, C-M, M-S and M-M) in turn and assigning a systematic uncertainty of half the spread of these results. Since these numbers contain information from multiple ensembles and the NPR calculations are based on a subset of the configurations, we propagate these small uncertainties in an uncorrelated fashion. To this end we add statistical and systematic uncertainties in quadrature and generate bootstrap samples for each of the Z_{ij} by drawing from a Gaussian distribution with the appropriate mean and width. We provide numerical values of these chirally extrapolated renormalisation constants for each of the lattice spacings at $\mu = 2\,\text{GeV}$ (table B.9), $\mu = 2.5\,\text{GeV}$ (table B.10), and $\mu = 3\,\text{GeV}$ (table B.11).

5.3.2 Step scaling

When performing the renormalisation we have the freedom to choose the renormalisation scale μ within the Rome-Southampton window of our ensembles, which includes $2\,\text{GeV} \lesssim$

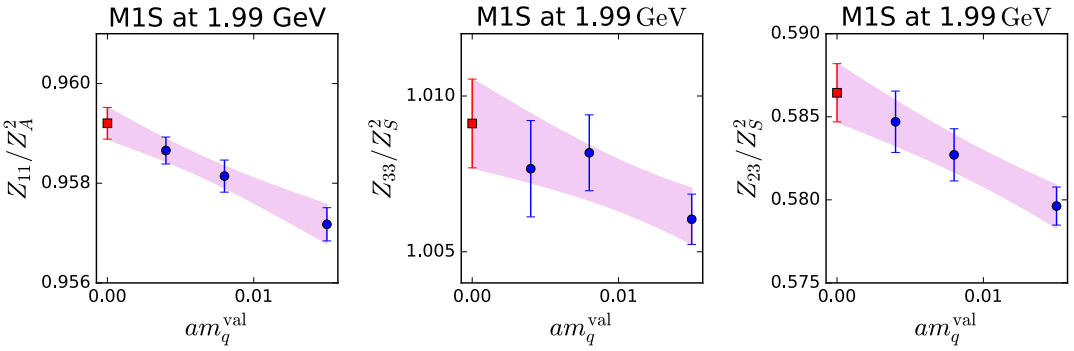

Figure 5.7: Extrapolation of the renormalisation constants to massless valence-quark limit for the example of the (11), (33) and (23) elements of the M1S ensemble close to 2 GeV. Results are presented in the RI/SMOM$^{(\gamma_\mu,\gamma_\mu)}$ scheme in the NPR basis.

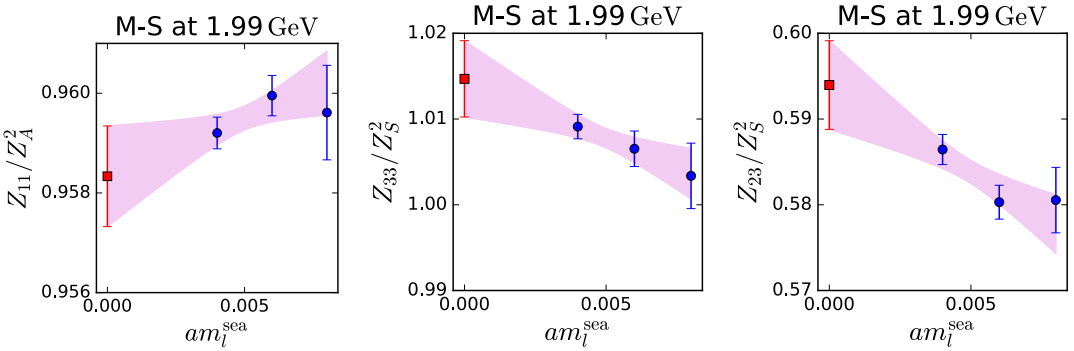

Figure 5.8: Extrapolation of the renormalisation constants to the zero light-sea quark mass limit for the example of the (11), (33) and (23) elements of the M-S ensembles close to 2 GeV. Results are presented in the RI/SMOM$^{(\gamma_\mu,\gamma_\mu)}$ scheme in the NPR basis.

$\mu \lesssim 3$ GeV. We note that higher scales are more susceptible to discretisation effects, whilst lower scales face larger errors in the perturbative matching to a continuum scheme such as $\overline{\mathrm{MS}}$. It is possible to scale the value of an operator renormalised at one scale to another using a scale evolution matrix, $\sigma(\mu_2, \mu_1)$, in a procedure called step-scaling as discussed in section 4.4. We can therefore choose a lower scale μ for non-perturbative renormalisation to reduce cutoff effects, and a higher scale μ' for matching to $\overline{\mathrm{MS}}$. This distance is bridged using non-perturbative running

$$O_i^{\overline{\mathrm{MS}}}(\mu') = R_{ij}^{\overline{\mathrm{MS}}\leftarrow\mathrm{RI}}(\mu')\sigma_{jk}(\mu', \mu)O_k^{\mathrm{RI}}(\mu), \tag{5.27}$$

O_i being any of the quantities in eqn (5.26). The matching factors $R_{ij}^{\overline{\mathrm{MS}}\leftarrow\mathrm{RI}}$ are computed in next-to-leading order perturbation theory and presented in section 4.3 for both schemes.

We define the continuum scale evolution matrix for the renormalisation of the four-quark operators as

$$\sigma(\mu_2, \mu_1) = \lim_{a^2\to 0} Z(\mu_2, a)Z^{-1}(\mu_1, a), \tag{5.28}$$

where $Z(\mu, a)$ is the 5×5 block-diagonal matrix. The numerical values of the scaling matrix at each lattice spacing are reported in table B.12 in appendix B. We perform this continuum limit using the chirally extrapolated renormalisation constants from all lattice spacings using a linear fit in a^2. In the few cases where the quality of fit does not lead to an acceptable p-value, we rescale the uncertainty by $\sqrt{\chi^2/\text{d.o.f.}}$. In figure 5.9 we compare our non-perturbative step-scaling results to leading order (LO) and next-to-leading order (NLO) perturbation theory. We observe that while the results from NLO perturbation theory are closer to the non-perturbative results compared to those from LO perturbation theory, the non-perturbative results are still clearly significant.

Since we have mapped out the region $2\,\text{GeV} \lesssim \mu \lesssim 3\,\text{GeV}$, we can further split (5.28) into multiple smaller steps $\Delta = (\mu_2 - \mu_1)/N$, i.e. we can compute the product

$$\prod_{k=0}^{N-1} \sigma(\mu_1 + k\Delta + \Delta, \mu_1 + k\Delta)\,. \tag{5.29}$$

Hence, alongside directly renormalising at 3 GeV, we can also renormalise the result at 2 GeV and step scale to 3 GeV in one step, or in multiple steps – this allows us to probe the effect the scale of the renormalisation has.

The numerical values for the step-scaling matrices for the bag parameters in the RI/SMOM$^{(\gamma_\mu,\gamma_\mu)}$-scheme and in the SUSY basis are given by

$$\sigma_{\text{bag}}(3\,\text{GeV}, 2\,\text{GeV}) = \begin{bmatrix} 0.98021(53) & 0.0 & 0.0 & 0.0 & 0.0 \\ 0.0 & 0.9194(22) & -0.0630(16) & 0.0 & 0.0 \\ 0.0 & -0.00284(35) & 0.6846(19) & 0.0 & 0.0 \\ 0.0 & 0.0 & 0.0 & 0.9988(24) & 0.0784(25) \\ 0.0 & 0.0 & 0.0 & 0.00838(59) & 0.7542(24) \end{bmatrix}, \tag{5.30}$$

$$\sigma_{\text{bag}}(3 \xleftarrow{\Delta=0.5} 2\,\text{GeV}) = \begin{bmatrix} 0.98030(35) & 0.0 & 0.0 & 0.0 & 0.0 \\ 0.0 & 0.9199(22) & -0.0634(15) & 0.0 & 0.0 \\ 0.0 & -0.00260(31) & 0.6863(17) & 0.0 & 0.0 \\ 0.0 & 0.0 & 0.0 & 0.9990(25) & 0.0778(24) \\ 0.0 & 0.0 & 0.0 & 0.00860(44) & 0.7552(23) \end{bmatrix}, \tag{5.31}$$

$$\sigma_{\text{bag}}(3 \xleftarrow{\Delta=0.33} 2\,\text{GeV}) = \begin{bmatrix} 0.98030(29) & 0.0 & 0.0 & 0.0 & 0.0 \\ 0.0 & 0.9178(18) & -0.0630(16) & 0.0 & 0.0 \\ 0.0 & -0.00342(24) & 0.6863(16) & 0.0 & 0.0 \\ 0.0 & 0.0 & 0.0 & 0.9973(19) & 0.0774(22) \\ 0.0 & 0.0 & 0.0 & 0.00842(53) & 0.7552(16) \end{bmatrix}. \tag{5.32}$$

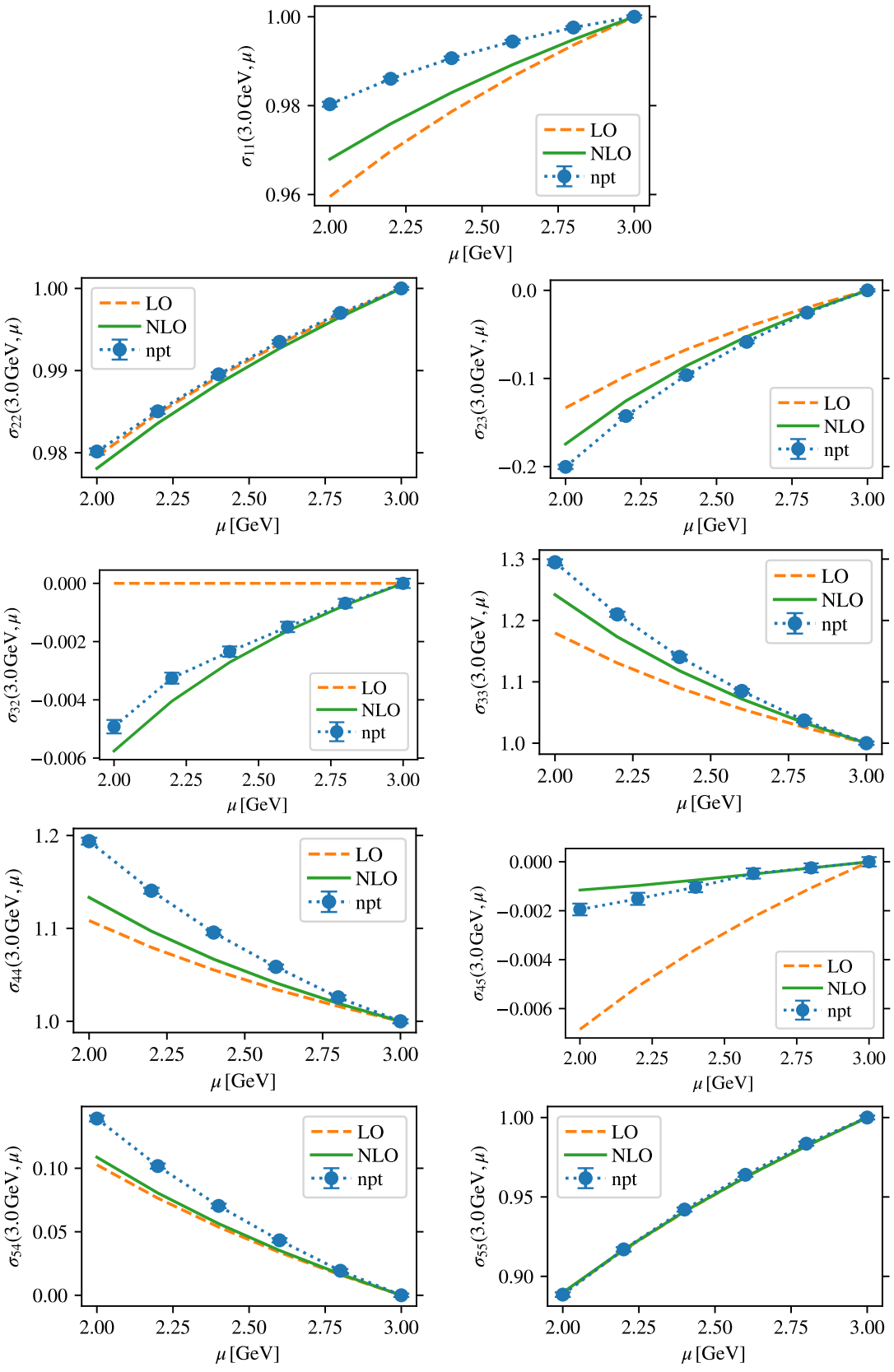

Figure 5.9: Comparison of the scale evolution matrix $\sigma(3\,\mathrm{GeV},\mu)$ in the RI/SMOM$^{(\gamma_\mu,\gamma_\mu)}$ scheme and NPR basis evaluated non-perturbatively (blue circles), perturbatively at leading order (orange dashed lines) and next-to-leading order (green solid lines).

Similarly, the numerical values for the step-scaling matrices for the ratio parameters in the RI/SMOM$^{(\gamma_\mu,\gamma_\mu)}$-scheme and in the SUSY basis are given by

$$\sigma_{\text{rat}}(3\,\text{GeV}, 2\,\text{GeV}) = \begin{bmatrix} 1.0 & 0.0 & 0.0 & 0.0 & 0.0 \\ 0.0 & 1.2153(28) & -0.08396(60) & 0.0 & 0.0 \\ 0.0 & -0.00426(52) & 0.90868(42) & 0.0 & 0.0 \\ 0.0 & 0.0 & 0.0 & 1.3186(42) & 0.1018(15) \\ 0.0 & 0.0 & 0.0 & 0.00976(68) & 0.99984(59) \end{bmatrix}, \tag{5.33}$$

$$\sigma_{\text{rat}}(3 \xleftarrow{\Delta=0.5} 2\,\text{GeV}) = \begin{bmatrix} 1.0 & 0.0 & 0.0 & 0.0 & 0.0 \\ 0.0 & 1.2149(25) & -0.08315(50) & 0.0 & 0.0 \\ 0.0 & -0.00374(43) & 0.90889(40) & 0.0 & 0.0 \\ 0.0 & 0.0 & 0.0 & 1.3190(35) & 0.1023(14) \\ 0.0 & 0.0 & 0.0 & 0.01083(44) & 0.99940(59) \end{bmatrix}, \tag{5.34}$$

$$\sigma_{\text{rat}}(3 \xleftarrow{\Delta=0.33} 2\,\text{GeV}) = \begin{bmatrix} 1.0 & 0.0 & 0.0 & 0.0 & 0.0 \\ 0.0 & 1.2141(33) & -0.08249(72) & 0.0 & 0.0 \\ 0.0 & -0.00502(44) & 0.90883(53) & 0.0 & 0.0 \\ 0.0 & 0.0 & 0.0 & 1.3184(39) & 0.1018(13) \\ 0.0 & 0.0 & 0.0 & 0.01002(68) & 0.99915(42) \end{bmatrix}. \tag{5.35}$$

Therefore it is possible to scale our operators, once renormalised and extrapolated to the continuum limit, from μ_1 to μ_2. By renormalising at $\mu = 2\,\text{GeV}$, where lattice artefacts are less significant, and step-scaling our results in RI/SMOM to $\mu = 3\,\text{GeV}$ before perturbatively matching to $\overline{\text{MS}}$, we also reduce the errors associated with the truncation of the perturbative series at lower scales.

5.4 Results

The ratio and bag parameters in the $\overline{\text{MS}}$ scheme at a scale μ' are obtained via

$$\mathcal{B}_1^{\overline{\text{MS}}}(\mu') = R_{11}^{\overline{\text{MS}}\leftarrow\text{RI}}(\mu') \left[\lim_{a\to 0} \sigma_{\text{bag},11}(\mu',\mu)\right] \left[\lim_{\substack{a\to 0 \\ m_\pi \to m_\pi^{\text{phys}}}} \frac{Z_{11}^{\text{RI}}}{Z_A^2}(a\mu)\mathcal{B}_1^{\text{bare}}\right] \tag{5.36}$$

$$N_i\mathcal{B}_{i>1}^{\overline{\text{MS}}}(\mu') = \left(\frac{R_{ij}}{R_S^2}\right)^{\overline{\text{MS}}\leftarrow\text{RI}}(\mu') \left[\lim_{a\to 0} \sigma_{\text{bag},jk}(\mu',\mu)\right] \left[\lim_{\substack{a\to 0 \\ m_\pi \to m_\pi^{\text{phys}}}} \frac{Z_{kl}^{\text{RI}}}{Z_S^2}(a\mu)N_l\mathcal{B}_{l>1}^{\text{bare}}\right] \tag{5.37}$$

$$R_{i>1}^{\overline{\text{MS}}}(\mu') = \left(\frac{R_{ij}}{R_{11}}\right)^{\overline{\text{MS}}\leftarrow\text{RI}}(\mu') \left[\lim_{a\to 0} \sigma_{\text{rat},jk}(\mu',\mu)\right] \left[\lim_{\substack{a\to 0 \\ m_\pi \to m_\pi^{\text{phys}}}} \frac{Z_{kl}^{\text{RI}}}{Z_{11}}(a\mu)R_{l>1}^{\text{bare}}\right]. \tag{5.38}$$

The matching factors R_S and R_{11} are required for matching the denominators in the bag and ratio parameters to the $\overline{\text{MS}}$ scheme. Note that in the continuum limit $Z_A^{\text{RI}} = 1 = Z_A^{\overline{\text{MS}}}$ and therefore a separate conversion factor is not needed for it in $\mathcal{B}_1$. In the equations above Z-factors are implicitly in the chiral limit $Z(a\mu) = \lim_{m_q^{\text{val}}\to 0\, m_q^{\text{sea}}\to 0} Z(am_q^{\text{val}}, am_q^{\text{sea}}, a\mu)$.

Having computed these chirally extrapolated Z-factors, the scale evolution matrices in the continuum limit, and using the matching factors R_{ij} known from perturbation theory, the final step is to perform the chiral and continuum limit extrapolation for the renormalised bag and ratio parameters while assembling an error budget corresponding to each step in the above equations.

5.4.1 Chiral and continuum fits

To recover continuum results at physical quark masses we perform a simultaneous chiral-continuum limit fit. Our fit ansatz is based on NLO SU(2) chiral perturbation theory (χPT), covered in more detail in sections 2.3.3 & 2.5.4, and includes a chiral logarithm term. Furthermore our fit function is linear in a^2 and m_π^2 and the mistuning of the strange quark mass $\delta_{m_s}^{\text{sea}}$. It is given by

$$Y_i(a^2, m_\pi^2, m_s^{\text{sea}}) = Y_i^{\text{phys}} \left(1 + \alpha_i (a\Lambda)^2 + \beta_i \frac{m_\pi^2 - (m_\pi^{\text{phys}})^2}{(m_\pi^{\text{phys}})^2} + \gamma_i \delta_{m_s}^{\text{sea}} + L_i^Y(m_\pi) - L_i^Y(m_\pi^{\text{phys}}) \right). \tag{5.39}$$

where $Y \in \{\mathcal{B}, R\}$ is the quantity of interest. $\Lambda = \Lambda_{\text{QCD}}$ is the typical QCD scale and we take the isospin-averaged pion mass to be $m_\pi^{\text{phys}} = (2m_\pi^\pm + m_\pi^0)/3 \approx 138\,\text{MeV}$ [6]. Y_i^{phys}, α, β and γ are fit parameters, while $\delta_{m_s}^{\text{sea}} = (m_s^{\text{sea}} - m_s^{\text{phys}})/m_s^{\text{phys}}$ parameterises the mistuning of the sea strange quark mass. The chiral logarithms are given by $L_i^Y(m_\pi) = C_i^Y\, m_\pi^2\, \log(m_\pi^2/\Lambda^2)/(16\pi^2 f_\pi^2)$, where the coefficients C_i are known constants with numerical values $C_i^{\mathcal{B}} = -0.5$ for $i = 1, 2, 3$ and $C_i^{\mathcal{B}} = 0.5$ for $i = 4, 5$, and we take $f_\pi = 130.41(23)\,\text{MeV}$ [6]. For the ratios R_2 and R_3 the chiral logarithms vanish ($C_2^R = C_3^R = 0$) and finally $C_4^R = C_5^R = 1$.

In this section we present the chiral-continuum limit fits in the RI/SMOM$^{(\gamma_\mu,\gamma_\mu)}$ and RI/SMOM$^{(\not{q},\not{q})}$ schemes at $\mu = 2\,\text{GeV}$ and in the SUSY basis. We show these fits for the ratios R_i in figures 5.11 & 5.13 and for the bag parameters $\mathcal{B}_i$ in figures 5.12 & 5.14. The data points represent the renormalised bag or ratio parameters where we have corrected for the sea quark mistuning and chiral logarithm dependence. The data points from each ensemble therefore only carry lattice spacing and chiral dependence, which are depicted in the left and right panels of each figure respectively. The black data point represents the physical value at zero lattice spacing and at the physical pion mass, Y_i^{phys}, and the coloured bands are reconstructed fit trajectories for each ensemble. We also report the χ^2/d.o.f and corresponding p-value for each fit.

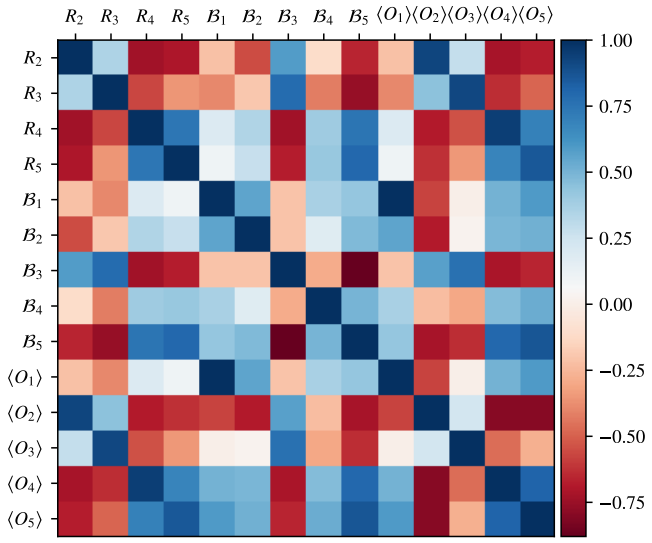

Figure 5.10: Heat-map of the statistical correlation matrix between the renormalised $\mathcal{B}_i$, R_i and the $\langle K|O_i^+|\overline{K}\rangle$ in $\overline{\text{MS}}$ at 3 GeV.

Since we find that the results from the C2S ensemble — which is at the heaviest pion mass and the coarsest lattice spacing — is not always well described by the fit ansatz, we remove it from our central fits. We find that the data is well described by the fit function in eqn (5.39) in all cases with acceptable p-values ($> 5\%$) for all fits presented. The statistical correlation matrix between the $\mathcal{B}_i$, R_i and $\langle K|O_i^+|\overline{K}\rangle$ (computed by combining R_i with $\mathcal{B}_1$ and other appropriate factors) is illustrated in the form of a heat-map in figure 5.10.

Our central fit results in the two intermediate schemes – RI/SMOM$^{(\gamma_\mu,\gamma_\mu)}$ and RI/SMOM$^{(\not{q},\not{q})}$ – are obtained from a chiral-continuum limit fit at $\mu = 2$ GeV performed in the SUSY basis. These results are then step-scaled to 3 GeV (e.g. using the matrix provided in eqn (5.30)) and perturbatively matched to $\overline{\text{MS}}$. In the following sections we will present the results of the chiral-continuum limit fits and assemble the full uncertainty budget relating to the lattice computation in the intermediate RI/SMOM schemes at 3 GeV. Only subsequently do we match these results perturbatively to $\overline{\text{MS}}$. This allows us to cleanly separate the uncertainties due to the perturbative matching to $\overline{\text{MS}}$ from those arising in the lattice calculation.

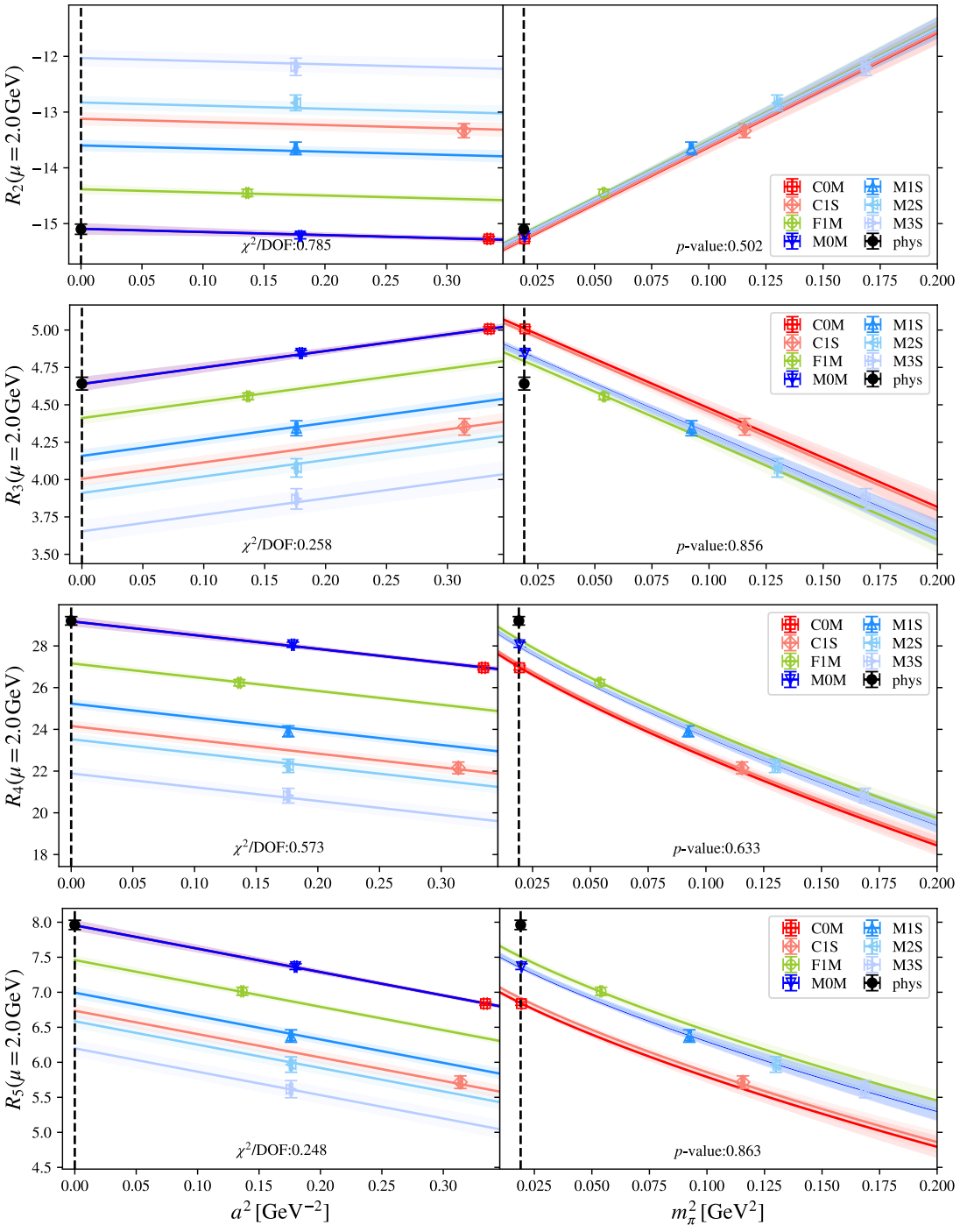

Figure 5.11: Chiral-continuum limit fit to BSM ratio parameters R_{2-5} in the SUSY basis, renormalised in the RI/SMOM$^{(\gamma_\mu,\gamma_\mu)}$ scheme.

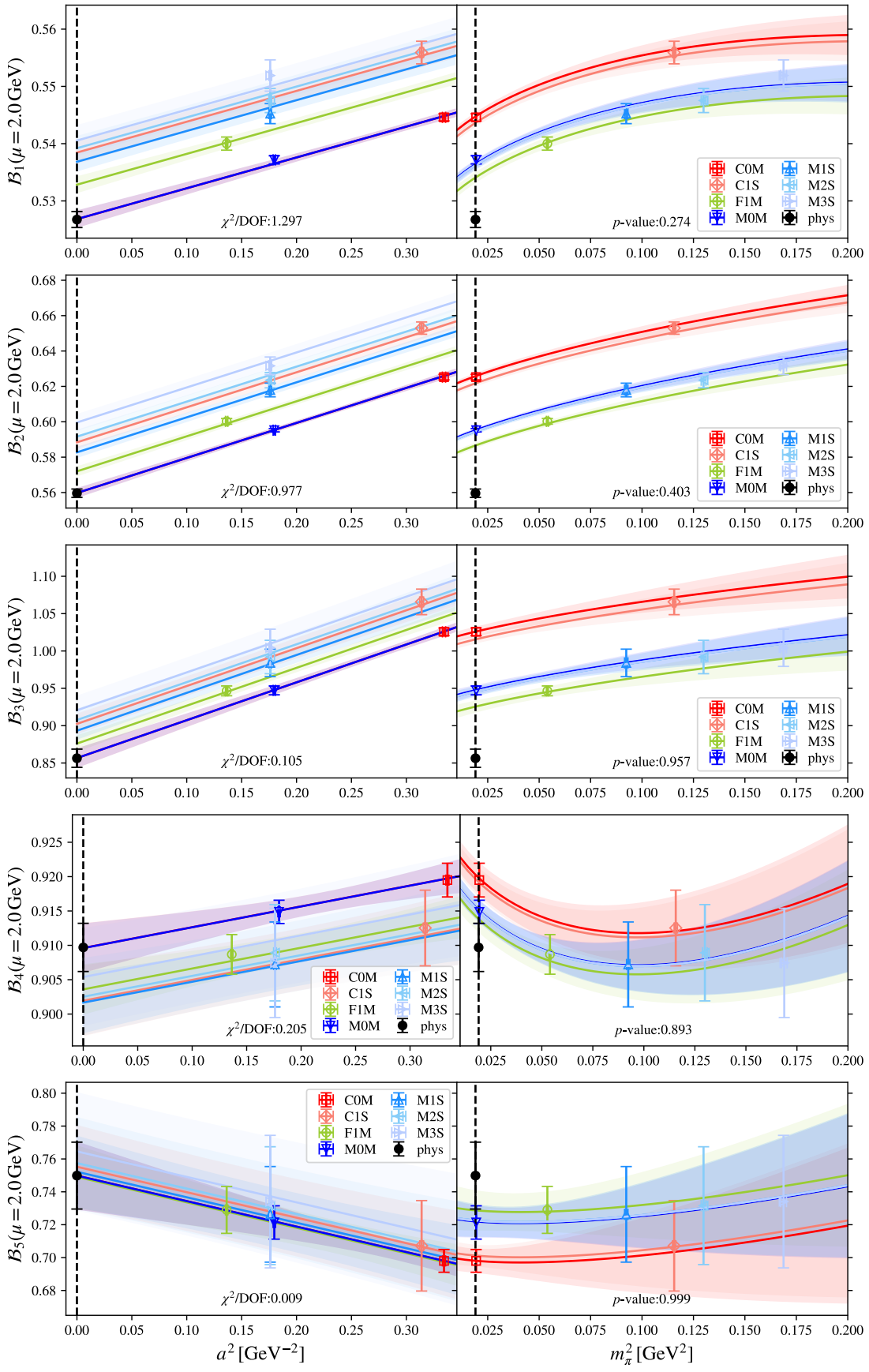

Figure 5.12: Chiral-continuum limit fit to the standard model bag parameter $\mathcal{B}_1$ (*top*) and BSM bag parameters $\mathcal{B}_{2-5}$ in the SUSY basis, renormalised in the RI/SMOM$^{(\gamma_\mu,\gamma_\mu)}$ scheme.

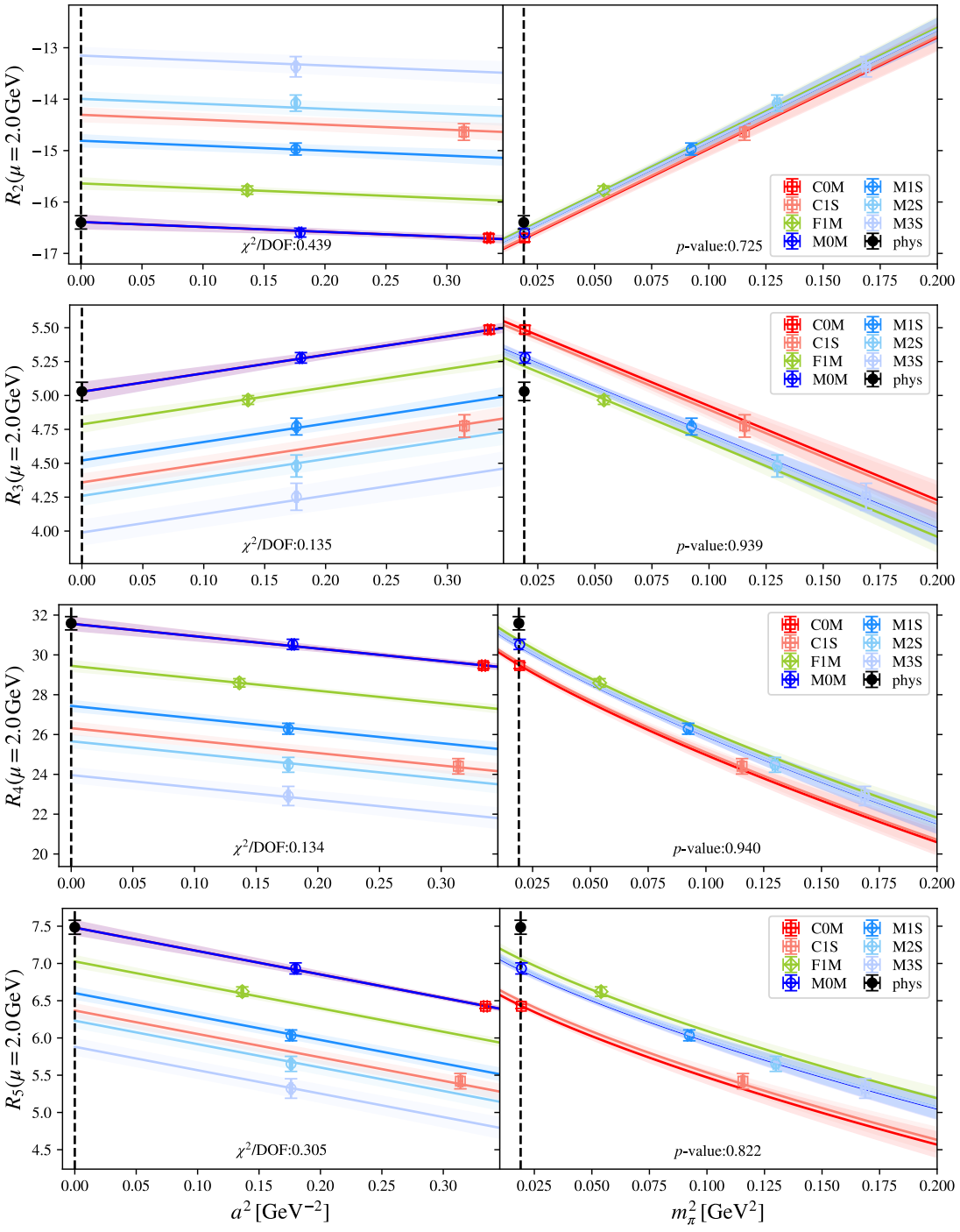

Figure 5.13: Chiral-continuum limit fit to BSM ratio parameters R_{2-5} in the SUSY basis, renormalised in the RI/SMOM$^{(\not{q},\not{q})}$ scheme.

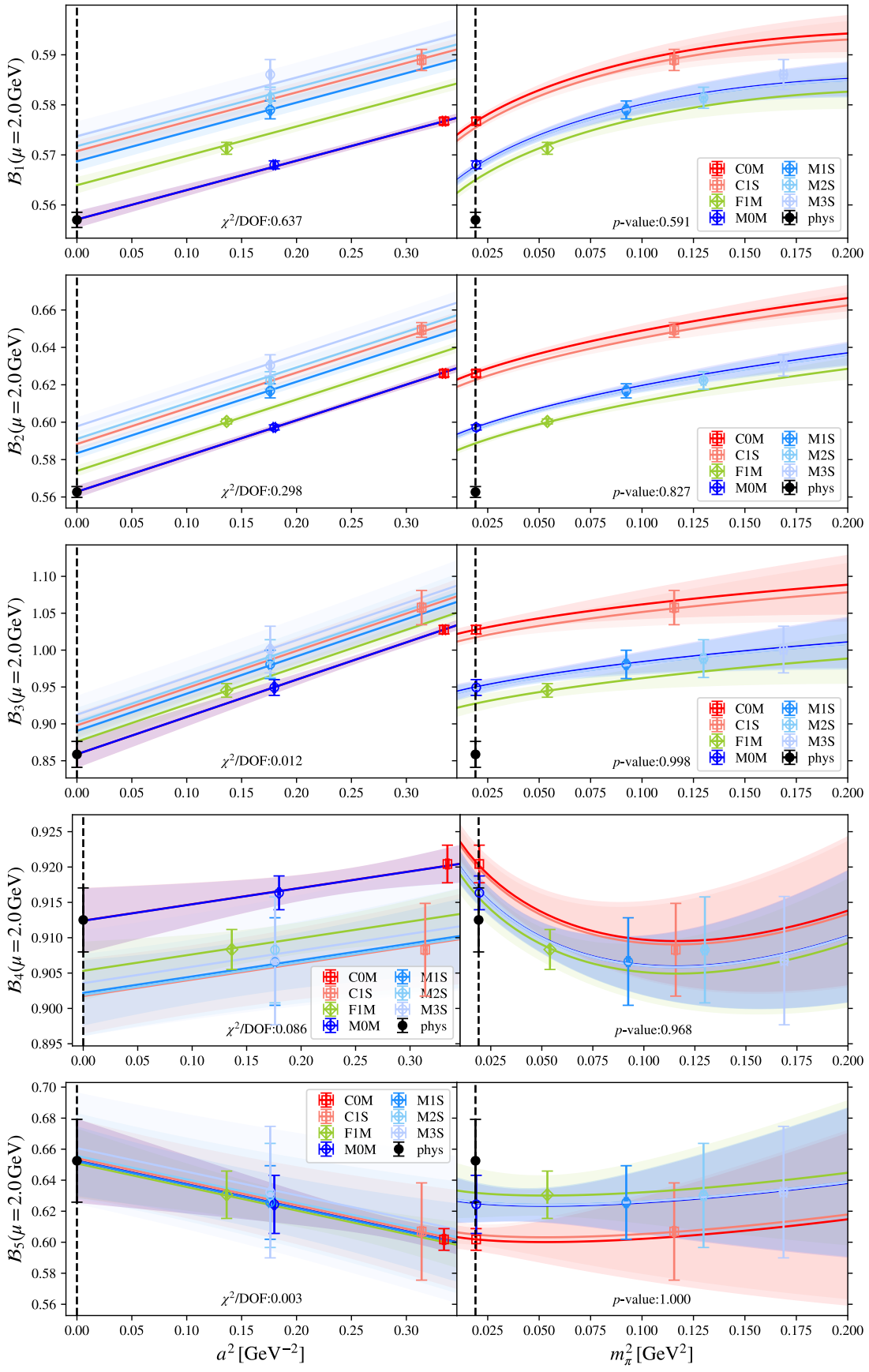

Figure 5.14: Chiral-continuum limit fit to the standard model bag parameter $\mathcal{B}_1$ (*top*) and BSM bag parameters $\mathcal{B}_{2-5}$ in the SUSY basis, renormalised in the RI/SMOM$^{(q,q)}$ scheme.

5.4.2 Error budget

In this section we quantify all relevant sources of uncertainties; we consider variations to the data and the fit ansatz; variations of the renormalisation procedure; and uncertainties stemming from the perturbative matching. We quantify the uncertainties for the variations by considering

$$\delta_i^{\text{var}}(\mu) = \frac{|Y_i^{\text{central}} - Y_i^{\text{variation}}|}{\frac{1}{2}(Y_i^{\text{central}} + Y_i^{\text{variation}})}\,, \tag{5.40}$$

where $Y \in \{\mathcal{B}, R\}$.

Chiral extrapolation

The two precise data points at physical pion masses make the mass extrapolation element of the fit very benign. We quantify the associated uncertainty by varying the pion mass cut applied to the data by removing terms from our fit form and by repeating the fits using the alternative correlator fit results. For each of these variations we compute the associated δ (see eqn (5.40)) – which measures the shift in central value – and list the corresponding values in table 5.6. For all ratios and bag parameters this error is well below 1% and typically sub-statistical. For each observable we assign the maximum of those values as the systematic uncertainty associated to the chiral extrapolation listed as "chiral" in table 5.9.

Discretisation effects

The good chiral symmetry of domain wall fermions constrains $O(a)$ and $O(a^3)$ terms to be small. The $O(a^2)$ effects are controlled and removed by our three lattice spacings present in the fit. Power counting suggests that $O(a^4)$ effects for hadronic physics scales with a 1.73 GeV coarsest inverse lattice spacing will remain small on all data points. However, the same is not necessarily true for hard, off-shell vertex functions where the momenta are chosen as the best compromise for a Rome-Southampton window. The leading unremoved discretisation effects are thus likely to come from the non-perturbative renormalisation, and may be probed by comparing different ways of renormalising our data.

Our central chiral-continuum limit fit is based on data renormalised at $\mu = 2\,\text{GeV}$ which is then step-scaled to 3 GeV by the step-scaling function $\sigma(3\,\text{GeV}, 2\,\text{GeV})$ presented in eqn (5.30) for the bag parameters. We compare the results obtained this way to using the alternative prescription to obtain the scaling function (see eqn (5.29)) with $N = 2, 3$ and to performing the continuum limit to data renormalised directly at $\mu = 3\,\text{GeV}$. We compute and report the associated values for δ_i in table 5.7.

(γ_μ, γ_μ)	Central fit	no δ_{m_s}	no $L(m_\pi)$	$m_\pi < 440$ MeV	$m_\pi < 370$ MeV	$m_\pi < 350$ MeV	alt fit
R_2	$-15.106(87)$	0.22%	-	0.46%	0.05%	0.08%	0.45%
R_3	4.643(41)	0.42%	-	0.28%	0.10%	0.11%	0.21%
R_4	29.22(19)	0.51%	0.59%	0.58%	0.04%	0.06%	0.49%
R_5	7.965(62)	0.10%	0.47%	0.50%	0.00%	0.05%	0.13%
$\mathcal{B}_1$	0.5268(13)	0.10%	0.21%	0.49%	0.02%	0.06%	0.40%
$\mathcal{B}_2$	0.5596(23)	0.05%	0.17%	0.06%	0.01%	0.08%	0.02%
$\mathcal{B}_3$	0.856(11)	0.06%	0.28%	0.02%	0.07%	0.06%	0.00%
$\mathcal{B}_4$	0.9097(35)	0.03%	0.17%	0.08%	0.01%	0.02%	0.06%
$\mathcal{B}_5$	0.750(19)	0.02%	0.24%	0.18%	0.02%	0.03%	0.13%

$(\not{q}, \not{q})$	Central fit	no δ_{m_s}	no $L(m_\pi)$	$m_\pi < 440$ MeV	$m_\pi < 370$ MeV	$m_\pi < 350$ MeV	alt fit
R_2	$-16.40(13)$	0.47%	-	0.47%	0.13%	0.15%	0.38%
R_3	5.030(68)	0.77%	-	0.07%	0.22%	0.22%	0.00%
R_4	31.59(33)	1.06%	1.21%	0.56%	0.11%	0.11%	0.45%
R_5	7.486(94)	0.61%	1.23%	0.84%	0.07%	0.06%	0.07%
$\mathcal{B}_1$	0.5570(15)	0.12%	0.24%	0.37%	0.03%	0.03%	0.34%
$\mathcal{B}_2$	0.5627(29)	0.24%	0.27%	0.18%	0.02%	0.03%	0.01%
$\mathcal{B}_3$	0.859(18)	0.11%	0.43%	0.12%	0.02%	0.02%	0.10%
$\mathcal{B}_4$	0.9125(45)	0.19%	0.28%	0.12%	0.01%	0.03%	0.11%
$\mathcal{B}_5$	0.653(27)	0.13%	0.53%	0.18%	0.11%	0.12%	0.39%

Table 5.6: Chiral-continuum limit fit systematics depending on choice of ansatz at $\mu = 2.0$ GeV in the RI/SMOM$^{(\gamma_\mu,\gamma_\mu)}$ (*top*) and RI/SMOM$^{(\not{q},\not{q})}$ (*bottom*) schemes in the SUSY basis. The first column shows the central value with statistical uncertainty, whilst the remaining columns quantify variations arising from different choices in the data that enters the fit as well as the model to which the chiral dependence is fitted. The last column illustrates the effect of using the alternative choice of correlation function fits underlying the analysis.

(γ_μ, γ_μ)	$\sigma(3\,\text{GeV}, 2\,\text{GeV})$	$\sigma(3 \xleftarrow{\Delta=0.5} 2)$	$\sigma(3 \xleftarrow{\Delta=0.33} 2)$	NPR at 3 GeV	rcsb	SUSY←NPR
R_2	−18.37(10)	0.12%	0.13%	0.17%	0.11%	0.02%
R_3	5.485(36)	0.18%	0.50%	0.37%	0.14%	0.15%
R_4	38.60(27)	0.02%	0.02%	0.48%	0.09%	0.01%
R_5	10.932(47)	0.11%	0.01%	0.97%	0.03%	1.22%
$\mathcal{B}_1$	0.5164(14)	0.00%	0.01%	0.01%	0.04%	0.01%
$\mathcal{B}_2$	0.5150(12)	0.04%	0.20%	0.45%	0.03%	0.05%
$\mathcal{B}_3$	0.7624(52)	0.32%	0.24%	1.51%	0.06%	0.15%
$\mathcal{B}_4$	0.9107(19)	0.02%	0.16%	0.02%	0.01%	0.02%
$\mathcal{B}_5$	0.7792(79)	0.11%	0.24%	0.38%	0.00%	0.26%

$(\not{q}, \not{q})$	$\sigma(3\,\text{GeV}, 2\,\text{GeV})$	$\sigma(3 \xleftarrow{\Delta=0.5} 2)$	$\sigma(3 \xleftarrow{\Delta=0.33} 2)$	NPR at 3 GeV	rcsb	SUSY←NPR
R_2	−19.53(13)	0.10%	0.35%	0.15%	0.28%	0.03%
R_3	5.818(52)	0.66%	0.12%	0.20%	0.20%	0.15%
R_4	40.99(33)	0.16%	0.06%	0.20%	0.23%	0.02%
R_5	10.490(86)	0.35%	0.30%	0.82%	0.13%	2.25%
$\mathcal{B}_1$	0.5342(15)	0.01%	0.11%	0.00%	0.08%	0.00%
$\mathcal{B}_2$	0.5155(21)	0.02%	0.05%	0.63%	0.19%	0.04%
$\mathcal{B}_3$	0.7649(91)	0.20%	0.16%	1.88%	0.28%	0.01%
$\mathcal{B}_4$	0.9137(33)	0.02%	0.18%	0.19%	0.03%	0.10%
$\mathcal{B}_5$	0.708(15)	0.01%	0.05%	0.10%	0.01%	0.07%

Table 5.7: Bag and ratio parameters at $\mu = 3$ GeV in the RI/SMOM$^{(\gamma_\mu,\gamma_\mu)}$ (*top*) and RI/SMOM$^{(\not{q},\not{q})}$ (*bottom*) schemes in the SUSY basis. Central value comes from performing the chiral-continuum limit fit at $\mu = 2\,\text{GeV}$ and non-perturbative scaling the result to $\mu = 3\,\text{GeV}$ using $\sigma(3\,\text{GeV}, 2\,\text{GeV})$. We also list variations where the continuum step-scaling is obtained in steps, or the data is renormalised directly at 3 GeV. The central value uses Z-factors with chirally vanishing elements removed (masked) from $(P\Lambda)^T$ before the inversion $Z = F((P\Lambda)^T)^{-1}$. We list the percent shift in the result in foregoing this step, labelled residual chiral symmetry breaking (rcsb). We also compare with performing the entire analysis in the NPR basis and then rotating to the SUSY basis.

For our main analysis we extract the bare matrix elements and renormalisation factors in the NPR basis, transform them to the SUSY basis and then perform the various analysis steps. Performing the entire analysis in the NPR basis and converting the final values to the SUSY basis causes a reshuffling of discretisation effects. The corresponding δ_i are presented in the column labelled SUSY $\leftarrow$ NPR in table 5.7.

We take the maximum of these variations as our estimate for the systematic uncertainties due to higher order discretisation effects, labelled "discr" in table 5.9.

Residual chiral symmetry breaking

Domain wall fermions provide a good approximation to chiral symmetry, however a small degree of residual chiral symmetry breaking is present in the data. Chiral symmetry restricts the allowed mixing pattern to be block-diagonal. For our central analysis we impose this, by setting the chirally forbidden elements of Z_{ij} to zero which we refer to as "masking". To test the effect residual chiral symmetry breaking has on our results, we repeat the entire analysis without masking. We find that the deviations are well below the percent level, indicating that our approximation to chiral symmetry is very well controlled. We report the associated systematic uncertainties in tables 5.7–5.9 as "rcsb".

Finite Volume Effects

Finite volume effects (FVEs) could be neglected in our previous studies, but at this level of precision we need to revisit this assumption. We estimate these effects using chiral perturbation theory and note that the finite volume corrections appear with the same pre-factors C_i^Y as the chiral logarithms [73]. The FVEs are given by [220]

$$C_i^Y \frac{m_\pi^2}{(4\pi f_\pi)^2} \frac{12\sqrt{2\pi}\exp\left(-m_\pi L\right)}{(m_\pi L)^{3/2}} \,. \tag{5.41}$$

The leading order FVEs cancel in the ratios R_2 and R_3. Numerically evaluating eqn (5.41) for our ensembles, we find that the largest effect is observed on the M1S ensemble, where the estimate of finite size effects is 1.1 per-mille for the bag parameters and 2.1 per-mille for R_4 and R_5. Noting that this is a sub-leading effect (see table 5.9) and that the FVEs on the ensembles which are most constraining for the fit (C0M, M0M, F1M) are more than a factor three smaller than this, we conclude that FVEs remain negligible at our current level of precision.

scheme		R_2	R_3	R_4	R_5	$\mathcal{B}_1$	$\mathcal{B}_2$	$\mathcal{B}_3$	$\mathcal{B}_4$	$\mathcal{B}_5$
$\overline{\text{MS}} \leftarrow \text{RI/SMOM}^{(\gamma_\mu,\gamma_\mu)}$	central	-18.73	5.781	41.45	10.80	0.5185	0.4759	0.728	0.8862	0.6977
	stat	0.60%	0.69%	0.72%	0.43%	0.28%	0.24%	0.72%	0.21%	1.02%
	chiral	0.21%	0.42%	0.61%	0.46%	0.20%	0.17%	0.29%	0.17%	0.25%
	rcsb	0.10%	0.15%	0.09%	0.03%	0.04%	0.03%	0.06%	0.01%	0.00%
	discr	0.16%	0.53%	0.49%	1.23%	0.01%	0.44%	1.61%	0.16%	0.38%
	total	0.66%	0.98%	1.07%	1.38%	0.35%	0.53%	1.79%	0.32%	1.12%
$\overline{\text{MS}} \leftarrow \text{RI/SMOM}^{(\not{q},\not{q})}$	central	-19.07	6.059	42.43	10.49	0.5295	0.4829	0.764	0.9070	0.6788
	stat	0.68%	0.92%	0.81%	0.83%	0.29%	0.43%	1.24%	0.36%	2.21%
	chiral	0.48%	0.78%	1.25%	1.26%	0.24%	0.27%	0.44%	0.29%	0.51%
	rcsb	0.29%	0.21%	0.23%	0.13%	0.08%	0.19%	0.29%	0.03%	0.01%
	discr	0.34%	0.65%	0.20%	2.30%	0.10%	0.64%	1.92%	0.19%	0.10%
	total	0.95%	1.39%	1.52%	2.75%	0.40%	0.83%	2.34%	0.50%	2.27%

Table 5.8: Central values and combined systematic errors for ratio and bag parameters at $\mu = 3\,\text{GeV}$ in $\overline{\text{MS}}$ after converting from the two RI/SMOM schemes — (γ_μ, γ_μ) and $(\not{q}, \not{q})$, in the SUSY basis. We list the errors arising from statistics, chiral extrapolation, residual chiral symmetry breaking, and discretisation and combine it into total uncertainties.

scheme		R_2	R_3	R_4	R_5	$\mathcal{B}_1$	$\mathcal{B}_2$	$\mathcal{B}_3$	$\mathcal{B}_4$	$\mathcal{B}_5$
RI/SMOM$^{(\gamma_\mu,\gamma_\mu)}$	central	−18.37	5.485	38.60	10.93	0.5164	0.5150	0.762	0.9107	0.7792
	stat	0.59%	0.66%	0.72%	0.44%	0.28%	0.24%	0.69%	0.22%	1.02%
	chiral	0.22%	0.42%	0.59%	0.47%	0.21%	0.17%	0.28%	0.17%	0.24%
	rcsb	0.11%	0.14%	0.09%	0.03%	0.04%	0.03%	0.06%	0.01%	0.00%
	discr	0.17%	0.50%	0.48%	1.22%	0.01%	0.45%	1.51%	0.16%	0.38%
	total	0.66%	0.94%	1.05%	1.38%	0.35%	0.54%	1.68%	0.31%	1.11%
RI/SMOM$^{(\not{q},\not{q})}$	central	−19.53	5.818	40.99	10.49	0.5342	0.5155	0.765	0.9137	0.7078
	stat	0.68%	0.90%	0.81%	0.83%	0.29%	0.42%	1.20%	0.36%	2.19%
	chiral	0.47%	0.77%	1.21%	1.23%	0.24%	0.27%	0.43%	0.28%	0.53%
	rcsb	0.28%	0.20%	0.23%	0.13%	0.08%	0.19%	0.28%	0.03%	0.01%
	discr	0.35%	0.66%	0.20%	2.25%	0.11%	0.63%	1.88%	0.19%	0.10%
	total	0.94%	1.37%	1.48%	2.69%	0.40%	0.83%	2.29%	0.49%	2.25%
$\overline{\text{MS}}$	(γ_μ,γ_μ)	−18.73	5.781	41.45	10.80	0.5185	0.4759	0.728	0.8862	0.6977
	$(\not{q},\not{q})$	−19.07	6.059	42.43	10.49	0.5295	0.4829	0.764	0.9070	0.6788
	central	−18.90	5.920	41.94	10.64	0.5240	0.4794	0.746	0.8966	0.6882
	lattice	0.66%	0.96%	1.06%	1.40%	0.34%	0.52%	1.75%	0.32%	1.14%
	PT	0.91%	2.35%	1.17%	1.47%	1.05%	0.74%	2.40%	1.16%	1.38%
	total	1.12%	2.54%	1.57%	2.03%	1.10%	0.90%	2.97%	1.20%	1.79%

Table 5.9: Central values and combined systematic errors for ratio and bag parameters in the SUSY basis at $\mu = 3\,\text{GeV}$ in the two RI/SMOM schemes — (γ_μ,γ_μ) and $(\not{q},\not{q})$ — as well as in $\overline{\text{MS}}$. For the RI/SMOM schemes we list the errors arising from statistics, chiral extrapolation, residual chiral symmetry breaking and discretisation effects and combine them into total uncertainties. For the $\overline{\text{MS}}$ values we list the separate conversions from (γ_μ,γ_μ) and $(\not{q},\not{q})$. The central values are defined as the average of those two numbers and the perturbative truncation error as half their difference. The lattice error is taken from the (γ_μ,γ_μ) scheme (see table 5.8 for scheme-wise error budget) .

Perturbative matching

The dominant source of uncertainty arises in the conversion of our results to $\overline{\text{MS}}$ where the matching is done in perturbation theory to one-loop. The truncation of the perturbative series leads to an uncertainty. We have defined two intermediate RI/SMOM schemes, differentiated by their projectors and use these to estimate the size of this error. We expect results in $\overline{\text{MS}}$ to be independent of the intermediate renormalisation scheme. We take our central value as the average between the results obtained from the two intermediate schemes and associate a truncation uncertainty of half their difference. For definiteness we assign the relative error from the (γ_μ, γ_μ) scheme to quantify the combined lattice uncertainty in our final results. The estimate of the perturbative truncation uncertainty is quoted as "PT" in the last column of table 5.9.

5.4.3 Self-consistency check

Having determined the R_i and the $\mathcal{B}_i$ parameters we can perform a self-consistency check. Recalling the definitions in eqns (5.6) & (5.9) we consider

$$\frac{N_i \mathcal{B}_i}{R_i} = \frac{8}{3} \frac{(m_s(\mu) + m_d(\mu))^2}{m_K^2} \mathcal{B}_1 \,, \quad i = 2, \cdots, 5 \,. \tag{5.42}$$

The right hand side is independent of i and hence the ratios from each operator should give compatible results. The black data points in figure 5.15 display this comparison for the results at $\mu = 3\,\text{GeV}$ in RI/SMOM$^{(\gamma_\mu,\gamma_\mu)}$ (top) and $\overline{\text{MS}}$ (bottom). The R_i and $\mathcal{B}_i$ have notably different — and sometimes steep — approaches to the continuum limit. The good agreement between the different results gives us confidence that uncertainties in general and discretisation effects in particular have been well estimated.

We compare our $\overline{\text{MS}}$ results to the value obtained by evaluating the right hand side using external inputs. We use the isospin-symmetrised kaon mass $m_K = (m_{K^0} + m_{K^\pm})/2 =$

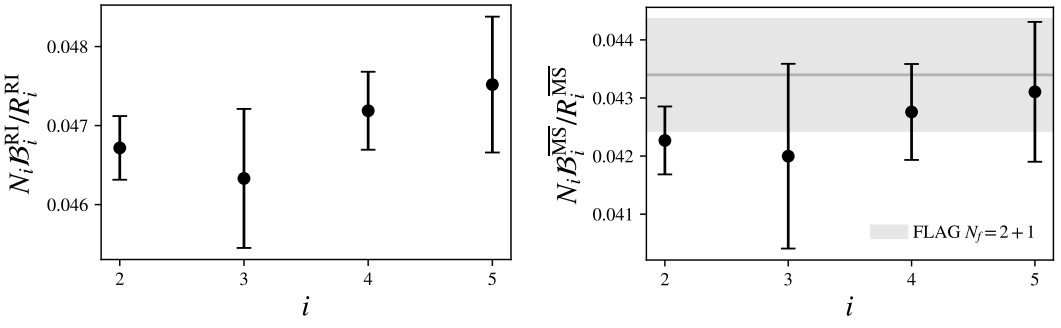

Figure 5.15: Self-consistency check by forming the ratio eqn (5.42) at $\mu = 3\,\text{GeV}$. The data points are from our calculations in the RI/SMOM$^{(\gamma_\mu,\gamma_\mu)}$ scheme (top) and in the $\overline{\text{MS}}$ scheme (bottom). For the $\overline{\text{MS}}$ plot we show the expected value using FLAG inputs as the grey horizontal band.

496.144(9) MeV [6]. We take FLAG [221] values for the $N_f = 2+1+1$ [5,222–227] and $N_f = 2+1$ [3,77,77,81,83,228–234] isospin-symmetrised light quark mass and strange quark mass in $\overline{\text{MS}}$ at $\mu = 2\,\text{GeV}$, together with $\hat{B}_K$, the renormalisation group invariant (RGI) value for $\mathcal{B}_1$,

$$\begin{aligned} N_f = 2{+}1{+}1: &\quad m_{ud} = 3.410(43)\,\text{MeV} \quad m_s = 93.44(68)\,\text{MeV} \quad \hat{B}_K = 0.717(24)\ , \\ N_f = 2{+}1: &\quad m_{ud} = 3.364(41)\,\text{MeV} \quad m_s = 92.03(88)\,\text{MeV} \quad \hat{B}_K = 0.7625(97)\,. \end{aligned} \tag{5.43}$$

and run them to $\mu = 3\,\text{GeV}$, allowing us to construct the right hand side of eqn (5.42) (the conversion of the four-quark operators at a given scale to RGI operators is shown in section 4.5). This is shown as the grey band in the lower plot in figure 5.15.

Furthermore, we can use the constant value in both the RI/SMOM and $\overline{\text{MS}}$ schemes, combining it with our value for $\mathcal{B}_1$, to predict the sum of the quark masses (see also the discussion in [74]). From our result for $i = 2$ we find:

$$\begin{aligned} (m_s + m_{ud})^{\text{RI}}(3\,\text{GeV}) &= 91.38(41)\,\text{MeV}, \\ (m_s + m_{ud})^{\overline{\text{MS}}}(3\,\text{GeV}) &= 86.29(79)\,\text{MeV}. \end{aligned} \tag{5.44}$$

We compare this to the corresponding FLAG values

$$\begin{aligned} N_f = 2{+}1{+}1: (m_s + m_{ud})^{\overline{\text{MS}}}(3\,\text{GeV}) &= 88.18(63)\,\text{MeV}, \\ N_f = 2{+}1: (m_s + m_{ud})^{\overline{\text{MS}}}(3\,\text{GeV}) &= 86.34(79)\,\text{MeV}. \end{aligned} \tag{5.45}$$

5.4.4 Comparison to literature

Our final results in the $\overline{\text{MS}}$ scheme at 3 GeV, where the first error is the RI/SMOM error and the second is the uncertainty from the matching to $\overline{\text{MS}}$, are:

$$\begin{aligned} \mathcal{B}_1^{\overline{\text{MS}}} &= \ \ 0.5240(17)(54) \\ \mathcal{B}_2^{\overline{\text{MS}}} &= \ \ 0.4794(25)(35) \\ \mathcal{B}_3^{\overline{\text{MS}}} &= \ \ 0.746(13)(17) \\ \mathcal{B}_4^{\overline{\text{MS}}} &= \ \ 0.897(02)(10) \\ \mathcal{B}_5^{\overline{\text{MS}}} &= \ \ 0.6882(78)(94) \\ R_2^{\overline{\text{MS}}} &= -18.90(12)(17) \\ R_3^{\overline{\text{MS}}} &= \ \ 5.92(05)(13) \\ R_4^{\overline{\text{MS}}} &= \ \ 41.94(44)(46) \\ R_5^{\overline{\text{MS}}} &= \ \ 10.64(14)(15)\,. \end{aligned} \tag{5.46}$$

	ETM12 [4]	ETM15 [5]	RBC-UKQCD12 [211]	SWME15 [3]	RBC-UKQCD16 [2]		THIS WORK
N_f	2	2+1+1	2+1	2+1	2+1	2+1	2+1
scheme	RI/MOM	RI/MOM	RI/MOM	1 loop	RI/SMOM	RI/MOM	RI/SMOM
$\mathcal{B}_2$	0.47(2)	0.46(3)(1)	0.43(5)	0.525(1)(23)	0.488(7)(17)	0.417(6)(2)	0.4794(25)(35)
$\mathcal{B}_3$	0.78(4)	0.79(5)(1)	0.75(9)	0.773(6)(35)	0.743(14)(65)	0.655(12)(44)	0.746(13)(17)
$\mathcal{B}_4$	0.76(3)	0.78(4)(3)	0.69(7)	0.981(3)(62)	0.920(12)(16)	0.745(9)(28)	0.897(02)(10)
$\mathcal{B}_5$	0.58(3)	0.49(4)(1)	0.47(6)	0.751(7)(68)	0.707(8)(44)	0.555(6)(53)	0.6882(78)(94)

Table 5.10: Results from calculations of BSM bag parameters in $\overline{\text{MS}}(\mu = 3\,\text{GeV})$ from RBC-UKQCD, SWME and ETM show tensions for $\mathcal{B}_4$ and $\mathcal{B}_5$. The results obtained by ETM, which were renormalised via RI/MOM, agree with RBC-UKQCD's results obtained via RI/MOM. The SWME results, obtained via a 1 loop intermediate scheme agree with RBC-UKQCD's results obtained via RI/SMOM, for both γ_μ and $\not{q}$ [8]. This suggests tensions arise from the implementation of intermediate schemes, in particular caused by RI/MOM exhibiting exceptional infrared behaviour which is absent in RI/SMOM. All results are shown in the SUSY basis.

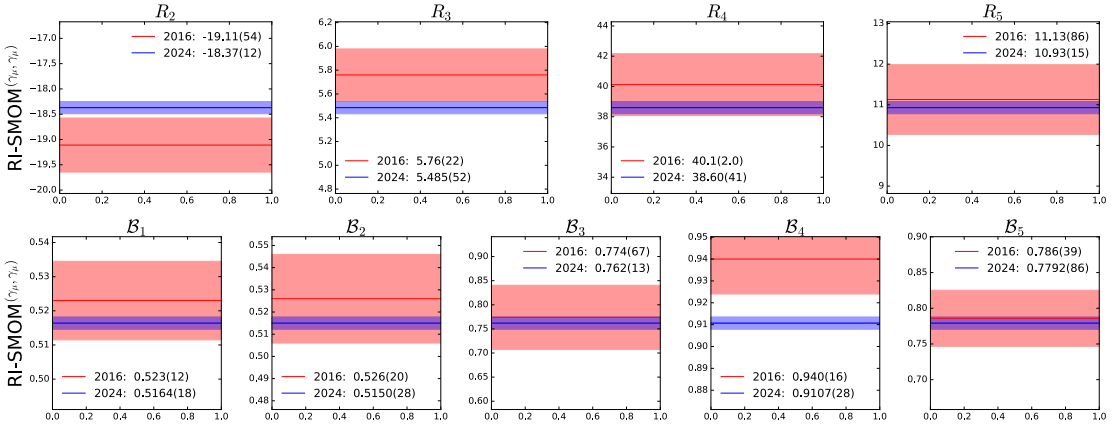

Figure 5.16: Comparison of the R_i and $\mathcal{B}_i$ in RI/SMOM$^{(\gamma_\mu,\gamma_\mu)}$ at $\mu = 3\,\text{GeV}$ to the previous RBC-UKQCD results [2].

In figure 5.16 we compare our results in the RI/SMOM scheme at $\mu = 3\,\text{GeV}$ to the previous RBC-UKQCD determination [2]. The addition of two physical pion mass ensembles and a third lattice spacing helps to constrain the chiral and continuum limit extrapolations respectively, yielding a significantly reduced uncertainty. Given the significantly different data set, we find good agreement between our previous result and this work.

Figure 5.17 shows a comparison of our BSM bag parameters with previous lattice results available in the literature. Early studies of BSM kaon mixing [74, 75, 89] were performed in the quenched approximation. They were followed by dynamical simulations with N_f quark flavours by several collaborations: RBC-UKQCD ($N_f = 2+1$) [2, 211], SWME ($N_f = 2+1$) [3, 235, 236], and ETM ($N_f = 2$) [4] and ($N_f = 2+1+1$) [5]. In contrast to results for the SM operator, there are tensions between the different collaborations' results for some of the BSM operators, as shown in table 5.10 and summarised in the FLAG report [221]. We note that a similar discrepancy is observed in neutral $B_{(s)}$-mixing [221, 237].

In [2, 72], it was proposed that the source of these tensions was the choice of the intermediate renormalisation scheme. Specifically, it was proposed that the symmetric momentum subtraction scheme RI/SMOM (which has non-exceptional kinematics) advocated by RBC-UKQCD has several beneficial features compared to the previously used RI/MOM (which has exceptional kinematics). This is likely due to the exceptional (divergent in the massless limit), infrared non-perturbative "pion pole" behaviour in the RI/MOM vertex functions, which must be correctly modelled and subtracted, while the mass is simultaneously taken to zero to establish a mass independent scheme. This behaviour is absent in the RI/SMOM scheme, giving greater theoretical control as it avoids the possibility of imperfect modelling of the non-perturbative pole systematically affecting the result. The results obtained from two RI/SMOM schemes are in agreement with each other and with the perturbatively renormalised results from the SWME

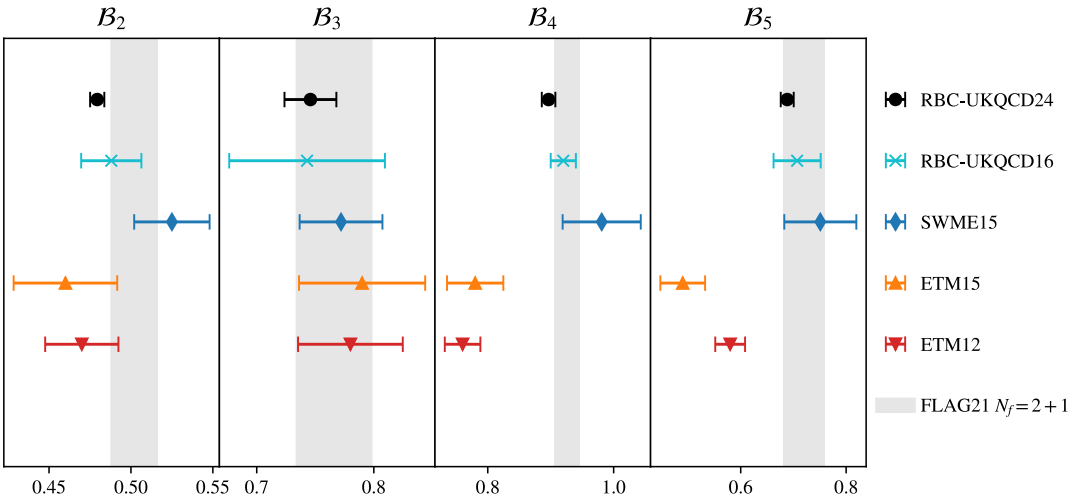

Figure 5.17: Comparison of our results for the BSM bag parameters in $\overline{\text{MS}}$ at 3 GeV with previous results (RBC-UKQCD16 [2], SWME15 [3], ETM12 [4], ETM15 [5]).

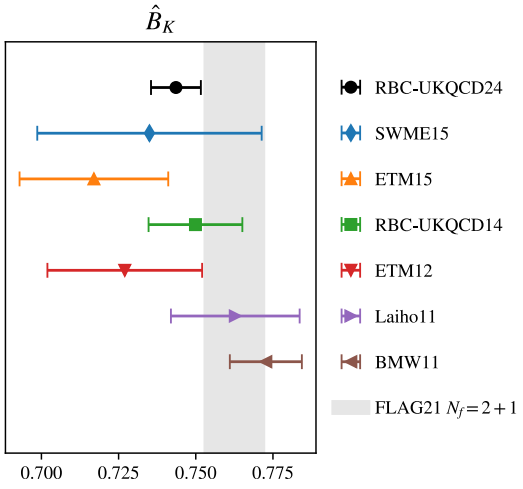

Figure 5.18: Comparison of our results for the RGI SM bag parameter $\hat{B}_K$ with previous results.

collaboration [3, 235, 236], while the calculation with RI/MOM agreed with previous RBC-UKQCD [211] and ETM [4, 5] results which also used RI/MOM. Values for $\hat{B}_K$ and the BSM $\mathcal{B}_i$ estimated in a large-N_c (number of colours) expansion may be found in [238, 239].

Our value for the SM bag parameter $B_K = \mathcal{B}_1$ shows good consistency with our collaboration's most-recent previous result, $B_K^{\overline{\text{MS}}\leftarrow\text{SMOM}^{(q,q)}}(3\,\text{GeV}) = 0.530(11)$ [77]. A different fitting procedure in which the physical point data was over-weighted was employed in Ref. [77] and, while it also included the coarse and medium ensembles included in this work, it included a different third lattice spacing with a heavier pion mass. Further, it combined additional coarser ensembles with a different gauge action in a global fit, and reweighting factors to adjust the sea strange mass to the physical values. In

this work we instead leave the sea-strange mass dependence as a fit parameter. Given the differences in the underlying correlator data and the various fitting procedures, the consistency of the results is reassuring.

We convert our result above for B_K at scale $\mu = 3\,\text{GeV}$ to the RGI value

$$\hat{B}_K = 0.7436(82). \tag{5.47}$$

A comparison of our $\hat{B}_K$ with previous lattice results [2,3,76–86] is shown in figure 5.18, where good agreement is seen.

5.5 Conclusions and outlook

In the study presented in this chapter we have performed the first calculation of beyond the standard model (BSM) neutral kaon mixing matrix elements with data directly simulated with physical quark masses in the isospin symmetric limit of pure $N_f = 2 + 1$ QCD. This paper improves upon the most recent RBC/UKQCD BSM kaon mixing calculation [2, 72] by adding a third lattice spacing and including two data points at the physical light quark mass. The status of this work has been previously reported in [240, 241] and our final results are now published in [9]. Using an increased level of volume averaging, with many $\mathbb{Z}_2$ wall sources on each configuration, we have been able to obtain a much greater reduction in statistical errors compared to our previous publications, even with physical quark masses.

All sources of systematic uncertainties have been estimated. For each of the bag parameters and ratios of matrix elements a simultaneous fit has been performed to the mass and lattice spacing dependence. Direct simulation at physical quark masses leaves the mass dependence of this extrapolation a negligible systematic. With the inclusion of a third lattice spacing we can test the validity of a^2 scaling and find that in the range covered by our data it works well. We assess discretisation uncertainties by considering different renormalisation points and/or different ways of obtaining the non-perturbative scaling matrix. The self-consistency check of comparing ratios $N_i\mathcal{B}_i/R_i$ increases our confidence that the discretisation effects have been well estimated, since those ratios approach the continuum limit in notably different ways.

The dominant systematic error comes from perturbative matching from the RI/SMOM scheme to $\overline{\text{MS}}$ at the 3 GeV renormalisation point. This key error was assessed by comparing two different intermediate RI/SMOM schemes after continuum extrapolation. If the matching were non-perturbative the intermediate scheme would be irrelevant, but with truncated, perturbative matching the results differ due to the truncation error. The differences are of the order 1-3%.

The prospects for further improvements of this calculation are as follows: we believe that the RI/SMOM scheme results are sufficiently precise that there is no purpose in further reduction in the error within the isospin symmetric pure QCD approximation. Instead, strong isospin breaking and QED must be addressed if greater accuracy is required. For our final results a significant source of error stems from the perturbative matching to $\overline{\text{MS}}$. This could be addressed by raising the matching scale at which we convert operators. The convergence is logarithmic in the energy scale and this will not lead to a rapid improvement in the calculation. It would be better to accompany this with a two-loop calculation of the scheme change factors presented in [72]. The quadratic suppression in α_s would be more beneficial than an increase in the renormalisation scale towards the b-threshold.

Consequently, we believe our results are a robust determination that in the short term may only be further improved with an additional loop in the perturbative matching, or by the inclusion of isospin breaking effects.

Finally, it is worth noting that a similar analysis performed in the pion sector allows to one to extract the matrix elements which could dominate the short-distance contribution to neutrino-less double beta decays, see for example [242, 243]. In particular, the renormalisation factors computed here could be employed for such a study.

5.6 Towards D, B and B_s-meson mixing

The analysis framework used in our study of neutral kaon mixing can be extended to the study of the mixing of D, B and B_s mesons, and there is ongoing work within the RBC-UKQCD collaboration for computing the bag parameters in these systems, in particular for B and B_s meson mixing [244,245]. This will enable use to determine, from first principles, several quantities that provide stringent tests on the SM or constrain BSM physics, as discussed in section 2.5.6.

The non-perturbative renormalisation procedure for computing the observables in these systems is identical to that in neutral kaon mixing but applied instead to $\Delta\mathcal{C} = 2$ and $\Delta\mathcal{B} = 2$ operators. These computations are based on $N_f = 2 + 1$ DWF ensembles generated by the RBC-UKQCD and JLQCD [246] collaborations; their main properties are listed in table 5.11. These ensembles feature pion masses from $m_\pi = 430\,\text{Mev}$ down to the physical range of $m_\pi = 139\,\text{MeV}$ and six values of lattice spacing ranging from $a^{-1} = 1.7\,\text{GeV}$ up to $a^{-1} = 4.5\,\text{GeV}$.

The notable feature of this dataset compared to the one used so far in this chapter is that the light and strange quarks are simulated using the same DWF action as used in the study of neutral kaon mixing, while the heavy quarks are simulated using stout-smeared [247] Möbius DWF.

name	X/a	T/a	a^{-1}[GeV]	m_π[MeV]	$m_\pi L$	$N_{\text{conf}} \times N_{\text{src}}$
C0M	48	96	1.730(4)	139	3.9	90×48
C1S	24	64	1.785(5)	340	4.6	100×32
C2S	24	64	1.785(5)	431	5.8	99×32
M0M	64	128	2.359(7)	139	3.8	82×64
M1S	32	64	2.383(9)	304	4.1	83×32
M2S	32	64	2.383(9)	361	4.8	76×32
M3S	32	64	2.383(9)	411	5.5	80×32
KEKC1L	48	128	2.453(4)	226	4.4	100×24
KEKC1S	32	64	2.453(4)	230	3.0	100×16
KEKC2a	32	64	2.453(4)	309	4.0	100×16
KEKC2b	32	64	2.453(4)	310	4.0	100×16
F1M	48	96	2.708(10)	232	4.0	72×48
KEKM1a	48	96	3.610(9)	300	3.9	50×24
KEKM1b	48	96	3.610(9)	297	3.9	50×24
KEKF1	64	128	4.496(9)	284	4.0	50×32

Table 5.11: Summary of the main parameters of the RBC-UKQCD and JLQCD ensembles used for the ongoing study of D, B, and B_s-meson mixing.

The relevant renormalisation factors have been computed as part of this PhD project and the numerical values are reported in tables B.13 - B.27 in appendix B.

It is important to note that the non-perturbative renormalisation procedure defined by the RI/SMOM scheme prescribes renormalisation constants in the massless limit. While this is an acceptable approximation in the study of neutral kaon mixing, the NPR process fails to account for heavy quark discretisation effects when used in heavy meson systems such as $B_s - \overline{B}_s$ mixing. In the next chapter we will discuss an extension to the RI/SMOM scheme with the aim of addressing cutoff effects introduced by the use of heavy quarks on the lattice.

Chapter 6

Charm quark mass using massive NPR

The charm and bottom quarks are distinguished from the up, down and strange quarks by their much heavier masses, with $m_q \gg \Lambda_{\rm QCD}$, and are therefore known as heavy quarks. The study of heavy quark observables, such as the spectra of the heavy hadrons, provides a testing ground for QCD in the non-perturbative regime. The weak decays of heavy hadrons, for example, are critical to the determination of the elements of the Cabibbo-Kobayashi-Maskawa (CKM) matrix.

At present there is a wealth of input from heavy flavour experiments such as the LHCb at CERN and Belle II at KEK, as well as older data from BaBar, Belle, CLEO and BESIII. Given the increase in experimental data, there is a need for improving precision of theoretical inputs in order to extract Standard Model (SM) parameters such as the CKM matrix elements. Lattice QCD provides an *ab initio* method for computing the necessary inputs from heavy quark observables.

However, in order to make reliable predictions for heavy quark observables on the lattice one must demonstrate that physical results are independent of lattice discretisation effects. This condition is met when the relevant distance scales of the calculation are much larger than the lattice spacing a. In the case of heavy quarks, the relevant scale is associated with the inverse of their mass $1/m_q$, and present day lattices (with $a \sim 0.1$ fm) typically fail to meet the criterion $am_q \ll 1$ (with $am_b \approx 2.5$ and $am_c \approx 0.75$).

Renormalised quantities on the lattice can be related to their bare and continuum counterparts as

$$\begin{aligned} \langle \mathcal{O} \rangle^S_{\rm lat}(am_q, a\mu) &= Z^S_{\mathcal{O}}(a\mu) \langle \mathcal{O} \rangle^{\rm bare}_{\rm lat}(am_q) \\ &= \langle \mathcal{O} \rangle^S_{\rm cont} \left(\frac{m_q}{\mu} \right) \left[1 + \hat{\delta}(am_q, a\mu) \right], \end{aligned} \tag{6.1}$$

where $Z^S_{\mathcal{O}}(a\mu)$ is a multiplicative renormalisation constant (or matrix when operators mix under renormalisation) in some scheme S at some renormalisation scale μ, and $\hat{\delta}$ denotes lattice artefacts. Non-perturbative renormalisation (NPR) schemes, such as the RI/SMOM scheme [199] introduced in chapter 4, often define renormalisation constants in the limit of vanishing quark masses, that is, the chiral limit of QCD. The renormalisation conditions are chosen such that the renormalised vector and axial current correlators satisfy the Ward identities (WIs) derived using the symmetries of the theory. In order to recover physics with subdominant discretisation effects in the continuum limit one demands that $\lim_{a\to 0} \hat{\delta}(am_q, a\mu) \lesssim O(a^2 m_q^2)$, which is satisfied when the scales are well resolved as $m_q \ll \mu \ll a^{-1}$. As we know in case of heavy quarks on the lattice this hierarchy is violated with $am_q \not\ll 1$ and $m_q \sim \mu$, therefore the use of these *massless* NPR schemes for heavy quark observables neglects am_q-sized discretisation effects and leads to violations of WIs.

An alternative to the RI/SMOM scheme was proposed in [248], prescribing renormalisation conditions away from the chiral limit such that the desirable properties of the massless scheme are preserved, in particular the WIs are satisfied at finite quark masses. This *massive* scheme, known as RI/mSMOM, provides a prescription for the non-perturbative renormalisation of fermion bilinear operators, in particular for scalar and pseudoscalar densities as well as vector and axial currents, computed at some finite value of the renormalised mass. This scheme can therefore be expected to reabsorb some of the am_q-sized lattice artefacts in the continuum limit for heavy quark observables.

In this chapter, we report the details of a pilot numerical implementation of the RI/mSMOM scheme in the study of the renormalised charm quark mass on the lattice. The status of this work has previously been reported in [11] and the final results are presented in [10].

6.1 RI/mSMOM

In this section we summarise the main ideas of the massive momentum-subtraction scheme (originally detailed in [248]). Note that the definitions of Green's functions and propagators as well as the use of symmetric kinematics in this scheme match those of the RI/SMOM scheme, as described in section 4.1; they are repeated in this section in order to make the discussion self-contained. Note also that to match the numerical simulations we work with Euclidean quantities.

Renormalisation conditions for quark bilinear operators are usually expressed in terms of Green's functions of quark bilinear operators between two external off-shell quark lines in a fixed (Landau) gauge

$$\mathcal{O}^F_\Gamma = \overline{\psi}_f \Gamma \tau^F \psi_{f'}, \tag{6.2}$$

$$G^F_\Gamma(p_2, p_1) = \langle \psi_f(p_2) \mathcal{O}^F_\Gamma(q) \overline{\psi}_{f'}(p_1) \rangle, \tag{6.3}$$

where ψ_f and $\psi_{f'}$ are quark fields of flavours f and f' respectively, and $q = p_1 - p_2$ (see figure 4.1 for conventions used). τ^F is some generator of an $SU(N_f)$ flavour symmetry, which generates a non-singlet flavour transformation, with F denoting the adjoint index. Γ indicates the Dirac structure of the operator; we are interested in scalar, 'S' ($\Gamma = \mathbb{1}$), pseudoscalar, 'P' ($\Gamma = i\gamma_5$), vector, 'V' ($\Gamma = \gamma^\mu$), and axial vector, 'A' ($\Gamma = \gamma^\mu\gamma_5$) bilinears. The quark propagator is defined as

$$S_f(p) = \langle \psi_f(p)\overline{\psi}_f(p)\rangle = \frac{1}{i\not{p} + m_f + \Sigma(p)}, \tag{6.4}$$

and the amputated Green's function is obtained by amputating each leg with the inverse quark propagator of the corresponding flavour

$$\Lambda^F_\Gamma(p_1, p_2) = S_f^{-1}(p_2) G^F_\Gamma(p_2, p_1) S_{f'}^{-1}(p_1). \tag{6.5}$$

Renormalised (subscript 'R') and bare quantities (no subscript) are related via renormalisation constants Z as

$$\begin{aligned} \psi_R = Z_q^{1/2}\psi, \quad m_R = Z_m m, \quad \mathcal{O}_{\Gamma,R} = Z_\Gamma \mathcal{O}_\Gamma, \\ \implies S_R(p) = Z_q S(p), \quad \Lambda_{\Gamma,R}(p_1,p_2) = \frac{Z_\Gamma}{Z_q}\Lambda_\Gamma(p_1,p_2). \end{aligned} \tag{6.6}$$

Recall from section 4.1 that the Z-factors in the RI/SMOM scheme are defined by imposing the condition (in the chiral limit of QCD)

$$\begin{aligned} &\lim_{m_R\to 0} \hat{P}^F_\Gamma \left[\Lambda^F_{\Gamma,R}(a,p_1,p_2)\right]_{\text{sym}} = F_\Gamma \equiv \hat{P}^F_\Gamma \left[\Lambda^{F,(0)}_\Gamma(p_1,p_2)\right]_{\text{sym}}, \\ \implies &\lim_{m_R\to 0} \frac{Z_\Gamma}{Z_q}(a,\mu)\hat{P}^F_\Gamma \left[\Lambda^F_\Gamma(a,p_1,p_2)\right]_{\text{sym}} = F_\Gamma\,, \end{aligned} \tag{6.7}$$

where $\Lambda^{(0)}_\Gamma$ is the tree level amputated Green's function, $\hat{P}_\Gamma$ is a projector, and F_Γ is the corresponding tree level value. Note that the adjoint flavour index F is suppressed for the remainder of this discussion as we assume that the bilinears are all flavour non-singlet. 'sym' denotes the symmetric momentum configuration characteristic to the RI/SMOM scheme used from setting the renormalisation scale

$$p_1^2 = p_2^2 = q^2 \equiv \mu^2. \tag{6.8}$$

Since the renormalisation conditions are imposed in the limit of renormalised mass $m_R \to 0$, the renormalisation constants are therefore by contruction mass-independent and functions of the renormalisation scale μ only

$$Z^{\text{SMOM}} = Z^{\text{SMOM}}(a\mu). \tag{6.9}$$

In contrast, the RI/mSMOM renormalisation conditions are imposed at finite renormalised masses

$$\lim_{m_R\to\overline{m}_R}\frac{Z_\Gamma}{Z_q}(a,\mu)\tilde{P}_\Gamma\left[\Lambda_\Gamma(a,p_1,p_2)\right]_{\text{sym}}=\tilde{F}_\Gamma, \tag{6.10}$$

where $\tilde{P}_\Gamma$ and $\tilde{F}_\Gamma$ are the projectors and tree level values in the RI/mSMOM scheme given below explicitly:

$$Z_m: \quad \lim_{m_R\to\overline{m}_R}\frac{1}{m_R}\left\{\text{Tr}\left[S_R(p)^{-1}\right]_{p^2=\mu^2}+\frac{1}{2}\,\text{Tr}\left[\left(iq\cdot\Lambda_{\text{A},R}\right)\gamma_5\right]_{\text{sym}}\right\}=12, \tag{6.11}$$

$$Z_P: \quad \lim_{m_R\to\overline{m}_R}\text{Tr}\left[\Lambda_{\text{P},R}\gamma_5\right]_{\text{sym}}=12i, \tag{6.12}$$

$$Z_S: \quad \lim_{m_R\to\overline{m}_R}\text{Tr}\left[\Lambda_{\text{S},R}\right]_{\text{sym}}+\frac{2}{q^2}\,\text{Tr}\left[2m_R\Lambda_{P,R}\gamma_5\not{q}\right]=12, \tag{6.13}$$

$$Z_V: \quad \lim_{m_R\to\overline{m}_R}\frac{1}{q^2}\,\text{Tr}\left[(q\cdot\Lambda_{\text{V},R})\not{q}\right]_{\text{sym}}=12, \tag{6.14}$$

$$Z_A: \quad \lim_{m_R\to\overline{m}_R}\frac{1}{q^2}\,\text{Tr}\left[(q\cdot\Lambda_{\text{A},R}+2m_R\Lambda_{P,R})\gamma_5\not{q}\right]_{\text{sym}}=12, \tag{6.15}$$

$$Z_q: \quad \lim_{m_R\to\overline{m}_R}\frac{1}{p^2}\,\text{Tr}\left[-iS_R(p)^{-1}\not{p}\right]_{\text{sym}}=12. \tag{6.16}$$

Note that these renormalisation conditions are identical to those in the "$\not{q}$" variation of the RI/SMOM scheme for bilinear operators, except for the additional mass terms in eqn (6.13) and eqn (6.15).

The renormalisation constants in this mass-dependent scheme are now functions of the renormalisation scale μ as well as the bare mass (corresponding to the finite renormalised mass $\overline{m}_R$) at which they are evaluated

$$Z^{\text{mSMOM}}=Z^{\text{mSMOM}}(a\mu,a\overline{m}), \tag{6.17}$$

$$\text{with}\quad \overline{m}_R=\lim_{a\to0}Z_m^{\text{mSMOM}}(a\mu,a\overline{m})\,\overline{m}. \tag{6.18}$$

The RI/mSMOM scale $\overline{m}_R$

In the massive scheme, the renormalisation conditions are imposed at some arbitrary but finite renormalised mass scale $\overline{m}_R$. One could consider varying $\overline{m}_R$ in order to determine a value where the continuum extrapolation of a lattice observable of interest has mild discretisation errors. The cutoff effects in different observables may need to be treated with different values of $\overline{m}_R$. It is therefore useful to view this scale as a *tunable* parameter. Note however that each choice of $\overline{m}_R$, strictly speaking, corresponds to a different RI/mSMOM scheme, therefore observables renormalised using different values of the renormalised mass need to be converted to some common scheme (in the continuum limit) before they can be compared.

These Z-factors inherit the properties of those in the RI/SMOM (and $\overline{\text{MS}}$) scheme such that in the continuum limit

$$Z_A = Z_V = 1, \quad Z_S = Z_P = 1/Z_m, \tag{6.19}$$

and the renormalised quantities satisfy the vector and axial WIs at finite mass

$$q_\mu \Lambda^\mu_{V,R}(p_1, p_2) = iS^{-1}_{f,R}(p_2) - iS^{-1}_{f',R}(p_1), \tag{6.20}$$

$$q_\mu \Lambda^\mu_{A,R}(p_1, p_2) = -2m_R \Lambda_{P,R}(p_1, p_2) + i\gamma_5 S^{-1}_{f',R}(p_1) + S^{-1}_{f,R}(p_2) i\gamma_5. \tag{6.21}$$

6.2 Charm quark mass

In this project, we carry out a first numerical implementation of the RI/mSMOM scheme by studying the renormalised charm quark mass which is defined as

$$m^{\text{mSMOM}}_{c,R}(\mu, \overline{m}_R) = \lim_{a\to 0} Z^{\text{mSMOM}}_m(a\mu, a\overline{m})\, m_c, \tag{6.22}$$

with the goal of absorbing discretisation errors in the continuum extrapolation. This can be quantified by comparing to the same extrapolation using the massless scheme. We can then match to the $\overline{\text{MS}}$ scheme using continuum perturbation theory (which removes the $\overline{m}_R$-dependence) in order to compare our results with those in the literature at the same scale μ

$$m^{\overline{\text{MS}}}_{c,R}(\mu) = R^{\overline{\text{MS}}\leftarrow\text{mSMOM}}_m \left(\frac{\overline{m}_R}{\mu}\right) m^{\text{mSMOM}}_{c,R}(\mu, \overline{m}_R). \tag{6.23}$$

6.2.1 Ingredients and simulation details

For the numerical simulation, we use six RBC/UKQCD ensembles [8, 77, 84, 105] with Iwasaki gauge action (section 3.1.1) and domain wall fermion action (section 3.1.4).

ens	X/a	T/a	a^{-1}[GeV]	M_π[MeV]	am_l	am_s
C1M	24	64	1.7295(38)	276	0.005	0.0362
C1S	24	64	1.7848(50)	340	0.005	0.04
M0M	64	128	2.3586(70)	139	0.000678	0.02661
M1M	32	64	2.3586(70)	286	0.004	0.02661
M1S	32	64	2.3833(86)	304	0.004	0.03
F1M	48	96	2.708(10)	232	0.002144	0.02144
F1S	48	96	2.785(11)	267	0.002144	0.02144

Table 6.1: Summary of the main parameters of the ensembles used in this work. The first letters – C, M or F – stand for coarse, medium and fine, respectively and the last letters – M or S –stand for Möbius and Shamir kernels, respectively. Note that the ensemble M0M is not used in the main analysis.

ens	am_{input}
C1M	0.05, 0.1, 0.15, 0.2, 0.3
C1S	0.05, 0.1, 0.15, 0.2, 0.3, 0.33
M1M	0.05, 0.1, 0.15, 0.225, 0.3, 0.32, 0.34
M1S	0.05, 0.1, 0.15, 0.225, 0.3, 0.32, 0.34, 0.36, 0.375
F1M	0.033, 0.066, 0.099, 0.132, 0.198, 0.264, 0.33, 0.36
F1S	0.033, 0.066, 0.099, 0.132, 0.198, 0.264, 0.33, 0.36, 0.396

Table 6.2: (Heavy) input quark masses am_{input} that were simulated in addition to am_l, $2am_l$, $am_s/2$ and am_s.

These are $N_f = 2 + 1$ gauge ensembles with dynamical up, down and strange quarks. There are three lattice spacings labelled as 'coarse' (C), 'medium' (M) and 'fine' (F), each with either Shamir or Möbius domain-wall kernels (see eqns (3.50) & (3.51)) denoted by last letter 'S' or 'M'. The parameters of these kernels are chosen such that a combined continuum limit with all six ensembles in possible [77]. All six ensembles are simulated at unphysical pion masses; in order to investigate the pion mass dependence of our results we also use data from the physical pion mass ensemble M0M which differs from M1M only in pion mass and volume. The main properties of these seven ensembles are listed in table 6.1. Large parts of the data used in this project were generated using the Grid and Hadrons framework [215–217].

In order to compute the renormalised charm quark mass in the RI/mSMOM scheme as given in eqn (6.22), we need the following ingredients:

1. bare quark masses: on each lattice, we compute the value of the residual mass am_{res} using the asymptotic behaviour of the ratio of the mid-point current (J_{5q}) over the pseudoscalar density (J_5), as defined in eqn (3.47) over a range of input masses am_{input}. This procedure is shown in figures 6.1a and 6.1b using the M1M

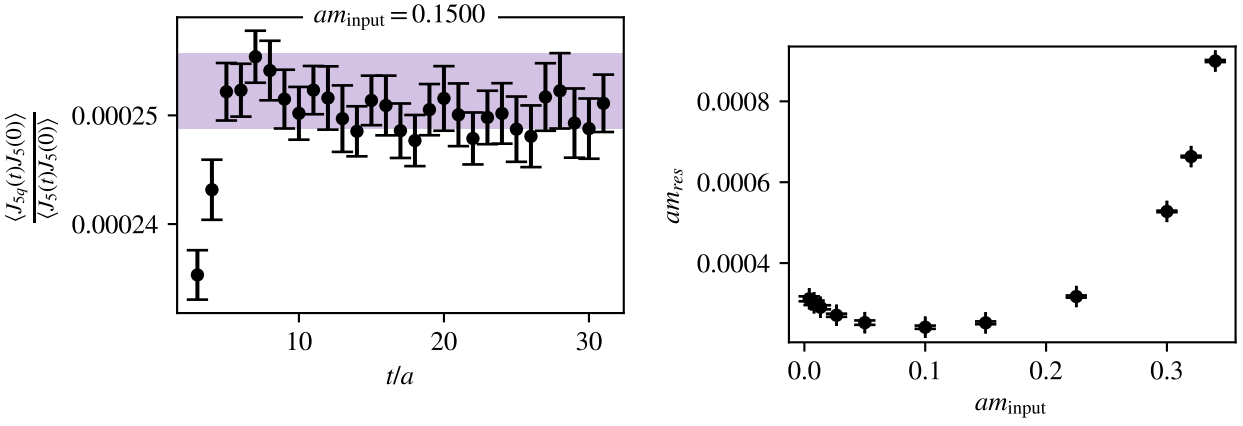

(a) am_{res} derived from the ratio of mid-point current over pseudoscalar density (see eqn (3.47)).

(b) am_{res} measurements over a range of input bare heavy quark masses.

Figure 6.1: am_{res} measurements on the M1M ensemble.

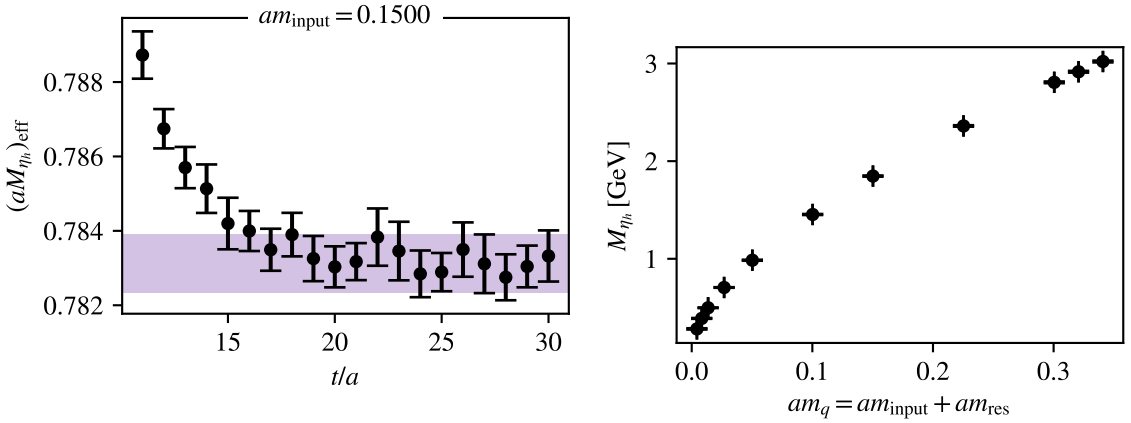

(a) aM_{η_h} derived from the effective mass of the pseudoscalar two-point function (see eqn (3.89)).

(b) M_{η_h} measurements over a range of input bare heavy quark masses.

Figure 6.2: M_{η_h} measurements on the M1M ensemble.

ensemble as an example. The corresponding bare quark masses in lattice units are defined as

$$am_q = am_{\text{input}} + am_{\text{res}}, \tag{6.24}$$

where the input masses range from am_l up to the heaviest values that can be accommodated on the lattice given its DWF parameters. The values of chosen input masses for each ensemble is listed in table 6.2.

2. the bare charm mass m_c: on each lattice, we compute the quark-connected two-point function of the flavour-diagonal pseudoscalar meson interpolator[1] denoted as the η_h meson. Note that we use a mild Jacobi smearing (see eqn (3.80)) to improve the overlap with the ground state for heavy masses. From the ground state of the two-point function we extract the meson mass M_{η_h} in physical units over a range of bare quark masses (in lattice units) am_q (the coverage of η_h masses over the available range of bare quark mass m_q over all six ensembles is shown in figure 6.5). This procedure in shown in figures 6.2a and 6.2b once again using the M1M ensemble as an example. The bare charm mass can then be computed by interpolating to the value of the bare mass corresponding to the physical value of the η_c meson mass, $M_{\eta_c}^{\text{PDG}} = 2.9839(4)\,\text{GeV}$ [6], as

$$m_c = (am_c) \cdot a^{-1}, \tag{6.25}$$

$$am_c = am_q(M_{\eta_h} = M_{\eta_c}^{\text{PDG}}). \tag{6.26}$$

3. the bare mass $\overline{m}$: following the same procedure as the one used to determine am_c, we can compute the bare mass corresponding to the RI/mSMOM scheme

[1] The contribution from quark-disconnected pieces to the mass of the η_c meson (since we are ultimately interested in the charm quark mass) has been estimated to be negligibly small [249].

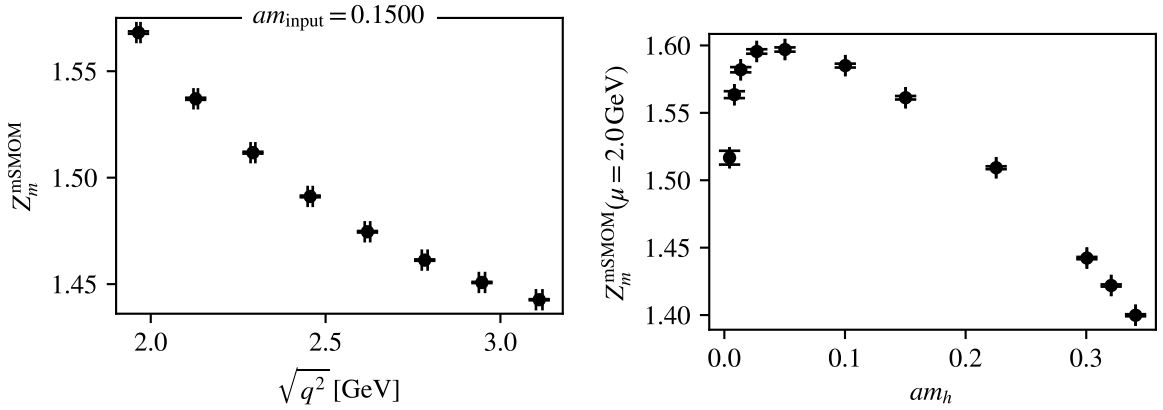

(a) Z_m computed from eqn (6.11) over a range of momenta.

(b) Z_m (interpolated to $\mu = 2$ GeV) over a range of bare quark masses.

Figure 6.3: Z_m^{mSMOM} measurements on the M1M ensemble.

reference scale by choosing an arbitrary reference η_h mass scale $\overline{M}$. The bare mass $\overline{m}$ is therefore determined by interpolating to this reference scale as

$$\overline{m} = (a\overline{m}) \cdot a^{-1}, \tag{6.27}$$

$$a\overline{m} = am_q(M_{\eta_h} = \overline{M}). \tag{6.28}$$

Note that this choice of the reference pseudoscalar meson mass $\overline{M}$ ultimately corresponds to choosing the RI/mSMOM mass scale $\overline{m}_R$.

4. renormalisation constant Z_m^{mSMOM}: we see from eqn (6.11) that in order to calculate Z_m, we need to also compute Z_q, Z_P. Z_m and Z_A can then be extracted from the coupled equations

$$\frac{1}{Z_m m}\left\{\text{Tr}\left[Z_q S(p)^{-1}\right]_{p^2=\mu^2} + \frac{1}{2}\frac{Z_A}{Z_q}\text{Tr}\left[(iq\cdot\Lambda_A(p_1,p_2))\,\gamma_5\right]_{\text{sym}}\right\} = 12,$$
$$\frac{1}{q^2}\left\{\frac{Z_A}{Z_q}\text{Tr}\left[(q\cdot\Lambda_A(p_1,p_2))\gamma_5 \not{q}\right]_{\text{sym}} + 2m\frac{Z_m Z_P}{Z_q}\text{Tr}\left[\Lambda_P(p_1,p_2)\gamma_5\not{q}\right]_{\text{sym}}\right\} = 12.$$

On each ensemble, for each choice of bare mass, we compute bare propagators and Green's functions for $\Gamma = S, P, V, A$ by choosing lattice momenta $ap_1 = (p, p, 0, 0)$ and $ap_2 = (p, 0, p, 0)$, where

$$p = \frac{2\pi}{L}(n + \theta). \tag{6.29}$$

In order to cover the range of physical momenta $2\,\text{GeV} \lesssim q \lesssim 3\,\text{GeV}$ (see figure 6.3a), we use twist angles $\theta \in \{0, 0.25, 0.5, 0.75\}$ in order to interpolate between the integer Fourier modes $n \in \{3, 4, 5\}$ on the coarse and medium ensembles, and $n \in \{4, 5, 6\}$ on the fine ensembles. This is then repeated for each choice of bare quark mass as shown in figure 6.3b. We therefore compute the renormalisation

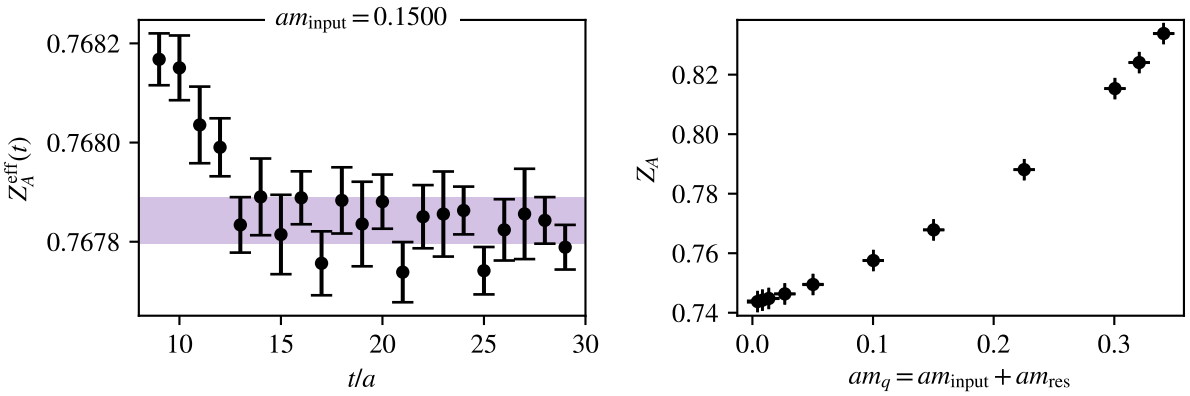

(a) Z_A derived from the ratio of conserved over local axial current.

(b) Z_A measurements over a range of bare quark masses.

Figure 6.4: Z_A measurements on the M1M ensemble.

constant for quark masses as a function of the renormalisation scale μ and the bare quark mass in lattice units am_q as shown in figure 6.6.

5. renormalisation constant Z_A: note that in practice we find it convenient to replace the renormalisation condition for Z_A in eqn (6.15) with a direct determination of Z_A from the asymptotic time behaviour of the ratio of conserved ($j_{\mathcal{A}}$) over local (j_A) axial currents (see eqn (3.44))[2]. We adopt the definition of this ratio from [250] in order to avoid as much systematic error as possible:

$$Z_A = Z_A^{\text{eff}}(t)\Big|_{t\gg a^{-1}} = \frac{1}{2}\left[\frac{C(t+\frac{1}{2}) + C(t-\frac{1}{2})}{2L(t)} + \frac{2C(t+\frac{1}{2})}{L(t)+L(t+1)}\right]_{t\gg a^{-1}}, \quad (6.30)$$

$$\text{with} \quad C(t+\tfrac{1}{2}) := \langle j_{\mathcal{A}}(t) j_5(0)\rangle, \quad L(t) := \langle j_A(t) j_5(0)\rangle. \quad (6.31)$$

This procedure is shown in figure 6.4a, and then repeated for the various bare quark masses as shown in figure 6.4b. Note that conserved axial current is defined not on lattice sites but instead on the links between sites, therefore the conserved current correlator C has a $\frac{1}{2}$ in its argument.

6. renormalisation constant Z_m^{SMOM}: we also compute the renormalisation constants in the massless RI/SMOM scheme in order to make a comparison with the massive scheme, using the ($\not{q}$) projectors as listed in eqns 4.10–4.19. Once again, we use the Z_A computed from the ratio of conserved over local axial currents in this process.

Note that the values of am_{res}, aM_{η_h} and Z_A are computed from choosing the value and error of a datapoint in the plateau region in the $t/a \gg 1$ limit. The numerical values of these as well as those of Z_m^{mSMOM} and Z_m^{SMOM} are listed explicitly for all ensembles in tables C.1 – C.6.

[2]These currents carry an index μ corresponding to $\gamma_\mu\gamma_5$ in the kernel, and we construct the ratios using the temporal component only ($\mu = 4$).

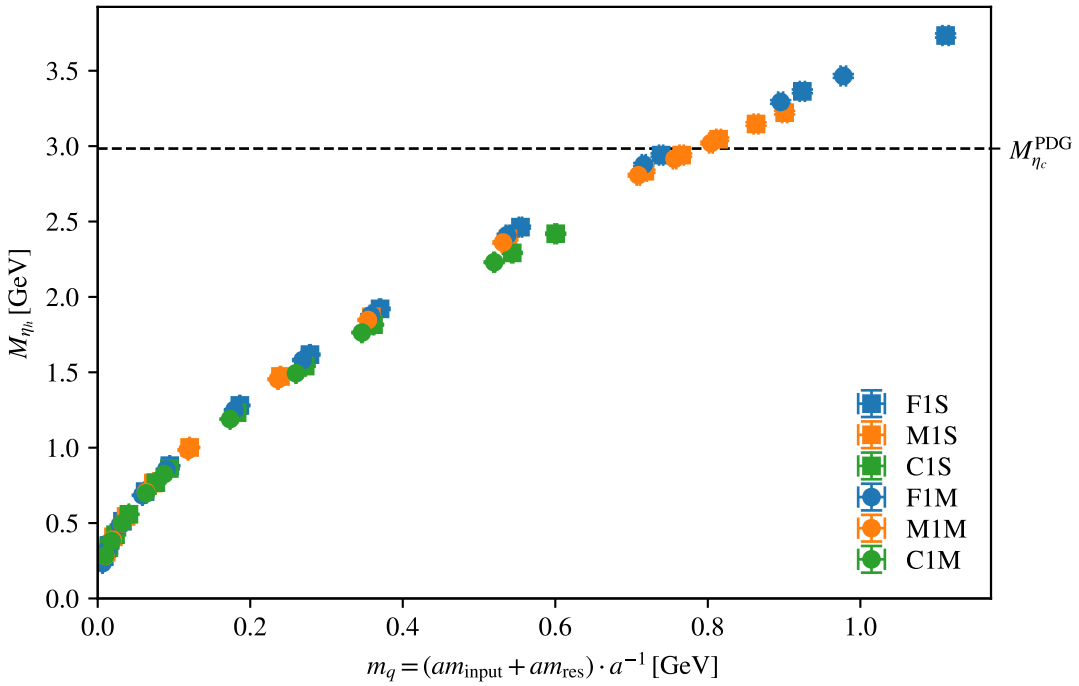

Figure 6.5: Coverage of the quark mass dependence of our data. Note that on the coarse ensembles we don't reach the physical charm quark mass scale.

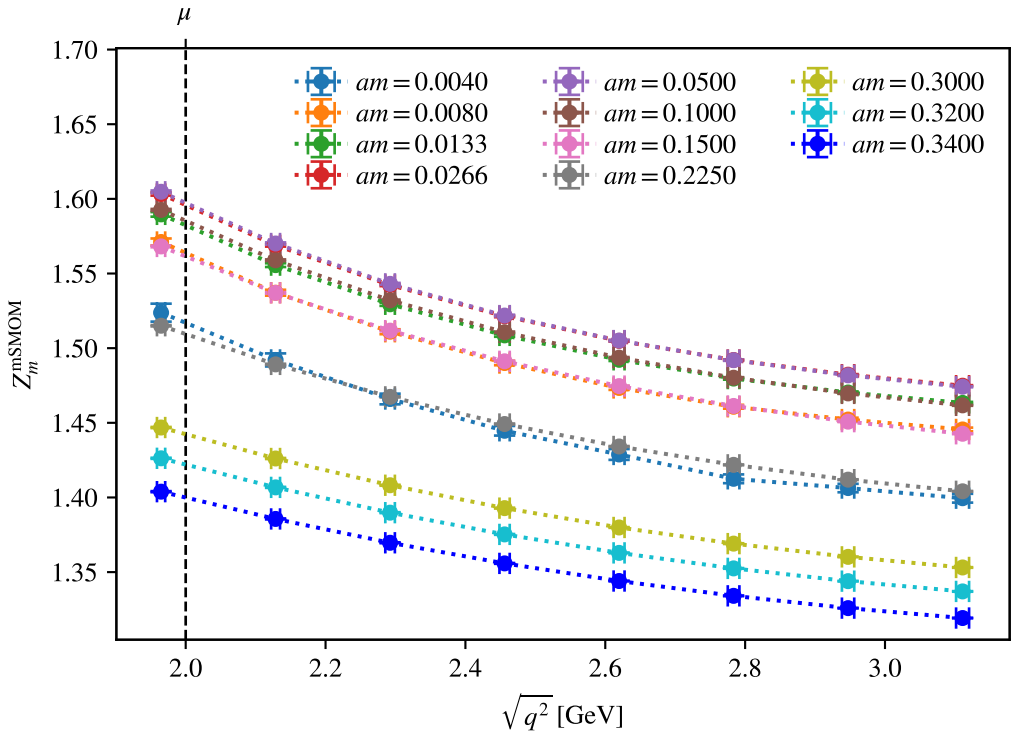

Figure 6.6: Z_m in the RI/mSMOM scheme computed over a range of momenta for various values of bare input quark masses $am = am_{\mathrm{input}}$ on the M1M ensemble, interpolated to a chosen value of the renormalisation scale ($\mu = 2$ GeV case illustrated here).

6.2.2 Strategy

Our strategy for computing the renormalised charm quark mass in the RI/mSMOM scheme is as follows:

(a) Interpolate Z_m^{mSMOM} to a common renormalisation scale μ for each bare quark mass to obtain $Z_m^{\text{mSMOM}}(a\mu, am_q)$ on all ensembles as shown in figure 6.6.

(b) Choose a mass scale at which the RI/mSMOM renormalisation conditions are imposed ($\overline{m}_R$): this is done indirectly via choosing an η_h meson mass $\overline{M}$. Interpolate to find the corresponding bare quark mass in lattice units $a\overline{m}$ on each ensemble.

(c) Interpolate the renormalisation constants to this mass scale on each ensemble $Z_m^{\text{mSMOM}}(a\mu, a\overline{m})$.

(d) Choose a mass scale corresponding to the quark mass to be renormalised. Ideally we should work at the charm scale, using $M_{\eta_c}^{\text{PDG}}$ as our reference mass, however our choice of DWF parameters does not allow for direct simualations at the physical charm scale on the coarsest ensembles (see figure 6.5). We therefore instead carry out the renormalisation procedure at lower bare quark masses and extrapolate to the charm scale (as well as renormalising directly at the charm scale using only two lattice spacings) – for this purpose, we choose a meson mass scale M, and compute the corresponding bare quark mass $m = am_q(M) \cdot a^{-1}$ by interpolating.

(e) For a given choice of (μ, $\overline{M}$, M), carry out two continuum extrapolations

  (a) combine $Z_m(a\mu, a\overline{m})$ with $\overline{m}$ on all ensembles to obtain the RI/mSMOM scheme-defining renormalised mass

$$\overline{m}_R = \lim_{a\to 0} Z_m^{\text{mSMOM}}(a\mu, a\overline{m})(a\overline{m}) \cdot a^{-1}. \tag{6.32}$$

  (b) combine $Z_m(a\mu, a\overline{m})$ with m on all ensembles to obtain the renormalised mass

$$m_R^{\text{mSMOM}}(\mu, \overline{m}_R) = \lim_{a\to 0} Z_m^{\text{mSMOM}}(a\mu, a\overline{m})(am) \cdot a^{-1}. \tag{6.33}$$

(f) Keeping the choices of (μ, $\overline{M}$) fixed, vary the choice of M and extrapolate to $M = M_{\eta_c}^{\text{PDG}}$ to obtain $m_{c,R}^{\text{mSMOM}}(\mu, \overline{m}_R)$ and derive a systematic error that accounts for the lack of physical charm scale coverage on the course ensembles.

(g) Finally, repeat the analysis for different choices of μ and $\overline{M}$ in order to determine the *ideal* choice of $\overline{M}$ (and thereby $\overline{m}_R$) for a given μ.

In our analysis, we choose the renormalisation scale $\mu \in \{2.0, 2.5, 3.0\}$, and the reference mass scales as fractions of the η_c meson mass as $M, \overline{M} \in \{0.5, 0.6, 0.7, 0.75, 0.8, 0.9, 1.0\} \times M_{\eta_c}^{\text{PDG}}$.

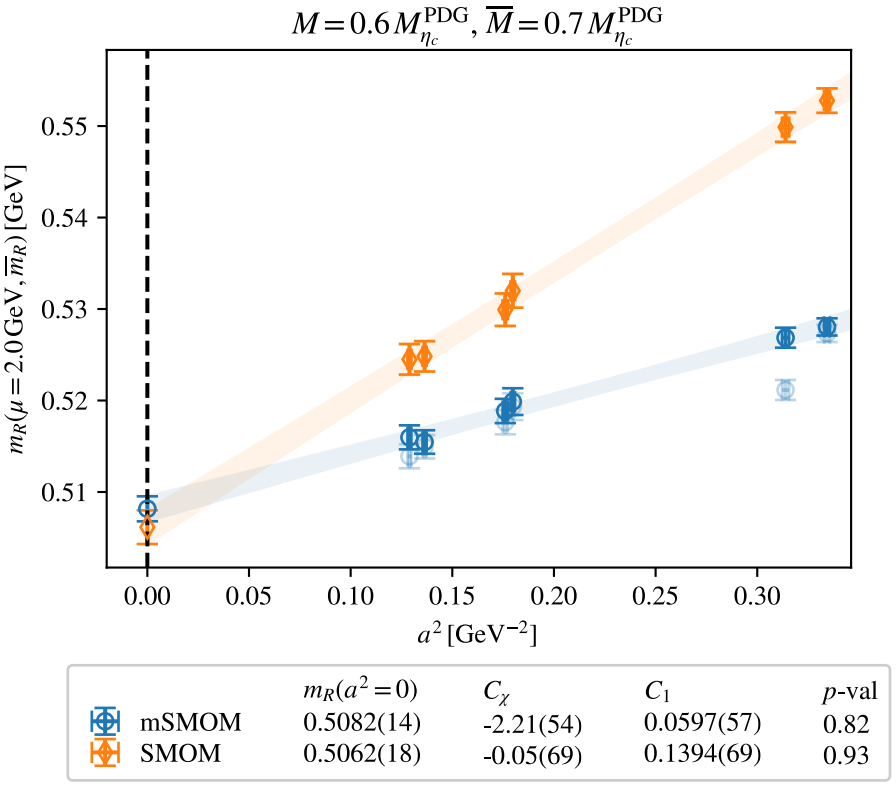

	$m_R(a^2=0)$	C_χ	C_1	p-val
mSMOM	0.5082(14)	-2.21(54)	0.0597(57)	0.82
SMOM	0.5062(18)	-0.05(69)	0.1394(69)	0.93

Figure 6.7: Limit $a \to 0$ for fixed choice of $(\mu,\ \overline{M},\ M)$ comparing approach to the continuum in the massless (RI/SMOM) versus massive (RI/mSMOM) schemes. Values of fit parameters (see eqn (6.34)) and p-value indicated in the legend. Opaque data points are obtained from original data points (faint) by subtracting $C_\chi a m_{\rm res}$.

6.2.3 Continuum extrapolation

Having chosen $(\mu,\ \overline{M},\ M)$ and determined the corresponding bare quark masses and renormalisation constant $(Z_m(\mu, a\overline{m}),\ \overline{m},\ m)$ on each ensemble, we perform the continuum limit of the renormalised quark mass. The most general ansatz we consider for our continuum extrapolations is given by

$$m_R(a\Lambda) = m_R(a^2 = 0) + C_\chi a m_{\rm res} + C_1\,(a\Lambda)^2\,, \tag{6.34}$$

where the coefficient C_χ captures the scaling violations stemming from the residual chiral symmetry breaking in our data. The size of this coefficient is of $O(1)$, however the size of $am_{\rm res}$ is typically small (see tables C.1 & C.2). We tried adding a term proportional to a^4 and found that its coefficient is in practice compatible with zero, and therefore it is not needed to describe the data and excluded from the ansatz.

In figure 6.7 we show the continuum extrapolation for the choice $\mu = 2.0$ GeV, $\overline{M} = 0.7\, M_{\eta_c}^{\rm PDG}$, and $M = 0.6\, M_{\eta_c}^{\rm PDG}$. In addition to the RI/mSMOM data points (blue circles) we also show the approach to the continuum limit using Z_m in the massless RI/SMOM scheme (orange circles) computed in the chiral limit. We clearly observe

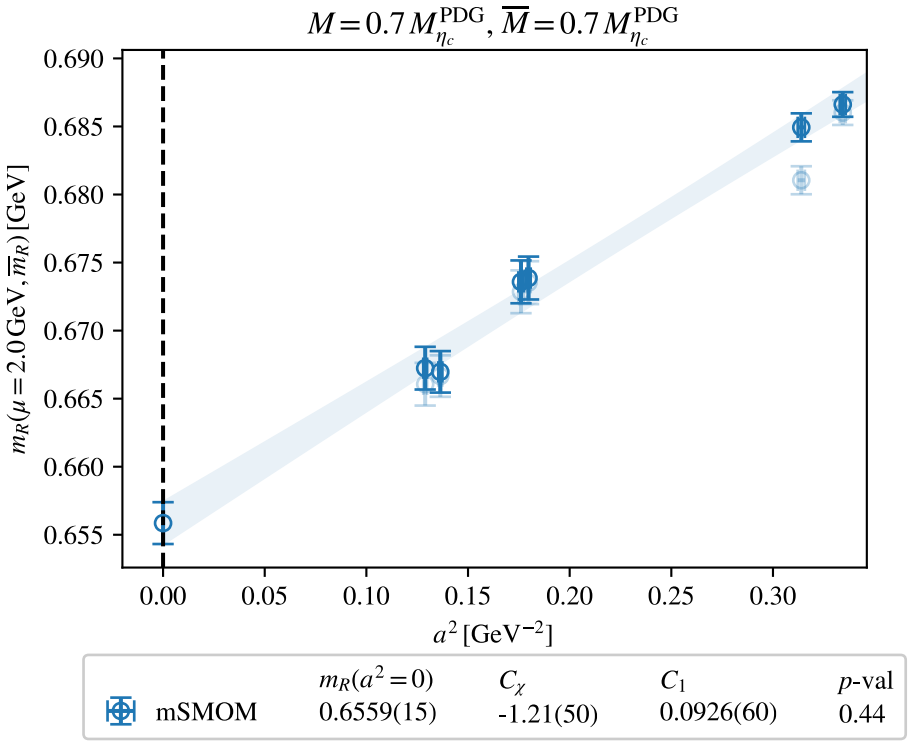

Figure 6.8: Continuum limit with $M = \overline{M}$ for computing the RI/mSMOM scheme-defining renormalised mass scale $\overline{m}_R$.

that the data has smaller discretisation effects in the massive scheme than the massless scheme - this is also indicated by the value of the fit parameter of the term proportional to a^2 given by C_1 in the plot.

The original RI/mSMOM data points are shown as the faint blue symbols while the opaque symbols represent the value once the residual mass contribution ($C_\chi a m_{\mathrm{res}}$) is corrected for. We notice that this only significantly affects the C1S data point, which is expected since residual chiral symmetry breaking effects are known to decrease by decreasing the lattice spacings and increasing the extent of the fifth dimension L_s . Note that the residual chiral symmetry breaking of our choice of Möbius kernel is expected to the same as that of the Shamir kernel with twice the extent of the fifth dimension. Since $L_s(\mathrm{C1S}) = 16$ and $L_s(\mathrm{C1M}) = 24$, the C1M ensemble effectively has thrice the extent of the fifth dimension in comparison to C1S.

We also show, in figure 6.8, the continuum extrapolation for computing the renormalised mass scale $\overline{m}_R$ (at which the renormalisation conditions are imposed). By choosing $M = \overline{M}$ we get $m_R = \overline{m}_R$ in the RI/mSMOM scheme.

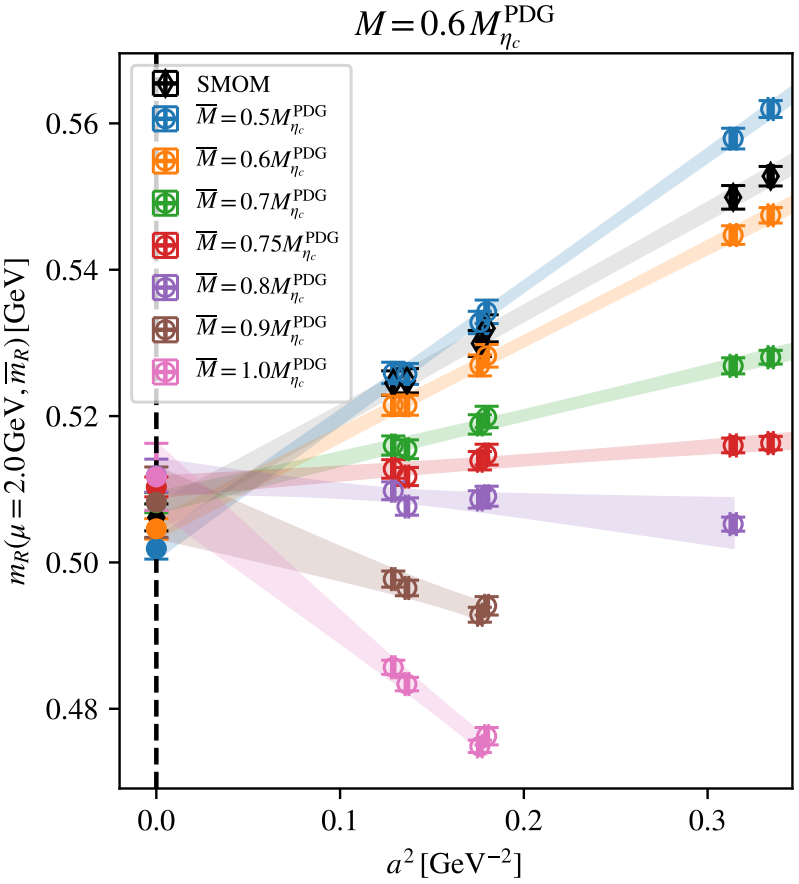

Figure 6.9: Variations of the renormalisation mass scale $\overline{M}$ at a fixed value of M. Data points shown here have been corrected for the $am_{\rm res}$ contribution in the ansatz (see eqn (6.34)). For the largest values of $\overline{M}$ we lose coverage on the coarse ensembles and therefore exclude them from the fit.

6.2.4 Varying $\overline{m}_R$

As described in the beginning over this section, the finite mass scale at which the RI/mSMOM renormalisation conditions are imposed, $\overline{m}_R$, is a tunable parameter that can be freely varied within the range of our data. In figure 6.7 we present fits to the ansatz in eqn (6.34) with $M = 0.6 \times M_{\eta_c}^{\rm PDG}$ for a single choice of $\overline{M} = 0.7 \times M_{\eta_c}^{\rm PDG}$. As we see in figure 6.8, this corresponds to a renormalisation mass scale $\overline{m}_R = 0.6559(15)$.

We also study the absorption of cutoff effects by varying the choice to $\overline{M}$ (and therefore $\overline{m}_R$) as shown in figure 6.9. It is important to note that each choice of $\overline{M}$ corresponds to a *different* RI/mSMOM scheme and therefore the values of the continuum extrapolations from the various $\overline{M}$s at $a^2 = 0$ are not directly comparable. However, it is clearly visible that while the approach to the continuum is well described by a fit linear in a^2 in all cases, the slope varies strongly with the choice of $\overline{M}$. It is therefore possible, for a given observable, to choose an ideal $\overline{m}_R$ in order to obtain the flattest possible continuum slope. This is one of the key features of the massive scheme.

6.2.5 Systematic errors

Interpolations

In order to complete steps (a)–(c) in section 6.2.2, we perform interpolations in $\sqrt{q^2}$ and am_q. As our data has broad coverage, we perform these interpolations locally as polynomial fits to data points closest to the target value. In order to estimate any systematic uncertainties stemming from these interpolations we use the following variations:

1. linear interpolation between the two closest bracketing data points
2. quadratic interpolation between the two data points which bracket the target value and nearest other data point to the left or right
3. cubic interpolation between the four closest data points

We take the fit value of variation 2 as our central value and in addition to its statistical uncertainty we assign half the spread of all variations as a systematic uncertainty. The numerical values of Z_m in the RI/mSMOM and RI/SMOM schemes interpolated to a few different choices of μ using this procedure are listed in tables C.3–C.6.

Continuum extrapolation

In order to assess the systematics uncertainties associated to the continuum limit extrapolation associated with a given choice of M and $\overline{M}$, we use the following variations in ansatze and ensembles:

1. all ensembles on which the hadron mass M can be simulated using the ansatz in eqn (6.34)
2. all ensembles except C1S (which has the largest am_{res} value by far) and excluding the C_χ term from the ansatz
3. only the three Möbius ensembles (all of which have smaller am_{res} values compared to the Shamir ones) and excluding the C_χ term from the ansatz

We take the fit value of variation 1 as our central value and in addition to its statistical uncertainty we assign half the spread of all variations as a systematic uncertainty.

0.32	M0M	M1M	M0M/M1M
aM_{η_h}	1.23636(19)	1.23593(61)	1.00035(53)
am_{res}	0.0006613(18)	0.0006617(21)	0.9993(41)
Z_A	0.824110(43)	0.824154(95)	0.99995(12)
0.34	M0M	M1M	M0M/M1M
aM_{η_h}	1.28092(18)	1.28049(61)	1.00033(50)
am_{res}	0.0009049(26)	0.0009004(28)	1.0050(43)
Z_A	0.833863(42)	0.833897(100)	0.99996(13)

Table 6.3: Comparison of observables between the M0M ($M_\pi = 139\,\mathrm{MeV}$) and the M1M ($M_\pi = 286\,\mathrm{MeV}$) ensembles for two mass points bracketing the physical charm quark mass.

Pion mass dependence

We also consider the size of potential effects afflicting our simulations which do not take place at the physical pion mass. In table 6.3 we contrast the values for aM_{η_h}, am_{res}, and Z_A on the M1M with those on the M0M (physical point) ensemble for two choices of the heavy bare quark mass that bracket the physics charm quark mass (am_c). These two ensembles differ only in their volume and pion masses. We observe that values on the two ensembles are compatible and therefore their ratios are compatible with unity. We further observe that the relative (albeit not statistically resolved) effect on the hadron mass is at the sub-per-mille level. We therefore conclude that any effects of unphysical pion masses in the data can be safely neglected and do not assign any systematic uncertainties accounting for this.

Physical charm scale

We are ultimately interested in the renormalised charm quark mass, and in order to compute it we follow step (f) of our strategy in section 6.2.2. This involves varying the choice of M for fixed values of μ and $\overline{m}$ in order to remain in the same scheme. For $M \in \{0.5, 0.6, 0.7, 0.75, 0.8, 0.9, 1.0\} \times M_{\eta_c}^{\mathrm{PDG}}$, we assemble the error budget of the steps up to and including the continuum extrapolation. We then combined these results to perform an inter/extrapolation to the physical charm quark mass. Strictly speaking this is not necessary since we already have a direct results at $M = M_{\eta_c}^{\mathrm{PDG}}$, however this continuum limit is only based on the medium and fine ensembles and therefore we prefer to supplement it by a parameterisation using different values of m_R/M as a function of M, as shown in figure 6.10.

In order to assemble a systematic error budget associated with this procedure, we fit data points in various intervals to the following ansatz

$$\frac{m_R}{M} = \alpha \frac{1}{M} + \beta + \gamma\, M. \tag{6.35}$$

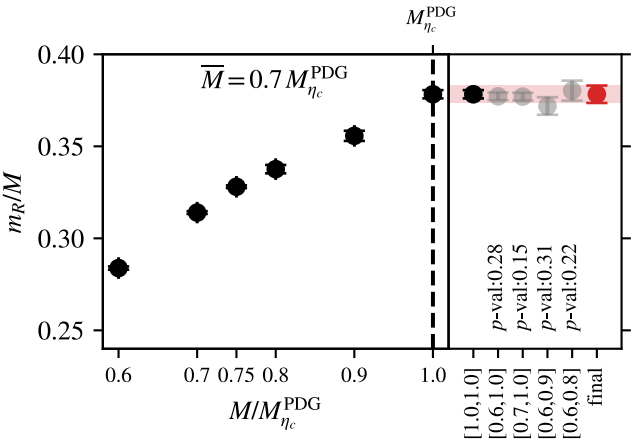

Figure 6.10: Left panel: results of continuum extrapolations of the renormalised mass at $\mu = 2\,\text{GeV}$ at $\overline{M} = 0.7 \times M_{\eta_c}^{\rm PDG}$ for various values of M. Right panels: results of fits using eqn (6.35) over various fit ranges and corresponding p-values. The red data point and corresponding band represents final value of $m_{c,R}$ in RI/mSMOM scheme at given choice of $\overline{M}$.

The intervals we consider, in terms of $M/M_{\eta_c}^{\rm PDG}$ are [0.6, 1.0], [0.7, 1.0], [0.6, 0.9] and [0.6, 0.8]. The results of these varaitions in fit ranges are shown in the right hand panel of figure 6.10. We use the direct determination at the charm quark mass ($M = M_{\eta_c}^{\rm PDG}$) as our central value, and to its uncertainty we conservatively associate a systematic uncertainty of half the spread of the variations.

Note that we quote the two uncertainties separately since the latter only arises from requiring the final number be based on continuum limits from more than two lattice spacings. With the addition of ensembles with finer lattice spacings such that a continuum limit may directly be obtained at the charm quark mass the uncertainty associated with the determination at the physical charm scale would be completely removed.

6.2.6 Conversion to $\overline{\rm MS}$

Finally, it remains to directly compare the results from different choices of $\overline{M}$ as well those from the RI/SMOM scheme by converting to a common scheme in the continuum. We do this in the phenomenologically relavant $\overline{\rm MS}$ scheme, and the conversion factor for quark masses in the RI/SMOM scheme has been computed to two-loop order in [201, 202]. In the Landau gauge for $N_{\rm color} = 3$ and $N_f = 2 + 1$ this explicitly given by

$$R_m^{\overline{\rm MS}\leftarrow\rm SMOM}(\mu) \simeq 1 - \left(\frac{\alpha_s(\mu)}{4\pi}\right) 0.6455188560 - \left(\frac{\alpha_s(\mu)}{4\pi}\right)^2 [10.56706916] + O(\alpha_s^3). \tag{6.36}$$

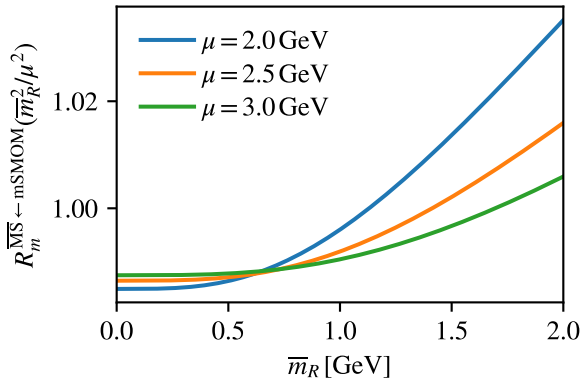

Figure 6.11: Conversion from the RI/mSMOM scheme to $\overline{\mathrm{MS}}$ in the Landau gauge as a function of the renormalised mass scale $\overline{m}_R$ for a few choices of the renormalisation scale μ (see eqn (6.37)).

The conversion factor $\overline{\mathrm{MS}}$ from the RI/mSMOM scheme has been computed at the one-loop level [248] and is given explicitly in the Landau gauge by [10]

$$R_m^{\overline{\mathrm{MS}}\leftarrow\mathrm{mSMOM}}(\mu,\overline{m}_R) = 1 + \frac{\alpha_s(\mu)}{4\pi} C_F \left[-4 + \frac{3}{2} C_0\left(\frac{\overline{m}_R^2}{\mu^2}\right) + 3\ln\left(\frac{\overline{m}_R^2+\mu^2}{\mu^2}\right) - 3\frac{\overline{m}_R^2}{\mu^2}\ln\left(\frac{\overline{m}_R^2}{\overline{m}_R^2+\mu^2}\right)\right], \tag{6.37}$$

where $C_0(x)$ is defined in [10] with $C_0(0) \equiv C_0$ from section 4.3. Note that using the massless condition $\overline{m}_R = 0$ in eqn (6.37) yields $C_F(4 - 3C_0/2) \approx 0.6455$, which is consistent with the one-loop coefficient in eqn (6.36) as expected.

The conversion to $\overline{\mathrm{MS}}$ as a function of the renormalised mass scale $\overline{m}_R$ is shown in figure 6.11 for a few different choices of μ. In this figure, the conversion from the massless scheme is represented by $\overline{m}_R = 0$.

Perturbative truncation error

In order to quantify the effects of truncation in the perturbative expansion for the RI/mSMOM mass renormalisation constant, in the (temporary) absence of perturbative two-loop calculations, we compare the one and two-loop contributions in the massless scheme (second and third term in eqn (6.36)) and use the relative difference between them as an indicator for the systematic truncation uncertainty. By this presciption we find that for $\mu = 2.0\,\mathrm{GeV}$ ($\mu = 2.5\,\mathrm{GeV}$, $\mu = 3.0\,\mathrm{GeV}$) the truncation uncertainty is a 0.38% (0.31%, 0.27%) effect. Note that the uncertainties related to one-loop truncation can be reduced or eliminated by extending the perturbative calculations for renormalisation constants in the RI/mSMOM scheme to higher loop orders.

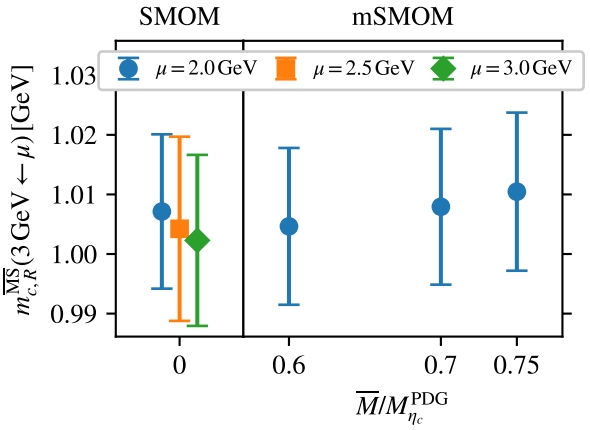

Figure 6.12: Results for the continuum-extrapolated renormalised charm quark mass at 3 GeV computed in RI/SMOM and RI/mSMOM (with variations in choice of $\overline{M}$) schemes and converted to $\overline{\mathrm{MS}}$ using results from $\mu = 2.0$, 2.5, 3.0 GeV. Numerical values are presented in table 6.4.

6.2.7 Results

Having converted our results from the RI/mSMOM and RI/SMOM schemes to the $\overline{\mathrm{MS}}$ scheme using matching in continuum perturbation theory, we now make a direct comparison of the value of the renormalised charm quark mass computed in the various schemes. Furthermore, within the $\overline{\mathrm{MS}}$ scheme we then run our results up to 3 GeV as well as down to the charm quark scale to quote $m_{c,R}^{\overline{\mathrm{MS}}}(3\,\mathrm{GeV})$ and $m_{c,R}^{\overline{\mathrm{MS}}}(m_{c,R}^{\overline{\mathrm{MS}}})$. To compute the strong coupling and running of the $\overline{\mathrm{MS}}$ quark mass we make use of RunDec [251–253] which in turn relies on 5-loop results for the beta function and the mass anomalous dimension [254–259].

Our final results from the charm quark mass in $\overline{\mathrm{MS}}$ at 3 GeV are shown in figure 6.12. We find good agreement between the massless and massive schemes as well as amongst the different values for $\overline{m}_R$ for the massive scheme. In the RI/SMOM scheme, we use results computed at $\mu = 3.0$ GeV directly as well as those computed at $\mu = 2.0$, 2.5 GeV and then ran up (using perturbatively running in $\overline{\mathrm{MS}}$) to 3 GeV. In the RI/mSMOM scheme, our results at 3 GeV are calculated by running up the values computed at $\mu = 2.0$ GeV. This is because while in the massive scheme the continuum limit is well controlled for determinations at 2 GeV, the values of $\overline{M}$ which significantly absord cutoff effects and therefore decrease the slop of the continuum extrapolation are not reachable on our current data set for larger values of the renormalisation scale μ, and thus we exclude them.

μ/GeV	$\overline{M}/M_{\eta_c}^{\rm PDG}$	$\overline{m}_R(\mu,\overline{m}_R)$	$m_{c,R}^{\rm RI}(\mu,\overline{m}_R)$	$\overline{m}_{c,R}^{\overline{\rm MS}}(\mu)$	$\overline{m}_{c,R}^{\overline{\rm MS}}(3\,{\rm GeV}\leftarrow\mu)$	$\overline{m}_{c,R}^{\overline{\rm MS}}(\overline{m}_{c,R}^{\overline{\rm MS}})$
2.0	0.60	0.5046(15)	1.127(7)(12)	1.112(7)(12)(4)	1.005(6)(11)(4)	1.289(6)(10)(3)
2.0	0.70	0.6559(16)	1.129(7)(12)	1.115(7)(12)(4)	1.008(6)(11)(4)	1.292(5)(10)(4)
2.0	0.75	0.7371(16)	1.130(6)(13)	1.118(6)(13)(4)	1.010(6)(11)(4)	1.294(5)(10)(4)
2.0	SMOM	—	1.136(9)(12)	1.114(9)(12)	1.007(8)(10)	1.291(8)(10)
2.5	0.60	0.4698(14)	1.052(7)(14)	1.038(7)(14)(3)	0.995(7)(14)(3)	1.280(6)(13)(3)
2.5	0.70	0.6124(16)	1.057(6)(15)	1.043(6)(15)(3)	1.000(6)(14)(3)	1.284(6)(13)(3)
2.5	0.75	0.6894(16)	1.059(6)(15)	1.046(6)(15)(3)	1.003(6)(15)(3)	1.287(5)(13)(3)
2.5	SMOM	—	1.066(11)(12)	1.048(10)(12)	1.004(10)(12)	1.288(9)(11)
3.0	0.60	0.4450(14)	0.998(7)(15)	0.986(7)(15)(3)	0.986(7)(15)(3)	1.271(6)(14)(2)
3.0	0.70	0.5811(15)	1.004(6)(15)	0.992(6)(15)(3)	0.992(6)(15)(3)	1.277(5)(14)(2)
3.0	0.75	0.6549(16)	1.008(6)(16)	0.995(6)(16)(3)	0.995(6)(16)(3)	1.280(5)(15)(2)
3.0	SMOM	—	1.018(8)(12)	1.002(8)(12)	1.002(8)(12)	1.287(8)(11)

Table 6.4: Summary of our final results for the renormalised charm quark mass (all quark masses are in units of GeV). The first uncertainty corresponds to that in the direct determination at the charm scale, the second to the inter/extrapolation from using $M < M_{\eta_c}^{\rm PDG}$, and the third (for RI/mSMOM$\to\overline{\rm MS}$ numbers) to the estimate of one-loop perturbative truncation error.

As our final number we quote our results obtained from RI/mSMOM at $\mu = 2\,\text{GeV}$ from the choice $\overline{M} = 0.7\,M_{\eta_c}^{\text{PDG}}$ which corresponds to $\overline{m}_R = 0.6559(16)\,\text{GeV}$. We find

$$m_{c,R}^{\text{mSMOM}}(2\,\text{GeV}, \overline{m}_R) = 1.129(7)(12)\,\text{GeV}\,, \tag{6.38}$$

$$m_{c,R}^{\overline{\text{MS}}}(2\,\text{GeV}) = 1.115(7)(12)(4)\,\text{GeV}\,, \tag{6.39}$$

$$m_{c,R}^{\overline{\text{MS}}}(3\,\text{GeV}) = 1.008(6)(11)(4)\,\text{GeV}\,, \tag{6.40}$$

$$m_{c,R}^{\overline{\text{MS}}}(m_{c,R}^{\overline{\text{MS}}}) = 1.292(5)(10)(4)\,\text{GeV}\,. \tag{6.41}$$

The first uncertainty comes from the determination of the renormalised charm quark mass directly at the charm scale, the second from the inter/extrapolation from using reference values $M < M_{\eta_c}^{\text{PDG}}$, and the third is the estimated one-loop perturbative truncation error in converting from RI/mSMOM to $\overline{\text{MS}}$. We end up with an overall 1.3% uncertainty in our result at 3 GeV. Note that we have not applied any additional uncertainties associated with the running in the $\overline{\text{MS}}$ scheme.

N_f	collaboration	$m_{c,R}^{\overline{\text{MS}}}(3\,\text{GeV})$	$m_{c,R}^{\overline{\text{MS}}}(m_{c,R}^{\overline{\text{MS}}})$
2+1	[10] RBC/UKQCD 24	1.008(6)(11)(4)	1.292(5)(10)(4)
	[260] ALPHA 21	1.007(16)	1.296(19)
	[261] Petreczky 19	1.001(16)	1.265(10)
	[262] Maezawa 16		1.267(12)
	[246] JLQCD 16	1.0033(96)	1.2871(123)
	[263] χQCD 14	1.006(5)(22)	1.304(5)(20)
	[234] HPQCD 10	0.986(6)	1.273(6)
	[264] HPQCD 08B	0.986(10)	1.268(9)
	[7] FLAG21 avg	0.992(5)	1.275(5)
2+1+1	[265] ALPHA 23	1.006(13)	1.296(16)
	[222] ETM 21A	$1.036(17)(^{+15}_{-8})$	$1.339(22)(^{+19}_{-10})(10)$
	[266] HPQCD 20A	0.9841(51)	1.2719(78)
	[226] HPQCD 18	0.9896(61)	1.2757(84)
	[223] FNAL/MILC/ TUMQCD 18	0.9837(43)(14)(33)(5)	1.273(4)(1)(10)
	[227] HPQCD 14A	0.9851(63)	1.2715(95)
	[267] ETM 14A	1.0557(22)(153)	1.3478(27)(195)
	[224] ETM 14	1.058(35)	1.348(46)
	[7] FLAG21 avg	0.988(11)	1.278(13)
	[6] PDG		1.27(2)

Table 6.5: Comparison of various lattice results and PDG evaluation for renormalised charm quark mass in $\overline{\text{MS}}$ scheme at $\mu = 3$ GeV and at the charm mass scale. The results from this work indicated in red text, all other values except ALPHA 23 are from FLAG21 [7] including the average of lattice results (in orange). For a breakdown of individual values and errors, please refer to FLAG21 review.

6.2.8 Comparison to literature

The charm quark mass has previously been computed by various collaborations in various schemes. In table 6.5 we compare our results (in red) to results in the literature computed using $N_f = 2 + 1$ as well as $N_f = 2 + 1 + 1$. Most results presented in this table are computed in massless NPR schemes such as RI/SMOM, RI'/SMOM, the Schrödinger functional scheme and the X-space method, or heavy quark effective theory (HQET) methods to treat the heavy masses. Note that some computations have also used Symanzik improvement methods to tackle discretisation effects, see for example [223, 260]. Some of them also computed the charm mass from moments of pseudoscalar quarkonium correlation functions involving ratios of quark masses – in this case the Z_m factors would cancel out so no NPR procedure is needed.

We find good agreement with other $N_f = 2 + 1$ calculations and obtain similar uncertainties. Note that the leading uncertainty in our calculation arised from the the large of charm scale coverage on all three lattice spacings we use for computing the renormalised charm quark mass - this can be eliminated in the future with the use of an additional finer lattice spacing.

6.3 Conclusions and outlook

We have presented the first numerical implementation of the massive non-perturbative renormalisation scheme RI/mSMOM which was originally proposed in [248]. Our key findings include confirming that the use of a massive scheme indeed leads to absorption of discretisation effects related to the use of heavy quarks on the lattice, and that the finite renormalisation scale $\overline{m}_R$ acts as a tunable parameter for controlling this absorption; therefore we can use it to find the flattest approach to the continuum for our renormalised quantities of interest.

We observe good agreement between different RI/mSMOM schemes corresponding to different $\overline{m}_R$'s; this provides a non-trivial test for scrutinising and substantiating that the continuum limit is well-controlled and independent of the choice of the renormalisation mass scale.

The use of this massive scheme is in principle not restricted to heavy quark masses and can be useful for studying any observable with large discretisation effects relative to the desired statistical precision. In the future we envisage applications of the RI/mSMOM scheme to other bilinear operators as well as an extension to four-quark operators where it can find use in processes such as heavy meson decays and mixing.

Chapter 7

Conclusions

The ongoing search for New Physics calls for high precision tests on the parameters of the Standard Model (SM), as well as exploring beyond the Standard Model (BSM) theories. In this thesis, we use the framework of lattice quantum chromodynamics (QCD) to make high precision predictions for both SM and BSM parameters for neutral kaon mixing, and for the mass of the charm quark. The unifying theme in these projects is the use of regularisation-independent (RI) momentum subtraction (MOM) schemes for the non-perturbative renormalisation of lattice observables.

We present a study of neutral kaon mixing using $N_f = 2 + 1$ QCD data simulated directly with physical quark masses. This improves upon the most recent RBC/UKQCD calculation of BSM bag and ratio parameters [2,72] by utilising a third lattice spacing and two data points at the physical light quark masses. Our results for the SM bag parameter as well as the BSM bag parameters $\mathcal{B}_2$ and $\mathcal{B}_2$ are in good agreement with previous calculations [7]. Meanwhile, the results for $\mathcal{B}_4$ and B_5 confirm the tensions between calculations employing the RI/SMOM versus the RI/MOM schemes. We propose the source of this tension to be artefacts of the pion pole subtraction procedure needed when using exceptional kinematics in the RI/MOM scheme. This study is carried out with sufficient precision that further improvement will require addressing the strong and electromagnetic isospin breaking effects, and improving the perturbative matching from the RI scheme to the $\overline{\mathrm{MS}}$ scheme by an additional loop order. Our results stand at present to be the most precise determinations of the BSM bag parameters for neutral kaon mixing, and our methodology involves a comprehensive implementation and test of the RI/SMOM scheme.

The study of the short-distance contributions to neutral D, B and B_s meson mixing follows a similar strategy to that used in the kaon mixing project. The necessary non-perturbative renormalisation factors for these processes have also been computed as part of the thesis in order to contribute to the ongoing RBC/UKQCD study of heavy meson mixing.

We have also presented a first ever numerical implementation of an extension to the RI/SMOM scheme (imposed in the massless limit) for improving precision for heavy quark observables, called the RI/mSMOM scheme [248], where 'm' denotes *massive*. We impose renormalisation conditions at finite values of a fixed renormalised quark mass, and use the corresponding Z-factors to renormalise our bare lattice quantity of interest, in our case the charm quark mass. We find that our final value of the charm quark mass is in good agreement with the existing literature. Most importantly, we observe that the massive scheme helps absorb discretisation effects in heavy quark observables and therefore leads to a milder continuum extrapolation compared to the massless (RI/SMOM) scheme. We find that the finite renormalisation scale $\overline{m}_R$ behaves as a tunable parameter for controlling this absorption, and can be adjusted to find a flat continuum approach, depending on the observable of interest. The current results can be improved with the use of finer lattices and perturbative matching factors computed to higher loop order. We predict that this methodology of massive non-perturbative renormalisation will find use in the improvement of precision in other heavy quark observables, particularly if the scheme is extended to higher dimensional operators in the future.

Appendix A

Algebraic properties

A.1 Generators of $SU(2)$ and $SU(3)$

The generators of the $SU(2)$ Lie algebra are given by $t^a = \frac{1}{2}\sigma^a$ where σ^a are the three Pauli matrices given by

$$\sigma_1 = \begin{pmatrix} 0 & 1 \\ 1 & 0 \end{pmatrix}, \quad \sigma_2 = \begin{pmatrix} 0 & -i \\ -i & 0 \end{pmatrix}, \quad \sigma_3 = \begin{pmatrix} 1 & 0 \\ 0 & 1 \end{pmatrix}. \tag{A.1}$$

Similarly, the generators of the $SU(3)$ Lie algebra are given by $t^a = \frac{1}{2}\lambda^a$ where λ^a are the eight Gell-Mann matrices given by

$$\begin{aligned}
\lambda_1 &= \begin{pmatrix} 0 & 1 & 0 \\ 1 & 0 & 0 \\ 0 & 0 & 1 \end{pmatrix}, \quad \lambda_2 = \begin{pmatrix} 0 & -i & 0 \\ i & 0 & 0 \\ 0 & 0 & 0 \end{pmatrix}, \quad \lambda_3 = \begin{pmatrix} 1 & 0 & 0 \\ 0 & -1 & 0 \\ 0 & 0 & 0 \end{pmatrix}, \\
\lambda_4 &= \begin{pmatrix} 0 & 0 & 1 \\ 0 & 0 & 0 \\ 1 & 0 & 0 \end{pmatrix}, \quad \lambda_5 = \begin{pmatrix} 0 & 0 & -i \\ 0 & 0 & 0 \\ i & 0 & 0 \end{pmatrix}, \\
\lambda_6 &= \begin{pmatrix} 0 & 0 & 0 \\ 0 & 0 & 1 \\ 0 & 1 & 0 \end{pmatrix}, \quad \lambda_7 = \begin{pmatrix} 0 & 0 & 0 \\ 0 & 0 & -i \\ 0 & i & 0 \end{pmatrix}, \quad \lambda_8 = \frac{1}{\sqrt{3}} \begin{pmatrix} 1 & 0 & 0 \\ 0 & 1 & 0 \\ 0 & 0 & -2 \end{pmatrix}.
\end{aligned} \tag{A.2}$$

A.2 Gamma matrices

The generators of the Lorentz group[1] algebra are commonly represented as $S_{\mu\nu} = \frac{1}{4}[\gamma_\mu, \gamma_\mu]$, where the gamma matrices are the four generators of Clifford algebra, given by (in Euclidean space)

$$\begin{aligned} \gamma_1 &= \begin{pmatrix} 0 & 0 & 0 & -i \\ 0 & 0 & -i & 0 \\ 0 & i & 0 & 0 \\ i & 0 & 0 & 0 \end{pmatrix}, \quad \gamma_2 = \begin{pmatrix} 0 & 0 & 0 & -1 \\ 0 & 0 & 1 & 0 \\ 0 & 1 & 0 & 0 \\ -1 & 0 & 0 & 0 \end{pmatrix}, \\ \gamma_3 &= \begin{pmatrix} 0 & 0 & -i & 0 \\ 0 & 0 & 0 & i \\ i & 0 & 0 & 0 \\ 0 & -i & 0 & 0 \end{pmatrix}, \quad \gamma_4 = \begin{pmatrix} 0 & 0 & 1 & 0 \\ 0 & 0 & 0 & 1 \\ 1 & 0 & 0 & 0 \\ 0 & 1 & 0 & 0 \end{pmatrix}. \end{aligned} \tag{A.3}$$

These matrices are Hermitian and satisfy the Clifford group algebra

$$\gamma_\mu^\dagger = (\gamma_\mu)^{-1} = \gamma_\mu, \quad \{\gamma_\mu, \gamma_\nu\} = 2\delta_{\mu\nu}\mathbb{1}_{4\times 4}. \tag{A.4}$$

We also define a useful combination of these matrices

$$\gamma_5 = \gamma_1\gamma_2\gamma_3\gamma_4 = \begin{pmatrix} 1 & 0 & 0 & 0 \\ 0 & 1 & 0 & 0 \\ 0 & 0 & -1 & 0 \\ 0 & 0 & 0 & -1 \end{pmatrix}, \tag{A.5}$$

which is also Hermitian and anticommutes with the other matrices:

$$\gamma_5^\dagger = (\gamma_5)^{-1} = \gamma_5, \quad \{\gamma_\mu, \gamma_5\} = 0. \tag{A.6}$$

[1] defined as $SO(3,1)$ in Minkowski spacetime and $SU(2) \times SU(2)$ in Euclidean spacetime

Appendix B

Numerical results for meson mixing

$a\mu$	1.11072	1.20328	1.29584	1.3884	1.48096	1.57352
Z_{11}/Z_A^2	0.93224(13)	0.929176(89)	0.926290(94)	0.923561(69)	0.920933(61)	0.918361(48)
Z_{22}/Z_A^2	1.051566(67)	1.050490(35)	1.049666(44)	1.049023(34)	1.048781(30)	1.048699(22)
Z_{23}/Z_A^2	0.34329(10)	0.32562(10)	0.31148(13)	0.299919(76)	0.29116(11)	0.284410(79)
Z_{32}/Z_A^2	0.025241(32)	0.026859(24)	0.028691(14)	0.030482(26)	0.032458(19)	0.034417(25)
Z_{33}/Z_A^2	0.70331(21)	0.73972(25)	0.77188(10)	0.79997(14)	0.825201(70)	0.847377(98)
Z_{44}/Z_A^2	0.76990(16)	0.80063(30)	0.82823(13)	0.85250(18)	0.874776(87)	0.89460(11)
Z_{45}/Z_A^2	−0.020531(33)	−0.023123(42)	−0.025770(20)	−0.028259(33)	−0.030843(17)	−0.033323(22)
Z_{54}/Z_A^2	−0.32217(13)	−0.30334(14)	−0.28828(13)	−0.27607(12)	−0.26659(12)	−0.259125(92)
Z_{55}/Z_A^2	1.134435(46)	1.112601(64)	1.094144(44)	1.0786529(50)	1.065350(26)	1.0539165(45)
Z_A/Z_S	1.197636(72)	1.17094(20)	1.14850(10)	1.129805(85)	1.113751(82)	1.100262(50)
$a\mu$	1.66608	1.75864	1.8512	1.94376	2.03632	2.12888
Z_{11}/Z_A^2	0.915757(55)	0.913126(40)	0.910350(50)	0.907465(35)	0.904293(46)	0.900905(32)
Z_{22}/Z_A^2	1.049000(28)	1.049402(14)	1.050175(21)	1.050999(11)	1.052146(28)	1.053327(10)
Z_{23}/Z_A^2	0.279843(79)	0.276699(69)	0.275435(81)	0.275145(75)	0.276453(90)	0.278507(72)
Z_{32}/Z_A^2	0.036556(21)	0.038698(21)	0.041039(19)	0.043385(14)	0.045971(20)	0.048580(12)
Z_{33}/Z_A^2	0.867628(13)	0.885835(87)	0.9026943(41)	0.918149(54)	0.932898(25)	0.946640(39)
Z_{44}/Z_A^2	0.913142(39)	0.930040(97)	0.946110(20)	0.960969(61)	0.975488(25)	0.989038(43)
Z_{45}/Z_A^2	−0.035922(23)	−0.038460(22)	−0.041150(20)	−0.043791(16)	−0.046625(22)	−0.049431(13)
Z_{54}/Z_A^2	−0.253672(91)	−0.249596(86)	−0.247137(88)	−0.245600(78)	−0.245377(91)	−0.245835(73)
Z_{55}/Z_A^2	1.043880(31)	1.034942(24)	1.026894(25)	1.019469(17)	1.012461(21)	1.005738(14)
Z_A/Z_S	1.088466(27)	1.078253(51)	1.069232(11)	1.061227(34)	1.0539537(99)	1.047396(20)

Table B.1: Values of Z_{ij}/Z_A^2 for chirally non-vanishing matrix elements for all simulated momenta (in lattice units) on the C0M ensemble for $am_q^{\mathrm{val}} = 0.0181$. All values are given in the RI/SMOM$^{(\gamma_\mu,\gamma_\mu)}$ scheme and in the SUSY basis.

$a\mu$	1.11072	1.20328	1.29584	1.3884	1.48096	1.57352
Z_{11}/Z_A^2	0.93303(14)	0.92976(10)	0.926881(61)	0.924165(55)	0.921484(68)	0.918880(68)
Z_{22}/Z_A^2	1.05273(21)	1.05138(14)	1.05029(10)	1.049571(83)	1.048996(48)	1.048999(58)
Z_{23}/Z_A^2	0.34130(42)	0.32407(26)	0.31001(20)	0.29859(18)	0.28941(16)	0.28323(17)
Z_{32}/Z_A^2	0.02531(10)	0.027037(68)	0.028790(64)	0.030600(50)	0.032438(40)	0.034450(40)
Z_{33}/Z_A^2	0.70746(75)	0.74339(45)	0.77453(36)	0.80253(31)	0.82744(22)	0.84920(15)
Z_{44}/Z_A^2	0.77313(64)	0.80384(41)	0.83043(34)	0.85469(29)	0.87662(22)	0.89624(16)
Z_{45}/Z_A^2	−0.020645(77)	−0.023393(61)	−0.025895(49)	−0.028387(37)	−0.030866(34)	−0.033424(40)
Z_{54}/Z_A^2	−0.32073(41)	−0.30201(25)	−0.28694(17)	−0.27477(15)	−0.26502(17)	−0.25790(14)
Z_{55}/Z_A^2	1.13440(25)	1.11216(22)	1.09381(15)	1.07834(11)	1.065043(81)	1.053610(73)
Z_A/Z_S	1.19361(87)	1.16783(38)	1.14668(31)	1.12820(22)	1.11209(19)	1.09915(11)
$a\mu$	1.66608	1.75864	1.8512	1.94376	2.03632	2.12888
Z_{11}/Z_A^2	0.916271(66)	0.913647(62)	0.910979(58)	0.907958(59)	0.904835(57)	0.901407(57)
Z_{22}/Z_A^2	1.049163(54)	1.049628(43)	1.050184(44)	1.051141(43)	1.052197(44)	1.053418(48)
Z_{23}/Z_A^2	0.27856(18)	0.27569(15)	0.27391(14)	0.27418(14)	0.27535(14)	0.27760(16)
Z_{32}/Z_A^2	0.036536(42)	0.038723(44)	0.040950(27)	0.043393(43)	0.045908(44)	0.048568(45)
Z_{33}/Z_A^2	0.86921(12)	0.88734(12)	0.90395(12)	0.91939(13)	0.93385(12)	0.94767(10)
Z_{44}/Z_A^2	0.91451(13)	0.93143(14)	0.94714(13)	0.96214(15)	0.97634(14)	0.99002(13)
Z_{45}/Z_A^2	−0.035943(41)	−0.038526(45)	−0.041070(30)	−0.043828(44)	−0.046588(44)	−0.049443(44)
Z_{54}/Z_A^2	−0.25237(15)	−0.24849(13)	−0.24567(14)	−0.24449(12)	−0.24416(12)	−0.24473(13)
Z_{55}/Z_A^2	1.043619(65)	1.034780(57)	1.026835(42)	1.019346(42)	1.012414(35)	1.005685(36)
Z_A/Z_S	1.08753(10)	1.077395(95)	1.068493(75)	1.060548(76)	1.053415(61)	1.046857(50)

Table B.2: Same as table B.1 but for the C1S ensemble for $am_q^{\mathrm{val}} = 0.005$.

$a\mu$	1.11072	1.20328	1.29584	1.3884	1.48096	1.57352
Z_{11}/Z_A^2	0.93191(15)	0.92887(10)	0.926097(77)	0.923495(73)	0.921020(94)	0.918454(72)
Z_{22}/Z_A^2	1.05171(15)	1.050485(93)	1.049645(83)	1.049098(72)	1.048722(86)	1.048781(64)
Z_{23}/Z_A^2	0.34132(33)	0.32419(30)	0.31003(26)	0.29875(24)	0.28985(28)	0.28339(21)
Z_{32}/Z_A^2	0.025215(80)	0.027035(48)	0.028793(41)	0.030617(44)	0.032426(51)	0.034531(46)
Z_{33}/Z_A^2	0.70614(29)	0.74217(37)	0.77411(29)	0.80213(27)	0.82646(20)	0.84921(24)
Z_{44}/Z_A^2	0.77195(27)	0.80249(32)	0.82992(28)	0.85436(25)	0.87568(18)	0.89625(25)
Z_{45}/Z_A^2	−0.020631(76)	−0.023284(54)	−0.025855(50)	−0.028421(52)	−0.030823(53)	−0.033466(54)
Z_{54}/Z_A^2	−0.32063(32)	−0.30217(28)	−0.28714(22)	−0.27510(21)	−0.26550(25)	−0.25819(18)
Z_{55}/Z_A^2	1.13305(26)	1.11148(20)	1.09330(13)	1.07791(10)	1.06485(11)	1.053406(58)
Z_A/Z_S	1.19289(55)	1.16840(34)	1.14640(27)	1.12798(23)	1.11248(14)	1.09896(17)
$a\mu$	1.66608	1.75864	1.8512	1.94376	2.03632	2.12888
Z_{11}/Z_A^2	0.915930(67)	0.913308(61)	0.910629(79)	0.907679(57)	0.904565(59)	0.901155(61)
Z_{22}/Z_A^2	1.049033(69)	1.049516(68)	1.050148(77)	1.051112(66)	1.052184(64)	1.053426(65)
Z_{23}/Z_A^2	0.27882(19)	0.27598(19)	0.27443(26)	0.27459(19)	0.27575(19)	0.27805(20)
Z_{32}/Z_A^2	0.036609(46)	0.038786(47)	0.040972(56)	0.043468(50)	0.045989(50)	0.048651(52)
Z_{33}/Z_A^2	0.86908(20)	0.88714(18)	0.90343(12)	0.91920(14)	0.93371(12)	0.94751(12)
Z_{44}/Z_A^2	0.91443(22)	0.93129(20)	0.94668(15)	0.96202(17)	0.97625(15)	0.98993(15)
Z_{45}/Z_A^2	−0.035998(53)	−0.038575(53)	−0.041093(60)	−0.043899(53)	−0.046662(55)	−0.049514(56)
Z_{54}/Z_A^2	−0.25274(17)	−0.24885(17)	−0.24622(23)	−0.24494(18)	−0.24461(17)	−0.24522(17)
Z_{55}/Z_A^2	1.043492(53)	1.034652(47)	1.026738(50)	1.019273(43)	1.012344(36)	1.005655(35)
Z_A/Z_S	1.08747(14)	1.07744(12)	1.068669(67)	1.060647(73)	1.053495(59)	1.046974(54)

Table B.3: Same as table B.1 but for the C2S ensemble for $am_q^{\rm val} = 0.01$.

$a\mu$	0.83304	0.90246	0.97188	1.0413	1.11072	1.18014
Z_{11}/Z_A^2	0.958988(97)	0.955260(77)	0.951956(63)	0.948999(54)	0.946321(49)	0.943862(44)
Z_{22}/Z_A^2	1.057128(69)	1.054565(53)	1.052259(39)	1.050256(31)	1.048545(29)	1.047115(26)
Z_{23}/Z_A^2	0.36433(11)	0.343648(95)	0.325562(76)	0.309833(61)	0.296224(48)	0.284531(41)
Z_{32}/Z_A^2	0.019120(23)	0.019958(21)	0.020854(21)	0.021806(16)	0.022810(13)	0.023861(14)
Z_{33}/Z_A^2	0.63286(11)	0.667899(93)	0.699247(92)	0.727410(91)	0.752780(79)	0.775695(66)
Z_{44}/Z_A^2	0.71349(12)	0.742350(80)	0.768119(85)	0.791317(91)	0.812296(88)	0.831380(81)
Z_{45}/Z_A^2	−0.011925(30)	−0.013791(24)	−0.015561(21)	−0.017270(20)	−0.018933(19)	−0.020564(19)
Z_{54}/Z_A^2	−0.348785(70)	−0.325324(55)	−0.305376(49)	−0.288383(46)	−0.273897(36)	−0.261559(33)
Z_{55}/Z_A^2	1.200961(89)	1.174212(71)	1.151620(52)	1.132360(44)	1.115798(39)	1.101441(33)
Z_A/Z_S	1.26232(14)	1.23099(11)	1.204535(86)	1.181992(83)	1.162686(65)	1.146034(51)
$a\mu$	1.24956	1.31898	1.3884	1.45782	1.52724	1.59666
Z_{11}/Z_A^2	0.941580(40)	0.939424(36)	0.937357(31)	0.935354(27)	0.933384(26)	0.931427(25)
Z_{22}/Z_A^2	1.045950(25)	1.045024(24)	1.044326(22)	1.043838(20)	1.043536(16)	1.043405(14)
Z_{23}/Z_A^2	0.274557(43)	0.266140(46)	0.259132(48)	0.253406(45)	0.248829(41)	0.245282(37)
Z_{32}/Z_A^2	0.024952(15)	0.026087(15)	0.027273(15)	0.028508(14)	0.029793(14)	0.031128(14)
Z_{33}/Z_A^2	0.796468(59)	0.815346(53)	0.832571(45)	0.848340(39)	0.862844(35)	0.876249(30)
Z_{44}/Z_A^2	0.848835(74)	0.864868(68)	0.879678(59)	0.893421(53)	0.906244(50)	0.918274(45)
Z_{45}/Z_A^2	−0.022173(20)	−0.023775(20)	−0.025379(19)	−0.026991(18)	−0.028617(17)	−0.030261(16)
Z_{54}/Z_A^2	−0.251073(35)	−0.242200(35)	−0.234755(36)	−0.228569(34)	−0.223491(31)	−0.219390(29)
Z_{55}/Z_A^2	1.088899(29)	1.077860(21)	1.068094(13)	1.0593997(83)	1.051604(11)	1.044563(12)
Z_A/Z_S	1.131563(42)	1.118926(33)	1.107811(23)	1.097986(20)	1.089246(19)	1.081423(16)

Table B.4: Same as table B.1 but for the M0M ensemble for $am_q^{\mathrm{val}} = 0.0133$.

$a\mu$	0.83304	0.90246	0.97188	1.0413	1.11072	1.18014
Z_{11}/Z_A^2	0.95866(27)	0.95479(24)	0.95131(20)	0.94835(17)	0.94594(14)	0.94335(15)
Z_{22}/Z_A^2	1.05863(24)	1.05561(17)	1.05283(11)	1.05060(10)	1.04902(10)	1.047373(78)
Z_{23}/Z_A^2	0.36666(42)	0.34511(40)	0.32651(31)	0.31022(27)	0.29709(24)	0.28490(15)
Z_{32}/Z_A^2	0.01927(13)	0.02016(11)	0.020953(63)	0.021960(45)	0.022876(56)	0.023976(33)
Z_{33}/Z_A^2	0.63178(68)	0.66790(65)	0.69929(51)	0.72810(37)	0.75237(37)	0.77607(16)
Z_{44}/Z_A^2	0.71203(63)	0.74187(62)	0.76777(49)	0.79149(33)	0.81164(35)	0.83146(18)
Z_{45}/Z_A^2	−0.01197(11)	−0.013999(81)	−0.015696(78)	−0.017368(41)	−0.019037(56)	−0.020694(43)
Z_{54}/Z_A^2	−0.35142(49)	−0.32709(41)	−0.30657(35)	−0.28915(28)	−0.27495(26)	−0.26220(20)
Z_{55}/Z_A^2	1.20251(48)	1.174820(78)	1.15166(16)	1.13231(16)	1.11609(15)	1.101308(99)
Z_A/Z_S	1.2629(14)	1.2305(12)	1.20420(72)	1.18148(47)	1.16311(51)	1.14592(24)
$a\mu$	1.24956	1.31898	1.3884	1.45782	1.52724	1.59666
Z_{11}/Z_A^2	0.94111(13)	0.93899(11)	0.937051(99)	0.93495(10)	0.932999(96)	0.931072(90)
Z_{22}/Z_A^2	1.046175(55)	1.045212(37)	1.044577(53)	1.044027(36)	1.043714(34)	1.043592(32)
Z_{23}/Z_A^2	0.27494(13)	0.26650(12)	0.25961(19)	0.25385(12)	0.24930(13)	0.24578(13)
Z_{32}/Z_A^2	0.025059(26)	0.026205(25)	0.027322(35)	0.028620(30)	0.029916(29)	0.031257(27)
Z_{33}/Z_A^2	0.79677(15)	0.81571(16)	0.83239(16)	0.84859(15)	0.86306(15)	0.87648(14)
Z_{44}/Z_A^2	0.84892(15)	0.86504(15)	0.87937(18)	0.89355(15)	0.90638(15)	0.91844(14)
Z_{45}/Z_A^2	−0.022302(39)	−0.023901(32)	−0.025446(33)	−0.027116(33)	−0.028756(33)	−0.030412(30)
Z_{54}/Z_A^2	−0.25166(17)	−0.24272(14)	−0.23537(20)	−0.22911(14)	−0.22405(14)	−0.21994(15)
Z_{55}/Z_A^2	1.088774(81)	1.077719(65)	1.068125(64)	1.059205(33)	1.051443(40)	1.044415(36)
Z_A/Z_S	1.13157(10)	1.11884(12)	1.10792(13)	1.09803(10)	1.08928(11)	1.08143(11)

Table B.5: Same as table B.1 but for the M1S ensemble for $am_q^{\mathrm{val}} = 0.004$.

$a\mu$	0.83304	0.90246	0.97188	1.0413	1.11072	1.18014
Z_{11}/Z_A^2	0.95882(22)	0.95467(28)	0.95137(21)	0.94845(18)	0.94618(12)	0.943542(87)
Z_{22}/Z_A^2	1.05787(21)	1.05505(25)	1.05259(14)	1.05040(11)	1.048925(97)	1.047247(64)
Z_{23}/Z_A^2	0.36442(27)	0.34387(35)	0.32565(19)	0.30979(16)	0.29637(13)	0.28464(20)
Z_{32}/Z_A^2	0.01905(11)	0.019983(93)	0.020959(69)	0.021904(51)	0.022841(73)	0.023947(43)
Z_{33}/Z_A^2	0.63323(69)	0.66850(84)	0.69999(46)	0.72813(38)	0.75302(39)	0.77602(31)
Z_{44}/Z_A^2	0.71353(69)	0.74286(83)	0.76871(54)	0.79182(42)	0.81237(43)	0.83152(29)
Z_{45}/Z_A^2	−0.01181(13)	−0.01395(14)	−0.01574(10)	−0.017382(81)	−0.018987(95)	−0.020660(63)
Z_{54}/Z_A^2	−0.34923(38)	−0.32582(39)	−0.30562(23)	−0.28849(18)	−0.27411(18)	−0.26180(19)
Z_{55}/Z_A^2	1.20114(29)	1.17430(24)	1.15153(11)	1.13202(13)	1.11582(18)	1.10120(12)
Z_A/Z_S	1.2599(10)	1.22880(87)	1.20273(64)	1.18065(50)	1.16242(29)	1.14564(32)
$a\mu$	1.24956	1.31898	1.3884	1.45782	1.52724	1.59666
Z_{11}/Z_A^2	0.941317(63)	0.939163(54)	0.937235(92)	0.935166(39)	0.933226(30)	0.931291(24)
Z_{22}/Z_A^2	1.046103(36)	1.045117(35)	1.044408(62)	1.043985(56)	1.043666(71)	1.043536(74)
Z_{23}/Z_A^2	0.27466(13)	0.26619(15)	0.25902(12)	0.25354(16)	0.24899(16)	0.24545(17)
Z_{32}/Z_A^2	0.025044(44)	0.026201(47)	0.027326(55)	0.028634(52)	0.029921(56)	0.031255(55)
Z_{33}/Z_A^2	0.79680(26)	0.81578(29)	0.83283(29)	0.84882(27)	0.86329(28)	0.87669(25)
Z_{44}/Z_A^2	0.84903(29)	0.86517(31)	0.87984(27)	0.89384(28)	0.90668(30)	0.91874(27)
Z_{45}/Z_A^2	−0.022298(54)	−0.023908(52)	−0.025438(66)	−0.027131(50)	−0.028758(57)	−0.030402(59)
Z_{54}/Z_A^2	−0.25126(17)	−0.24230(18)	−0.23471(12)	−0.22872(15)	−0.22362(14)	−0.21951(14)
Z_{55}/Z_A^2	1.088655(92)	1.07757(10)	1.06792(11)	1.059226(94)	1.051439(87)	1.044419(79)
Z_A/Z_S	1.13121(21)	1.11859(19)	1.10771(17)	1.09773(15)	1.08904(16)	1.08123(13)

Table B.6: Same as table B.1 but for the M2S ensemble for $am_q^{\mathrm{val}} = 0.006$.

$a\mu$	0.83304	0.90246	0.97188	1.0413	1.11072	1.18014
Z_{11}/Z_A^2	0.95828(42)	0.95462(40)	0.95138(35)	0.94851(29)	0.94589(26)	0.94340(20)
Z_{22}/Z_A^2	1.05754(21)	1.05471(15)	1.05237(10)	1.05041(12)	1.048624(90)	1.047155(83)
Z_{23}/Z_A^2	0.36552(53)	0.34385(41)	0.32570(37)	0.31005(34)	0.29653(28)	0.28468(28)
Z_{32}/Z_A^2	0.019240(78)	0.020098(98)	0.020971(75)	0.021903(70)	0.022899(56)	0.023887(42)
Z_{33}/Z_A^2	0.63244(77)	0.66864(54)	0.69997(43)	0.72786(40)	0.75295(23)	0.77586(38)
Z_{44}/Z_A^2	0.71290(66)	0.74271(53)	0.76851(40)	0.79152(37)	0.81223(23)	0.83130(38)
Z_{45}/Z_A^2	−0.01207(12)	−0.01379(11)	−0.015619(83)	−0.017364(78)	−0.018993(66)	−0.020594(43)
Z_{54}/Z_A^2	−0.34975(49)	−0.32602(47)	−0.30588(41)	−0.28890(38)	−0.27440(31)	−0.26193(29)
Z_{55}/Z_A^2	1.20103(43)	1.17450(46)	1.15165(34)	1.13233(26)	1.11573(19)	1.10121(20)
Z_A/Z_S	1.2590(15)	1.22834(56)	1.20252(33)	1.18059(33)	1.16145(32)	1.14525(31)
$a\mu$	1.24956	1.31898	1.3884	1.45782	1.52724	1.59666
Z_{11}/Z_A^2	0.94115(19)	0.93903(17)	0.93710(16)	0.93506(13)	0.93311(12)	0.93118(11)
Z_{22}/Z_A^2	1.045938(64)	1.045015(56)	1.044340(52)	1.043868(41)	1.043563(32)	1.043433(34)
Z_{23}/Z_A^2	0.27469(28)	0.26632(28)	0.25932(21)	0.25359(21)	0.24904(21)	0.24550(21)
Z_{32}/Z_A^2	0.024974(38)	0.026116(32)	0.027334(41)	0.028542(25)	0.029816(25)	0.031145(27)
Z_{33}/Z_A^2	0.79653(37)	0.81531(37)	0.83264(11)	0.84830(24)	0.86273(23)	0.87610(20)
Z_{44}/Z_A^2	0.84870(36)	0.86468(36)	0.87962(14)	0.89328(25)	0.90604(24)	0.91805(21)
Z_{45}/Z_A^2	−0.022195(37)	−0.023802(32)	−0.025418(42)	−0.027027(28)	−0.028643(28)	−0.030285(28)
Z_{54}/Z_A^2	−0.25140(29)	−0.24255(29)	−0.23510(22)	−0.22891(23)	−0.22383(23)	−0.21973(22)
Z_{55}/Z_A^2	1.08868(16)	1.07767(13)	1.067983(81)	1.05932(12)	1.051520(89)	1.044481(76)
Z_A/Z_S	1.13106(26)	1.11870(24)	1.10756(12)	1.09791(15)	1.08925(14)	1.08145(12)

Table B.7: Same as table B.1 but for the M3S ensemble for $am_q^{\rm val} = 0.008$.

$a\mu$	0.74048	0.78676	0.83304	0.87932	0.9256
Z_{11}/Z_A^2	0.97058(44)	0.96714(43)	0.96417(31)	0.96155(21)	0.95914(20)
Z_{22}/Z_A^2	1.06145(47)	1.05897(36)	1.05663(22)	1.05443(12)	1.052470(59)
Z_{23}/Z_A^2	0.37433(51)	0.35796(51)	0.34320(36)	0.32981(36)	0.31723(29)
Z_{32}/Z_A^2	0.01734(15)	0.017710(78)	0.018264(60)	0.018852(84)	0.019339(66)
Z_{33}/Z_A^2	0.60909(78)	0.63519(95)	0.65877(80)	0.68059(77)	0.70144(50)
Z_{44}/Z_A^2	0.69546(93)	0.7167(11)	0.73580(83)	0.75349(76)	0.77059(52)
Z_{45}/Z_A^2	−0.00927(14)	−0.01052(18)	−0.01164(16)	−0.01272(13)	−0.01391(10)
Z_{54}/Z_A^2	−0.36206(57)	−0.34311(47)	−0.32635(25)	−0.31134(27)	−0.29755(26)
Z_{55}/Z_A^2	1.23021(85)	1.20821(54)	1.18901(26)	1.17173(18)	1.15615(27)
Z_A/Z_S	1.2876(14)	1.26232(65)	1.24121(75)	1.2213(10)	1.20291(51)
$a\mu$	0.97188	1.01816	1.06444	1.11072	1.157
Z_{11}/Z_A^2	0.95701(21)	0.95499(15)	0.95309(11)	0.95130(11)	0.949629(86)
Z_{22}/Z_A^2	1.05085(10)	1.049255(47)	1.047825(11)	1.046592(11)	1.045533(30)
Z_{23}/Z_A^2	0.30588(21)	0.29543(17)	0.28624(15)	0.27793(14)	0.27047(11)
Z_{32}/Z_A^2	0.019872(39)	0.020425(25)	0.021006(26)	0.021649(29)	0.022316(25)
Z_{33}/Z_A^2	0.72062(39)	0.73859(30)	0.75488(19)	0.77017(20)	0.78452(20)
Z_{44}/Z_A^2	0.78627(42)	0.80084(36)	0.81413(22)	0.82673(21)	0.83866(19)
Z_{45}/Z_A^2	−0.014951(79)	−0.015945(54)	−0.016942(44)	−0.017995(32)	−0.019037(19)
Z_{54}/Z_A^2	−0.28537(23)	−0.27419(19)	−0.26442(16)	−0.25563(15)	−0.24776(14)
Z_{55}/Z_A^2	1.14256(30)	1.13008(13)	1.118872(69)	1.108751(42)	1.099595(76)
Z_A/Z_S	1.18710(36)	1.17325(29)	1.16076(22)	1.14953(16)	1.13945(12)

Table B.8: Same as table B.1 but for the F1M ensemble for $am_q^{\mathrm{val}} = 0.0021$.

	C-M	C-S	M-M	M-S	F-M
a^{-1} [GeV]	1.7295(38)	1.7848(50)	2.3586(70)	2.3833(86)	2.708(10)
Z_{11}/Z_A^2	0.93258(26)(0)	0.93444(77)(1)	0.96021(51)(2)	0.9579(12)(0)	0.97120(69)(47)
Z_{22}/Z_S^2	1.0703(26)(0)	1.0788(37)(2)	1.1185(18)(0)	1.1237(64)(1)	1.1405(27)(18)
Z_{23}/Z_S^2	-0.06092(49)(8)	-0.0603(10)(0)	-0.04045(55)(5)	-0.0387(10)(0)	-0.03054(62)(27)
Z_{32}/Z_S^2	0.0343(31)(3)	0.0403(74)(1)	0.1135(47)(1)	0.120(11)(0)	0.1522(57)(6)
Z_{33}/Z_S^2	1.6094(53)(13)	1.643(13)(0)	1.9107(85)(9)	1.948(21)(0)	2.064(10)(6)
Z_{44}/Z_S^2	1.0113(21)(2)	1.0161(35)(2)	1.0134(11)(0)	1.0160(51)(0)	1.0122(21)(16)
Z_{45}/Z_S^2	-0.07270(48)(4)	-0.07384(98)(6)	-0.06217(46)(7)	-0.06268(98)(0)	-0.05774(49)(44)
Z_{54}/Z_S^2	-0.23507(99)(38)	-0.2417(31)(1)	-0.2851(20)(2)	-0.2940(46)(2)	-0.3119(22)(15)
Z_{55}/Z_S^2	1.4762(38)(9)	1.4994(96)(6)	1.6718(64)(5)	1.699(15)(0)	1.7670(74)(55)

Table B.9: Elements of $Z_{ij}/Z_{A/S}^2$ extrapolated to the massless limit. All results are provided in RI/SMOM$^{(\gamma_\mu,\gamma_\mu)}$ at $\mu = 2.0\,\text{GeV}$ in the SUSY basis. The first parenthesis is the statistical error and the second is the systematic error.

	C-M	C-S	M-M	M-S	F-M
a^{-1} [GeV]	1.7295(38)	1.7848(50)	2.3586(70)	2.3833(86)	2.708(10)
Z_{11}/Z_A^2	0.92273(29)(1)	0.92491(52)(0)	0.94913(20)(0)	0.94752(86)(2)	0.95950(43)(33)
Z_{22}/Z_S^2	1.05048(77)(4)	1.0519(13)(0)	1.08128(96)(1)	1.0830(21)(0)	1.0964(11)(6)
Z_{23}/Z_S^2	-0.07511(48)(3)	-0.07280(82)(2)	-0.04932(29)(0)	-0.04900(66)(1)	-0.04007(40)(17)
Z_{32}/Z_S^2	-0.0228(16)(1)	-0.0162(45)(0)	0.0447(28)(1)	0.0465(63)(1)	0.0746(37)(0)
Z_{33}/Z_S^2	1.3816(30)(7)	1.4014(83)(2)	1.5913(50)(6)	1.603(11)(0)	1.6981(67)(17)
Z_{44}/Z_S^2	1.02458(44)(3)	1.02303(97)(4)	1.01873(49)(7)	1.0201(14)(0)	1.01595(76)(71)
Z_{45}/Z_S^2	-0.07967(51)(2)	-0.07835(69)(1)	-0.06134(25)(1)	-0.06193(46)(0)	-0.05599(23)(24)
Z_{54}/Z_S^2	-0.18458(58)(19)	-0.1880(18)(0)	-0.2130(11)(1)	-0.2162(26)(1)	-0.2305(15)(5)
Z_{55}/Z_S^2	1.3170(21)(5)	1.3310(60)(1)	1.4581(36)(3)	1.4673(80)(5)	1.5267(46)(17)

Table B.10: Elements of $Z_{ij}/Z_{A/S}^2$ extrapolated to the massless limit. All results are provided in RI/SMOM$^{(\gamma_\mu,\gamma_\mu)}$ at $\mu = 2.5\,\text{GeV}$ in the SUSY basis. The first parenthesis is the statistical error and the second is the systematic error.

	C-M	C-S	M-M	M-S	F-M
a^{-1} [GeV]	1.7295(38)	1.7848(50)	2.3586(70)	2.3833(86)	2.708(10)
Z_{11}/Z_A^2	0.91427(17)(0)	0.91641(55)(0)	0.94123(17)(1)	0.94044(67)(0)	0.95157(31)(27)
Z_{22}/Z_S^2	1.03795(18)(4)	1.03874(73)(2)	1.05744(45)(5)	1.0596(10)(0)	1.06947(54)(36)
Z_{23}/Z_S^2	-0.08818(26)(2)	-0.08564(98)(0)	-0.05786(22)(0)	-0.05804(54)(0)	-0.04741(25)(25)
Z_{32}/Z_S^2	-0.0589(10)(0)	-0.0532(31)(0)	0.0036(18)(0)	0.0052(44)(0)	0.0300(24)(1)
Z_{33}/Z_S^2	1.2568(19)(2)	1.2711(59)(2)	1.4093(34)(4)	1.4206(79)(1)	1.4919(44)(11)
Z_{44}/Z_S^2	1.03009(18)(0)	1.02856(45)(0)	1.02098(20)(0)	1.02223(60)(0)	1.01811(29)(38)
Z_{45}/Z_S^2	-0.08895(23)(2)	-0.08683(80)(0)	-0.06453(14)(1)	-0.06486(36)(0)	-0.05716(16)(22)
Z_{54}/Z_S^2	-0.16199(30)(9)	-0.1636(11)(0)	-0.17286(72)(9)	-0.1757(17)(0)	-0.1842(10)(3)
Z_{55}/Z_S^2	1.2268(12)(1)	1.2368(41)(1)	1.3299(24)(2)	1.3389(57)(1)	1.3852(31)(10)

Table B.11: Elements of $Z_{ij}/Z_{A/S}^2$ extrapolated to the massless limit. All results are provided in RI/SMOM$^{(\gamma_\mu,\gamma_\mu)}$ at $\mu = 3.0\,\text{GeV}$ in the SUSY basis. The first parenthesis is the statistical error and the second is the systematic error.

	C-M	C-S	M-M	M-S	F-M
a^{-1} [GeV]	1.7848(50)	1.7295(38)	2.3833(86)	2.3586(70)	2.708(10)
σ_{22}	1.1866(15)	1.18862(99)	1.2055(27)	1.1980(16)	1.2047(16)
σ_{23}	-0.020560(36)	-0.02201(14)	-0.01408(33)	-0.01294(22)	-0.01165(18)
σ_{32}	-0.09661(26)	-0.09870(19)	-0.09318(55)	-0.09034(41)	-0.08994(17)
σ_{33}	0.94800(88)	0.95149(38)	0.92958(89)	0.93208(35)	0.92586(49)
σ_{44}	1.2441(30)	1.2447(15)	1.2844(46)	1.2748(21)	1.2910(23)
σ_{45}	-0.00982(21)	-0.01235(22)	-0.00146(54)	-0.00159(23)	0.00067(30)
σ_{54}	0.0439(12)	0.04063(45)	0.0711(17)	0.06801(83)	0.0774(10)
σ_{55}	1.017341(75)	1.018409(16)	1.00827(44)	1.00994(39)	1.00838(48)

Table B.12: Chirally-allowed elements of the non-perturbative scaling matrix $\sigma(3\,\mathrm{GeV}, 2\,\mathrm{GeV})$ using chirally extrapolated Z-factors in the RI/SMOM$^{(\gamma_\mu,\gamma_\mu)}$ scheme.

$a\mu$	1.11072	1.20328	1.29584	1.3884	1.48096	1.57352
Z_{11}/Z_A^2	0.93235(12)	0.930948(88)	0.929722(89)	0.928614(68)	0.927563(67)	0.926531(48)
Z_{22}/Z_A^2	1.039486(30)	1.038385(23)	1.037520(30)	1.036817(28)	1.036436(27)	1.036179(21)
Z_{23}/Z_A^2	0.27092(21)	0.25411(13)	0.24089(15)	0.23032(11)	0.22235(12)	0.21618(11)
Z_{32}/Z_A^2	0.023380(29)	0.024540(24)	0.025808(19)	0.027050(22)	0.028394(22)	0.029717(20)
Z_{33}/Z_A^2	0.79345(24)	0.82453(27)	0.85076(16)	0.87279(19)	0.89181(12)	0.90802(12)
Z_{44}/Z_A^2	0.84305(24)	0.86848(30)	0.89036(18)	0.90903(21)	0.92559(13)	0.93996(13)
Z_{45}/Z_A^2	−0.020341(39)	−0.022309(37)	−0.024207(29)	−0.025963(29)	−0.027728(22)	−0.029384(21)
Z_{54}/Z_A^2	−0.25178(22)	−0.23565(16)	−0.22275(17)	−0.21229(15)	−0.20406(14)	−0.19742(12)
Z_{55}/Z_A^2	1.077851(72)	1.061843(56)	1.048719(28)	1.037957(15)	1.0289812(85)	1.021435(12)
Z_A/Z_S	1.12682(11)	1.10782(17)	1.09227(10)	1.07960(10)	1.068979(79)	1.060187(69)
$a\mu$	1.66608	1.75864	1.8512	1.94376	2.03632	2.12888
Z_{11}/Z_A^2	0.925433(56)	0.924268(40)	0.922942(48)	0.921474(35)	0.919730(43)	0.917743(31)
Z_{22}/Z_A^2	1.036183(22)	1.036271(14)	1.036590(18)	1.0369620(93)	1.037529(19)	1.0381303(82)
Z_{23}/Z_A^2	0.21182(10)	0.208671(93)	0.206929(91)	0.205998(81)	0.206181(94)	0.206967(72)
Z_{32}/Z_A^2	0.031139(23)	0.032547(17)	0.034062(19)	0.035572(12)	0.037212(17)	0.038864(11)
Z_{33}/Z_A^2	0.922341(74)	0.93482(11)	0.946051(44)	0.956100(70)	0.965466(23)	0.974045(47)
Z_{44}/Z_A^2	0.952997(87)	0.96454(11)	0.975220(53)	0.984853(72)	0.993996(31)	1.002350(48)
Z_{45}/Z_A^2	−0.031085(25)	−0.032721(19)	−0.034427(20)	−0.036092(13)	−0.037861(18)	−0.039613(12)
Z_{54}/Z_A^2	−0.19232(11)	−0.18828(11)	−0.185421(98)	−0.183269(88)	−0.182041(95)	−0.181339(79)
Z_{55}/Z_A^2	1.0149373(73)	1.009251(29)	1.004184(13)	0.999548(20)	0.995166(11)	0.990929(15)
Z_A/Z_S	1.052675(41)	1.046296(64)	1.040764(26)	1.035939(41)	1.031622(15)	1.027768(25)

Table B.13: Values of Z_{ij}/Z_A^2 for chirally non-vanishing matrix elements for all the simulated momenta (in lattice units) on the C0M ensemble for $am_q^{\text{val}} = 0.0181$ using the heavy-light action combination. All values are given in the RI/SMOM$^{(\gamma_\mu,\gamma_\mu)}$ scheme and in the SUSY basis.

$a\mu$	1.11072	1.20328	1.29584	1.3884	1.48096	1.57352
Z_{11}/Z_A^2	0.93277(15)	0.93124(12)	0.930126(74)	0.929054(64)	0.927993(66)	0.926935(75)
Z_{22}/Z_A^2	1.04038(18)	1.03899(15)	1.03802(11)	1.037284(86)	1.036678(51)	1.036422(52)
Z_{23}/Z_A^2	0.26941(31)	0.25280(31)	0.23984(23)	0.22944(21)	0.22120(16)	0.21536(19)
Z_{32}/Z_A^2	0.023533(60)	0.024719(83)	0.025975(71)	0.027204(52)	0.028434(30)	0.029785(44)
Z_{33}/Z_A^2	0.79732(45)	0.82769(58)	0.85301(43)	0.87487(38)	0.89351(20)	0.90942(16)
Z_{44}/Z_A^2	0.84623(38)	0.87123(52)	0.89229(41)	0.91090(36)	0.92706(20)	0.94129(18)
Z_{45}/Z_A^2	−0.020574(66)	−0.022580(71)	−0.024397(60)	−0.026133(46)	−0.027803(28)	−0.029512(44)
Z_{54}/Z_A^2	−0.25087(32)	−0.23459(27)	−0.22177(18)	−0.21132(17)	−0.20294(16)	−0.19649(15)
Z_{55}/Z_A^2	1.07794(22)	1.06140(19)	1.04849(14)	1.03777(11)	1.028752(55)	1.021205(69)
Z_A/Z_S	1.12245(67)	1.10425(42)	1.09043(33)	1.07822(23)	1.06766(14)	1.05934(11)
$a\mu$	1.66608	1.75864	1.8512	1.94376	2.03632	2.12888
Z_{11}/Z_A^2	0.925846(69)	0.924697(65)	0.923436(58)	0.921893(64)	0.920196(62)	0.918195(61)
Z_{22}/Z_A^2	1.036338(52)	1.036466(40)	1.036670(35)	1.037075(36)	1.037586(35)	1.038206(38)
Z_{23}/Z_A^2	0.21089(18)	0.20789(16)	0.20589(12)	0.20519(13)	0.20531(14)	0.20618(15)
Z_{32}/Z_A^2	0.031162(48)	0.032597(45)	0.034040(23)	0.035594(41)	0.037187(41)	0.038859(42)
Z_{33}/Z_A^2	0.92361(12)	0.93608(12)	0.947143(99)	0.95719(11)	0.96635(11)	0.974959(88)
Z_{44}/Z_A^2	0.95416(14)	0.96576(14)	0.97621(11)	0.98591(14)	0.99484(13)	1.00324(12)
Z_{45}/Z_A^2	−0.031145(47)	−0.032806(43)	−0.034422(25)	−0.036135(42)	−0.037854(41)	−0.039628(42)
Z_{54}/Z_A^2	−0.19130(15)	−0.18739(13)	−0.18431(12)	−0.18231(12)	−0.18103(12)	−0.18039(13)
Z_{55}/Z_A^2	1.014744(58)	1.009133(48)	1.004127(30)	0.999458(41)	0.995136(31)	0.990901(30)
Z_A/Z_S	1.051968(93)	1.045594(85)	1.040131(63)	1.035367(53)	1.031159(48)	1.027316(38)

Table B.14: Same as table B.13 but for the C1S ensemble for $am_q^{\mathrm{val}} = 0.005$.

$a\mu$	1.11072	1.20328	1.29584	1.3884	1.48096	1.57352
Z_{11}/Z_A^2	0.93185(12)	0.93048(11)	0.929401(83)	0.928444(80)	0.927537(90)	0.926536(82)
Z_{22}/Z_A^2	1.03959(11)	1.03832(10)	1.037517(83)	1.036930(75)	1.036494(75)	1.036310(69)
Z_{23}/Z_A^2	0.26982(44)	0.25327(34)	0.24010(26)	0.22975(24)	0.22159(25)	0.21563(22)
Z_{32}/Z_A^2	0.023468(66)	0.024744(61)	0.025956(51)	0.027198(54)	0.028466(44)	0.029863(52)
Z_{33}/Z_A^2	0.79516(37)	0.82618(36)	0.85228(26)	0.87427(26)	0.89305(14)	0.90947(23)
Z_{44}/Z_A^2	0.84414(27)	0.86965(31)	0.89150(27)	0.91035(26)	0.92664(14)	0.94132(25)
Z_{45}/Z_A^2	−0.020496(68)	−0.022506(63)	−0.024352(59)	−0.026151(63)	−0.027824(48)	−0.029560(59)
Z_{54}/Z_A^2	−0.25117(38)	−0.23509(30)	−0.22224(22)	−0.21186(21)	−0.20343(23)	−0.19689(20)
Z_{55}/Z_A^2	1.07677(20)	1.06086(18)	1.04803(11)	1.037394(88)	1.028567(67)	1.021053(65)
Z_A/Z_S	1.12304(48)	1.10571(27)	1.09063(21)	1.07819(19)	1.067867(89)	1.05920(14)
$a\mu$	1.66608	1.75864	1.8512	1.94376	2.03632	2.12888
Z_{11}/Z_A^2	0.925516(76)	0.924365(72)	0.923114(77)	0.921607(69)	0.919905(70)	0.917914(70)
Z_{22}/Z_A^2	1.036285(75)	1.036416(69)	1.036664(62)	1.037092(64)	1.037614(61)	1.038243(61)
Z_{23}/Z_A^2	0.21126(22)	0.20830(21)	0.20640(22)	0.20571(21)	0.20580(21)	0.20670(21)
Z_{32}/Z_A^2	0.031240(52)	0.032663(52)	0.034094(47)	0.035674(53)	0.037272(53)	0.038950(54)
Z_{33}/Z_A^2	0.92351(19)	0.93588(16)	0.946789(99)	0.95697(13)	0.96620(11)	0.97481(11)
Z_{44}/Z_A^2	0.95409(22)	0.96561(19)	0.97590(12)	0.98575(16)	0.99474(15)	1.00316(15)
Z_{45}/Z_A^2	−0.031210(58)	−0.032862(56)	−0.034475(50)	−0.036215(56)	−0.037939(56)	−0.039713(57)
Z_{54}/Z_A^2	−0.19178(20)	−0.18786(19)	−0.18489(20)	−0.18287(19)	−0.18157(19)	−0.18094(19)
Z_{55}/Z_A^2	1.014648(57)	1.009037(44)	1.004055(35)	0.999394(34)	0.995060(28)	0.990852(25)
Z_A/Z_S	1.05192(12)	1.045669(96)	1.040306(51)	1.035502(59)	1.031252(47)	1.027423(44)

Table B.15: Same as table B.13 but for the C2S ensemble for $am_q^{\mathrm{val}} = 0.01$.

$a\mu$	0.83304	0.90246	0.97188	1.0413	1.11072	1.18014
Z_{11}/Z_A^2	0.953269(94)	0.951003(74)	0.949124(61)	0.947545(52)	0.946196(48)	0.945021(45)
Z_{22}/Z_A^2	1.044946(70)	1.042524(55)	1.040366(42)	1.038503(33)	1.036908(30)	1.035567(27)
Z_{23}/Z_A^2	0.29383(12)	0.27302(11)	0.255221(87)	0.240061(67)	0.227183(53)	0.216304(46)
Z_{32}/Z_A^2	0.018498(27)	0.019059(23)	0.019657(24)	0.020289(18)	0.020952(15)	0.021641(16)
Z_{33}/Z_A^2	0.728485(96)	0.761444(75)	0.789991(87)	0.814818(91)	0.836467(76)	0.855400(66)
Z_{44}/Z_A^2	0.79345(13)	0.819367(68)	0.841871(90)	0.861577(98)	0.878901(92)	0.894224(87)
Z_{45}/Z_A^2	−0.013442(34)	−0.014943(25)	−0.016308(24)	−0.017582(23)	−0.018777(21)	−0.019917(21)
Z_{54}/Z_A^2	−0.273254(74)	−0.252689(59)	−0.235340(58)	−0.220667(53)	−0.208233(44)	−0.197700(39)
Z_{55}/Z_A^2	1.129055(77)	1.108252(68)	1.091028(46)	1.076635(34)	1.064503(29)	1.054200(28)
Z_A/Z_S	1.17572(11)	1.151868(83)	1.132033(68)	1.115418(73)	1.101459(56)	1.089658(45)
$a\mu$	1.24956	1.31898	1.3884	1.45782	1.52724	1.59666
Z_{11}/Z_A^2	0.943979(41)	0.943027(37)	0.942133(32)	0.941276(29)	0.940430(28)	0.939579(27)
Z_{22}/Z_A^2	1.034456(26)	1.033548(24)	1.032827(22)	1.032275(20)	1.031866(16)	1.031583(14)
Z_{23}/Z_A^2	0.207157(48)	0.199517(54)	0.193189(56)	0.188014(54)	0.183835(50)	0.180512(46)
Z_{32}/Z_A^2	0.022351(17)	0.023084(18)	0.023843(17)	0.024629(16)	0.025440(16)	0.026274(15)
Z_{33}/Z_A^2	0.872039(62)	0.886700(57)	0.899693(51)	0.911250(46)	0.921589(43)	0.930894(38)
Z_{44}/Z_A^2	0.907868(81)	0.920066(76)	0.931047(68)	0.940981(61)	0.950021(58)	0.958297(54)
Z_{45}/Z_A^2	−0.021011(22)	−0.022074(22)	−0.023115(21)	−0.024142(20)	−0.025161(18)	−0.026174(17)
Z_{54}/Z_A^2	−0.188774(41)	−0.181219(43)	−0.174850(46)	−0.169508(44)	−0.165048(41)	−0.161345(39)
Z_{55}/Z_A^2	1.045382(26)	1.037775(18)	1.031177(11)	1.0254224(84)	1.020359(12)	1.015865(12)
Z_A/Z_S	1.079593(38)	1.070978(30)	1.063541(22)	1.057094(20)	1.051465(21)	1.046517(19)

Table B.16: Same as table B.13 but for the M0M ensemble for $am_q^{\mathrm{val}} = 0.0133$.

$a\mu$	0.83304	0.90246	0.97188	1.0413	1.11072	1.18014
Z_{11}/Z_A^2	0.95261(24)	0.95035(26)	0.94825(21)	0.94670(18)	0.94554(15)	0.94438(15)
Z_{22}/Z_A^2	1.04620(23)	1.04341(17)	1.04073(10)	1.03867(11)	1.03719(10)	1.035775(85)
Z_{23}/Z_A^2	0.29609(48)	0.27485(45)	0.25641(39)	0.24057(33)	0.22807(24)	0.21695(20)
Z_{32}/Z_A^2	0.018755(85)	0.01925(12)	0.019795(73)	0.020483(39)	0.021101(32)	0.021810(35)
Z_{33}/Z_A^2	0.72788(66)	0.76104(76)	0.78974(63)	0.81543(43)	0.83631(30)	0.85561(20)
Z_{44}/Z_A^2	0.79243(60)	0.81856(72)	0.84127(57)	0.86166(37)	0.87853(26)	0.89420(22)
Z_{45}/Z_A^2	−0.013655(84)	−0.015222(84)	−0.016502(82)	−0.017714(35)	−0.018928(35)	−0.020101(48)
Z_{54}/Z_A^2	−0.27589(50)	−0.25484(42)	−0.23680(41)	−0.22163(33)	−0.20933(27)	−0.19857(25)
Z_{55}/Z_A^2	1.13012(38)	1.10863(11)	1.09088(17)	1.07641(16)	1.06447(10)	1.053966(91)
Z_A/Z_S	1.1747(12)	1.1509(12)	1.13146(73)	1.11468(44)	1.10153(39)	1.08948(28)
$a\mu$	1.24956	1.31898	1.3884	1.45782	1.52724	1.59666
Z_{11}/Z_A^2	0.94340(14)	0.94248(12)	0.94167(11)	0.94078(11)	0.93995(10)	0.939135(97)
Z_{22}/Z_A^2	1.034657(60)	1.033702(41)	1.033023(42)	1.032459(33)	1.032048(34)	1.031776(29)
Z_{23}/Z_A^2	0.20781(17)	0.20011(15)	0.19388(16)	0.18871(15)	0.18455(17)	0.18125(16)
Z_{32}/Z_A^2	0.022500(33)	0.023238(28)	0.023973(29)	0.024784(33)	0.025602(34)	0.026444(30)
Z_{33}/Z_A^2	0.87215(16)	0.88692(16)	0.89962(12)	0.91138(14)	0.92170(15)	0.93103(15)
Z_{44}/Z_A^2	0.90782(16)	0.92013(15)	0.93088(13)	0.94105(14)	0.95011(15)	0.95843(14)
Z_{45}/Z_A^2	−0.021183(46)	−0.022234(36)	−0.023253(30)	−0.024311(35)	−0.025342(37)	−0.026366(33)
Z_{54}/Z_A^2	−0.18959(21)	−0.18195(17)	−0.17564(18)	−0.17027(17)	−0.16581(17)	−0.16209(18)
Z_{55}/Z_A^2	1.045192(75)	1.037563(63)	1.031075(44)	1.025211(35)	1.020178(38)	1.015685(34)
Z_A/Z_S	1.07963(10)	1.07094(11)	1.063606(89)	1.057145(92)	1.051509(95)	1.046550(96)

Table B.17: Same as table B.13 but for the M1S ensemble for $am_q^{\mathrm{val}} = 0.004$.

$a\mu$	0.83304	0.90246	0.97188	1.0413	1.11072	1.18014
Z_{11}/Z_A^2	0.95273(23)	0.95018(28)	0.94832(20)	0.94677(16)	0.94575(12)	0.944549(75)
Z_{22}/Z_A^2	1.04555(21)	1.04280(29)	1.04055(18)	1.03848(14)	1.03704(12)	1.035615(84)
Z_{23}/Z_A^2	0.29447(14)	0.27356(49)	0.25565(26)	0.24032(19)	0.22752(12)	0.21673(21)
Z_{32}/Z_A^2	0.018511(90)	0.019119(92)	0.019805(72)	0.020423(62)	0.021062(60)	0.021769(52)
Z_{33}/Z_A^2	0.72830(56)	0.7616(10)	0.79037(50)	0.81523(43)	0.83660(34)	0.85548(28)
Z_{44}/Z_A^2	0.79312(70)	0.81939(94)	0.84219(61)	0.86185(46)	0.87891(34)	0.89420(29)
Z_{45}/Z_A^2	−0.01352(11)	−0.01511(16)	−0.01654(12)	−0.017732(93)	−0.018892(65)	−0.020050(73)
Z_{54}/Z_A^2	−0.27405(25)	−0.25353(49)	−0.23589(27)	−0.22107(19)	−0.20864(12)	−0.19823(18)
Z_{55}/Z_A^2	1.12887(30)	1.10816(28)	1.090836(84)	1.07620(13)	1.064248(93)	1.05392(10)
Z_A/Z_S	1.1723(10)	1.14974(90)	1.13028(68)	1.11420(52)	1.10083(31)	1.08929(30)
$a\mu$	1.24956	1.31898	1.3884	1.45782	1.52724	1.59666
Z_{11}/Z_A^2	0.943587(60)	0.942644(54)	0.941835(70)	0.940973(42)	0.940165(36)	0.939343(32)
Z_{22}/Z_A^2	1.034560(59)	1.033628(50)	1.032926(62)	1.032421(62)	1.032003(72)	1.031722(76)
Z_{23}/Z_A^2	0.20755(15)	0.19986(19)	0.19345(16)	0.18842(18)	0.18427(17)	0.18094(19)
Z_{32}/Z_A^2	0.022483(53)	0.023236(54)	0.023971(49)	0.024793(61)	0.025606(63)	0.026437(60)
Z_{33}/Z_A^2	0.87216(28)	0.88697(33)	0.89995(16)	0.91161(28)	0.92191(30)	0.93124(26)
Z_{44}/Z_A^2	0.90792(33)	0.92028(36)	0.93126(19)	0.94135(31)	0.95039(32)	0.95872(29)
Z_{45}/Z_A^2	−0.021170(67)	−0.022245(63)	−0.023253(55)	−0.024319(61)	−0.025338(66)	−0.026348(65)
Z_{54}/Z_A^2	−0.18923(17)	−0.18159(19)	−0.17514(14)	−0.16990(16)	−0.16543(15)	−0.16169(16)
Z_{55}/Z_A^2	1.045113(86)	1.037469(96)	1.030956(42)	1.025238(84)	1.020191(76)	1.015711(72)
Z_A/Z_S	1.07924(22)	1.07064(22)	1.063359(74)	1.05686(14)	1.05130(15)	1.04635(12)

Table B.18: Same as table B.13 but for the M2S ensemble for $am_q^{\mathrm{val}} = 0.006$.

$a\mu$	0.83304	0.90246	0.97188	1.0413	1.11072	1.18014
Z_{11}/Z_A^2	0.95238(44)	0.95019(41)	0.94839(36)	0.94695(28)	0.94563(25)	0.94449(21)
Z_{22}/Z_A^2	1.04510(24)	1.04244(18)	1.040309(96)	1.03859(12)	1.036982(84)	1.035594(85)
Z_{23}/Z_A^2	0.29483(46)	0.27317(39)	0.25539(41)	0.24045(38)	0.22779(34)	0.21671(31)
Z_{32}/Z_A^2	0.018602(89)	0.01921(11)	0.019795(88)	0.020424(77)	0.021055(41)	0.021684(45)
Z_{33}/Z_A^2	0.72811(61)	0.76224(56)	0.79071(44)	0.81515(37)	0.83636(30)	0.85535(40)
Z_{44}/Z_A^2	0.79279(55)	0.81967(57)	0.84221(42)	0.86170(36)	0.87864(28)	0.89397(40)
Z_{45}/Z_A^2	−0.013445(72)	−0.01494(12)	−0.016381(90)	−0.017713(85)	−0.018881(48)	−0.019973(45)
Z_{54}/Z_A^2	−0.27453(48)	−0.25345(46)	−0.23595(44)	−0.22139(41)	−0.20904(37)	−0.19833(32)
Z_{55}/Z_A^2	1.12928(34)	1.10836(44)	1.09093(30)	1.07658(22)	1.06441(15)	1.05400(16)
Z_A/Z_S	1.1715(14)	1.14878(58)	1.12966(33)	1.11377(27)	1.10029(27)	1.08882(29)
$a\mu$	1.24956	1.31898	1.3884	1.45782	1.52724	1.59666
Z_{11}/Z_A^2	0.94348(19)	0.94256(18)	0.94174(17)	0.94091(14)	0.94009(13)	0.93926(12)
Z_{22}/Z_A^2	1.034437(67)	1.033535(54)	1.032864(44)	1.032313(42)	1.031897(38)	1.031616(43)
Z_{23}/Z_A^2	0.20750(32)	0.19991(32)	0.19366(26)	0.18842(24)	0.18423(25)	0.18090(25)
Z_{32}/Z_A^2	0.022393(45)	0.023136(39)	0.023926(31)	0.024691(35)	0.025493(34)	0.026325(35)
Z_{33}/Z_A^2	0.87196(41)	0.88655(40)	0.89958(15)	0.91110(23)	0.92141(23)	0.93071(20)
Z_{44}/Z_A^2	0.90762(40)	0.91979(39)	0.93087(16)	0.94077(25)	0.94979(24)	0.95807(21)
Z_{45}/Z_A^2	−0.021060(44)	−0.022130(38)	−0.023199(35)	−0.024207(37)	−0.025217(36)	−0.026230(36)
Z_{54}/Z_A^2	−0.18933(33)	−0.18178(33)	−0.17544(28)	−0.17004(26)	−0.16556(27)	−0.16184(26)
Z_{55}/Z_A^2	1.04517(12)	1.037571(99)	1.031049(73)	1.025340(88)	1.020266(63)	1.015773(55)
Z_A/Z_S	1.07905(25)	1.07076(24)	1.063299(84)	1.05701(12)	1.05145(13)	1.04653(10)

Table B.19: Same as table B.13 but for the M3S ensemble for $am_q^{\rm val} = 0.008$.

$a\mu$	0.74048	0.78676	0.83304	0.87932	0.9256
Z_{11}/Z_A^2	0.96277(32)	0.96053(30)	0.95855(22)	0.95688(12)	0.955404(88)
Z_{22}/Z_A^2	1.04878(49)	1.04663(31)	1.04441(27)	1.04229(13)	1.040468(60)
Z_{23}/Z_A^2	0.30460(60)	0.28806(61)	0.27331(44)	0.26001(47)	0.24754(33)
Z_{32}/Z_A^2	0.01716(22)	0.017126(66)	0.017557(91)	0.018019(92)	0.018361(74)
Z_{33}/Z_A^2	0.70568(81)	0.7303(12)	0.75211(96)	0.77259(98)	0.79195(64)
Z_{44}/Z_A^2	0.77702(85)	0.7963(13)	0.81313(97)	0.82875(93)	0.84409(63)
Z_{45}/Z_A^2	−0.01129(14)	−0.01223(16)	−0.01316(16)	−0.01408(15)	−0.01495(11)
Z_{54}/Z_A^2	−0.28401(55)	−0.26758(52)	−0.25297(30)	−0.23990(37)	−0.22771(29)
Z_{55}/Z_A^2	1.15268(74)	1.13516(32)	1.11997(13)	1.10649(14)	1.09462(19)
Z_A/Z_S	1.19339(50)	1.17474(79)	1.15946(95)	1.1444(11)	1.13053(63)
$a\mu$	0.97188	1.01816	1.06444	1.24956	1.43468
Z_{11}/Z_A^2	0.95422(14)	0.953129(95)	0.952102(76)	0.948906(45)	0.946446(40)
Z_{22}/Z_A^2	1.03902(11)	1.037577(51)	1.036223(22)	1.032507(20)	1.030387(10)
Z_{23}/Z_A^2	0.23661(20)	0.22660(18)	0.21801(16)	0.19188(11)	0.175507(75)
Z_{32}/Z_A^2	0.018685(53)	0.019022(43)	0.019385(43)	0.021042(21)	0.022892(19)
Z_{33}/Z_A^2	0.80898(42)	0.82479(38)	0.83851(24)	0.88335(19)	0.91607(12)
Z_{44}/Z_A^2	0.85749(42)	0.86991(40)	0.88067(26)	0.91690(19)	0.94439(12)
Z_{45}/Z_A^2	−0.015698(75)	−0.016458(60)	−0.017123(55)	−0.019843(23)	−0.022400(19)
Z_{54}/Z_A^2	−0.21722(23)	−0.20754(19)	−0.19925(15)	−0.17378(11)	−0.157398(76)
Z_{55}/Z_A^2	1.08446(23)	1.07510(11)	1.066908(72)	1.041878(50)	1.025013(33)
Z_A/Z_S	1.11884(38)	1.10855(36)	1.09959(30)	1.07240(14)	1.053778(61)

Table B.20: Same as table B.13 but for the F1M ensemble for $am_q^{\mathrm{val}} = 0.0021$.

$a\mu$	0.74048	0.83304	0.9256	1.01816
Z_{11}/Z_A^2	0.94751(13)	0.94519(12)	0.943856(74)	0.943399(69)
Z_{22}/Z_A^2	1.04376(21)	1.03925(13)	1.035808(72)	1.033121(82)
Z_{23}/Z_A^2	0.28774(16)	0.25475(33)	0.22879(15)	0.20821(17)
Z_{32}/Z_A^2	0.01785(16)	0.018407(53)	0.018884(48)	0.019342(28)
Z_{33}/Z_A^2	0.73334(42)	0.78233(44)	0.82007(22)	0.85082(12)
Z_{44}/Z_A^2	0.79300(43)	0.83127(30)	0.86088(22)	0.88523(11)
Z_{45}/Z_A^2	−0.01299(16)	−0.014778(35)	−0.016383(48)	−0.017556(31)
Z_{54}/Z_A^2	−0.26672(21)	−0.23570(28)	−0.21156(14)	−0.19236(15)
Z_{55}/Z_A^2	1.11790(22)	1.08911(22)	1.067424(79)	1.05133(10)
Z_A/Z_S	1.16750(86)	1.13422(84)	1.11004(20)	1.09069(14)
$a\mu$	1.11072	1.20328	1.29584	1.3884
Z_{11}/Z_A^2	0.943139(50)	0.943258(61)	0.943445(42)	0.943748(45)
Z_{22}/Z_A^2	1.030880(38)	1.029155(34)	1.027797(26)	1.026713(25)
Z_{23}/Z_A^2	0.19172(15)	0.17847(13)	0.16789(12)	0.159366(95)
Z_{32}/Z_A^2	0.019822(19)	0.020256(16)	0.020751(21)	0.021226(18)
Z_{33}/Z_A^2	0.87543(13)	0.89552(12)	0.91210(11)	0.925857(70)
Z_{44}/Z_A^2	0.90510(12)	0.92156(12)	0.935463(98)	0.947243(75)
Z_{45}/Z_A^2	−0.018663(23)	−0.019564(17)	−0.020423(21)	−0.021179(16)
Z_{54}/Z_A^2	−0.17690(14)	−0.16439(12)	−0.15421(10)	−0.145818(92)
Z_{55}/Z_A^2	1.038671(29)	1.028986(29)	1.021248(21)	1.015072(21)
Z_A/Z_S	1.07587(12)	1.064241(80)	1.054687(70)	1.047021(40)

Table B.21: Same as table B.13 but for the KEKC1L ensemble for $am_q^{\mathrm{val}} = 0.0035$.

$a\mu$	0.83304	0.97188	1.11072
Z_{11}/Z_A^2	0.94458(36)	0.94295(16)	0.94285(16)
Z_{22}/Z_A^2	1.03877(27)	1.034282(98)	1.030869(66)
Z_{23}/Z_A^2	0.25548(65)	0.21805(37)	0.19195(37)
Z_{32}/Z_A^2	0.01877(17)	0.019220(89)	0.019821(61)
Z_{33}/Z_A^2	0.7800(12)	0.83697(70)	0.87474(43)
Z_{44}/Z_A^2	0.8292(12)	0.87394(58)	0.90444(38)
Z_{45}/Z_A^2	−0.01491(12)	−0.017101(78)	−0.018646(74)
Z_{54}/Z_A^2	−0.23636(65)	−0.20185(31)	−0.17728(33)
Z_{55}/Z_A^2	1.08868(50)	1.05871(27)	1.03874(15)
Z_A/Z_S	1.1365(20)	1.09926(55)	1.07685(39)
$a\mu$	1.24956	1.3884	1.52724
Z_{11}/Z_A^2	0.94302(13)	0.94356(13)	0.943946(88)
Z_{22}/Z_A^2	1.028588(69)	1.026742(63)	1.025656(36)
Z_{23}/Z_A^2	0.17340(22)	0.15974(21)	0.15030(16)
Z_{32}/Z_A^2	0.020605(44)	0.021254(54)	0.022080(41)
Z_{33}/Z_A^2	0.90412(33)	0.92538(16)	0.94231(16)
Z_{44}/Z_A^2	0.92877(33)	0.94681(19)	0.96177(20)
Z_{45}/Z_A^2	−0.020133(47)	−0.021206(61)	−0.022354(42)
Z_{54}/Z_A^2	−0.15969(22)	−0.14619(22)	−0.13651(15)
Z_{55}/Z_A^2	1.02492(14)	1.015118(71)	1.007862(46)
Z_A/Z_S	1.05926(22)	1.047292(91)	1.038245(72)

Table B.22: Same as table B.13 but for the KEKC1S ensemble for $am_q^{\mathrm{val}} = 0.0035$.

$a\mu$	0.55536	0.62478	0.6942	0.76362	0.83304	0.90246	0.97188	1.0413
Z_{11}/Z_A^2	0.95181(68)	0.94898(78)	0.94639(38)	0.94521(36)	0.94400(37)	0.94314(27)	0.94275(22)	0.94257(19)
Z_{22}/Z_A^2	1.04998(61)	1.04680(78)	1.04436(31)	1.04193(22)	1.03854(21)	1.036486(79)	1.034345(38)	1.032479(44)
Z_{23}/Z_A^2	0.3784(10)	0.3395(12)	0.3071(11)	0.27924(87)	0.25523(61)	0.23523(40)	0.21841(37)	0.20425(34)
Z_{32}/Z_A^2	0.01692(70)	0.01798(40)	0.01833(22)	0.01840(11)	0.018488(80)	0.018983(73)	0.019301(60)	0.019619(59)
Z_{33}/Z_A^2	0.5912(14)	0.6534(26)	0.7040(19)	0.7464(12)	0.78035(56)	0.81155(64)	0.83640(55)	0.85735(44)
Z_{44}/Z_A^2	0.6788(16)	0.7293(26)	0.7693(20)	0.8029(12)	0.82893(50)	0.85388(57)	0.87357(51)	0.89030(41)
Z_{45}/Z_A^2	−0.00850(58)	−0.01003(35)	−0.01215(19)	−0.013867(90)	−0.014794(64)	−0.016252(88)	−0.017217(60)	−0.018061(55)
Z_{54}/Z_A^2	−0.3574(10)	−0.31734(98)	−0.28565(100)	−0.25899(73)	−0.23644(59)	−0.21771(40)	−0.20201(39)	−0.18884(37)
Z_{55}/Z_A^2	1.20746(93)	1.1658(13)	1.13382(79)	1.10840(40)	1.08851(36)	1.07152(22)	1.05828(15)	1.04743(13)
Z_A/Z_S	1.2665(69)	1.2195(35)	1.1850(26)	1.1571(17)	1.13660(79)	1.11487(57)	1.09914(51)	1.08631(45)
$a\mu$	1.11072	1.18014	1.24956	1.31898	1.3884	1.45782	1.52724	1.59666
Z_{11}/Z_A^2	0.94269(24)	0.94264(16)	0.94285(15)	0.94307(14)	0.94347(18)	0.94356(13)	0.94379(12)	0.94398(12)
Z_{22}/Z_A^2	1.030859(62)	1.029617(38)	1.028508(44)	1.027592(45)	1.026782(68)	1.026188(55)	1.025658(53)	1.025214(54)
Z_{23}/Z_A^2	0.19237(40)	0.18220(28)	0.17359(29)	0.16635(28)	0.16001(36)	0.15494(28)	0.15048(27)	0.14672(27)
Z_{32}/Z_A^2	0.019780(78)	0.020317(44)	0.020642(43)	0.021004(42)	0.021268(74)	0.021755(44)	0.022131(46)	0.022509(48)
Z_{33}/Z_A^2	0.87436(27)	0.89069(29)	0.90395(26)	0.91549(21)	0.92520(13)	0.93448(18)	0.94227(15)	0.94914(12)
Z_{44}/Z_A^2	0.90397(27)	0.91754(28)	0.92858(24)	0.93838(20)	0.94664(14)	0.95482(17)	0.96174(15)	0.96792(12)
Z_{45}/Z_A^2	−0.018622(92)	−0.019542(40)	−0.020166(44)	−0.020770(44)	−0.021228(79)	−0.021889(49)	−0.022404(49)	−0.022904(51)
Z_{54}/Z_A^2	−0.17767(40)	−0.16802(30)	−0.15976(29)	−0.15269(28)	−0.14644(34)	−0.14127(27)	−0.13666(26)	−0.13265(25)
Z_{55}/Z_A^2	1.03882(12)	1.030997(67)	1.024739(62)	1.019457(46)	1.015122(59)	1.011116(29)	1.007805(26)	1.004878(22)
Z_A/Z_S	1.07631(29)	1.06684(24)	1.05923(15)	1.052785(96)	1.04735(10)	1.042381(92)	1.038197(79)	1.034583(62)

Table B.23: Same as table B.13 but for the KEKC2a ensemble for $am_q^{\mathrm{val}} = 0.0070$.

$a\mu$	0.55536	0.62478	0.6942	0.76362	0.83304	0.90246	0.97188	1.0413
Z_{11}/Z_A^2	0.95270(46)	0.94981(40)	0.94732(30)	0.94548(34)	0.94415(23)	0.94358(20)	0.94301(17)	0.94278(14)
Z_{22}/Z_A^2	1.0491(10)	1.04781(47)	1.04431(43)	1.04167(41)	1.03874(18)	1.03652(18)	1.03421(12)	1.032394(91)
Z_{23}/Z_A^2	0.3793(13)	0.3412(11)	0.30753(94)	0.27957(64)	0.25534(33)	0.23547(39)	0.21831(27)	0.20418(24)
Z_{32}/Z_A^2	0.01817(64)	0.01712(37)	0.01764(16)	0.01803(13)	0.01838(13)	0.018817(27)	0.019148(35)	0.019450(54)
Z_{33}/Z_A^2	0.5894(16)	0.6498(16)	0.7013(13)	0.74420(75)	0.78046(66)	0.81038(54)	0.83566(41)	0.85660(39)
Z_{44}/Z_A^2	0.6767(13)	0.7258(16)	0.7670(11)	0.80086(60)	0.82956(63)	0.85305(51)	0.87298(40)	0.88961(39)
Z_{45}/Z_A^2	−0.00744(49)	−0.00981(38)	−0.01179(14)	−0.013369(60)	−0.01485(14)	−0.016067(69)	−0.017035(50)	−0.017882(51)
Z_{54}/Z_A^2	−0.3581(11)	−0.3194(11)	−0.28636(76)	−0.25959(50)	−0.23619(34)	−0.21795(36)	−0.20204(26)	−0.18890(25)
Z_{55}/Z_A^2	1.20884(98)	1.16764(75)	1.13511(46)	1.10933(55)	1.08827(35)	1.07228(28)	1.05874(20)	1.04777(12)
Z_A/Z_S	1.2781(32)	1.2268(23)	1.1887(19)	1.1597(15)	1.13721(50)	1.11606(53)	1.10013(40)	1.08733(32)
$a\mu$	1.11072	1.18014	1.24956	1.31898	1.3884	1.45782	1.52724	1.59666
Z_{11}/Z_A^2	0.94268(13)	0.94287(12)	0.94302(11)	0.94323(11)	0.94344(11)	0.943728(95)	0.943955(88)	0.944135(82)
Z_{22}/Z_A^2	1.030820(96)	1.029544(64)	1.028424(66)	1.027503(56)	1.026773(70)	1.026104(44)	1.025591(43)	1.025163(43)
Z_{23}/Z_A^2	0.19203(23)	0.18202(25)	0.17331(22)	0.16594(21)	0.15991(23)	0.15457(20)	0.15013(20)	0.14637(20)
Z_{32}/Z_A^2	0.019848(71)	0.020168(42)	0.020539(44)	0.020899(47)	0.021294(62)	0.021645(45)	0.022027(43)	0.022411(43)
Z_{33}/Z_A^2	0.87500(32)	0.89028(23)	0.90377(17)	0.91546(20)	0.92545(20)	0.93440(15)	0.94220(13)	0.94911(12)
Z_{44}/Z_A^2	0.90456(38)	0.91715(23)	0.92836(19)	0.93825(22)	0.94688(24)	0.95468(17)	0.96161(15)	0.96781(14)
Z_{45}/Z_A^2	−0.018713(71)	−0.019385(42)	−0.020043(44)	−0.020649(47)	−0.021255(64)	−0.021771(47)	−0.022299(45)	−0.022802(44)
Z_{54}/Z_A^2	−0.17739(23)	−0.16786(24)	−0.15952(22)	−0.15239(21)	−0.14637(22)	−0.14098(19)	−0.13639(19)	−0.13240(19)
Z_{55}/Z_A^2	1.03857(17)	1.031164(53)	1.024849(34)	1.019544(28)	1.015040(33)	1.011174(37)	1.007854(39)	1.004946(35)
Z_A/Z_S	1.07646(17)	1.06720(17)	1.05933(10)	1.05281(13)	1.04733(10)	1.042409(74)	1.038243(65)	1.034621(67)

Table B.24: Same as table B.13 but for the KEKC2b ensemble for $am_q^{\rm val} = 0.0070$.

$a\mu$	0.37024	0.41652	0.4628	0.50908	0.55536	0.60164	0.64792	0.6942
Z_{11}/Z_A^2	0.9800(10)	0.97629(32)	0.97311(42)	0.96958(33)	0.96636(35)	0.96417(10)	0.96200(15)	0.960346(66)
Z_{22}/Z_A^2	1.0630(18)	1.0599(12)	1.05772(34)	1.05386(26)	1.05036(31)	1.04655(16)	1.04353(15)	1.04084(15)
Z_{23}/Z_A^2	0.4334(30)	0.39550(97)	0.36304(53)	0.33380(50)	0.30841(86)	0.28528(60)	0.26511(48)	0.24739(43)
Z_{32}/Z_A^2	0.01655(100)	0.01604(26)	0.01592(36)	0.01576(34)	0.01589(18)	0.015818(91)	0.015827(85)	0.015915(69)
Z_{33}/Z_A^2	0.5014(49)	0.5575(11)	0.60911(90)	0.65103(34)	0.68951(65)	0.72100(48)	0.74959(44)	0.77451(53)
Z_{44}/Z_A^2	0.6086(42)	0.6568(21)	0.70022(95)	0.73345(37)	0.76283(34)	0.78703(38)	0.80917(41)	0.82834(42)
Z_{45}/Z_A^2	−0.00095(95)	−0.0051(10)	−0.00697(60)	−0.00843(27)	−0.00923(15)	−0.010191(29)	−0.011153(47)	−0.011989(76)
Z_{54}/Z_A^2	−0.4253(29)	−0.3818(11)	−0.34382(90)	−0.31235(65)	−0.28653(57)	−0.26384(60)	−0.24410(46)	−0.22710(37)
Z_{55}/Z_A^2	1.3157(27)	1.2668(24)	1.2247(14)	1.19038(81)	1.16300(39)	1.14017(52)	1.12087(40)	1.10478(22)
Z_A/Z_S	1.367(12)	1.3129(39)	1.2717(19)	1.2389(24)	1.2071(10)	1.1838(11)	1.16214(70)	1.14345(51)
$a\mu$	0.74048	0.78676	0.83304	0.87932	0.9256	0.97188	1.01816	1.06444
Z_{11}/Z_A^2	0.959114(84)	0.958245(46)	0.957511(54)	0.956962(45)	0.956439(64)	0.956171(31)	0.955939(33)	0.955808(31)
Z_{22}/Z_A^2	1.03830(14)	1.03613(14)	1.034110(79)	1.032323(74)	1.030796(95)	1.029368(67)	1.028142(52)	1.027045(49)
Z_{23}/Z_A^2	0.23178(40)	0.21761(44)	0.20501(30)	0.19375(22)	0.18399(31)	0.17507(19)	0.16721(20)	0.16016(18)
Z_{32}/Z_A^2	0.016029(70)	0.016124(26)	0.016170(25)	0.016251(27)	0.016401(68)	0.016462(21)	0.016577(11)	0.016699(12)
Z_{33}/Z_A^2	0.79623(24)	0.81583(47)	0.83326(36)	0.84881(30)	0.86257(14)	0.87483(24)	0.88590(25)	0.89589(21)
Z_{44}/Z_A^2	0.84492(34)	0.85985(34)	0.87329(27)	0.88525(24)	0.89599(20)	0.90554(19)	0.91425(20)	0.92217(16)
Z_{45}/Z_A^2	−0.012556(88)	−0.013149(45)	−0.013694(34)	−0.014168(28)	−0.014644(77)	−0.015013(12)	−0.0153968(86)	−0.015746(14)
Z_{54}/Z_A^2	−0.21218(31)	−0.19903(34)	−0.18726(22)	−0.17677(19)	−0.16772(24)	−0.15944(17)	−0.15214(18)	−0.14558(16)
Z_{55}/Z_A^2	1.09102(14)	1.07950(20)	1.06920(12)	1.06031(14)	1.052600(74)	1.04594(11)	1.040048(96)	1.034857(94)
Z_A/Z_S	1.12715(37)	1.11371(35)	1.10229(26)	1.09216(19)	1.083434(53)	1.07571(18)	1.06907(16)	1.06315(13)

Table B.25: Same as table B.13 but for the KEKM1a ensemble for $am_q^{\mathrm{val}} = 0.0042$.

$a\mu$	0.37024	0.41652	0.4628	0.50908	0.55536	0.60164	0.64792	0.6942
Z_{11}/Z_A^2	0.98136(70)	0.9770(14)	0.97292(89)	0.96929(52)	0.96590(30)	0.96351(34)	0.96155(28)	0.96013(11)
Z_{22}/Z_A^2	1.0628(21)	1.06160(73)	1.05799(95)	1.05384(43)	1.05016(28)	1.04658(24)	1.04358(22)	1.04083(17)
Z_{23}/Z_A^2	0.4362(19)	0.3976(11)	0.3641(11)	0.33351(54)	0.31013(27)	0.28600(18)	0.26586(30)	0.24819(55)
Z_{32}/Z_A^2	0.01478(69)	0.0165(11)	0.01594(40)	0.01578(15)	0.01596(10)	0.01578(13)	0.016013(65)	0.016044(47)
Z_{33}/Z_A^2	0.4925(49)	0.5588(13)	0.60895(75)	0.6530(14)	0.68656(39)	0.72045(96)	0.74903(12)	0.77377(57)
Z_{44}/Z_A^2	0.6050(47)	0.6566(11)	0.69915(93)	0.7345(19)	0.76028(71)	0.7868(11)	0.80875(31)	0.82775(45)
Z_{45}/Z_A^2	−0.0044(16)	−0.00496(23)	−0.00623(43)	−0.00791(17)	−0.00919(20)	−0.01025(14)	−0.01121(12)	−0.011953(70)
Z_{54}/Z_A^2	−0.4275(17)	−0.3832(13)	−0.3457(11)	−0.31321(43)	−0.28832(20)	−0.26441(29)	−0.24486(28)	−0.22777(45)
Z_{55}/Z_A^2	1.3202(27)	1.2675(17)	1.2260(13)	1.19153(25)	1.16356(22)	1.14018(15)	1.12104(31)	1.10516(18)
Z_A/Z_S	1.3905(35)	1.3239(53)	1.2741(33)	1.2364(20)	1.2097(32)	1.1842(18)	1.1615(11)	1.14289(24)
$a\mu$	0.74048	0.78676	0.83304	0.87932	0.9256	0.97188	1.01816	1.06444
Z_{11}/Z_A^2	0.958945(70)	0.958071(77)	0.957334(67)	0.956746(48)	0.956274(64)	0.955976(60)	0.955766(50)	0.955615(45)
Z_{22}/Z_A^2	1.03840(10)	1.03609(16)	1.034078(74)	1.032341(71)	1.030798(35)	1.029389(43)	1.028147(39)	1.027060(48)
Z_{23}/Z_A^2	0.23261(27)	0.21829(22)	0.20590(19)	0.19457(22)	0.184596(65)	0.17562(14)	0.16768(12)	0.16064(14)
Z_{32}/Z_A^2	0.016106(58)	0.016189(85)	0.016251(59)	0.016349(39)	0.016467(26)	0.016535(37)	0.016641(40)	0.016767(42)
Z_{33}/Z_A^2	0.79561(31)	0.81510(42)	0.83220(32)	0.84796(32)	0.86209(12)	0.87442(34)	0.88554(29)	0.89558(25)
Z_{44}/Z_A^2	0.84446(22)	0.85934(51)	0.87245(37)	0.88465(31)	0.89564(14)	0.90522(33)	0.91398(28)	0.92196(24)
Z_{45}/Z_A^2	−0.012596(70)	−0.013193(79)	−0.013698(57)	−0.014204(43)	−0.014691(42)	−0.015064(35)	−0.015435(39)	−0.015794(42)
Z_{54}/Z_A^2	−0.21287(14)	−0.19948(23)	−0.18786(21)	−0.17741(21)	−0.168183(71)	−0.15988(13)	−0.15253(11)	−0.14597(12)
Z_{55}/Z_A^2	1.09132(13)	1.07957(11)	1.069359(77)	1.060530(98)	1.052644(90)	1.045968(31)	1.040108(44)	1.034922(50)
Z_A/Z_S	1.12759(82)	1.11428(40)	1.10291(22)	1.09254(20)	1.08372(26)	1.07605(22)	1.06926(20)	1.06331(14)

Table B.26: Same as table B.13 but for the KEKM1b ensemble for $am_q^{\mathrm{val}} = 0.0042$.

$a\mu$	0.41652	0.45123	0.48594	0.52065	0.55536	0.59007
Z_{11}/Z_A^2	0.98193(35)	0.97880(25)	0.97613(17)	0.97367(26)	0.97151(21)	0.96999(19)
Z_{22}/Z_A^2	1.06035(32)	1.05655(37)	1.05309(28)	1.04972(19)	1.046608(74)	1.04398(15)
Z_{23}/Z_A^2	0.35525(38)	0.33146(63)	0.31115(60)	0.29168(46)	0.27450(38)	0.25849(32)
Z_{32}/Z_A^2	0.014822(88)	0.015181(89)	0.01494(14)	0.014879(41)	0.015015(69)	0.014826(41)
Z_{33}/Z_A^2	0.61762(56)	0.6515(11)	0.67965(100)	0.70662(77)	0.73018(52)	0.75154(65)
Z_{44}/Z_A^2	0.70959(39)	0.7353(11)	0.7580(10)	0.77892(89)	0.79679(44)	0.81284(73)
Z_{45}/Z_A^2	−0.00593(37)	−0.006656(82)	−0.007629(63)	−0.008583(85)	−0.009408(81)	−0.009817(63)
Z_{54}/Z_A^2	−0.33645(53)	−0.31164(77)	−0.28957(73)	−0.26967(62)	−0.25265(36)	−0.23703(48)
Z_{55}/Z_A^2	1.22906(42)	1.20287(55)	1.17985(49)	1.15944(30)	1.14157(22)	1.12686(26)
Z_A/Z_S	1.2779(13)	1.24683(95)	1.22072(77)	1.19724(70)	1.17793(48)	1.16128(49)
$a\mu$	0.62478	0.65949	0.6942	0.72891	0.76362	0.79833
Z_{11}/Z_A^2	0.96847(16)	0.96725(19)	0.96629(15)	0.96543(15)	0.96466(13)	0.96401(12)
Z_{22}/Z_A^2	1.04144(11)	1.03915(14)	1.037295(64)	1.03533(10)	1.033615(91)	1.032101(73)
Z_{23}/Z_A^2	0.24425(24)	0.23123(27)	0.21951(29)	0.20860(20)	0.19864(21)	0.18967(19)
Z_{32}/Z_A^2	0.014814(37)	0.014795(28)	0.014860(29)	0.014751(35)	0.014765(32)	0.014781(22)
Z_{33}/Z_A^2	0.77064(55)	0.78808(53)	0.80439(31)	0.81843(39)	0.83181(38)	0.84389(27)
Z_{44}/Z_A^2	0.82730(58)	0.84043(53)	0.85297(30)	0.86332(43)	0.87345(41)	0.88261(29)
Z_{45}/Z_A^2	−0.010360(55)	−0.010829(46)	−0.011365(29)	−0.011636(38)	−0.011992(34)	−0.012325(24)
Z_{54}/Z_A^2	−0.22328(37)	−0.21084(35)	−0.19961(29)	−0.18953(28)	−0.18023(27)	−0.17192(23)
Z_{55}/Z_A^2	1.11371(20)	1.10209(17)	1.09174(10)	1.08270(13)	1.07446(13)	1.06720(13)
Z_A/Z_S	1.14645(33)	1.13366(35)	1.12207(23)	1.11239(27)	1.10322(24)	1.09519(15)

Table B.27: Same as table B.13 but for the KEKF1 ensemble for $am_q^{\mathrm{val}} = 0.0030$.

Appendix C

Numerical results for massive NPR

(a) C1S

am_{input}	$am_{\text{res}} \times 10^3$	aM_{η_h}	Z_A
0.0050	3.162(19)	0.1885(29)	0.71796(44)
0.0100	3.085(18)	0.2367(21)	0.71822(28)
0.0200	2.938(16)	0.3129(15)	0.71942(17)
0.0400	2.720(12)	0.4304(10)	0.72235(12)
0.0500	2.644(22)	0.4829(18)	0.72413(27)
0.1000	2.427(15)	0.6904(14)	0.73344(23)
0.1500	2.420(11)	0.8636(11)	0.74507(19)
0.2000	2.6192(92)	1.01733(94)	0.75960(15)
0.3000	4.530(18)	1.28409(79)	0.80194(14)
0.3300	6.455(18)	1.35527(38)	0.821474(90)

(b) M1S

am_{input}	$am_{\text{res}} \times 10^3$	aM_{η_h}	Z_A
0.0040	0.6727(72)	0.1290(24)	0.74486(27)
0.0080	0.6561(64)	0.1714(16)	0.74542(15)
0.0150	0.6319(55)	0.2283(11)	0.746212(91)
0.0300	0.5977(42)	0.32118(69)	0.747987(58)
0.0500	0.5767(52)	0.42023(76)	0.75062(11)
0.1000	0.5479(35)	0.61780(44)	0.758721(100)
0.1500	0.5602(29)	0.78382(43)	0.769158(89)
0.2250	0.6677(29)	1.00056(52)	0.789767(76)
0.3000	1.0409(41)	1.18880(56)	0.817587(74)
0.3200	1.2562(65)	1.23385(41)	0.826456(79)
0.3400	1.6053(82)	1.27801(40)	0.836317(81)
0.3600	2.189(11)	1.32043(39)	0.847392(85)
0.3750	2.936(12)	1.35187(55)	0.857047(90)

(c) F1S

am_{input}	$am_{\text{res}} \times 10^3$	aM_{η_h}	Z_A
0.0021	0.9769(95)	0.0994(18)	0.76231(18)
0.0043	0.9722(88)	0.1263(13)	0.76263(11)
0.0107	0.9565(62)	0.18387(86)	0.763139(55)
0.0214	0.9393(43)	0.25453(57)	0.764180(44)
0.0330	0.9291(36)	0.31626(41)	0.765486(42)
0.0660	0.9188(24)	0.45975(34)	0.769873(38)
0.0990	0.9251(18)	0.58074(34)	0.775231(37)
0.1320	0.9463(14)	0.68965(34)	0.781619(36)
0.1980	1.0427(11)	0.88429(32)	0.797730(37)
0.2640	1.2577(11)	1.05584(28)	0.818823(38)
0.3300	1.7485(18)	1.20763(25)	0.845736(38)
0.3960	3.1873(46)	1.34062(22)	0.880386(40)

Table C.1: Numerical results for am_{res}, aM_{η_h} and Z_A^{PCAC} on the Shamir ensembles.

(a) C1M

am_{input}	$am_{\text{res}} \times 10^3$	aM_{η_h}	Z_A
0.0050	0.601(12)	0.1642(34)	0.71302(34)
0.0100	0.574(11)	0.2203(22)	0.71337(19)
0.0181	0.5330(95)	0.2886(14)	0.71443(12)
0.0362	0.4642(79)	0.40331(87)	0.717257(77)
0.0500	0.450(17)	0.4769(22)	0.71979(19)
0.1000	0.361(12)	0.6877(14)	0.72921(11)
0.1500	0.3210(100)	0.8637(11)	0.74087(11)
0.2000	0.3172(94)	1.01971(85)	0.75528(13)
0.3000	0.599(16)	1.28930(50)	0.79647(16)

(b) M1M

am_{input}	$am_{\text{res}} \times 10^3$	aM_{η_h}	Z_A
0.0040	0.3116(61)	0.1196(26)	0.74376(24)
0.0080	0.3018(56)	0.1651(16)	0.74421(13)
0.0133	0.2907(51)	0.2113(12)	0.744798(86)
0.0266	0.2709(39)	0.29939(79)	0.746330(56)
0.0500	0.2527(54)	0.4178(17)	0.749495(88)
0.1000	0.2414(40)	0.6163(11)	0.757548(60)
0.1500	0.2523(35)	0.78311(79)	0.767843(47)
0.2250	0.3173(27)	1.00082(63)	0.788084(41)
0.3000	0.5277(20)	1.19017(57)	0.815321(43)
0.3200	0.6634(21)	1.23610(64)	0.824062(46)
0.3400	0.8998(26)	1.28063(63)	0.833810(56)

(c) F1M

am_{input}	$am_{\text{res}} \times 10^3$	aM_{η_h}	Z_A
0.0021	0.2399(56)	0.0865(21)	0.75927(21)
0.0043	0.2390(52)	0.1172(16)	0.75952(11)
0.0107	0.2343(43)	0.1795(10)	0.760226(53)
0.0214	0.2286(36)	0.25287(54)	0.761281(42)
0.0330	0.2244(31)	0.31620(38)	0.762536(41)
0.0660	0.2201(21)	0.46183(32)	0.766829(40)
0.0990	0.2248(15)	0.58391(32)	0.772132(39)
0.1320	0.2378(12)	0.69368(30)	0.778456(38)
0.1980	0.29064(77)	0.88979(25)	0.794371(35)
0.2640	0.39970(57)	1.06271(21)	0.815121(32)
0.3300	0.66808(62)	1.21606(19)	0.841614(31)
0.3600	1.0280(12)	1.27967(19)	0.856367(32)

Table C.2: Numerical results for am_{res}, aM_{η_h} and Z_A^{PCAC} on the Möbius ensembles.

(a) C1S

am_q	$Z_m^{\text{mSMOM}}(2.0\,\text{GeV})$	$Z_m^{\text{mSMOM}}(2.5\,\text{GeV})$	$Z_m^{\text{mSMOM}}(3.0\,\text{GeV})$
0.008162(19)	1.3145(72)	1.2392(37)	1.2362(36)
0.013085(18)	1.4381(35)	1.3763(24)	1.3701(23)
0.022938(16)	1.5245(18)	1.4698(14)	1.4627(13)
0.042720(12)	1.5706(13)	1.51846(80)	1.51128(66)
0.052644(22)	1.5772(14)	1.52530(98)	1.51804(88)
0.102427(15)	1.5763(12)	1.52468(79)	1.51631(68)
0.152420(11)	1.5542(11)	1.50388(68)	1.49448(56)
0.2026192(92)	1.52098(97)	1.47342(59)	1.46347(45)
0.304530(18)	1.42069(79)	1.38114(51)	1.37158(39)
0.336455(18)	1.37464(69)	1.33792(43)	1.32877(31)

(b) M1S

am_q	$Z_m^{\text{mSMOM}}(2.0\,\text{GeV})$	$Z_m^{\text{mSMOM}}(2.5\,\text{GeV})$	$Z_m^{\text{mSMOM}}(3.0\,\text{GeV})$
0.0046727(72)	1.5055(54)	1.4206(37)	1.3871(30)
0.0086561(64)	1.5557(28)	1.4737(19)	1.4379(15)
0.0156319(55)	1.5802(19)	1.5002(13)	1.46327(86)
0.0305977(42)	1.5930(18)	1.5131(11)	1.47522(65)
0.0505767(52)	1.5951(18)	1.5144(11)	1.47581(67)
0.1005479(35)	1.5838(17)	1.5039(11)	1.46439(66)
0.1505602(29)	1.5596(16)	1.4844(11)	1.44536(65)
0.2256677(29)	1.5066(13)	1.44203(94)	1.40589(61)
0.3010409(41)	1.4377(10)	1.38470(80)	1.35296(55)
0.3212562(65)	1.41695(96)	1.36683(77)	1.33638(53)
0.3416053(82)	1.39437(90)	1.34712(73)	1.31796(52)
0.362189(11)	1.36951(84)	1.32504(70)	1.29721(50)
0.377936(12)	1.34809(80)	1.30567(67)	1.27886(49)

(c) F1S

am_q	$Z_m^{\text{mSMOM}}(2.0\,\text{GeV})$	$Z_m^{\text{mSMOM}}(2.5\,\text{GeV})$	$Z_m^{\text{mSMOM}}(3.0\,\text{GeV})$
0.0030769(95)	1.4979(65)	1.4231(50)	1.3995(47)
0.0052722(88)	1.5265(38)	1.4478(27)	1.4142(25)
0.0116565(62)	1.5759(23)	1.4921(14)	1.4501(10)
0.0223393(43)	1.5918(20)	1.5054(12)	1.46001(76)
0.0339291(36)	1.5935(20)	1.5059(12)	1.45912(76)
0.0669188(24)	1.5923(20)	1.5036(12)	1.45510(79)
0.0999251(18)	1.5822(18)	1.4956(12)	1.44677(81)
0.1329463(14)	1.5662(17)	1.4837(12)	1.43561(80)
0.1990427(11)	1.5208(14)	1.4498(10)	1.40544(76)
0.2652577(11)	1.4630(11)	1.40425(90)	1.36518(69)
0.3317485(18)	1.39618(86)	1.34857(75)	1.31516(60)
0.3991873(46)	1.31942(67)	1.28125(62)	1.25326(52)

Table C.3: Z_m in the RI/mSMOM (massive) scheme interpolated to various renormalisation scales μ for various bare heavy quark masses on the Shamir ensembles.

(a) C1M

am_q	$Z_m^{\mathrm{mSMOM}}(2.0\,\mathrm{GeV})$	$Z_m^{\mathrm{mSMOM}}(2.5\,\mathrm{GeV})$	$Z_m^{\mathrm{mSMOM}}(3.0\,\mathrm{GeV})$
0.005601(12)	1.5754(64)	1.5305(73)	1.5451(63)
0.010574(11)	1.6088(35)	1.5621(23)	1.5678(27)
0.0186330(95)	1.6211(22)	1.5758(14)	1.5776(13)
0.0366642(79)	1.6232(15)	1.57780(84)	1.57731(68)
0.050450(17)	1.6185(14)	1.57268(92)	1.57135(81)
0.100361(12)	1.5996(11)	1.55238(64)	1.54883(51)
0.1503210(100)	1.57247(100)	1.52577(58)	1.52075(46)
0.2003172(94)	1.53813(91)	1.49351(57)	1.48761(45)
0.300599(16)	1.44377(74)	1.40606(53)	1.39986(45)

(b) M1M

am_q	$Z_m^{\mathrm{mSMOM}}(2.0\,\mathrm{GeV})$	$Z_m^{\mathrm{mSMOM}}(2.5\,\mathrm{GeV})$	$Z_m^{\mathrm{mSMOM}}(3.0\,\mathrm{GeV})$
0.0043116(61)	1.5167(51)	1.4401(30)	1.4041(29)
0.0083018(56)	1.5635(26)	1.4854(17)	1.4499(13)
0.0135907(51)	1.5820(19)	1.5039(12)	1.46793(80)
0.0268709(39)	1.5955(17)	1.51671(99)	1.47972(57)
0.0502527(54)	1.5970(16)	1.51711(98)	1.47921(59)
0.1002414(40)	1.5851(14)	1.50588(93)	1.46699(55)
0.1502523(35)	1.5612(13)	1.48653(88)	1.44804(54)
0.2253173(27)	1.5093(11)	1.44500(78)	1.40930(51)
0.3005277(20)	1.44227(85)	1.38926(67)	1.35783(46)
0.3206634(21)	1.42193(81)	1.37182(64)	1.34164(44)
0.3408998(26)	1.39986(76)	1.35257(61)	1.32366(43)

(c) F1M

am_q	$Z_m^{\mathrm{mSMOM}}(2.0\,\mathrm{GeV})$	$Z_m^{\mathrm{mSMOM}}(2.5\,\mathrm{GeV})$	$Z_m^{\mathrm{mSMOM}}(3.0\,\mathrm{GeV})$
0.0023399(56)	1.4816(58)	1.3925(46)	1.3457(40)
0.0045390(52)	1.5229(31)	1.4358(24)	1.3906(20)
0.0109343(43)	1.5766(21)	1.4889(15)	1.4429(10)
0.0216286(36)	1.5924(19)	1.5041(13)	1.45734(87)
0.0332244(31)	1.5942(19)	1.5054(13)	1.45821(85)
0.0662201(21)	1.5935(19)	1.5042(13)	1.45612(85)
0.0992248(15)	1.5838(18)	1.4967(13)	1.44852(86)
0.1322378(12)	1.5683(16)	1.4853(12)	1.43784(85)
0.19829064(77)	1.5243(14)	1.4525(11)	1.40862(80)
0.26439970(57)	1.4682(11)	1.40846(95)	1.36961(72)
0.33066808(62)	1.40308(86)	1.35444(79)	1.32105(63)
0.3610280(12)	1.36962(78)	1.32550(72)	1.29456(59)

Table C.4: Z_m in the RI/mSMOM (massive) scheme interpolated to various renormalisation scales μ for various bare heavy quark masses on the Möbius ensembles.

(a) C1S

am_q	$Z_m^{\mathrm{SMOM}}(2.0\,\mathrm{GeV})$	$Z_m^{\mathrm{SMOM}}(2.5\,\mathrm{GeV})$	$Z_m^{\mathrm{SMOM}}(3.0\,\mathrm{GeV})$
0.008162(19)	1.5398(19)	1.4727(12)	1.4281(11)
0.013085(18)	1.5388(13)	1.47178(99)	1.42749(86)
0.022938(16)	1.5342(11)	1.46817(86)	1.42469(73)
0.042720(12)	1.5205(10)	1.45901(80)	1.41750(67)

(b) M1S

am_q	$Z_m^{\mathrm{SMOM}}(2.0\,\mathrm{GeV})$	$Z_m^{\mathrm{SMOM}}(2.5\,\mathrm{GeV})$	$Z_m^{\mathrm{SMOM}}(3.0\,\mathrm{GeV})$
0.0046727(72)	1.5709(26)	1.4887(14)	1.4376(11)
0.0086561(64)	1.5686(20)	1.4876(13)	1.43630(98)
0.0156319(55)	1.5643(17)	1.4851(13)	1.43422(94)
0.0305977(42)	1.5516(15)	1.4780(12)	1.42910(91)

(c) F1S

am_q	$Z_m^{\mathrm{SMOM}}(2.0\,\mathrm{GeV})$	$Z_m^{\mathrm{SMOM}}(2.5\,\mathrm{GeV})$	$Z_m^{\mathrm{SMOM}}(3.0\,\mathrm{GeV})$
0.0030769(95)	1.5795(20)	1.4940(14)	1.4382(11)
0.0052722(88)	1.5795(19)	1.4935(13)	1.4376(10)
0.0116565(62)	1.5764(18)	1.4916(13)	1.4362(10)
0.0223393(43)	1.5672(16)	1.4867(12)	1.43275(98)

Table C.5: Z_m in the RI/SMOM (massless) scheme interpolated to various renormalisation scales μ for various bare heavy quark masses on the Shamir ensembles.

(a) C1M

am_q	$Z_m^{\mathrm{SMOM}}(2.0\,\mathrm{GeV})$	$Z_m^{\mathrm{SMOM}}(2.5\,\mathrm{GeV})$	$Z_m^{\mathrm{SMOM}}(3.0\,\mathrm{GeV})$
0.005601(12)	1.5419(15)	1.47525(94)	1.43143(83)
0.010574(11)	1.5424(11)	1.47448(81)	1.43052(64)
0.0186330(95)	1.53875(99)	1.47170(72)	1.42803(57)
0.0366642(79)	1.52670(91)	1.46351(66)	1.42131(54)

(b) M1M

am_q	$Z_m^{\mathrm{SMOM}}(2.0\,\mathrm{GeV})$	$Z_m^{\mathrm{SMOM}}(2.5\,\mathrm{GeV})$	$Z_m^{\mathrm{SMOM}}(3.0\,\mathrm{GeV})$
0.0043116(61)	1.5735(20)	1.4909(12)	1.43843(97)
0.0083018(56)	1.5703(22)	1.4891(12)	1.43735(85)
0.0135907(51)	1.5672(19)	1.4871(11)	1.43589(82)
0.0268709(39)	1.5570(16)	1.4811(10)	1.43159(78)

(c) F1M

am_q	$Z_m^{\mathrm{SMOM}}(2.0\,\mathrm{GeV})$	$Z_m^{\mathrm{SMOM}}(2.5\,\mathrm{GeV})$	$Z_m^{\mathrm{SMOM}}(3.0\,\mathrm{GeV})$
0.0023399(56)	1.5792(22)	1.4926(17)	1.4377(11)
0.0045390(52)	1.5791(20)	1.4926(15)	1.4373(10)
0.0109343(43)	1.5758(18)	1.4905(14)	1.4356(10)
0.0216286(36)	1.5672(17)	1.4859(13)	1.4324(10)

Table C.6: Z_m in the RI/SMOM (massless) scheme interpolated to various renormalisation scales μ for various bare heavy quark masses on the Möbius ensembles.

References

[1] J. Charles et al., *Current status of the Standard Model CKM fit and constraints on $\Delta F = 2$ New Physics*, Phys. Rev. D **91** (2015) 073007 [arXiv:1501.05013].

[2] RBC/UKQCD collaboration, N. Garron, R. J. Hudspith and A. T. Lytle, *Neutral Kaon Mixing Beyond the Standard Model with $n_f = 2 + 1$ Chiral Fermions Part 1: Bare Matrix Elements and Physical Results*, JHEP **11** (2016) 001 [arXiv:1609.03334].

[3] SWME collaboration, B. J. Choi et al., *Kaon BSM B-parameters using improved staggered fermions from $N_f = 2 + 1$ unquenched QCD*, Phys. Rev. D **93** (2016) 014511 [arXiv:1509.00592].

[4] ETM collaboration, V. Bertone et al., *Kaon Mixing Beyond the SM from N_f=2 tmQCD and model independent constraints from the UTA*, JHEP **03** (2013) 089 [arXiv:1207.1287], [Erratum: JHEP07,143(2013)].

[5] ETM collaboration, N. Carrasco, P. Dimopoulos, R. Frezzotti, V. Lubicz, G. C. Rossi, S. Simula et al., *ΔS=2 and ΔC=2 bag parameters in the standard model and beyond from N_f=2+1+1 twisted-mass lattice QCD*, Phys. Rev. D **92** (2015) 034516 [arXiv:1505.06639].

[6] Particle Data Group collaboration, R. L. Workman et al., *Review of Particle Physics*, PTEP **2022** (2022) 083C01.

[7] Flavour Lattice Averaging Group (FLAG) collaboration, Y. Aoki et al., *FLAG Review 2021*, Eur. Phys. J. C **82** (2022) 869 [arXiv:2111.09849].

[8] P. A. Boyle, L. Del Debbio, A. Jüttner, A. Khamseh, F. Sanfilippo and J. T. Tsang, *The decay constants $\mathbf{f_D}$ and $\mathbf{f_{D_s}}$ in the continuum limit of $\mathbf{N_f = 2 + 1}$ domain wall lattice QCD*, JHEP **12** (2017) 008 [arXiv:1701.02644].

[9] RBC, UKQCD collaboration, P. A. Boyle, F. Erben, J. M. Flynn, N. Garron, J. Kettle, R. Mukherjee et al., *Kaon mixing beyond the standard model with physical masses*, Phys. Rev. D **110** (2024) 034501 [arXiv:2404.02297].

[10] RBC, UKQCD collaboration, L. Del Debbio, F. Erben, J. M. Flynn, R. Mukherjee and J. T. Tsang, *Absorbing discretization effects with a massive renormalization scheme: The charm-quark mass*, Phys. Rev. D **110** (2024) 054512 [arXiv:2407.18700].

[11] L. Del Debbio, F. Erben, J. Flynn, R. Mukherjee and J. T. Tsang, *Charm quark mass using a massive nonperturbative renormalisation scheme*, PoS **LATTICE2023** (2024) 294 [arXiv:2312.16537].

[12] C.-N. Yang and R. L. Mills, *Conservation of Isotopic Spin and Isotopic Gauge Invariance*, Phys. Rev. **96** (1954) 191.

[13] S. L. Glashow, *The renormalizability of vector meson interactions*, Nucl. Phys. **10** (1959) 107.

[14] S. L. Glashow, *Partial Symmetries of Weak Interactions*, Nucl. Phys. **22** (1961) 579.

[15] A. Salam and J. C. Ward, *Weak and electromagnetic interactions*, Nuovo Cim. **11** (1959) 568.

[16] A. Salam and J. C. Ward, *Electromagnetic and weak interactions*, Phys. Lett. **13** (1964) 168.

[17] S. Weinberg, *A Model of Leptons*, Phys. Rev. Lett. **19** (1967) 1264.

[18] P. W. Higgs, *Broken Symmetries and the Masses of Gauge Bosons*, Phys. Rev. Lett. **13** (1964) 508.

[19] P. W. Higgs, *Broken symmetries, massless particles and gauge fields*, Phys. Lett. **12** (1964) 132.

[20] F. Englert and R. Brout, *Broken Symmetry and the Mass of Gauge Vector Mesons*, Phys. Rev. Lett. **13** (1964) 321.

[21] J. D. Bjorken and S. L. Glashow, *Elementary Particles and SU(4)*, Phys. Lett. **11** (1964) 255.

[22] SLAC-SP-017 collaboration, J. E. Augustin et al., *Discovery of a Narrow Resonance in e^+e^- Annihilation*, Phys. Rev. Lett. **33** (1974) 1406.

[23] E598 collaboration, J. J. Aubert et al., *Experimental Observation of a Heavy Particle J*, Phys. Rev. Lett. **33** (1974) 1404.

[24] N. Cabibbo, *Unitary Symmetry and Leptonic Decays*, Phys. Rev. Lett. **10** (1963) 531.

[25] M. Kobayashi and T. Maskawa, *CP Violation in the Renormalizable Theory of Weak Interaction*, Prog. Theor. Phys. **49** (1973) 652.

[26] E288 collaboration, S. W. Herb et al., *Observation of a Dimuon Resonance at 9.5-GeV in 400-GeV Proton-Nucleus Collisions*, Phys. Rev. Lett. **39** (1977) 252.

[27] CDF collaboration, F. Abe et al., *Observation of top quark production in $\bar{p}p$ collisions*, Phys. Rev. Lett. **74** (1995) 2626 [arXiv:hep-ex/9503002].

[28] UA1 collaboration, G. Arnison et al., *Experimental Observation of Isolated Large Transverse Energy Electrons with Associated Missing Energy at $\sqrt{s} = 540$ GeV*, Phys. Lett. B **122** (1983) 103.

[29] UA1 collaboration, G. Arnison et al., *Experimental Observation of Lepton Pairs of Invariant Mass Around 95-GeV/c**2 at the CERN SPS Collider*, Phys. Lett. B **126** (1983) 398.

[30] DONUT collaboration, K. Kodama et al., *Observation of tau neutrino interactions*, Phys. Lett. B **504** (2001) 218 [arXiv:hep-ex/0012035].

[31] ATLAS collaboration, G. Aad et al., *Observation of a new particle in the search for the Standard Model Higgs boson with the ATLAS detector at the LHC*, Phys. Lett. B **716** (2012) 1 [arXiv:1207.7214].

[32] CMS collaboration, S. Chatrchyan et al., *Observation of a New Boson at a Mass of 125 GeV with the CMS Experiment at the LHC*, Phys. Lett. B **716** (2012) 30 [arXiv:1207.7235].

[33] G. R. Farrar and M. E. Shaposhnikov, *Baryon asymmetry of the universe in the standard electroweak theory*, Phys. Rev. D **50** (1994) 774 [arXiv:hep-ph/9305275].

[34] M. B. Gavela, M. Lozano, J. Orloff and O. Pene, *Standard model CP violation and baryon asymmetry. Part 1: Zero temperature*, Nucl. Phys. B **430** (1994) 345 [arXiv:hep-ph/9406288].

[35] P. Huet and E. Sather, *Electroweak baryogenesis and standard model CP violation*, Phys. Rev. D **51** (1995) 379 [arXiv:hep-ph/9404302].

[36] P. A. M. Dirac, *The fundamental equations of quantum mechanics*, Proc. Roy. Soc. Lond. A **109** (1925) 642.

[37] R. P. Feynman, *Space-time approach to nonrelativistic quantum mechanics*, Rev. Mod. Phys. **20** (1948) 367.

[38] C. S. Wu, E. Ambler, R. W. Hayward, D. D. Hoppes and R. P. Hudson, *Experimental Test of Parity Conservation in β Decay*, Phys. Rev. **105** (1957) 1413.

[39] T. D. Lee and C.-N. Yang, *Question of Parity Conservation in Weak Interactions*, Phys. Rev. **104** (1956) 254.

[40] J. H. Christenson, J. W. Cronin, V. L. Fitch and R. Turlay, *Evidence for the* 2π *Decay of the* K_2^0 *Meson*, Phys. Rev. Lett. **13** (1964) 138.

[41] H. Fritzsch, M. Gell-Mann and H. Leutwyler, *Advantages of the Color Octet Gluon Picture*, Phys. Lett. B **47** (1973) 365.

[42] H. D. Politzer, *Reliable Perturbative Results for Strong Interactions?*, Phys. Rev. Lett. **30** (1973) 1346.

[43] D. J. Gross and F. Wilczek, *Ultraviolet Behavior of Nonabelian Gauge Theories*, Phys. Rev. Lett. **30** (1973) 1343.

[44] LHCb collaboration, R. Aaij et al., *Observation of* $J/\psi\phi$ *structures consistent with exotic states from amplitude analysis of* $B^+ \to J/\psi\phi K^+$ *decays*, Phys. Rev. Lett. **118** (2017) 022003 [arXiv:1606.07895].

[45] LHCb collaboration, R. Aaij et al., *Amplitude analysis of* $B^+ \to J/\psi\phi K^+$ *decays*, Phys. Rev. D **95** (2017) 012002 [arXiv:1606.07898].

[46] LHCb collaboration, R. Aaij et al., *Observation of structure in the* J/ψ *-pair mass spectrum*, Sci. Bull. **65** (2020) 1983 [arXiv:2006.16957].

[47] LHCb collaboration, R. Aaij et al., *Observation of* $J/\psi p$ *Resonances Consistent with Pentaquark States in* $\Lambda_b^0 \to J/\psi K^- p$ *Decays*, Phys. Rev. Lett. **115** (2015) 072001 [arXiv:1507.03414].

[48] LHCb collaboration, R. Aaij et al., *Observation of a* $J/\psi\Lambda$ *Resonance Consistent with a Strange Pentaquark Candidate in B-*$\to J/\psi\Lambda p^-$ *Decays*, Phys. Rev. Lett. **131** (2023) 031901 [arXiv:2210.10346].

[49] M. Gell-Mann, *The symmetry group of vector and axial vector currents*, Physics Physique Fizika **1** (1964) 63.

[50] M. Gell-Mann, R. J. Oakes and B. Renner, *Behavior of current divergences under SU(3) x SU(3)*, Phys. Rev. **175** (1968) 2195.

[51] M. E. Peskin and D. V. Schroeder, *An Introduction to quantum field theory*. Addison-Wesley, Reading, USA, 1995.

[52] K. Fujikawa, *Path Integral Measure for Gauge Invariant Fermion Theories*, Phys. Rev. Lett. **42** (1979) 1195.

[53] M. Gell-Mann, *The Eightfold Way: A Theory of strong interaction symmetry*, .

[54] M. Gell-Mann, *A Schematic Model of Baryons and Mesons*, Phys. Lett. **8** (1964) 214.

[55] S. Aoki et al., *Review of lattice results concerning low-energy particle physics*, Eur. Phys. J. C **77** (2017) 112 [arXiv:1607.00299].

[56] H. Leutwyler, *On the foundations of chiral perturbation theory*, Annals Phys. **235** (1994) 165 [arXiv:hep-ph/9311274].

[57] RBC-UKQCD collaboration, C. Allton et al., *Physical Results from 2+1 Flavor Domain Wall QCD and SU(2) Chiral Perturbation Theory*, Phys. Rev. D **78** (2008) 114509 [arXiv:0804.0473].

[58] J. Goldstone, A. Salam and S. Weinberg, *Broken Symmetries*, Phys. Rev. **127** (1962) 965.

[59] G. S. Guralnik, C. R. Hagen and T. W. B. Kibble, *Global Conservation Laws and Massless Particles*, Phys. Rev. Lett. **13** (1964) 585.

[60] L. Wolfenstein, *Parametrization of the Kobayashi-Maskawa Matrix*, Phys. Rev. Lett. **51** (1983) 1945.

[61] S. Aoki et al., *Review of Lattice Results Concerning Low-Energy Particle Physics*, Eur. Phys. J. C **74** (2014) 2890 [arXiv:1310.8555].

[62] C. A. Baker et al., *An Improved experimental limit on the electric dipole moment of the neutron*, Phys. Rev. Lett. **97** (2006) 131801 [arXiv:hep-ex/0602020].

[63] R. D. Peccei and H. R. Quinn, *CP Conservation in the Presence of Instantons*, Phys. Rev. Lett. **38** (1977) 1440.

[64] RBC, UKQCD collaboration, Z. Bai et al., *Standard Model Prediction for Direct CP Violation in $K \to \pi\pi$ Decay*, Phys. Rev. Lett. **115** (2015) 212001 [arXiv:1505.07863].

[65] RBC, UKQCD collaboration, R. Abbott et al., *Direct CP violation and the $\Delta I = 1/2$ rule in $K \to \pi\pi$ decay from the standard model*, Phys. Rev. D **102** (2020) 054509 [arXiv:2004.09440].

[66] A. J. Buras, D. Guadagnoli and G. Isidori, *On ϵ_K Beyond Lowest Order in the Operator Product Expansion*, Phys. Lett. B **688** (2010) 309 [arXiv:1002.3612].

[67] A. J. Buras and D. Guadagnoli, *Correlations among new CP violating effects in $\Delta F = 2$ observables*, Phys. Rev. D **78** (2008) 033005 [arXiv:0805.3887].

[68] N. H. Christ, *Computing the long-distance contribution to the kaon mixing parameter ϵ_K*, PoS **LATTICE2011** (2011) 277 [arXiv:1201.2065].

[69] Z. Bai, *Long distance part of ϵ_K from lattice QCD*, PoS **LATTICE2016** (2017) 309 [arXiv:1611.06601].

[70] Z. Bai, N. H. Christ, J. M. Karpie, C. T. Sachrajda, A. Soni and B. Wang, *Long-distance contribution to εK from lattice QCD*, Phys. Rev. D **109** (2024) 054501 [arXiv:2309.01193].

[71] F. Gabbiani, E. Gabrielli, A. Masiero and L. Silvestrini, *A Complete analysis of FCNC and CP constraints in general SUSY extensions of the standard model*, Nucl. Phys. B **477** (1996) 321 [arXiv:hep-ph/9604387].

[72] RBC, UKQCD collaboration, P. A. Boyle, N. Garron, R. J. Hudspith, C. Lehner and A. T. Lytle, *Neutral kaon mixing beyond the Standard Model with $n_f = 2 + 1$ chiral fermions. Part 2: non perturbative renormalisation of the $\Delta F = 2$ four-quark operators*, JHEP **10** (2017) 054 [arXiv:1708.03552].

[73] D. Becirevic and G. Villadoro, *Remarks on the hadronic matrix elements relevant to the SUSY K0 - anti-K0 mixing amplitude*, Phys. Rev. D **70** (2004) 094036 [arXiv:hep-lat/0408029].

[74] R. Babich, N. Garron, C. Hoelbling, J. Howard, L. Lellouch and C. Rebbi, *K0 - anti-0 mixing beyond the standard model and CP-violating electroweak penguins in quenched QCD with exact chiral symmetry*, Phys. Rev. D **74** (2006) 073009 [arXiv:hep-lat/0605016].

[75] A. Donini, V. Gimenez, L. Giusti and G. Martinelli, *Renormalization group invariant matrix elements of Delta S = 2 and Delta I = 3/2 four fermion operators without quark masses*, Phys. Lett. B **470** (1999) 233 [arXiv:hep-lat/9910017].

[76] SWME collaboration, T. Bae et al., *Neutral kaon mixing from new physics: matrix elements in $N_f = 2 + 1$ lattice QCD*, Phys. Rev. D **88** (2013) 071503 [arXiv:1309.2040].

[77] RBC, UKQCD collaboration, T. Blum et al., *Domain wall QCD with physical quark masses*, Phys. Rev. D **93** (2016) 074505 [arXiv:1411.7017].

[78] SWME collaboration, T. Bae et al., *Improved determination of BK with staggered quarks*, Phys. Rev. D **89** (2014) 074504 [arXiv:1402.0048].

[79] T. Bae et al., *Update on B_K and ε_K with staggered quarks*, PoS **LATTICE2013** (2014) 476 [arXiv:1310.7319].

[80] RBC, UKQCD collaboration, R. Arthur et al., *Domain Wall QCD with Near-Physical Pions*, Phys. Rev. D **87** (2013) 094514 [arXiv:1208.4412].

[81] J. Laiho and R. S. Van de Water, *Pseudoscalar decay constants, light-quark masses, and B_K from mixed-action lattice QCD*, PoS **LATTICE2011** (2011) 293 [arXiv:1112.4861].

[82] SWME collaboration, T. Bae et al., *Kaon B-parameter from improved staggered fermions in $N_f = 2 + 1$ QCD* , Phys. Rev. Lett. **109** (2012) 041601 [arXiv:1111.5698].

[83] BMW collaboration, S. Durr et al., *Precision computation of the kaon bag parameter*, Phys. Lett. B **705** (2011) 477 [arXiv:1106.3230].

[84] Y. Aoki et al., *Continuum Limit of B_K from 2+1 Flavor Domain Wall QCD*, Phys. Rev. D **84** (2011) 014503 [arXiv:1012.4178].

[85] T. Bae, Y.-C. Jang, C. Jung, H.-J. Kim, J. Kim, K. Kim et al., *B_K using HYP-smeared staggered fermions in $N_f = 2 + 1$ unquenched QCD*, Phys. Rev. D **82** (2010) 114509 [arXiv:1008.5179].

[86] C. Aubin, J. Laiho and R. S. Van de Water, *The Neutral kaon mixing parameter B(K) from unquenched mixed-action lattice QCD*, Phys. Rev. D **81** (2010) 014507 [arXiv:0905.3947].

[87] G. Buchalla, A. J. Buras and M. E. Lautenbacher, *Weak decays beyond leading logarithms*, Rev. Mod. Phys. **68** (1996) 1125 [arXiv:hep-ph/9512380].

[88] ETM collaboration, V. Bertone et al., *Kaon Mixing Beyond the SM from N_f=2 tmQCD and model independent constraints from the UTA*, JHEP **03** (2013) 089 [arXiv:1207.1287], [Erratum: JHEP 07, 143 (2013)].

[89] C. R. Allton, L. Conti, A. Donini, V. Gimenez, L. Giusti, G. Martinelli et al., *B parameters for Delta S = 2 supersymmetric operators*, Phys. Lett. B **453** (1999) 30 [arXiv:hep-lat/9806016].

[90] SWME collaboration, J. Leem et al., *Calculation of BSM Kaon B-parameters using Staggered Quarks*, PoS **LATTICE2014** (2014) 370 [arXiv:1411.1501].

[91] T. Ruf, *Measurements of Discrete Symmetries in the Neutral Kaon System with the CPLEAR (PS195) Experiment*, Adv. Ser. Direct. High Energy Phys. **23** (2015) 237.

[92] T. Inami and C. S. Lim, *Effects of Superheavy Quarks and Leptons in Low-Energy Weak Processes k(L) —> mu anti-mu, K+ —> pi+ Neutrino anti-neutrino and K0 <—> anti-K0*, Prog. Theor. Phys. **65** (1981) 297 [Erratum: Prog.Theor.Phys. 65, 1772 (1981)].

[93] C. W. Bernard, T. Blum and A. Soni, *SU(3) flavor breaking in hadronic matrix elements for B - anti-B oscillations*, Phys. Rev. D **58** (1998) 014501 [arXiv:hep-lat/9801039].

[94] UTfit collaboration, M. Bona et al., *The Unitarity Triangle Fit in the Standard Model and Hadronic Parameters from Lattice QCD: A Reappraisal after the Measurements of Delta m(s) and BR(B —> tau nu(tau))*, JHEP **10** (2006) 081 [arXiv:hep-ph/0606167].

[95] HFLAV collaboration, Y. S. Amhis et al., *Averages of b-hadron, c-hadron, and τ-lepton properties as of 2018*, Eur. Phys. J. C **81** (2021) 226 [arXiv:1909.12524].

[96] A. Lenz and U. Nierste, *Theoretical update of $B_s - \bar{B}_s$ mixing*, JHEP **06** (2007) 072 [arXiv:hep-ph/0612167].

[97] M. Beneke, G. Buchalla and I. Dunietz, *Width Difference in the $B_s - \bar{B}_s$ System*, Phys. Rev. D **54** (1996) 4419 [arXiv:hep-ph/9605259], [Erratum: Phys.Rev.D 83, 119902 (2011)].

[98] ETM collaboration, N. Carrasco et al., *B-physics from $N_f = 2$ tmQCD: the Standard Model and beyond*, JHEP **03** (2014) 016 [arXiv:1308.1851].

[99] HPQCD collaboration, E. Gamiz, C. T. H. Davies, G. P. Lepage, J. Shigemitsu and M. Wingate, *Neutral B Meson Mixing in Unquenched Lattice QCD*, Phys. Rev. D **80** (2009) 014503 [arXiv:0902.1815].

[100] Y. Aoki, T. Ishikawa, T. Izubuchi, C. Lehner and A. Soni, *Neutral B meson mixings and B meson decay constants with static heavy and domain-wall light quarks*, Phys. Rev. D **91** (2015) 114505 [arXiv:1406.6192].

[101] R. J. Dowdall, C. T. H. Davies, R. R. Horgan, G. P. Lepage, C. J. Monahan, J. Shigemitsu et al., *Neutral B-meson mixing from full lattice QCD at the physical point*, Phys. Rev. D **100** (2019) 094508 [arXiv:1907.01025].

[102] C. Albertus et al., *Neutral B-meson mixing from unquenched lattice QCD with domain-wall light quarks and static b-quarks*, Phys. Rev. D **82** (2010) 014505 [arXiv:1001.2023].

[103] A. Bazavov et al., *Neutral B-meson mixing from three-flavor lattice QCD: Determination of the SU(3)-breaking ratio \xi*, Phys. Rev. D **86** (2012) 034503 [arXiv:1205.7013].

[104] Fermilab Lattice, MILC collaboration, A. Bazavov et al., *$B^0_{(s)}$-mixing matrix elements from lattice QCD for the Standard Model and beyond*, Phys. Rev. D **93** (2016) 113016 [arXiv:1602.03560].

[105] RBC/UKQCD collaboration, P. A. Boyle, L. Del Debbio, N. Garron, A. Juttner, A. Soni, J. T. Tsang et al., *SU(3)-breaking ratios for $D_{(s)}$ and $B_{(s)}$ mesons*, arXiv:1812.08791.

[106] E. Dalgic, A. Gray, E. Gamiz, C. T. H. Davies, G. P. Lepage, J. Shigemitsu et al., *$B^0_s - \bar{B}^0_s$ mixing parameters from unquenched lattice QCD*, Phys. Rev. D **76** (2007) 011501 [arXiv:hep-lat/0610104].

[107] D. King, A. Lenz and T. Rauh, *B_s mixing observables and $|V_{td}/V_{ts}|$ from sum rules*, JHEP **05** (2019) 034 [arXiv:1904.00940].

[108] L. Di Luzio, M. Kirk, A. Lenz and T. Rauh, *ΔM_s theory precision confronts flavour anomalies*, JHEP **12** (2019) 009 [arXiv:1909.11087].

[109] D. King, M. Kirk, A. Lenz and T. Rauh, *$|V_{cb}|$ and γ from B-mixing - Addendum to "B_s mixing observables and $|V_{td}/V_{ts}|$ from sum rules"*, arXiv:1911.07856, [Addendum: JHEP 03, 112 (2020)].

[110] N. Carrasco et al., *$D^0 - \bar{D}^0$ mixing in the standard model and beyond from N_f =2 twisted mass QCD*, Phys. Rev. D **90** (2014) 014502 [arXiv:1403.7302].

[111] A. Bazavov et al., *Short-distance matrix elements for D^0-meson mixing for $N_f = 2 + 1$ lattice QCD*, Phys. Rev. D **97** (2018) 034513 [arXiv:1706.04622].

[112] LHCb collaboration, R. Aaij et al., *Physics case for an LHCb Upgrade II - Opportunities in flavour physics, and beyond, in the HL-LHC era*, arXiv:1808.08865.

[113] E. Golowich, J. Hewett, S. Pakvasa and A. A. Petrov, *Relating D0-anti-D0 Mixing and D0 —> l+ l- with New Physics*, Phys. Rev. D **79** (2009) 114030 [arXiv:0903.2830].

[114] H. E. Haber, *The Status of the minimal supersymmetric standard model and beyond*, Nucl. Phys. B Proc. Suppl. **62** (1998) 469 [arXiv:hep-ph/9709450].

[115] Y. Nir, *CP violation: A New era*, in *55th Scottish Universities Summer School in Physics: Heavy Flavor Physics (SUSSP 2001)*, pp. 147–200, 9, 2001, arXiv:hep-ph/0109090.

[116] T. Goto, N. Kitazawa, Y. Okada and M. Tanaka, *Model independent analysis of $B\bar{B}$ mixing and CP violation in B decays*, Phys. Rev. D **53** (1996) 6662 [arXiv:hep-ph/9506311].

[117] J. P. Silva and L. Wolfenstein, *Detecting new physics from CP violating phase measurements in B decays*, Phys. Rev. D **55** (1997) 5331 [arXiv:hep-ph/9610208].

[118] Y. Grossman, Z. Ligeti and Y. Nir, *Future prospects of B physics*, Prog. Theor. Phys. **122** (2009) 125 [arXiv:0904.4262].

[119] G. Isidori, Y. Nir and G. Perez, *Flavor Physics Constraints for Physics Beyond the Standard Model*, Ann. Rev. Nucl. Part. Sci. **60** (2010) 355 [arXiv:1002.0900].

[120] UTfit collaboration, M. Bona et al., *Model-independent constraints on $\Delta F = 2$ operators and the scale of new physics*, JHEP **03** (2008) 049 [arXiv:0707.0636].

[121] C. G. Bollini and J. J. Giambiagi, *Lowest order divergent graphs in nu-dimensional space*, Phys. Lett. B **40** (1972) 566.

[122] C. G. Bollini and J. J. Giambiagi, *Dimensional Renormalization: The Number of Dimensions as a Regularizing Parameter*, Nuovo Cim. B **12** (1972) 20.

[123] G. 't Hooft and M. J. G. Veltman, *Regularization and Renormalization of Gauge Fields*, Nucl. Phys. B **44** (1972) 189.

[124] W. Pauli and F. Villars, *On the Invariant regularization in relativistic quantum theory*, Rev. Mod. Phys. **21** (1949) 434.

[125] K. G. Wilson, *Confinement of Quarks*, Phys. Rev. D **10** (1974) 2445.

[126] P. F. Bedaque, *Aharonov-Bohm effect and nucleon nucleon phase shifts on the lattice* , Phys. Lett. B **593** (2004) 82 [arXiv:nucl-th/0402051].

[127] UKQCD collaboration, J. M. Flynn, A. Juttner and C. T. Sachrajda, *A Numerical study of partially twisted boundary conditions*, Phys. Lett. B **632** (2006) 313 [arXiv:hep-lat/0506016].

[128] K. Symanzik, *Continuum Limit and Improved Action in Lattice Theories. 1. Principles and φ^4 Theory*, Nucl. Phys. B **226** (1983) 187.

[129] K. Symanzik, *Continuum Limit and Improved Action in Lattice Theories. 2. O(N) Nonlinear Sigma Model in Perturbation Theory*, Nucl. Phys. B **226** (1983) 205.

[130] M. Luscher and P. Weisz, *Computation of the Action for On-Shell Improved Lattice Gauge Theories at Weak Coupling*, Phys. Lett. B **158** (1985) 250.

[131] G. Curci, P. Menotti and G. Paffuti, *Symanzik's Improved Lagrangian for Lattice Gauge Theory*, Phys. Lett. B **130** (1983) 205 [Erratum: Phys.Lett.B 135, 516 (1984)].

[132] W. Bietenholz and U. J. Wiese, *Perfect lattice actions for quarks and gluons*, Nucl. Phys. B **464** (1996) 319 [arXiv:hep-lat/9510026].

[133] K. G. Wilson and J. B. Kogut, *The Renormalization group and the epsilon expansion*, Phys. Rept. **12** (1974) 75.

[134] K. G. Wilson, *The Renormalization Group: Critical Phenomena and the Kondo Problem*, Rev. Mod. Phys. **47** (1975) 773.

[135] Y. Iwasaki, *Renormalization Group Analysis of Lattice Theories and Improved Lattice Action. II. Four-dimensional non-Abelian SU(N) gauge model*, arXiv:1111.7054.

[136] Y. Iwasaki and T. Yoshie, *Renormalization Group Improved Action for SU(3) Lattice Gauge Theory and the String Tension*, Phys. Lett. B **143** (1984) 449.

[137] Y. Iwasaki, *Renormalization group analysis of lattice theories and improved lattice action: Two-dimensional non-linear O(N) sigma model*, Nucl. Phys. B **258** (1985) 141.

[138] RBC, UKQCD collaboration, D. J. Antonio et al., *First results from 2+1 Flavor Domain Wall QCD: Mass Spectrum, Topology Change and Chiral Symmetry with L(s) = 8*, Phys. Rev. D **75** (2007) 114501 [arXiv:hep-lat/0612005].

[139] RBC, UKQCD collaboration, Y. Aoki et al., *Continuum Limit Physics from 2+1 Flavor Domain Wall QCD*, Phys. Rev. D **83** (2011) 074508 [arXiv:1011.0892].

[140] H. B. Nielsen and M. Ninomiya, *No Go Theorem for Regularizing Chiral Fermions*, Phys. Lett. B **105** (1981) 219.

[141] M. Luscher, *Exact chiral symmetry on the lattice and the Ginsparg-Wilson relation*, Phys. Lett. B **428** (1998) 342 [arXiv:hep-lat/9802011].

[142] P. H. Ginsparg and K. G. Wilson, *A Remnant of Chiral Symmetry on the Lattice*, Phys. Rev. D **25** (1982) 2649.

[143] R. Narayanan and H. Neuberger, *Chiral determinant as an overlap of two vacua*, Nucl. Phys. B **412** (1994) 574 [arXiv:hep-lat/9307006].

[144] R. Narayanan and H. Neuberger, *Chiral fermions on the lattice*, Phys. Rev. Lett. **71** (1993) 3251 [arXiv:hep-lat/9308011].

[145] R. Narayanan and H. Neuberger, *Infinitely many regulator fields for chiral fermions*, Phys. Lett. B **302** (1993) 62 [arXiv:hep-lat/9212019].

[146] R. Narayanan and H. Neuberger, *A Construction of lattice chiral gauge theories*, Nucl. Phys. B **443** (1995) 305 [arXiv:hep-th/9411108].

[147] H. Neuberger, *Exactly massless quarks on the lattice*, Phys. Lett. B **417** (1998) 141 [arXiv:hep-lat/9707022].

[148] H. Neuberger, *More about exactly massless quarks on the lattice*, Phys. Lett. B **427** (1998) 353 [arXiv:hep-lat/9801031].

[149] C. G. Callan, Jr. and J. A. Harvey, *Anomalies and Fermion Zero Modes on Strings and Domain Walls*, Nucl. Phys. B **250** (1985) 427.

[150] D. B. Kaplan, *A Method for simulating chiral fermions on the lattice*, Phys. Lett. B **288** (1992) 342 [arXiv:hep-lat/9206013].

[151] Y. Shamir, *Constraints on the existence of chiral fermions in interacting lattice theories*, Phys. Rev. Lett. **71** (1993) 2691 [arXiv:hep-lat/9306023].

[152] Y. Shamir, *Anomalies and chiral defects fermions*, Nucl. Phys. B **417** (1994) 167 [arXiv:hep-lat/9310006].

[153] Y. Shamir, *Chiral fermions from lattice boundaries*, Nucl. Phys. B **406** (1993) 90 [arXiv:hep-lat/9303005].

[154] V. Furman and Y. Shamir, *Axial symmetries in lattice QCD with Kaplan fermions*, Nucl. Phys. B **439** (1995) 54 [arXiv:hep-lat/9405004].

[155] T. Blum and A. Soni, *QCD with domain wall quarks*, Phys. Rev. D **56** (1997) 174 [arXiv:hep-lat/9611030].

[156] T. Blum and A. Soni, *Domain wall quarks and kaon weak matrix elements*, Phys. Rev. Lett. **79** (1997) 3595 [arXiv:hep-lat/9706023].

[157] A. Borici, *Truncated overlap fermions: The Link between overlap and domain wall fermions*, NATO Sci. Ser. C **553** (2000) 41 [arXiv:hep-lat/9912040].

[158] A. D. Kennedy, *Algorithms for dynamical fermions*, arXiv:hep-lat/0607038.

[159] S. R. Sharpe, *Future of Chiral Extrapolations with Domain Wall Fermions*, in *Workshop on Domain Wall Fermions at Ten Years*, 6, 2007, arXiv:0706.0218.

[160] R. C. Brower, H. Neff and K. Orginos, *Mobius fermions: Improved domain wall chiral fermions*, Nucl. Phys. B Proc. Suppl. **140** (2005) 686 [arXiv:hep-lat/0409118].

[161] R. C. Brower, H. Neff and K. Orginos, *Mobius fermions*, Nucl. Phys. B Proc. Suppl. **153** (2006) 191 [arXiv:hep-lat/0511031].

[162] R. C. Brower, H. Neff and K. Orginos, *The Möbius domain wall fermion algorithm*, Comput. Phys. Commun. **220** (2017) 1 [arXiv:1206.5214].

[163] N. Metropolis, A. W. Rosenbluth, M. N. Rosenbluth, A. H. Teller and E. Teller, *Equation of state calculations by fast computing machines*, J. Chem. Phys. **21** (1953) 1087.

[164] P. T. Matthews and A. Salam, *The Green's functions of quantized fields*, Nuovo Cim. **12** (1954) 563.

[165] P. T. Matthews and A. Salam, *Propagators of quantized field*, Nuovo Cim. **2** (1955) 120.

[166] F. Fucito, E. Marinari, G. Parisi and C. Rebbi, *A Proposal for Monte Carlo Simulations of Fermionic Systems*, Nucl. Phys. B **180** (1981) 369.

[167] S. Duane, A. D. Kennedy, B. J. Pendleton and D. Roweth, *Hybrid Monte Carlo*, Phys. Lett. B **195** (1987) 216.

[168] N. Cabibbo and E. Marinari, *A New Method for Updating SU(N) Matrices in Computer Simulations of Gauge Theories*, Phys. Lett. B **119** (1982) 387.

[169] A. D. Kennedy and B. J. Pendleton, *Improved Heat Bath Method for Monte Carlo Calculations in Lattice Gauge Theories*, Phys. Lett. B **156** (1985) 393.

[170] S. L. Adler, *An Overrelaxation Method for the Monte Carlo Evaluation of the Partition Function for Multiquadratic Actions*, Phys. Rev. D **23** (1981) 2901.

[171] M. Creutz, *Overrelaxation and Monte Carlo Simulation*, Phys. Rev. D **36** (1987) 515.

[172] C. T. H. Davies, G. G. Batrouni, G. R. Katz, A. S. Kronfeld, G. P. Lepage, K. G. Wilson et al., *Fourier Acceleration in Lattice Gauge Theories. 1. Landau Gauge Fixing*, Phys. Rev. D **37** (1988) 1581.

[173] C. W. Bernard, D. Murphy, A. Soni and K. K. Yee, *Lattice Quark Propagator in Fixed Gauges*, Nucl. Phys. B Proc. Suppl. **17** (1990) 593.

[174] C. W. Bernard, A. Soni and K. K. Yee, *Applications of gauge fixed correlation functions of quarks and gluons*, Nucl. Phys. B Proc. Suppl. **20** (1991) 410.

[175] M. Schröck and H. Vogt, *Coulomb, Landau and Maximally Abelian Gauge Fixing in Lattice QCD with Multi-GPUs*, Comput. Phys. Commun. **184** (2013) 1907 [arXiv:1212.5221].

[176] L. Giusti, M. L. Paciello, C. Parrinello, S. Petrarca and B. Taglienti, *Problems on lattice gauge fixing*, Int. J. Mod. Phys. A **16** (2001) 3487 [arXiv:hep-lat/0104012].

[177] C. Gattringer and C. B. Lang, *Quantum chromodynamics on the lattice*, vol. 788. Springer, Berlin, 2010, 10.1007/978-3-642-01850-3.

[178] S.-J. Dong and K.-F. Liu, *Stochastic estimation with Z(2) noise*, Phys. Lett. B **328** (1994) 130 [arXiv:hep-lat/9308015].

[179] P. C. Hohenberg and B. I. Halperin, *Theory of Dynamic Critical Phenomena*, Rev. Mod. Phys. **49** (1977) 435.

[180] E. Nelson, *Derivation of the Schrodinger equation from Newtonian mechanics*, Phys. Rev. **150** (1966) 1079.

[181] G. Parisi and Y.-s. Wu, *Perturbation Theory Without Gauge Fixing*, Sci. Sin. **24** (1981) 483.

[182] UKQCD collaboration, M. Foster and C. Michael, *Quark mass dependence of hadron masses from lattice QCD*, Phys. Rev. D **59** (1999) 074503 [arXiv:hep-lat/9810021].

[183] P. A. Boyle, A. Juttner, C. Kelly and R. D. Kenway, *Use of stochastic sources for the lattice determination of light quark physics*, JHEP **08** (2008) 086 [arXiv:0804.1501].

[184] UKQCD collaboration, C. McNeile and C. Michael, *Decay width of light quark hybrid meson from the lattice*, Phys. Rev. D **73** (2006) 074506 [arXiv:hep-lat/0603007].

[185] A. S. Gambhir, A. Stathopoulos and K. Orginos, *Deflation as a Method of Variance Reduction for Estimating the Trace of a Matrix Inverse*, SIAM J. Sci. Comput. **39** (2017) A532 [arXiv:1603.05988].

[186] Hadron Spectrum collaboration, M. Peardon, J. Bulava, J. Foley, C. Morningstar, J. Dudek, R. G. Edwards et al., *A Novel quark-field creation operator construction for hadronic physics in lattice QCD*, Phys. Rev. D **80** (2009) 054506 [arXiv:0905.2160].

[187] L. Giusti, P. Hernandez, M. Laine, P. Weisz and H. Wittig, *Low-energy couplings of QCD from current correlators near the chiral limit*, JHEP **04** (2004) 013 [arXiv:hep-lat/0402002].

[188] T. A. DeGrand and S. Schaefer, *Improving meson two point functions in lattice QCD*, Comput. Phys. Commun. **159** (2004) 185 [arXiv:hep-lat/0401011].

[189] T. Blum, T. Izubuchi and E. Shintani, *Error reduction technique using covariant approximation and application to nucleon form factor*, PoS **LATTICE2012** (2012) 262 [arXiv:1212.5542].

[190] T. Blum, T. Izubuchi and E. Shintani, *New class of variance-reduction techniques using lattice symmetries*, Phys. Rev. D **88** (2013) 094503 [arXiv:1208.4349].

[191] E. Shintani, R. Arthur, T. Blum, T. Izubuchi, C. Jung and C. Lehner, *Covariant approximation averaging*, Phys. Rev. D **91** (2015) 114511 [arXiv:1402.0244].

[192] S. Gusken, U. Low, K. H. Mutter, R. Sommer, A. Patel and K. Schilling, *Nonsinglet Axial Vector Couplings of the Baryon Octet in Lattice QCD*, Phys. Lett. B **227** (1989) 266.

[193] B. Efron, *Bootstrap Methods: Another Look at the Jackknife*, Annals Statist. **7** (1979) 1.

[194] ALPHA collaboration, U. Wolff, *Monte Carlo errors with less errors*, Comput. Phys. Commun. **156** (2004) 143 [arXiv:hep-lat/0306017], [Erratum: Comput.Phys.Commun. 176, 383 (2007)].

[195] M. Luscher, *Volume Dependence of the Energy Spectrum in Massive Quantum Field Theories. 1. Stable Particle States*, Commun. Math. Phys. **104** (1986) 177.

[196] G. Colangelo, S. Durr and C. Haefeli, *Finite volume effects for meson masses and decay constants*, Nucl. Phys. B **721** (2005) 136 [arXiv:hep-lat/0503014].

[197] S. Capitani, *Lattice perturbation theory*, Phys. Rept. **382** (2003) 113 [arXiv:hep-lat/0211036].

[198] G. Martinelli, C. Pittori, C. T. Sachrajda, M. Testa and A. Vladikas, *A General method for nonperturbative renormalization of lattice operators*, Nucl. Phys. B **445** (1995) 81 [arXiv:hep-lat/9411010].

[199] C. Sturm, Y. Aoki, N. H. Christ, T. Izubuchi, C. T. C. Sachrajda and A. Soni, *Renormalization of quark bilinear operators in a momentum-subtraction scheme with a nonexceptional subtraction point*, Phys. Rev. D **80** (2009) 014501 [arXiv:0901.2599].

[200] Y. Aoki et al., *Non-perturbative renormalization of quark bilinear operators and B(K) using domain wall fermions*, Phys. Rev. D **78** (2008) 054510 [arXiv:0712.1061].

[201] M. Gorbahn and S. Jager, *Precise MS-bar light-quark masses from lattice QCD in the RI/SMOM scheme*, Phys. Rev. D **82** (2010) 114001 [arXiv:1004.3997].

[202] L. G. Almeida and C. Sturm, *Two-loop matching factors for light quark masses and three-loop mass anomalous dimensions in the RI/SMOM schemes*, Phys. Rev. D **82** (2010) 054017 [arXiv:1004.4613].

[203] E. Franco and V. Lubicz, *Quark mass renormalization in the MS-bar and RI schemes up to the NNLO order*, Nucl. Phys. B **531** (1998) 641 [arXiv:hep-ph/9803491].

[204] K. G. Chetyrkin and A. Retey, *Renormalization and running of quark mass and field in the regularization invariant and MS-bar schemes at three loops and four loops*, Nucl. Phys. B **583** (2000) 3 [arXiv:hep-ph/9910332].

[205] C. Lehner and C. Sturm, *Matching factors for Delta S=1 four-quark operators in RI/SMOM schemes*, Phys. Rev. D **84** (2011) 014001 [arXiv:1104.4948].

[206] J. A. Gracey, *Three loop* $\overline{\rm MS}$ *tensor current anomalous dimension in QCD*, Phys. Lett. B **488** (2000) 175 [arXiv:hep-ph/0007171].

[207] K. G. Chetyrkin, *Quark mass anomalous dimension to O (alpha-s**4)*, Phys. Lett. B **404** (1997) 161 [arXiv:hep-ph/9703278].

[208] M. Ciuchini, E. Franco, V. Lubicz, G. Martinelli, I. Scimemi and L. Silvestrini, *Next-to-leading order QCD corrections to Delta F = 2 effective Hamiltonians*, Nucl. Phys. B **523** (1998) 501 [arXiv:hep-ph/9711402].

[209] A. J. Buras, M. Misiak and J. Urban, *Two loop QCD anomalous dimensions of flavor changing four quark operators within and beyond the standard model*, Nucl. Phys. B **586** (2000) 397 [arXiv:hep-ph/0005183].

[210] M. Papinutto, C. Pena and D. Preti, *On the perturbative renormalization of four-quark operators for new physics*, Eur. Phys. J. C **77** (2017) 376 [arXiv:1612.06461], [Erratum: Eur.Phys.J.C 78, 21 (2018)].

[211] RBC, UKQCD collaboration, P. A. Boyle, N. Garron and R. J. Hudspith, *Neutral kaon mixing beyond the standard model with $N_f = 2 + 1$ chiral fermions*, Phys. Rev. **D86** (2012) 054028 [arXiv:1206.5737].

[212] G. Anzivino et al., *Workshop summary: Kaons@CERN 2023*, Eur. Phys. J. C **84** (2024) 377 [arXiv:2311.02923].

[213] A. J. Buras, *Kaon Theory: 50 Years Later*, in *KM50 Symposium, KEK, Tsukuba*, 7, 2023, arXiv:2307.15737.

[214] E. Goudzovski et al., *Weak Decays of Strange and Light Quarks*, arXiv:2209.07156.

[215] P. A. Boyle, G. Cossu, A. Yamaguchi and A. Portelli, *Grid: A next generation data parallel C++ QCD library*, PoS **LATTICE2015** (2016) 023.

[216] A. Yamaguchi, P. Boyle, G. Cossu, G. Filaci, C. Lehner and A. Portelli, *Grid: OneCode and FourAPIs*, PoS **LATTICE2021** (2022) 035 [arXiv:2203.06777].

[217] A. Portelli, N. Lachini, F. Erben, M. Marshall, F. Joswig, R. Hodgson et al., *aportelli/Hadrons: Hadrons v1.4*, 2023. 10.5281/zenodo.8023716.

[218] M. Lüscher, *Stochastic locality and master-field simulations of very large lattices*, EPJ Web Conf. **175** (2018) 01002 [arXiv:1707.09758].

[219] M. Bruno, M. Cè, A. Francis, P. Fritzsch, J. R. Green, M. T. Hansen et al., *Exploiting stochastic locality in lattice QCD: hadronic observables and their uncertainties*, JHEP **11** (2023) 167 [arXiv:2307.15674].

[220] D. Becirevic and G. Villadoro, *Impact of the finite volume effects on the chiral behavior of f(K) and B(K)*, Phys. Rev. D **69** (2004) 054010 [arXiv:hep-lat/0311028].

[221] Flavour Lattice Averaging Group (FLAG) collaboration, Y. Aoki et al., *FLAG Review 2021*, Eur. Phys. J. C **82** (2022) 869 [arXiv:2111.09849].

[222] Extended Twisted Mass collaboration, C. Alexandrou et al., *Quark masses using twisted-mass fermion gauge ensembles*, Phys. Rev. D **104** (2021) 074515 [arXiv:2104.13408].

[223] Fermilab Lattice, MILC, TUMQCD collaboration, A. Bazavov et al., *Up-, down-, strange-, charm-, and bottom-quark masses from four-flavor lattice QCD*, Phys. Rev. D **98** (2018) 054517 [arXiv:1802.04248].

[224] European Twisted Mass collaboration, N. Carrasco et al., *Up, down, strange and charm quark masses with N_f = 2+1+1 twisted mass lattice QCD*, Nucl. Phys. B **887** (2014) 19 [arXiv:1403.4504].

[225] D. Giusti, V. Lubicz, C. Tarantino, G. Martinelli, F. Sanfilippo, S. Simula et al., *Leading isospin-breaking corrections to pion, kaon and charmed-meson masses with Twisted-Mass fermions*, Phys. Rev. D **95** (2017) 114504 [arXiv:1704.06561].

[226] HPQCD collaboration, A. T. Lytle, C. T. H. Davies, D. Hatton, G. P. Lepage and C. Sturm, *Determination of quark masses from* $\mathbf{n_f = 4}$ *lattice QCD and the RI-SMOM intermediate scheme*, Phys. Rev. D **98** (2018) 014513 [arXiv:1805.06225].

[227] B. Chakraborty, C. T. H. Davies, B. Galloway, P. Knecht, J. Koponen, G. C. Donald et al., *High-precision quark masses and QCD coupling from* $n_f = 4$ *lattice QCD*, Phys. Rev. D **91** (2015) 054508 [arXiv:1408.4169].

[228] ALPHA collaboration, M. Bruno, I. Campos, P. Fritzsch, J. Koponen, C. Pena, D. Preti et al., *Light quark masses in* $N_\mathrm{f} = 2 + 1$ *lattice QCD with Wilson fermions*, Eur. Phys. J. C **80** (2020) 169 [arXiv:1911.08025].

[229] S. Durr, Z. Fodor, C. Hoelbling, S. D. Katz, S. Krieg, T. Kurth et al., *Lattice QCD at the physical point: Simulation and analysis details*, JHEP **08** (2011) 148 [arXiv:1011.2711].

[230] S. Durr, Z. Fodor, C. Hoelbling, S. D. Katz, S. Krieg, T. Kurth et al., *Lattice QCD at the physical point: light quark masses*, Phys. Lett. B **701** (2011) 265 [arXiv:1011.2403].

[231] A. Bazavov et al., *Staggered chiral perturbation theory in the two-flavor case and SU(2) analysis of the MILC data*, PoS **LATTICE2010** (2010) 083 [arXiv:1011.1792].

[232] ALPHA collaboration, M. Bruno, I. Campos, J. Koponen, C. Pena, D. Preti, A. Ramos et al., *Light and strange quark masses from* $N_f = 2 + 1$ *simulations with Wilson fermions*, PoS **LATTICE2018** (2019) 220 [arXiv:1903.04094].

[233] MILC collaboration, A. Bazavov et al., *MILC results for light pseudoscalars*, PoS **CD09** (2009) 007 [arXiv:0910.2966].

[234] C. McNeile, C. T. H. Davies, E. Follana, K. Hornbostel and G. P. Lepage, *High-Precision c and b Masses, and QCD Coupling from Current-Current Correlators in Lattice and Continuum QCD*, Phys. Rev. D **82** (2010) 034512 [arXiv:1004.4285].

[235] SWME collaboration, T. Bae et al., *Neutral kaon mixing from new physics: matrix elements in* $N_f = 2 + 1$ *lattice QCD*, Phys. Rev. **D88** (2013) 071503 [arXiv:1309.2040].

[236] SWME collaboration, J. Leem et al., *Calculation of BSM Kaon B-parameters using Staggered Quarks*, PoS **LATTICE2014** (2014) 370 [arXiv:1411.1501].

[237] J. T. Tsang and M. Della Morte, *B-physics from lattice gauge theory*, arXiv:2310.02705.

[238] A. J. Buras, J.-M. Gérard and W. A. Bardeen, *Large N Approach to Kaon Decays and Mixing 28 Years Later: $\Delta I = 1/2$ Rule, $\hat{B}_K$ and ΔM_K*, Eur. Phys. J. C **74** (2014) 2871 [arXiv:1401.1385].

[239] A. J. Buras and J.-M. Gérard, *Dual QCD Insight into BSM Hadronic Matrix Elements for $K^0 - \bar{K}^0$ Mixing from Lattice QCD*, Acta Phys. Polon. B **50** (2019) 121 [arXiv:1804.02401].

[240] P. Boyle, N. Garron, J. Kettle, A. Khamseh and J. T. Tsang, *BSM Kaon Mixing at the Physical Point*, EPJ Web Conf. **175** (2018) 13010 [arXiv:1710.09176].

[241] P. Boyle, N. Garron, R. J. Hudspith, A. Juttner, J. Kettle, A. Khamseh et al., *Beyond the Standard Model Kaon Mixing with Physical Masses*, PoS **LATTICE2018** (2019) 285 [arXiv:1812.04981].

[242] A. Nicholson et al., *Heavy physics contributions to neutrinoless double beta decay from QCD*, Phys. Rev. Lett. **121** (2018) 172501 [arXiv:1805.02634].

[243] W. Detmold, W. I. Jay, D. J. Murphy, P. R. Oare and P. E. Shanahan, *Neutrinoless double beta decay from lattice QCD: The short-distance π-$\to\pi$+e-e-amplitude*, Phys. Rev. D **107** (2023) 094501 [arXiv:2208.05322].

[244] J. T. Tsang, *Neutral meson mixing in the $B^0_{(s)}$ sector from Lattice QCD*, PoS **CKM2021** (2023) 107 [arXiv:2204.01259].

[245] P. Boyle, F. Erben, A. Jüttner, T. Kaneko, M. Marshall, A. Portelli et al., *BSM $B - \bar{B}$ mixing on JLQCD and RBC/UKQCD $N_f = 2 + 1$ DWF ensembles*, PoS **LATTICE2021** (2022) 224 [arXiv:2111.11287].

[246] K. Nakayama, B. Fahy and S. Hashimoto, *Short-distance charmonium correlator on the lattice with Möbius domain-wall fermion and a determination of charm quark mass*, Phys. Rev. D **94** (2016) 054507 [arXiv:1606.01002].

[247] C. Morningstar and M. J. Peardon, *Analytic smearing of SU(3) link variables in lattice QCD*, Phys. Rev. D **69** (2004) 054501 [arXiv:hep-lat/0311018].

[248] P. Boyle, L. Del Debbio and A. Khamseh, *Massive momentum-subtraction scheme*, Phys. Rev. D **95** (2017) 054505 [arXiv:1611.06908].

[249] C. T. H. Davies, C. McNeile, E. Follana, G. P. Lepage, H. Na and J. Shigemitsu, *Update: Precision D_s decay constant from full lattice QCD using very fine lattices*, Phys. Rev. D **82** (2010) 114504 [arXiv:1008.4018].

[250] T. Blum et al., *Quenched lattice QCD with domain wall fermions and the chiral limit*, Phys. Rev. D **69** (2004) 074502 [arXiv:hep-lat/0007038].

[251] K. G. Chetyrkin, J. H. Kuhn and M. Steinhauser, *RunDec: A Mathematica package for running and decoupling of the strong coupling and quark masses*, Comput. Phys. Commun. **133** (2000) 43 [arXiv:hep-ph/0004189].

[252] B. Schmidt and M. Steinhauser, *CRunDec: a C++ package for running and decoupling of the strong coupling and quark masses*, Comput. Phys. Commun. **183** (2012) 1845 [arXiv:1201.6149].

[253] F. Herren and M. Steinhauser, *Version 3 of RunDec and CRunDec*, Comput. Phys. Commun. **224** (2018) 333 [arXiv:1703.03751].

[254] P. A. Baikov, K. G. Chetyrkin and J. H. Kühn, *Quark Mass and Field Anomalous Dimensions to* $\mathcal{O}(\alpha_s^5)$, JHEP **10** (2014) 076 [arXiv:1402.6611].

[255] T. Luthe, A. Maier, P. Marquard and Y. Schröder, *Five-loop quark mass and field anomalous dimensions for a general gauge group*, JHEP **01** (2017) 081 [arXiv:1612.05512].

[256] P. A. Baikov, K. G. Chetyrkin and J. H. Kühn, *Five-loop fermion anomalous dimension for a general gauge group from four-loop massless propagators*, JHEP **04** (2017) 119 [arXiv:1702.01458].

[257] P. A. Baikov, K. G. Chetyrkin and J. H. Kühn, *Five-Loop Running of the QCD coupling constant*, Phys. Rev. Lett. **118** (2017) 082002 [arXiv:1606.08659].

[258] F. Herzog, B. Ruijl, T. Ueda, J. A. M. Vermaseren and A. Vogt, *The five-loop beta function of Yang-Mills theory with fermions*, JHEP **02** (2017) 090 [arXiv:1701.01404].

[259] T. Luthe, A. Maier, P. Marquard and Y. Schroder, *Complete renormalization of QCD at five loops*, JHEP **03** (2017) 020 [arXiv:1701.07068].

[260] ALPHA collaboration, J. Heitger, F. Joswig and S. Kuberski, *Determination of the charm quark mass in lattice QCD with* $2+1$ *flavours on fine lattices*, JHEP **05** (2021) 288 [arXiv:2101.02694].

[261] P. Petreczky and J. H. Weber, *Strong coupling constant and heavy quark masses in (2+1)-flavor QCD*, Phys. Rev. D **100** (2019) 034519 [arXiv:1901.06424].

[262] Y. Maezawa and P. Petreczky, *Quark masses and strong coupling constant in 2+1 flavor QCD*, Phys. Rev. D **94** (2016) 034507 [arXiv:1606.08798].

[263] Y.-B. Yang et al., *Charm and strange quark masses and* f_{D_s} *from overlap fermions*, Phys. Rev. D **92** (2015) 034517 [arXiv:1410.3343].

[264] HPQCD collaboration, I. Allison et al., *High-Precision Charm-Quark Mass from Current-Current Correlators in Lattice and Continuum QCD*, Phys. Rev. D **78** (2008) 054513 [arXiv:0805.2999].

[265] Alpha collaboration, A. Bussone, A. Conigli, J. Frison, G. Herdo íza, C. Pena, D. Preti et al., *Hadronic physics from a Wilson fermion mixed-action approach: charm quark mass and $D_{(s)}$ meson decay constants*, Eur. Phys. J. C **84** (2024) 506 [arXiv:2309.14154].

[266] HPQCD collaboration, D. Hatton, C. T. H. Davies, B. Galloway, J. Koponen, G. P. Lepage and A. T. Lytle, *Charmonium properties from lattice QCD+QED : Hyperfine splitting, J/ψ leptonic width, charm quark mass, and a_μ^c*, Phys. Rev. D **102** (2020) 054511 [arXiv:2005.01845].

[267] C. Alexandrou, V. Drach, K. Jansen, C. Kallidonis and G. Koutsou, *Baryon spectrum with $N_f = 2 + 1 + 1$ twisted mass fermions*, Phys. Rev. D **90** (2014) 074501 [arXiv:1406.4310].